Summer 8-9-2024

# Central Nervous System Antiviral Pharmacology

Sean N. Avedissian
*University of Nebraska Medical Center*

**Central Nervous System Antiviral Pharmacology**
By

**Sean N. Avedissian**

A Dissertation

Presented to the Faculty of the University of Nebraska Graduate College in Partial Fulfillment of the Requirements for the Degree of Doctor of Philosophy

Medical Sciences Interdepartmental Area Graduate Program
Clinical and Translational Research

Under the Supervision of Professor Courtney V. Fletcher, Pharm.D.

University of Nebraska Medical Center
Omaha, NE

August 2024

Supervisory Committee:

Kimberly Scarsi, Pharm.D., MS

Lani Zimmerman, Ph.D.

DJ. Murry, Pharm.D.

Anthony Podany, Pharm.D., Ph.D.

**Acknowledgements**

This dissertation would not be possible without the support of many people.

To my wife Natsumi, thank you for being my rock. I am thankful for your support and making sure that I always had time to devote to my studies, even after the birth of our son Liam.

To my parents, Alice and Alex, thank you for making sure I had all the tools necessary to succeed in life. You provided me with food, shelter, and love, and I would not be the man I am without your guys love and support.

Next, I would like to thank my primary mentor Courtney V. Fletcher. I am very lucky to be able to call you, my mentor. I am grateful for your mentorship since joining UNMC back in Aug 2019. Coming from a different research focus, you taught me how to apply my skills to antiviral pharmacokinetic research. As I may call you my mentor, you have become more than that and I hope you know how much you and Jean mean to the Avedissian family.

I would like to thank both Kim Scarsi and Anthony Podany, whom I have worked closely with over the past 5 years. Not only are you both members of my advisory committee, but I also consider you both close friends and colleagues.

I would also like to thank the other two members of my advisory committee. Drs. Zimmerman and Murry, you have each provided guidance and knowledge improving all aspects of my research.

To the members of the Antiviral Pharmacology Laboratory, Lee, Tim, Jon, Jeff, Malik, all the past members, Michelle, Ying, I appreciate your friendship and collaborations. Without your help, I would not have data to present in this dissertation.

Finally, I want to thank the participants from ACTG 5321 who enrolled in the clinical studies associated with the research in this dissertation.

**Abstract**

Soon after viral infection, viruses like Human Immunodeficiency Virus (HIV) and SARS-CoV-2 can disseminate throughout the body and establish reservoirs in the central nervous system (CNS). The persistence of viruses in cells of these reservoirs is a major obstacle to virus eradication. This is due to the abundance of cells/receptors that these viruses utilize to gain entry into cells found at these various reservoir sites. Consequently, these same anatomical sites also may be pharmacologic sanctuaries, as evidenced by concentrations of antiretroviral drugs (ARVs) and antivirals (AVs) that are lower in reservoirs than those in peripheral blood; in some cases, these low ARV concentrations have been associated with evidence for low-level ongoing virus replication in the CNS. Neurological complications associated with viral infection are well recognized with both HIV and SARs-CoV-2 infection and are a continuing problem. Ensuring that ARVs/AVs can cross the blood-brain barrier (BBB) and maintain adequate exposure to inhibit viral replication in the CNS is a pharmacotherapeutic challenge that requires attention, especially in recent years (i.e., NeuroHIV, Long COVID). Strategies to maximize these efforts include optimizing the selection of an ARV/AV and increased dosing/intervals of ARV/AV in hopes of achieving optimal pharmacodynamic (PD) endpoints in the CNS. The inhibitory concentration is commonly the level at which 50%, 90%, or 95% ($IC_{50-95}$) of *in-vitro* viral replication is inhibited utilizing wild-type viruses. Pharmacokinetic/pharmacodynamic (PK/PD) endpoints are further complicated as no clear exposure thresholds have been identified in the CSF or CNS. The lack of such information leaves gaps in our understanding of the relative efficacy of various ARVs/AVs in the CSF/CNS. Further, assessing drug concentrations in the CNS in patients is difficult as it requires invasive methods for CSF (i.e., lumbar puncture) and tissue collection. This brings to light the utilization of pre-clinical models for potential CNS penetration. The work conducted in this dissertation highlights novel pharmacologic methods used to assess CSF and CNS penetration of various ARVs for HIV and AVs for SARs-CoV-2 using both pre-clinical and clinical models.

## Table of Contents

# LIST OF TABLES

# LIST OF FIGURES

# LIST OF ABBREVIATIONS

Note: abbreviations for purchasing chemicals/reagents not included.

| | |
|---|---|
| -2LL | negative 2 log-likelihood |
| 3CLpro | 3C-like protease |
| 3TC | lamivudine |
| ACE-2 | angiotensin converting enzyme 2 receptor |
| ABC | abacavir |
| ACN | acetonitrile |
| ACTG | AIDS Clinical Trials Group |
| AIC | Akaike information criterion |
| AIDS | acquired immunodeficiency syndrome |
| APL | Antiviral Pharmacology Laboratory |
| AR | accumulation ratio |
| ART | antiretroviral therapy |
| ATV | atazanavir |
| ARV | antiretroviral |
| AUC | area under the curve |
| AV | antivirals |
| BBB | blood-brain barrier |
| BCB | blood-CSF barrier |
| BCRP | breast cancer resistance protein |
| BIC | bictegravir |
| CAB | cabotegravir |
| CA-HIV | cell-assocaited HIV |

| | |
|---|---|
| CDC | Centers for Disease Control and Prevention |
| CL | clearance |
| CL/F | clearance based off bioavailability |
| CNS | central nervous system |
| CSF | cerebrospinal fluid |
| COVID-19 | coronavirus infectious diseases 2019 |
| $C_{max}$ | maximum concentration |
| $C_{min}$ or $C_{Trough}$ | minimum concentration |
| COBI or /c | cobicistat |
| Ct | cycle threshold |
| CYP | cytochrome P450 |
| DTG | dolutegravir |
| DRV | darunavir |
| $EC_{50 \text{ or } 90}$ | effective concentrations goals |
| EFV | efavirenz |
| EPIC-HR | FDA integrated review from clinical studies |
| ESI | electrospray ionization |
| $EVOM^2$ | epithelial volt-ohm meter |
| eGFR | estimated glomerular filtration rate |
| F | bioavailability |
| FDA | Food and Drug Administration |
| F/T | freeze and thaw stability |
| FTC | emtricitabine |
| GALT | gut-associated lymphoid tissue |
| GeoM | geometric mean |
| GDS | global deficit score |

| | |
|---|---|
| GMR | geometric mean ratio |
| GSH | golden Syrian hamster |
| hBMECs | human brain microvascular endothelial cells |
| HAND | HIV-associated neurocognitive disorders |
| HIV | human immunodeficiency syndrome |
| HPLC | high performance liquid chromatography |
| IACUC | institutional animal care and use committee |
| $IC_{50-95}$ | concentration at which 50, 90 or 95% inhibition is achieved |
| INSTI | integrase strand transfer inhibitor |
| IQ | inhibitory quotient |
| IV | intravenous |
| Ka | oral absorption rate constant |
| Kp | plasma concentration-corrected brain concentrations |
| JAMs | junctional adhesion molecules |
| LC-MS/MS | liquid chromatography mass spectrometry with tandem mass spectrometry |
| LLOQ | lower limit of quantification (may also be expressed as LOQ) |
| LN | lymph nodes |
| LogP | lipophilicity coefficient |
| MBECs | microvascular brain endothelial cells |
| ME | matrix effect |
| MFI | mean fluorescence intensity |
| MIC | minimum inhibitory concentration |
| MMP9 | matrix metalloproteinase-9 |
| MRM | multiple-reaction-monitoring |
| MRP2 | multidrug resistance protein 2 |
| Mpro | peptidomimetic inhibitor of the SARS-CoV-2 main protease |

| | |
|---|---|
| NPAG | nonparametric adaptive grid |
| NAT2 | n-acetyl transferase 2 |
| NCA | non-compartmental analysis |
| NIH | National Institutes of Health |
| NNRTI | non-nucleoside reverse transcriptase inhibitor |
| NRTI | nucleoside/nucleotide reverse transcriptase inhibitor |
| nsp5 | nonstructural protein 5 protease |
| OATP2 | organic anion transporter 2 |
| OCT2 | organic cation transporter 2 |
| $P_{app}$ | passive apparent permeability |
| PASC | post-acute sequelae of COVID-19 |
| PBMC | peripheral blood mononuclear cells |
| PBPK | physiologically based pharmacokinetic |
| PD | pharmacodynamic |
| Pgp | P-glycoprotein |
| PK | pharmacokinetic |
| PLWH | people living with HIV |
| PO | by mouth |
| PTM | SIV-infected pigtailed macaques |
| PPS | post preparative stability |
| QC | quality control |
| NMR/r | ritonavir-boosted nirmatrelvir |
| RAL | raltegravir |
| RNA | ribonucleic acid |
| RT | room temperature |
| RT-PCR | real-time polymerase chain reaction |

| | |
|---|---|
| RTV | ritonavir (may also be expressed as r/ when co-administered with another agent) |
| STD | standard |
| $T_{1/2}$ | half life |
| TAF | tenofovir alafenamide |
| TEER | trans epithelial electrical resistance |
| TDF | tenofovir disoproxil fumarate |
| $T_{max}$ | time at which maximum concentration is first observed |
| TFV | tenofovir |
| UGT | uridine glucosyl transferase |
| ULOQ | upper limit of quantification |
| V/F | volume of distribution based on bioavailability |
| WHO | World Health Organization |
| ZDV (AZT) | zidovudine (azidothymidine) |

# Chapter 1: Introduction, Overview, Framework and Premise

## 1.1 CNS and BBB Overview

CNS is a complex system that acts as the processing center for everything in your body. It is comprised of the brain and spinal cord, where each contains specific cells important for everyday function. The CNS has various blood vessels that are required to provide oxygen, energy, metabolites, and nutrients to brain cells. For example, the brain requires 20% of the body's glucose and oxygen but only accounts for 2% of total body masse. Due to its importance, blood supply is closely monitored via the cardiovascular system that ensures continuous, oxygenated blood is always delivered and available to the CNS[1]. This is important as the blood flow indirectly controls the rate at which pharmacological agents reach the CNS (significant for orally and intravenously administered drugs). Control of what can get in and out of the CNS is regulated by an important barrier known as the blood-brain barrier (BBB).

The BBB is a protective vascular barrier keeping the brain safe from the detrimental effect of toxins and pathogens[2-4]. The BBB is a semipermeable border of endothelial cells that prevents entry of drugs from the blood stream into the CNS. The BBB restricts entry of pathogens, diffusion of solutes and large or hydrophilic molecules into the CSF, while allowing diffusion of hydrophobic and small polar molecules[5]. It is present at various places throughout the brain's vasculature which includes: (I) barrier by endothelial cells, (II) barrier by avascular arachnoid epithelium, and (III) barrier at the choroid plexus (aka: blood CSF barrier [BCB])[6]. The structural component of the BBB primarily includes microvascular brain endothelial cells (MBECs) lining the cerebral blood vessels[7], pericytes that share the basement membrane with endothelial cells[8], and astrocytes with their tendrils for communication with neighboring cells[9, 10] **(Figure 1).** Expression of tight

junction proteins, namely, occludins, claudins, junctional adhesion molecules, and cytoplasmic accessory proteins by MBECs, astrocytes, and pericytes play a pivotal role in barrier formation[11-13]. Despite tight junction formation by peripheral capillary endothelial cells, the TEER (transepithelial electrical resistance) value observed is 2-fold less when compared to the BBB, pointing to a bidirectional paracellular transport of molecules across the capillary endothelial cells[14, 15]. TEER is often used to assess strength and integrity of barriers via measurements of electrical resistance across cell layers in vitro[16]. The BBB-associated brain endothelial cells are distinct from capillary endothelial cells and exhibit extensive fenestration and enhanced tightness of intercellular junctions with lower pinocytotic function[14, 17, 18]. The unique features of the BBB enable ionic homeostasis and optimal nutrition maintenance in the CNS[19]. There is passive permeability for essential water-soluble nutrients across the BBB, while other nutrients engage with specific transporters for nervous tissue requirements[20, 21].

The constituent cells of the BBB express efflux transporters, including ATP-binding cassette (ABC) proteins P-glycoprotein (Pgp), and breast cancer resistance protein (BCRP)[22]. These efflux transporters, as crucial as they are to BBB regulation, can pump out pharmacologically important molecules from the brain[23, 24]. The critical role of these protein pumps has been shown in knock-out animals, confirming that many small molecules used as drugs are a substrate for these protein pumps and are excluded by the BBB resulting in lower efficacy for many drugs (e.g., chemotherapy)[25-27]. The BBB, being important for regulating which molecules can pass from the blood into the brain, can hinder drug penetration leading to sub-optimal drug concentrations in the CNS and making it difficult to treat CNS related infections[28, 29].

As mentioned previously, the CNS is comprised of many different types of cells. These cells express diverse types of receptors and transporters that can be targets for viral entry and infection (i.e., astrocytes/pericytes). It is important to note the difference between transporters and receptors. Receptors are cell membrane proteins that play a crucial role in cell signaling and communication. Transporters are also membrane proteins, but their primary function is to facilitate

movement of ions, molecules, and peptides across lipid bilayers. This dissertation will focus on HIV and Severe Acute Respiratory Syndrome Coronavirus 2 (SARs-CoV-2) infection in the CNS.

## 1.2 SARS-CoV-2 Infection and CNS

SARS-CoV2 is a single-stranded (positive-sense) RNA virus (Baltimore classification group IV) and is the causative agent of coronavirus infectious disease 2019 (COVID-19). Since the first cluster of cases back in 2019 in Wuhan, China, COVID-19 has now transitioned to an endemic[30]. SARS-CoV-2 utilizes the angiotensin converting enzyme 2 receptor (ACE-2) to gain entry into our cells. The ACE-2 receptor is expressed in several tissues, especially on epithelial cells of the lungs. Although SARS-CoV-2 is often referred to as a respiratory virus, in addition to the lung, it has been found in tissues including the brain, liver, intestine, feces, heart, and kidneys of individuals with COVID-19[31]. A summary of the lifecycle for SAR-CoV-2 can be found in **Figure 2.**

Post-acute sequelae of COVID-19 ([PASC], prevalence of ~7.5%), also known as Long COVID, is a chronic syndrome that affects some individuals who have recovered from acute COVID-19 illness[32]. While most people clear the virus, some experience persistent neuro-specific PASC (neuroPASC) symptoms (e.g., CNS disturbances)[33] lasting for months after the infection[34]. Based on available literature, the related incidence, risk factors, possible pathophysiology, and proposed management of neurological manifestations has been summarized by Moghimi et al.[35]. While the majority of SARs-CoV-2 infected persons no longer show symptoms after recovering from infection, some experience persistent neuro-specific PASC (neuroPASC) symptoms (e.g., depression, anxiety, difficulty concentrating, central nervous system [CNS] disturbances) [36]lasting months or even years after the infection[34, 37]. Interestingly, fatigue has been observed as one of the most common symptoms associated with Long COVID[38, 39]. The etiology of neuroPASC is

unclear, and the exact mechanisms of SARS-CoV-2 entry into the CNS are uncertain. Some theories for entry include infection of the endothelium, access through the BBB, and through nervous tissue conduits that bypass the BBB. Given that cells in the CNS can be infected with SARS-CoV2[40], it is plausible that CNS infections lead to the neurological complications described by neuroPASC[41-43]. Another theory is that neuroPASC is due to prolonged inflammation present in the CNS post-infection. This theory is supported by both clinical and animal data in persistent SARs-CoV-2 infection[44, 45]. Clinical data from autopsy sampling performed on the CNS of patients who died from COVID-19 found viral RNA, with patients having detectable CNS virus from 4-230 days after infection[46]. A study by Beckman et al. showed that COVID neuroinvasion (non-human primate model) was more significant and widespread throughout the olfactory cortex in older animals than younger ones. They also found axonal spread of the virus from the nasal olfactory epithelium. In the older monkeys, there was an increase in viral load, more pronounced cellular alterations, and neuroinflammation (unclear mechanism)[47]. Furthermore, preliminary data (under review) from our group utilizing the Golden Syrian Hamster (GSH) model has shown ongoing systemic inflammation for up to 35 days after infection **(Figure 3)** and has shown that cells of the BBB can get infected **(Figure 4).** Given data to support viral entry into the CNS[48], and the known neurological issues associated with neuroPASC, early and effective antiviral treatment of acute COVID-19 may offer hope in preventing or reducing neuroPASC occurrence and severity[49, 50].

## 1.3 HIV Infection and the CNS

HIV is a single-stranded RNA virus (classified under Baltimore group VI) belonging to the lentivirus genus within the retroviridae family. Its primary target is the immune system, gaining entry into cells through the CD4+ cellular receptor/co-receptor. Without intervention, the virus gradually destroys immune system cells like T cells, macrophages, and dendritic cells, resulting

in acquired immunodeficiency syndrome (AIDS)[51, 52]. A summary of the HIV lifecycle can be found in **Figure 5**. Globally, there were approximately 39 million persons living with HIV (PLWH) by the end of 2022, of these, 37.5 million were adults, and 1.5 million were children (<15 years old). Further, an estimated 1.5 million were classified as new infections and HIV-related mortality remains a significant contributor to infection-related deaths, causing around 630,000 AIDS-related fatalities in 2022. Notably, according to the WHO report on HIV, only an estimated 29.8 million (76%) PLWH are currently receiving antiretroviral therapy (ART) for their HIV.

In this 5th decade of the HIV epidemic, and despite the success of combination ART in achieving potent, long-term HIV suppression, HIV-associated neurocognitive disorders (HAND) remain common in PLWH and increase the risks of morbidity and mortality. A study in 1555 HIV-infected adults from 6 university clinics from across the United States found 52% of the patients had some form of HAND[53]. This estimation is within range with what other studies have shown for the occurrence of HAND (range: 15-55%) in PLWH[54, 55]. HAND is an end-organ manifestation of HIV infection and refers to a constellation of disorders in memory, concentration, attention, and motor skills. In the current ART era, there has been an increase in milder forms of HAND [mild neurocognitive disorder (MND) and asymptomatic neurocognitive impairment (ANI)] and a decrease in HIV-associated dementia. Recent data suggest that even in the setting of long-term viral suppression, there is evidence for ongoing progression of HAND[56].

Within one to two weeks after acquisition of HIV, the virus disseminates throughout the body and establishes multiple reservoir sites including the CNS, adipose tissue, male and female reproductive tracts, the secondary lymph nodes (LN) and gut-associated lymphoid tissue (GALT). The persistence of latent virus in cells of these reservoirs is a major obstacle to virus eradication. Furthermore, these same anatomical sites may be pharmacologic sanctuaries, as evidenced by concentrations of ARVs lower than those in peripheral blood, and in some cases associated with evidence for low-level ongoing virus replication[57, 58].

HIV infects perivascular macrophages, microglial cells and astrocytes at an early stage of infection[59]. Several lines of evidence suggest the brain represents a persistent and stable HIV reservoir. CSF viral escape is the presence of quantifiable CSF HIV-RNA in persons with undetectable plasma HIV-RNA or levels of CSF HIV-RNA that exceed plasma[60]. A recent study detected CSF viral escape in 55 (4.4%; 95% CI, 3.4-5.6) of 1264 PLWH who had plasma HIV-RNA <50 copies/mL[61]. CSF viral escape was independently associated with use of ritonavir-boosted protease inhibitors (PIs) and unboosted atazanavir (ATV). There were similar rates of neurocognitive impairment in those with (38.2%) and without (37.%) CSF escape. Not all cases of CSF viral escape are symptomatic; however, those that are would seem to provide strong evidence of a CNS viral reservoir containing replication competent virus[62].

The extent and significance of HIV persistence in the CSF in PLWH who have long-term plasma HIV-RNA suppression has not been well-described. HIV persistence and biomarkers of immune activation in CSF and neuropsychological evaluations were performed in 69 PLWH on long-term (median of 8.6 years) ART with viral suppression (67/69 with plasma HIV-RNA <40 copies/mL; 2 <100 copies/mL). HIV-DNA was detected in CSF in 48%[63]. The presence of CSF HIV-DNA was associated with significantly worse neurocognitive dysfunction measured via a 7-domain neuropsychological test battery and z score/deficit score assessment. Notably, it is important to mention that it was not surprising that CSF HIV-RNA was not detected given these patients were on long-term ART with viral suppression. CSF levels of immune activation (e.g., neopterin) were not associated with CSF HIV-DNA detection. Animal models provide important evidence on HIV replication and establishment of viral reservoirs in the brain. In SIV-infected rhesus macaques (RM), in-vivo imaging showed vRNA-positive cells were higher in brain tissues, likely due to poor ARVs penetration[57]. After six-months of ART, only a two-fold decrease in vRNA-positive cells was observed in brain versus >30-fold decrease in vRNA-positive cells in other LT compartments[57]. In SIV-infected pigtailed macaques (PTMs) receiving ART, 56% developed lymphocyte dominant encephalitis and meningitis due to infiltration of B and T immune cells[64].

These findings suggest that dysregulated immune responses in PLWH might contribute to the development of HAND. Recently, the majority of ART-treated, virally-suppressed PTMs (N=30) were shown to have replication-competent SIV in brain macrophages[65]. These data strongly indicate presence of a macrophage latent reservoir in the brain that could reestablish infection after treatment interruption. Collectively, these data argue the CNS has continued viral replication, is a viral reservoir and pharmacologic sanctuary, and therefore, an obstacle necessary to overcome to achieve HIV eradication and improve neurocognitive function.

## 1.4 SARS-CoV-2 Treatment Approaches

Currently, effective antivirals to treat COVID-19 are limited. Preventative measures in the form of vaccination remain the best line of defense to prevent negative outcomes post COVID-19 infection. Since the beginning of the pandemic in 2019, various therapeutic options have been explored as effort was shifted into advancing treatment for SARS-CoV-2. Currently, NIH guideline recommendations for treatment of COVID is divided by severity (mild/moderate), need of oxygenation, inpatient/outpatient status, and special populations[66]. This chapter will focus on recommendations for adult patients. A summary table for all severity risk by tier can be found on **Table 1.**

For management of nonhospitalized adults with mild to moderate COVID-19 who do not require supplemental oxygen, treatment with AV agents is only recommended for persons who are at high risk of progressing to severe COVID-19. For these persons it is recommended to start one of the preferred therapy as soon as possible: A). Ritonavir-boosted nirmatrelvir ([NMR/r] Paxlovid), or B). Remdesivir. As an alternative to the 2 preferred AVs, molnupiravir can be initiated. A summary of these recommendations for can be found on **Table 2.**

For management of hospitalized adults, treatment recommendations are further stratified by disease severity. Severity of disease ranges from “hospitalized for reasons other than Covid”

to “hospitalized and requires mechanical ventilation or extracorporeal membrane oxygenation”. Therapeutic recommendations will be different depending on disease severity. Briefly and starting from the least severity, only patients that don’t require oxygenation but are at high-risk of progressing to severe COVID-19 (based on **Table 1**) should be given remdesivir. Once patients require oxygenation, remdesivir and dexamethasone can be considered. If oxygen needs continue to increase and the patient shows signs of systemic inflammation, immunomodulators can be considered. If the oxygenation requires high flow nasal canula or noninvasive ventilation, a combination of dexamethasone, immunomodulators and remdesivir can be initiated. Finally, if the patient requires mechanical ventilation or extracorporeal membrane oxygenation, a 2$^{nd}$ immunomodulator (either baricitinib or tocilizumab) should be added. As this summary is an oversimplification, more details can be found on **Table 3.** It should be noted that for hospitalized patients, regardless of the disease severity, anticoagulation should be considered unless contraindicated.

A detailed summary of all currently recommended treatment options for COVID-19 for both hospitalized and non-hospitalized patients with duration and adjustments can be found on **Table 4.** Unfortunately, specific treatment recommendations for neuroPASC (aka Long COVID) are lacking.

## 1.5 HIV Treatment Approaches and Guideline Recommendations

A significant breakthrough in HIV and AIDS treatment occurred in the late 1990s with the introduction of three-drug combination ART. Combination ART aims to enhance the effectiveness of ARVs synergistically in treating HIV. Presently, the DHHS recommends initiating HIV treatment with a combination of two or three ARVs[67]. There are several classes of HIV therapies that target different processes of HIV replication. Currently, there are seven classes of ARVs:

nucleoside/nucleotide reverse transcriptase inhibitors (NRTIs), non-nucleoside reverse transcriptase inhibitors (NNTRIs), PIs, entry inhibitors (i.e., fusion inhibitors), integrase strand transfer inhibitors (INSTIs), CCR5 antagonists, and post-attachment inhibitors[67]. The overarching goals of HIV therapy, as outlined by the United States Department of Health and Human Services (DHHS), include achieving sustained suppression of plasma HIV RNA, restoring and maintaining immunological function, reducing HIV-associated morbidity, extending survival duration and quality, and preventing HIV transmission. The standard approach to HIV treatment has been triple drug therapy, involving three drugs from at least two different drug classes. Combination therapy is necessary due to HIV's rapid replication cycle and the high error rate of its viral polymerase during nucleotide incorporation. As such, with monotherapy, the virus can develop resistance mutations, making it challenging to treat and potentially passing on these mutations in the setting of HIV transmission. More recently, potent INSTI agents have been approved, significantly reducing HIV viral load within weeks of initiation (similar observation in PIs). This efficacy has led to the approval of dual therapy approaches to HIV treatment.

NRTIs were the first developed and approved class of ARVs. They mimic endogenous nucleotides and require cellular kinases for activation within the cell. Once incorporated into viral DNA, NRTIs function as chain terminators, lacking the necessary hydroxy group for DNA chain elongation. NNRTIs, similar to NRTIs, focus on the reverse transcriptase (RT) enzyme. However, their mode of action differs significantly from NRTIs. NNRTIs do not resemble endogenous nucleotides. Instead, they work by reducing the activity of HIV RT. These medications bind noncompetitively to a specific pocket within the subdomain of RT, causing allosteric inhibition of the enzyme by altering the position of critical amino acids within the catalytic site of the RT enzyme. Regarding INSTIs, integrase is a vital viral enzyme necessary for integrating viral DNA into the host genome. First, integrase cleaves the terminal dinucleotide from each 3’ end of the viral DNA. Second, the 3’ ends act as nucleophiles, initiating a strand transfer reaction, thereby integrating viral DNA into the host cell DNA. INSTIs function by inhibiting the second reaction,

thereby preventing the insertion of viral DNA into the host cell DNA. PIs block the viral enzyme protease, preventing the maturation of new virions and causing viral death. Fusion inhibitors block the merging of the HIV envelope with the host CD4 cell membrane, hindering viral entry into the cell. CCR5 antagonists prevent the attachment of the chemokine receptor 5 molecule to CD4, an essential step in viral entry. Post-attachment inhibitors prevent attachment of the CCR5 or CXCR4 co-receptor by binding to the CD4 receptor, collectively constituting a group of entry inhibitors.

Specific to CNS ARV treatment, **Table 5** gives a summary of select CSF penetration characteristics of ARV that are included in the regimens for treatment-naïve PLWH. Highlights of select features follow. NRTIs. Zidovudine (ZDV) has the best CNS penetration rank in brain and CSF and can be used in PLWH who have symptomatic CSF escape[62, 68]. Tenofovir (TFV) can be given as tenofovir disoproxil fumarate (TDF) or as tenofovir alafenamide (TAF). TDF may achieve higher CSF concentrations than TAF, based on a single PLWH who switched from a TDF- to a TAF-containing regimen and tenofovir CSF concentrations decreased from 3.30 to 0.46 ng/mL[69]. NRTIs are transported via OATs and changes in their activity due to co-administered drugs (e.g., probenecid) or genetic polymorphisms can affect the CSF concentrations of certain NRTIs[70]. PI. As a class, PIs achieve poor CSF exposure, although some, for example lopinavir, achieve CSF concentrations above the $IC_{50}$. PI CSF penetration can be increased with low-dose ritonavir (RTV or /r) or cobicistat (COBI or /c) co-administration[71, 72]. ATV CSF concentrations increased with ritonavir (from 7.9 to 10.3 vs. ng/mL), but did not always exceed the $IC_{50}$ (i.e., current standard pharmacodynamic [PD] measure)[73]. The IC is commonly the level at which 50, 90 or 95% (i.e., $IC_{50\text{-}95}$) of *in vitro* viral replication is inhibited utilizing wildtype viruses. A study in PLWH showed darunavir CSF concentrations were comparable when co-administered with either COBI or RTV (15.9 ng/mL vs. 16.4 ng/mL, p=0.58)[72]. PIs are substrates for Pgp, OAT1 and OAT2; similar to NRTIs, this can decrease their CSF penetration[74-76]. NNRTIs. Among the class, nevirapine has the highest CSF penetration[77]. Efavirenz (EFV) CSF concentrations are generally sufficient to suppress HIV in the CSF[78]. Srinivas et al. found CSF concentrations of 6 ARVs (TFV,

emtricitabine [FTC], raltegravir [RAL], maraviroc, ATV and EFV) were >13-fold lower than brain tissue in non-human primates, with poor agreement between CSF and brain tissue except for EFV (r= 0.91, P<0.001)[79]. Etravirine CSF concentrations were >$IC_{50}$ in twelve PLWH and viral suppression was achieved in both plasma and CSF[68]. A recent study in PLWH receiving intramuscular rilpivirine (and cabotegravir [CAB]) found CSF concentrations were 1.1-1.3% of plasma and exceeded the IC50[80]. INSTIs. RAL CSF concentrations exceed the IC95 and is used in regimens designed for improved CSF penetration. The fractional CSF penetration of dolutegravir is low, though concentrations were above the IC50[81]. This scenario is similar for bictegravir (BIC), with CSF concentrations above the $IC_{50}$ in 15 PLWH[82]. There are limited CSF penetration data on injectable CAB. CAB CSF concentrations were 0.3% of plasma and exceeded the $IC_{50}$ in 16 PLWH, who all had HIV-RNA <50 copies/mL in plasma and CSF[80].

Two guidelines often used for HIV treatment recommendations for adults/adolescents are the DHHS Recommendations for PLWH and the World Health Organization (WHO) First-Line ART Recommendations[67, 83]. Suttle differences in recommendations between the two guidelines can be found (**Table 6a and b**). For initial ARV treatment, the DHHS guidelines generally recommend two NRTIs administered in combination with a third active ARV drug from one of three classes: INSTI, NNRTI, or PI with booster. This guideline also supports the use of a two-drug regimen consisting of DTG plus 3TC for initial treatment. Alternative regimens are also recommended, which can be found in **Table 6a**. For the WHO guidelines, the first-line treatment recommendation consists of two NRTIs in combination with a third INSTI or NNRTI (TDF + 3TC [or FTC] + DTG or TDF + 3TC + EFV). Other important situational considerations for treatment are also mentioned in these guidelines, which can be found in greater detail in **Table 6b**.

## 1.6 CNS Pharmacology and Drug Penetration

For drugs to enter the CNS, they must first pass through the appropriate barriers (i.e., BBB, BCB). The BBB is a semipermeable border of endothelial cells that prevents entry of drugs from the blood stream into the CNS. It is comprised of endothelial cells, astrocytes and pericytes. The BBB restricts entry of pathogens, diffusion of solutes and large or hydrophilic molecules into the CSF, while allowing diffusion of hydrophobic and small polar molecules[5].

The degree of drug CNS penetration is dependent on the brain's permeability attributes and various drug characteristics that include molecular weight, protein binding, ionization, and lipid-water partition coefficient[81]. A highly protein-bound drug will have a lower extent of penetration. The blood-CSF barrier can play a role in CNS penetration. An in-depth description of the BCB has been published by Nau[84]. Higher penetration of ARVs into LN, gut and brain tissues of the BALB/c mouse model was associated with higher dissociation constant (pKa), higher lipophilicity (logP) and increased hydrophobicity[85]. Further, Lipinski's rule of five can also be used that postulates a lipophilicity range of 2.0 to 3.5 is a fundamental predictor for BBB penetration via passive diffusion[86]. The transporters, Pgp, organic anion transporters (OAT 1,2,3) and BCRP, found at the BBB also influence drug penetration due to transporter-mediated efflux and transport of organic anions across the cell membranes. This mechanism has been implicated in some refractory CNS disorders (i.e., refractory epilepsy)[87]. Transporter expression may be influenced by genetic polymorphisms. More specifics about certain ARVs and transporters can be found in section 1.7.

Specific to HIV, animal models have shown that ARV CSF penetration does not always correlate with brain tissue penetration[79]. Discrepancies have been attributed to ARV affinity for drug uptake and efflux at the BBB and blood-CSF barrier. Protein-binding plays a role as active transport of ARVs across the BBB and blood-CSF barrier disturbs the equilibrium of passive unbound drug movement (the "free drug hypothesis"), which may result in differences of ARV

concentrations in plasma, CSF and brain tissues[79]. The CSF has low binding protein concentrations compared with plasma and studies of ARVs in the CSF have found the drug present is mostly unbound. However, in 17 PLWH, etravirine had higher protein-binding in CSF (98.4%) than in plasma (96%)[88]. A methodological challenge for ARV quantitation in CSF was described by Mykris et al. who showed non-polar ARVs can adsorb to polypropylene collection tubes[89]. This suggests some re-examination of ARV concentrations in CSF in PLWH who are/are not virologically-suppressed may be warranted.

The goal of ART or AV is to inhibit viral replication throughout the body and maintain an undetectable viral load. This is achieved by optimizing PK/PD parameters such that sufficient concentrations are achieved to inhibit viral replication and minimize emergence of viral resistance, and so that the drug is safe and well-tolerated. The inhibitory quotient (IQ) is a useful concept to achieve the former (only validated in HIV, not SARS-CoV-2); it is the ratio of drug concentration achieved to the *in vitro* inhibitory concentration ($IC_{50-95}$). These in-vitro concentrations are often obtained in protein-free conditions, which for clinical translation of highly protein-bound drugs to concentrations necessary in plasma, requires protein-binding adjustment. Binding in the CSF, however, may be different from plasma. CNS PK/PD endpoints are further complicated as no clear exposure thresholds have been identified for both HIV and SARS-CoV-2 in the CSF. CSF viral loads are often used as a marker of AV activity given its established dose-concentration-response relationship for AVs in plasma. A comprehensive list for ARV pharmacological characteristics and potential CSF exposure can be found on **Table 6.**

## 1.7 ARV Metabolism and Transporters

It is also important to mention major metabolism pathways and transporter interactions as they can affect the PK of ARVs and potential drug concentrations in the CNS. PK interactions

include hepatic enzyme induction, enzyme inhibition, and protein-binding displacement. Importantly, these interactions may be reciprocal and, if unrecognized, could lead to subtherapeutic drug concentrations at target sties like the CNS. These interactions can affect the PK of the drugs, affecting their potential therapeutic utility. Drugs that induce primary metabolic enzymes and transporters may decrease plasma concentrations of drugs. Drugs that inhibit these metabolic enzymes or transporters may increase plasma concentrations. This same relationship is applicable to CNS concentrations. Studies have shown that transporters often work close together with drug-metabolizing enzymes for drug-specific absorption/elimination[90]. For example, DTG's major route of metabolism is via phase II uridine glucosyl transferase (UGT1A) metabolism with some cytochrome P450 3A (CYP3A) involvement. Drugs that induce these enzymes and transporters may decrease concentrations of DTG. Drugs that inhibit these enzymes may increase DTG concentrations. For example, ATV, a PI, is an inhibitor of UGT1A. In a study of adult patients who were receiving both DTG and ATV, plasma concentrations of DTG were significantly higher than those of patients who received other ARVs (2,399 [1,929-4,070] vs 738 [552-1,048], 603 [432-1,373] or 1,045 [856-1,115] ng/ml; $P<0.001$ for all comparisons)[91]. Pharmacologically, these types of interactions can be used to boost levels of drugs, as often seen with the co-administration of /r or /c in protease inhibitor regimens. Also, different adjustments to dosing strategies can be used to address these interactions (i.e., double the dose, half the dose, dose every other day) depending on the situation and the effect. The University of Liverpool DDI tool is a good resource that can be utilized to address most of these issues. Further, these metabolic effects can differ in certain situations, like with prodrugs that require activation. Prodrugs also differ depending on the specific type of activation, which is based on how the body converts the prodrug into the final active drug form (Type IAB [intracellular bioactivation], IIABC [extracellular bioactivation]). Consequently, a co-administered medication that induces an activating enzyme (Type 1B) for the drug of question would result in increased concentrations of that drug due to increased conversion. These effects should always be considered as it can affect

both activity and toxicity for a given drug. A list of ARVs with corresponding metabolic enzymes and drug transporter relationships can be found on **Table 7**. A comprehensive review of membrane transport considerations for drugs can be found in a manuscript published by Giacomini et al.[90]. Notable, food can also affect the absorption of ARVs (not discussed in detail) but should be noted for each ARV.

Less is known regarding the induction and inhibition potential of the non-CYP and UGT enzymes. For example, carboxylesterase 1 (CES1) is a non-CYP enzyme that catalyzes hydrolysis in drugs with ester or amide bonds. It is known to convert prodrugs to their active forms and may be important for cellular uptake of some agents such as TAF[92, 93]. Many substances like cannabidiol have been shown to inhibit CES1 in *in vitro* studies. The clinical relevance of drug interactions involving CES1 in PLWH is yet to be established.

In addition to drug-metabolizing enzymes, drug interactions can also involve inhibition or induction of intestinal transporters and inhibition of hepatic uptake transporters and transporters involved in renal secretion. Drug transporters are expressed in the small intestine, liver, kidney, BBB, BCB and maternal–fetal barrier[94]. Influx and efflux transporters facilitate the transport of drugs into and out of cells, respectively. Transporters can have major effects on drug disposition and pharmacologic effects, including toxicity, and can be the target of drug interactions. Influx transporters that increase oral absorption include the organic anion transporters (OAT), organic cation transporters (OCT), organic anion transporting polypeptides (OATP), peptide transporters (PPT), and large neutral amino acid transporter 1 (LAT). Conversely, efflux transporters can limit drug absorption by increasing the excretion of drugs into the intestinal lumen from the systemic circulation. Examples of these efflux transporter proteins that are most commonly cited as perpetrators of PK interactions include Pgp, BCRP, and multidrug resistance proteins (MRPs). A list of known transporter interactions with ARVs can be found on **Table 7**.

## 1.8 Overview, Focus and Framework of Thesis Research Project

The overarching focus of this dissertation was to study AV and ARV penetration into the CNS specifically for COVID-19 and HIV agents. This was accomplished by performing both pre-clinical and clinical studies that incorporated animal models, cell models, clinical models and Pharmacokinetics (PK). These different models allowed for evaluating the same drugs in different models which is useful when clinical sampling requires invasive methods for CSF collection.

The pre-clinical models, divided into *in vitro* and in vivo models, highlight ways of estimating CNS penetration pre-clinically. Chapter 2 of this dissertation will focus on *in vitro* methodology used to conduct the pharmacologic evaluations of CNS drug penetration. Specifically, it discusses a 4-cell transwell plate model that contains cells relevant to the BBB. Chapter 3 will transition to in vivo models where animals will be used to evaluate CSF levels of an AV.

The clinical studies conducted as part of this dissertation sought to answer whether effective CSF concentrations of 9 different ARVs as a regimen in PLWH would affect virus detection in the CNS. This was done by estimating CSF exposure of these 9 ARVS utilizing population PK methodologies. This will be discussed in greater detail in Chapter 4. Chapters 2 through 4, collectively showcase a translational approach (bench to bed) to AV/ARV CNS pharmacology (**Figure 6**). Finally, Chapter 5 summarizes the data presented in this dissertation, provides limitations of this work and presents options for future directions of research. The data and studies presented in this dissertation focus on three major objectives.

**Objective 1**

1). Develop a reliable *in vitro* cell model to estimate drug penetration into the BBB.

**Objective 2**

2). Determine if NMR can penetrate the CNS at adequate concentrations to treat SARS-CoV-2.

**Objective 3**

3A). Utilize PK modeling to standardize ARV exposure to allow for more accurate calculation of an IQ ratio and CSF penetration.

3B). Develop a regimen IQ for ART and investigate correlations with viral PD outcomes (i.e., viral DNA, inflammation, GSD score) in patients.

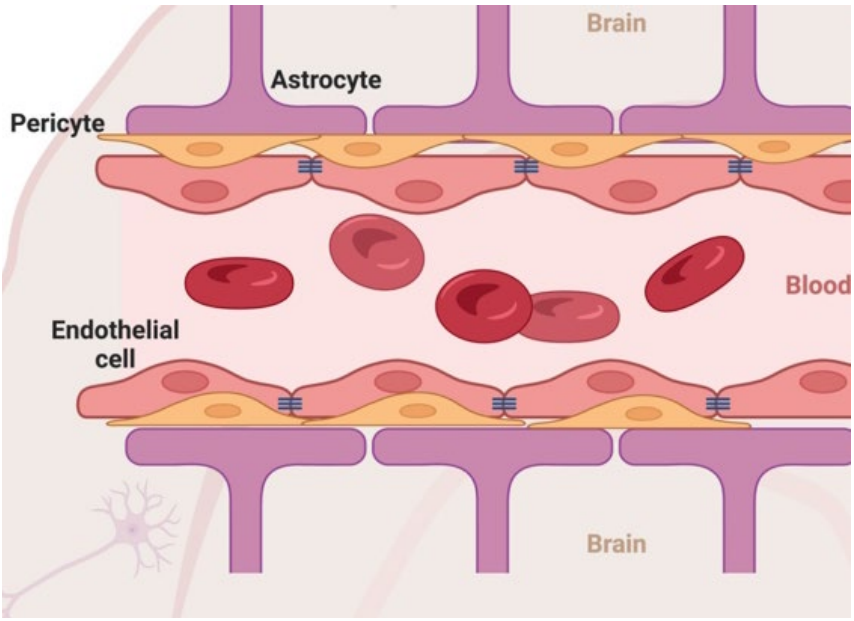


*Figure was generated utilizing Biorender.com

**Figure 1.** Presentation of BBB interplay with constituent cells of the BBB. Figure shows physiological depiction of how blood, brain and cell layers interact at the BBB.

Abbreviations: BBB, Blood-brain-barrier

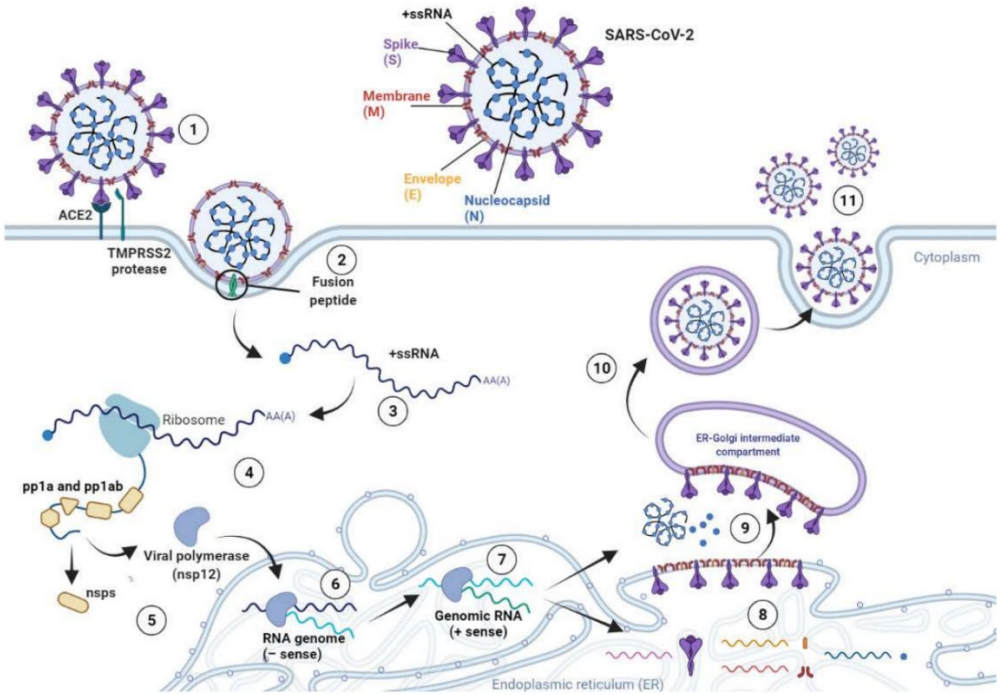


Image adapted from Rotondo et al.[95]

**Figure 2.** Lifecycle of SARS-CoV-2 shown in 11 steps. Step descriptions: (**1**) Binding between S glycoprotein and ACE-2 receptor on the surface of host cell. (**2**) Fusion peptide undertakes conformational changes allowing fusion and entry of virus into the cell cytoplasm. (**3**) Release of viral single-stranded positive RNA genome. (**4**) Viral genome is immediately transcribed by host cell ribosomes. (**5**) The translated RNA encodes polyproteins (pp1a and pp1ab) and the viral RNA-dependent RNA polymerase NSP12. (**6**) NSP12 produces full-length negative-sense copies of viral RNA. (**7**) The negative-sense RNA genome is employed as a template for generating the new positive-sense genomes. (**8**) The translation of the viral RNA occurs in the endoplasmic reticulum of host cells and leads to the synthesis of structural proteins. (**9**) Structural proteins move into the Golgi intermediate compartment where viral assembly occurs. (**10**) Mature viral progeny germinates from the intermediate compartment of the Golgi, and it is released as secretory vesicles. (**11**) Virions are secreted by exocytosis.

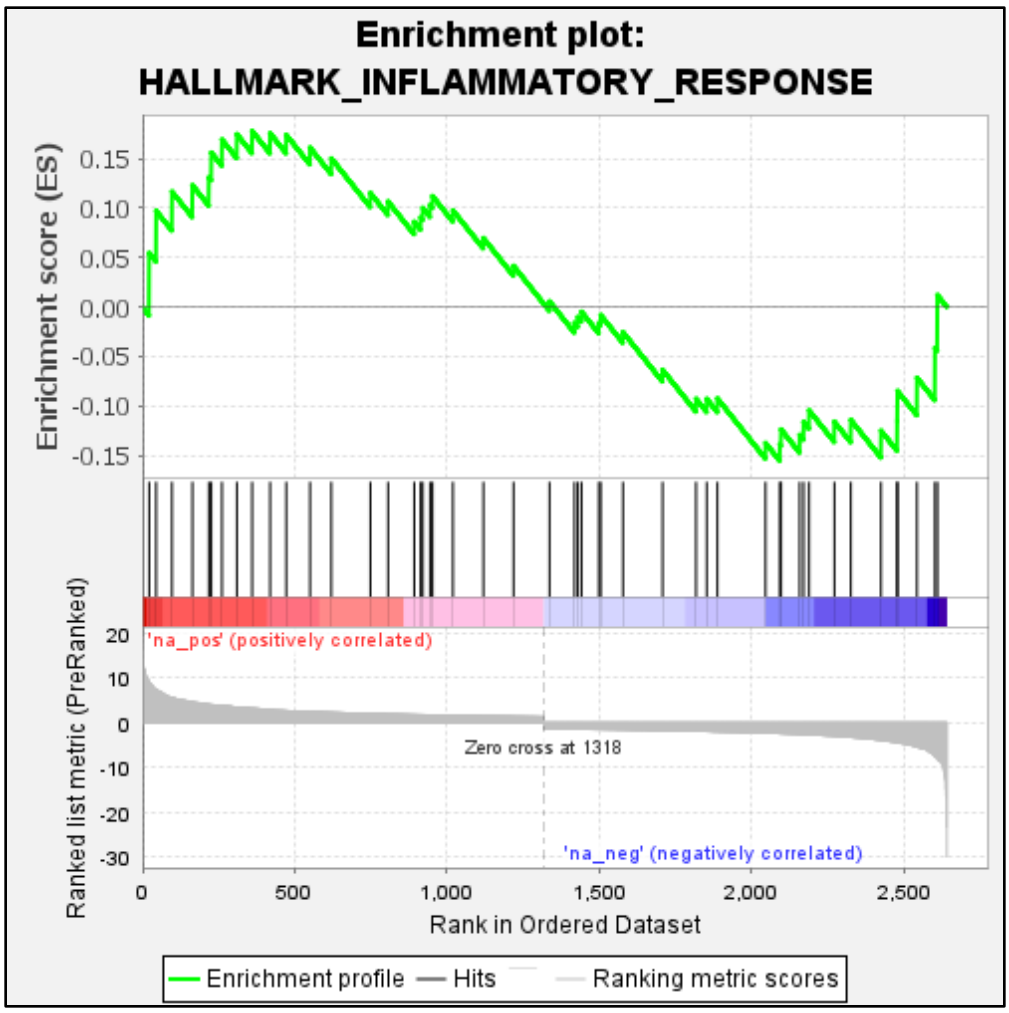


*Special thanks to Dr. Siddappa Byrareddy. Figure adapted from recent grant application. Data presented in this figure is preliminary data.

**Figure 3.** Using Gene Set Enrichment Analysis (GSEA), we observed a significant enrichment of genes associated with inflammatory responses within the HALLMARK_INFLAMMATORY_RESPONSE gene set (48 genes differentially regulated) up to 35 days post infection in Golden Syrian Hamsters (GSH).

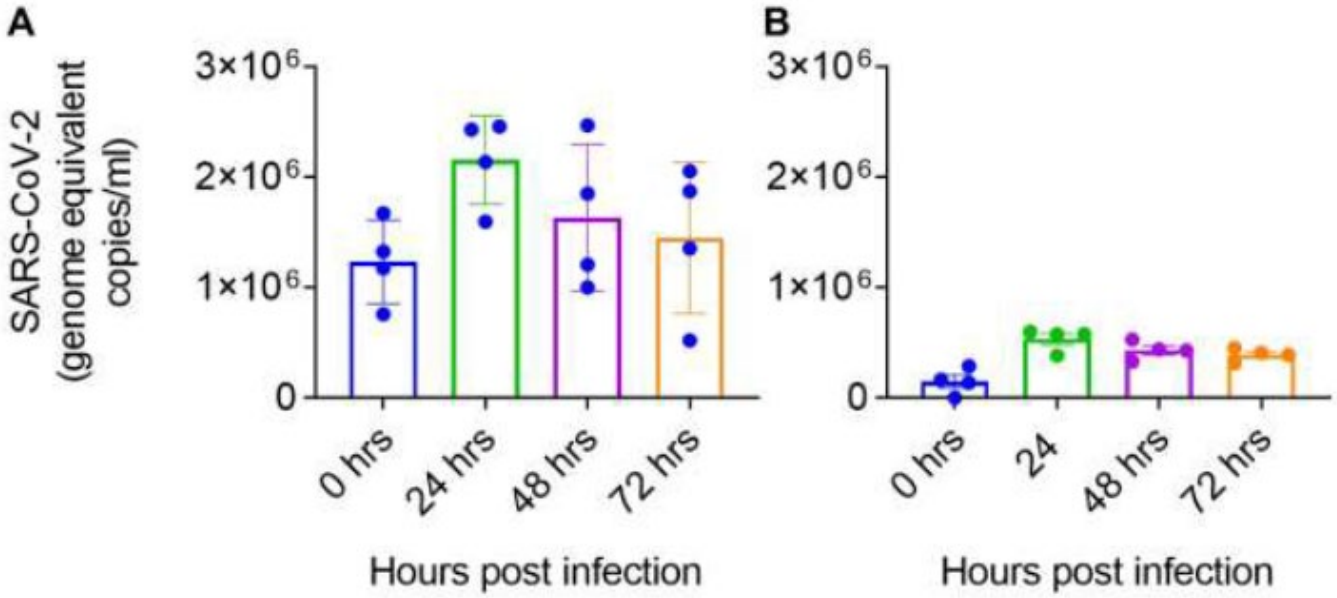


**Figure 4**. SARS-CoV-2 RNA copies in pericytes (a) and astrocytes (b) following viral infection. Circles represent four independent donor primary cells used to infect 1 multiplicity of infection of SARS-CoV-2.

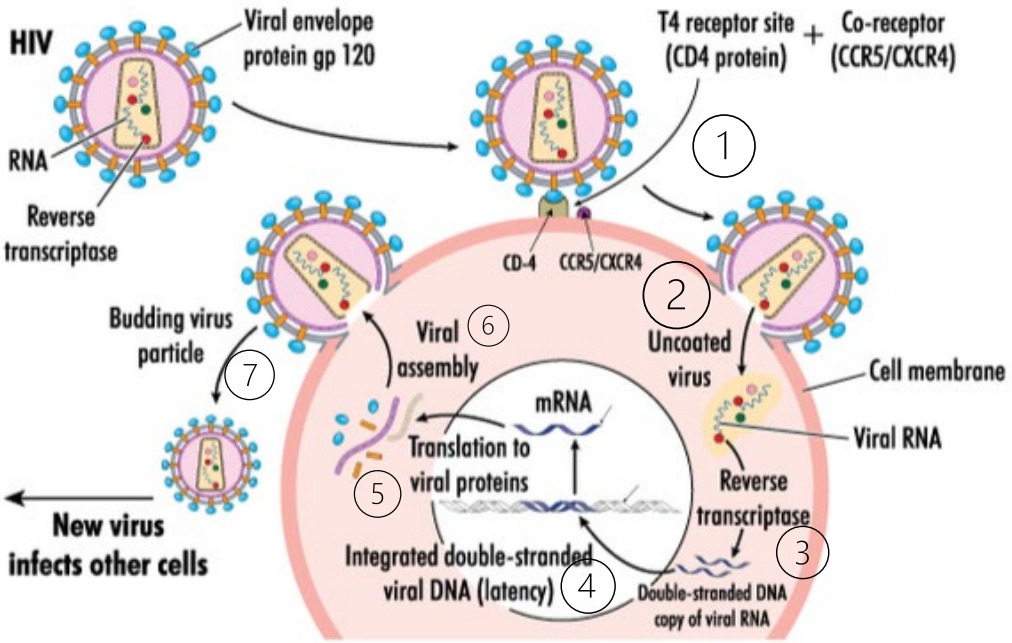


**Figure 5.** HIV lifecycle summary**.** (1) Binding: HIV binds to receptors on the surface of the CD4 cell. (2) Fusion: HIV envelope and the CD4 cell membrane join which allows HIV to enter the cell. (3) Reverse Transcription: HIV releases and uses reverse transcriptase to convert its genetic material into HIV DNA. This conversion allows HIV to enter the nucleus and combine wit the cell's genetic material. (4) Integration: HIV releases integrase and uses it to insert its viral DNA into the DNA of the cell. (5) Replication: Once integrated, HIV begins to use the machinery of the host cell to make long chains of HIV proteins which are the building blocks for more HIV. (6) Assembly: New HIV proteins and HIV RNA move to the surface of the cell and assemble into immature HIV. (7) Budding: Newly formed immature HIV pushes itself out of the host cell. The New HIV releases protease which breaks up long proteins chains in the immature virus creating mature virus.

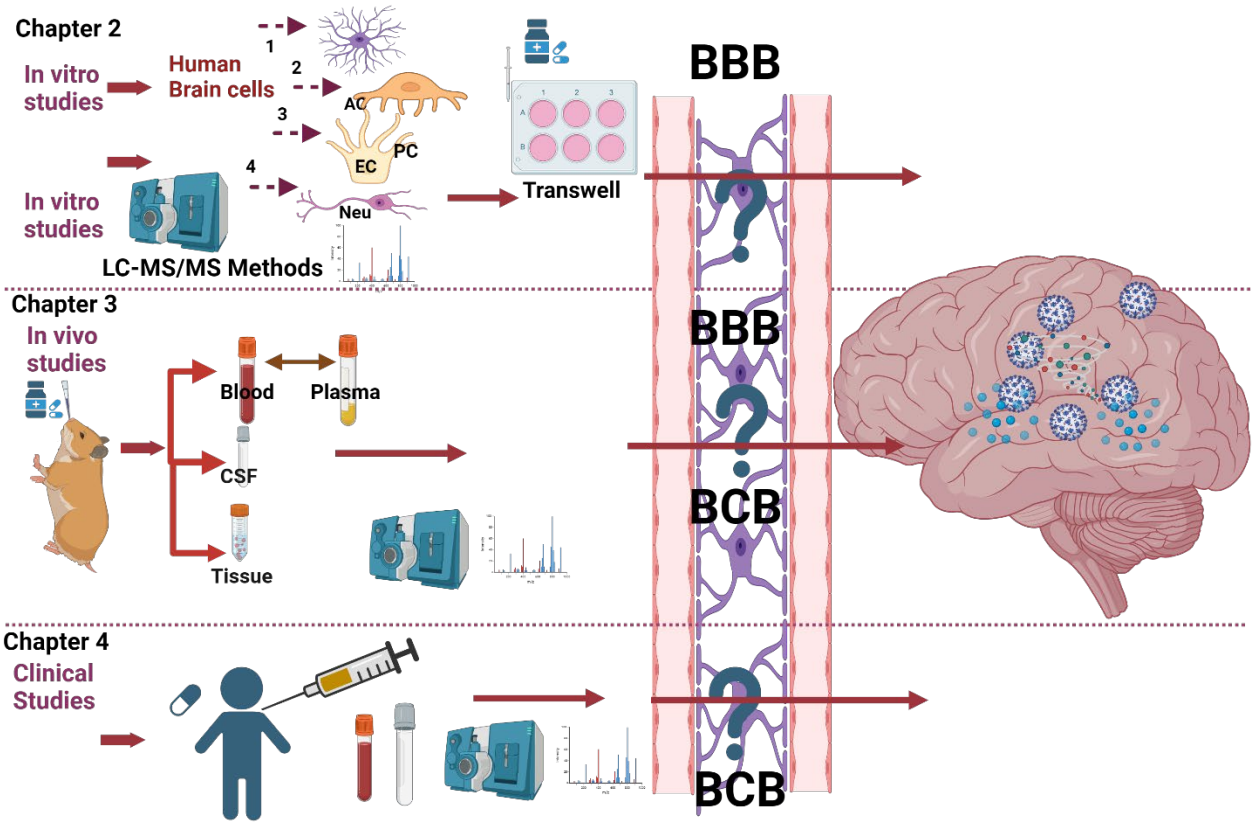


*Figure was generated utilizing Biorender.com

**Figure 6.** Overview of dissertation translational approach ("Bench to Bedside Application")

Abbreviations: BBB, blood-brain-barrier; BCB, blood-CSF-barrier

**Table 1.** NIH COVID-19 Risk Group Tier (from NIH guidelines)[66]

| Tier | Risk group |
|---|---|
| 1 | • People who are IC and are not expected to mount an adequate immune response to COVID-19 vaccination or SARS-CoV-2 infection due to their underlying conditions, regardless of vaccine status (see Immunocompromising Conditions below on NIH guidelines); or<br>• Unvaccinated individuals at the highest risk of severe disease (anyone ≥75 years or anyone ≥65 years with additional RF) |
| 2 | • Unvaccinated individuals not included in Tier 1 who are at risk of severe disease (anyone ≥65 years or anyone <65 years with clinical RF) |
| 3 | • Vaccinated individuals at risk of severe disease (anyone ≥65 years or anyone <65 years with clinical RF)<br>• Vaccinated individuals who are not up to date with their immunizations are likely at higher risk for severe disease; patients within this tier who are in this situation should be prioritized for treatment. |

*Vaccinated individuals who are not up to date with their immunizations are likely at higher risk of severe disease; patients within this tier who are in this situation should be prioritized for treatment

Abbreviations: IC, immunocompromised; RF, risk factors

**Table 2.** NIH COVID-19 Treatment Recommendations for Non-Hospitalized Patients (from NIH guidelines) [66]

| Patient Disposition | Recommendations |
|---|---|
| **All Patients** | Symptom management should be initiated for all patients **(AIII)**. • The Panel **recommends against** the use of **dexamethasone**[a] or other systemic corticosteroids **(AIIb)**, unless these agents are being used to treat an underlying condition **(AIII)**. |
| **Those who are at High risk of Progressing to Severe COVID-19**[bcd] | *Preferred therapies. Listed in order of preference:*<br>• **Ritonavir-boosted nirmatrelvir (Paxlovid)**[e] **(AIIa)**. Start as soon as possible and within 5 days of symptom onset. See footnote on drug-drug interactions[f].<br>• **Remdesivir**[e,g] **(BIIa)**. Start as soon as possible and within 7 days of symptom onset.<br>*Alternative therapy. For use when the preferred therapies are not available, feasible to use, or clinically appropriate:*[h]<br>• **Molnupiravir**[e,i] **(CIIa)**. Start as soon as possible and within 5 days of symptom onset.<br>*There is insufficient evidence for the Panel to recommend either for or against initiating these antiviral agents after the timeframes listed above.* |
| Each recommendation in the Guidelines receives a rating for the strength of the recommendation (A, B, or C) and a rating for the evidence that supports it (I, IIa, IIb, or III). See Guidelines Development (NIH guidelines) for more information. | |

[a]Currently a lack of data on the use of dexamethasone in outpatients with COVID-19. Using systemic glucocorticoids in outpatients with COVID-19 may cause harm.

[b]For risk factors, see Table 1 above. When deciding whether to prescribe an antiviral agent to a patient who has been vaccinated, clinicians should be aware of the conditions associated with a high risk of disease progression. These conditions include older age, a prolonged amount of time since the most recent vaccine dose (e.g., >6 months), and a decreased likelihood of an adequate immune response to vaccination due to a moderate to severe immunocompromising condition or the receipt of immunosuppressive medications. The number and severity of risk factors also affects the level of risk.

[c]For a discussion of potential treatment options for patients who are immunocompromised and have prolonged COVID-19 symptoms and evidence of ongoing viral replication, see the Special Considerations in People Who Are Immunocompromised (on NIH guidelines).

[d]Concerns about viral rebound or the recurrence of symptoms should not be a reason to avoid using antiviral therapies when their use is indicated.

[e]If a patient requires hospitalization after starting treatment, the full treatment course can be completed at the health care provider's discretion.

[f]NMR/r has significant drug-drug interactions, review for drug-drug interactions is recommended.

[g]Remdesivir requires an IV infusion once daily for 3 days.

[h]Molnupiravir appears to have lower efficacy than the other options.

[i]Molnupiravir for the treatment of COVID-19 in pregnant patients is not recommended unless there are no other options and therapy is clearly indicated (AIII).

**Table 3.** NIH COVID-19 Treatment Recommendations for Hospitalized Patients (from NIH guidelines) [66]

| Disease Severity | Therapy Recommendations | | Anticoagulant Therapy Recommendations |
|---|---|---|---|
| | Clinical Scenario | Recommendations | |
| **Hospitalized for Reasons Other Than COVID-19** | Patients with mild to moderate COVID-19 who are at high risk of progressing to severe COVID-19[a] | See Therapeutic Management of Nonhospitalized Adults With COVID 19 (NIH guidelines)[b] | For patients without an indication for therapeutic anticoagulation:<br><br>• **Prophylactic dose of heparin**, unless contraindicated **(AI)**; **(BIII)** for pregnant patients **Hospitalized but Does Not** |
| **Hospitalized but Does Not Require Supplemental Oxygen** | All patients | The Panel **recommends against** the use of **dexamethasone (AIIa)** or other systemic corticosteroids **(AIII)** for the treatment of COVID 19[c] | |
| | Those at high risk for progressing to severe COVID-19[a] | **Remdesivir[d] (BIIb)** for patients who are immunocompromised; **(BIII)** for other high-risk patients | |
| **Hospitalized and Requires Conventional Oxygen[e]** | Patients who require minimal conventional oxygen | **Remdesivir[d,f](BIIa)** | For nonpregnant patients with D-dimer levels above the ULN who do not have an increased bleeding risk:<br><br>• **Therapeutic dose of heparin[b] (CIIa)** For other patients:<br><br>• **Prophylactic dose of heparin**, unless contraindicated **(AI): (BIII)** for pregnant patients |
| | Most patients | Use **dexamethasone plus remdesivirf (BIIa)**. If remdesivir cannot be obtained, use **dexamethasone (BI)**. | |
| | Patients receiving dexamethasone and who have rapidly increasing oxygen needs and system inflammation | Add 1 of the following immunomodulators:g Preferred • **PO baricitinib (BIIa)** • **IV tocilizumab (BIIa)** Alternatives (Listed in Alphabetical Order) • **IV abatacept (CIIa)** • **IV infliximab (CIIa)** | |
| **Hospitalized and Requires HFNC Oxygen or NIV** | All patients | **Dexamethasone** should be administered to all patients **(AI)**. If not already initiated, promptly add 1 of the following immunomodulators:[g,i]<br>Preferred • **PO baricitinib (AI)** Preferred Alternative • **IV tocilizumab (BIIa)** Additional Alternatives (Listed in Alphabetical Order) • **IV abatacept (CIIa)** • **IV infliximab (CIIa)** Add remdesivir to 1 of the options above in certain patients (for examples, see footnote)[j] | For patients without an indication for therapeutic anticoagulation:<br>• **Prophylactic dose of heparin**, unless contraindicated **(AI)**; **(BIII)** for pregnant patients<br><br>For patients who get a therapeutic dose of heparin in a non-ICU setting and then transfer to the ICU, the Panel recommends switching to a **prophylactic dose of heparin**, unless there is another indication for therapeutic anticoagulation **(BIII)**. |
| **Hospitalized and Requires MV or ECMO** | All patients | **Dexamethasone** should be administered to all patients **(AI)**. If the patient has not already received a second immunomodulator, promptly add 1 of the following (listed in alphabetical order):[i,k]<br>• **PO baricitinib**[l] **(BIIa)**<br>• **IV tocilizumab**[l] **(BIIa)**<br>See footnote k for a discussion on the use of remdesivir. | |

[a]For a list of risk factors, see the CDC webpage Underlying Medical Conditions Associated With Higher Risk for Severe COVID-19.

[b]If the patient is hospitalized for reasons other than COVID-19, the treatment duration for remdesivir is 3 days.

[c]Corticosteroids that are prescribed for an underlying condition should be continued.

[d]Evidence suggests that the benefit of remdesivir is greatest when the drug is given early in the course of COVID-19 (e.g., within 10 days of symptom onset).

[e]Conventional oxygen refers to oxygen supplementation that is not HFNC oxygen, NIV, MV, or ECMO.

[f]If these patients progress to requiring HFNC oxygen, NIV, MV, or ECMO, the full course of remdesivir should still be completed.

[g]If none of the preferred or alternative options are available or feasible to use, the JAK inhibitor PO tofacitinib (CIIa) or the IL-6 inhibitor IV sarilumab (CIIa) can be used in combination with dexamethasone. Sarilumab is only commercially available as a SUBQ injection.

[h]Contraindications for the use of therapeutic anticoagulation in patients with COVID-19 include a PLT<50,000 cells/μL, Hgb <8 g/dL, the need for dual antiplatelet therapy, bleeding within the past 30 days that required an ED visit or hospitalization, a history of a bleeding disorder, or an inherited or active acquired bleeding disorder.

[i]Dexamethasone should be initiated immediately, If other immunomodulators cannot be obtained or are contraindicated, use dexamethasone alone (AI).

[j]Examples of patients who may benefit most from remdesivir include patients who are immunocompromised (BIIb); patients with evidence of ongoing viral replication (e.g., those with a low Ct value, as measured by an RT-PCR result or with a positive rapid antigen test result) (BIII); or patients who are within 10 days of symptom onset (CIIa).

[k]There is insufficient evidence for the Panel to recommend either for or against the use of remdesivir in hospitalized patients with COVID-19 who require MV or ECMO. Some Panel members would add remdesivir to immunomodulator therapy in patients who have recently been placed on MV or ECMO, who are immunocompromised, who have evidence of ongoing viral replication, or who are within 10 days of symptom onset. See text for more information.

[l]If PO baricitinib and IV tocilizumab are not available or feasible to use, tofacitinib can be used instead of baricitinib (CIIa), and sarilumab can be used instead of tocilizumab (CIIa).

**Table 4.** NIH COVID-19 Recommended Treatment Summary (from NIH guidelines)[66]

| Class | Drug Name | Regimen | Comments/Notes |
|---|---|---|---|
| Antivirals | **Ritonavir-Boosted Nirmatrelvir (Paxlovid [NMR/r])** | **eGFR ≥60 mL/min**<br>• Nirmatrelvir 300 mg with RTV 100 mg PO twice daily for 5 days<br>**eGFR ≥30 to <60 mL/min**<br>• Nirmatrelvir 150 mg with RTV 100 mg PO twice daily for 5 days<br>**eGFR <30 mL/min**<br>**• Not recommended**<br>• For more information on the use of this agent in patients with eGFR <30 mL/min, see Ritonavir-Boosted Nirmatrelvir (Paxlovid).<br>Severe Hepatic Impairment (Child-Pugh Class C)<br>• Not recommended | Clinicians should evaluate potential drug-drug interactions. See Drug-Drug Interactions Between Ritonavir-Boosted Nirmatrelvir (Paxlovid) and Concomitant Medications for more information (on NIH guidelines). |
| | **Remdesivir** | RDV 200 mg IV on Day 1, then RDV 100 mg IV once daily on Days 2 and 3. Administer each infusion over 30–120 minutes. | Patients should be monitored for ≥1 hour after the infusion as clinically appropriate. |
| | **Molnupiravir** | MOV 800 mg PO every 12 hours for 5 days | Before initiating MOV, assess the patient's pregnancy status as clinically indicated. See Molnupiravir for more information. |
| Immunomodulators/Monoclonal Antibodies | **Abatacept** | Abatacept 10 mg/kg actual body weight (up to 1,000 mg) administered as a single IV dose | • No adjustment based on eGFR |
| | **Baricitinib** | BAR dose is dependent on eGFR; duration of therapy is up to 14 days or until hospital discharge, whichever comes first. | • eGFR ≥60 mL/min/1.73 m2: BAR 4 mg PO once daily • eGFR 30 to <60 mL/min/1.73 m2: BAR 2 mg PO once daily • eGFR 15 to <30 mL/min/1.73 m2: BAR 1 mg PO once<br>• eGFR <15 mL/min/1.73 m2: **Not recommended**. |
| | **Tofacitinib** | 10 mg PO twice daily for up to 14 days or until hospital discharge, whichever comes first | • eGFR <60 mL/min/1.73 m2: tofacitinib 5 mg PO twice daily |
| | **Infliximab** | 5 mg/kg actual body weight administered as a single IV dose | • No adjustment based on eGFR |
| | **Sarilumab** | Use the single-dose, prefilled syringe (**not** the prefilled pen) for SUBQ injection. Reconstitute sarilumab 400 mg in 100 cc 0.9% NaCl and administer as an IV infusion over 1 hour. | • In the United States, the currently approved route of administration for sarilumab is SUBQ injection. In the REMAP-CAP trial, the SUBQ formulation was used to prepare the IV infusion. |
| | **Tocilizumab** | 8 mg/kg actual body weight (up to 800 mg) administered as a single IV dose | • In clinical trials, a third of the participants received a second dose of tocilizumab 8 hours after the first dose if no clinical improvement was observed. |
| Steroid (corticosteroids) | **Dexamethasone** | DEX 6 mg IV or PO once daily for up to 10 days or until hospital discharge, whichever comes first | • If DEX is not available, an equivalent dose of another corticosteroid may be used.<br>• For more information, see Systemic Corticosteroids (NIH guidelines). |
| Antigcoagulation | **Heparin** | Therapeutic dose of SUBQ LMWH or IV UFH | • Administer for 14 days or until hospital discharge (whichever comes first) unless there is a diagnosis of VTE or another indication for therapeutic anticoagulation. |
| | | Prophylactic dose of SUBQ LMWH or SUBQ UFH | • Administer for the duration of the hospital stay. |
| | **Key:** BAR = baricitinib; DEX = dexamethasone; eGFR = estimated glomerular filtration rate; IV = intravenous; LMWH = low-molecular-weight heparin; NaCl = sodium chloride; PO = oral; RDV = remdesivir; SUBQ = subcutaneous; UFH = unfractionated heparin; VTE = venous thromboembolism | | |

**Table 5.** ARV Pharmacologic Characteristics and Potential CSF Exposure

| Drug Class | Protein Binding (%) | Protein Free $IC_{50}$ (ng/mL) | CSF Concentration (ng/mL) Median values | CSF IQ | CPE |
|---|---|---|---|---|---|
| **NRTIs** | | | | | |
| **Abacavir** [81, 96] | 50 | 72 | 128 | 1.78 | 3 |
| **Lamivudine** [81] | 16-36 | 549.6 | 95 | 0.17 | 2 |
| **Emtricitabine** [97] | <4 | 70 | 68 | 0.97 | 3 |
| **Tenofovir Disoproxil Fumarate*** [97] | <7 | 11.5 | 6 | 0.52 | 1 |
| **Tenofovir Alafenamide*** | 80 | 0.03 | 0.46 | 15 | NA |
| **NNRTIs** | | | | | |
| **Doravirine** | 76 | 0.67 | NA | NA | NA |
| **Efavirenz** [81, 98] | 99.78 | 1.3 | 18.8 | 14.5 | 3 |
| **Rilpivirine** [80, 99] | >99 | 0.27 | 0.8 | 3.0 | NA |
| **INSTIs** | | | | | |
| **Bictegravir** [100] | >99 | 0.2 | 6.9 | 34.5 | NA |
| **Dolutegravir** [81] | >98.9 | 0.2 | 18.2 | 91 | NA |
| **Raltegravir** [81, 101] | 83 | 3.2 | 31 | 9.7 | 3 |
| **Cabotegravir (IM admin)** [80] | >99 | 0.10 | Q4: 12.7<br>Q8: 10.6 | 127 | NA |
| **PIs** | | | | | |
| **Atazanavir** [102] | 86 | 1.7 | 7.9 | 4.65 | 2 |
| **Darunavir** [102] | 95 | 0.4 | 30 | 75 | 3 |
| **CCR5I** | | | | | |
| **Maraviroc** [103] | 76 | 0.26 | 2.4 | 9.2 | 3 |

Abbreviations: NRTIs, Nucleoside reverse transcriptase inhibitors; NNRTIs, Non-nucleoside reverse transcriptase inhibitors; INSTIs, Integrase Strand Transfer Inhibitor; IM, Intramuscular; PIs, protease inhibitors; CCR5I, C-C chemokine receptor type 5 inhibitor; $IC_{50}$, inhibitory concentration at which 50%, of in-vitro viral replication is inhibited; CSF, cerebrospinal fluid, $EC_{50}$, concentration of a drug that gives 50% response; IQ, inhibitory quotient; CPE, CNS penetration effectiveness score; NA, not available.
*Based on active moiety of TFV

**Table 6.** Preferred and alterative first-line ART treatment recommendations by guideline A). DHHS[67] and B). WHO[83]

A).DHHS

| Key Considerations and Recommendations |
|---|
| • An initial ARV regimen for a person with HIV generally consists of two NRTIs inhibitors administered in combination with a third active ARV drug from one of three drug classes: INSTI, a NNRTI, or a PI with a pharmacokinetic enhancer (also known as a booster; the two drugs used for this purpose are COBI and RTV).<br><br>• Data also support the use of the two-drug regimen, DTG plus 3TC, for initial treatment.<br><br>• Before initiating ART in a person of childbearing potential, clinicians should discuss the person's intentions regarding pregnancy and a pregnancy test should be performed (AIII). Clinicians should refer to the Perinatal Guidelines for recommendations on initial ARV treatment around the time of conception and during pregnancy.<br><br>• The Panel on ARV Guidelines for Adults and Adolescents (the Panel) classifies the regimens below (in alphabetical order) as Recommended Initial Regimens for Most People with HIV.<br><br>For people with HIV who do not have a history of using CAB-LA as PrEP, the following regimens are recommended:<br>o BIC/TAF/FTC (AI)[a]<br>o DTG/ABC/3TC—only for individuals who are HLA-B*5701 negative and without chronic HBV coinfection (AI)<br>o DTG plus TAF or TDF[b] plus (FTC or 3TC) (AI)<br>o DTG/3TC (AI)—except for individuals with HIV RNA >500,000 copies/mL, HBV coinfection, or when ART is to be started before the results of HIV genotypic resistance testing for reverse transcriptase or HBV testing are available.<br>For people with HIV and a history of using CAB-LA as PrEP, INSTI genotypic resistance testing should be done before the start of ART. If treatment is begun prior to results of genotypic testing, the following regimen is recommended:<br>o Boosted DRV plus (TAF or TDF)[b] plus (FTC or 3TC)—pending the results of the genotype test (AIII).<br>• To address individual patient characteristics and needs, the Panel also provides a list of Recommended Initial Regimens in Certain Clinical Situations (see Table 6 on guidelines[67]).<br><br>• Given the many excellent options for initial therapy, selection of a regimen for a particular patient should be guided by factors such as virologic efficacy, toxicity, pill burden, dosing frequency, drug–drug interaction potential, resistance-test results, comorbid conditions, access, and cost. For guidance on choosing an ARV regimen based on selected clinical case scenarios, see Table 7 on guidelines. Also see Table 9 on guidelines for the advantages and disadvantages of different components in an ARV regimen.<br><br>• Patients without prior ART use who wish to begin long-acting intramuscular CAB and RPV should first achieve viral suppression on another regimen before switching to CA\B and RPV. |
| ***Rating of Recommendations:*** *A = Strong; B = Moderate; C = Weak*<br>***Rating of Evidence:*** *I = Data from randomized controlled trials; II = Data from well-designed nonrandomized trials, observational cohort studies with long-term clinical outcomes, relative bioavailability/bioequivalence studies, or regimen comparisons from randomized switch studies; III = Expert opinion*<br>[a] Bictegravir should not be initiated in pregnant people due to insufficient data in pregnancy.<br><br>[b] TAF and TDF are two forms of tenofovir that are approved by the U.S. Food and Drug Administration. TAF has fewer bone and kidney toxicities than TDF, while TDF is associated with lower lipid levels. Safety, cost, and access are among the factors to consider when choosing between these drugs. |

B).WHO

| Population | Preferred first-line regimen | Alternative first-line regimen | Special circumstances |
|---|---|---|---|
| Adults and adolescents | TDF + 3TC (or FTC) + DTG[a,b]<br>NRTI + NRTI + INSTI | TDF + 3TC + EFV 400 mg[b]<br>NRTI + NRTI + NNRTI | TDF + 3TC (or FTC) + EFV 600 mg[b]<br>AZT + 3TC + EFV 600 mg[b]<br>TDF + 3TC (or FTC) + PI/r[b]<br>TDF + 3TC (or FTC) + RAL<br>TAFc + 3TC (or FTC) + DTG<br>ABC + 3TC + DTG[a]<br>TDF + 3TC (or FTC) + PI/r[b] |
| [a] Section 4.8 of guidelines discusses toxicity considerations for pregnant and breastfeeding women.<br>[b] EFV-based ART should not be used in settings with national estimates of pretreatment resistance to EFV of 10% or higher. In settings with high HIV drug resistance prevalence and where DTG is unavailable or unsuitable due to toxicity, a boosted PI-based regimen should be used. The choice of PI/r will depend on programmatic characteristics. Alternatively, HIV drug resistance testing should be considered, where feasible, to guide first-line regimen selection.<br>[c] TAF may be considered for people with established osteoporosis and/or impaired kidney function. | | | |

Abbreviations: TDF, tenofovir disoproxil fumarate; FTC, emtricitabine; EFV, efavirenz; DTG, dolutegravir; RAL, raltegravir; EVG, elvitegravir; ATV, atazanavir; DRV, darunavir/ritonavir; BIC, bictegravir;

**Table 7.** ARV Metabolism and Transporter Interactions

| Class/Drug Name | Metabolized by CYP/UGT | Inducer CYP/UGT | Inhibitor CYP/UGT | Transported By | Transporter Inducer | Transporter Inhibitor |
|---|---|---|---|---|---|---|
| **NRTIs** | | | | | | |
| Tenofovir (TDF and TAF)* | No (TAF: CYP3A4 minimal) | No | No (TAF: weak CYP3A4 in vitro) | TDF: hOAT1/3, MRP4 TAF: Pgp, BCRP, OATP1B1/B3 | No | MRP1/2-3 |
| Emtricitabine (FTC) | No (limited) | No (limited) | No | No | No | MRP1/2-3 |
| Zidovudine (ZDV) | No (hepatic conjugation) | No | No | BCRP | No | BRCP (in vitro) |
| Lamivudine (3TC) | No (unchanged via renal) | No | No | MRP4, MRP8 (in vitro) | No | MRP1/2-3 |
| **Integrase Inhibitors** | | | | | | |
| Dolutegravir (DTG) | UGT1A 1(major), UGT1A3, 1A9 (minor), CYP3A4 (minor) | No | No | BRCP, Pgp | No | OCT2 (in vitro) |
| Raltegravir (RAL) | UGT1A | No | No | Unknown | No | No |
| Cabotegravir (CAB) | UGT1A1 (major), UGT1A9 (minor) | No | No | Pgp (in vitro), BCRP (in vitro) | No | OAT1/3 (in vitro) |
| Elvitegravir (EVG) | CYP3A4 UGT1A1 UGT1A3 | CYP2C9, UGT | No | OATP1B1, OATP1B3 | No | OATP1B3 |
| **Protease Inhibitors** | | | | | | |
| Lopinavir (LPV) | CYP3A | No | CYP3A | Pgp, MRP1/2, OATPs | No | BCRP (in vitro) |
| Ritonavir (r) | CYP3A4, CYP2D6 | CYP1A2, CYP2C8, CYP2C9, | CYP3A4, CYP2D6, | Pgp, MRP1 | MRP1 | MRP1, OATP-C, BCRP, Pgp |
| Atazanavir (ATV) | CYP3A4 | No | CYP3A4, UGT1A1, CYP2C8, | Pgp, MRPs, BCRP | Pgp, MRP1 | BCRP (in vitro), Pgp, MRPs, OATPs |
| Darunavir (DRV) | CYP3A4 | CYP2C9, CYP2C19 (w/ DRV/r, possibly /r effect), CYP2C8 (in vitro, DRV/r) | CYP3A4, CYP2D6 (w/ DRV/r, possibly /r effect) | Pgp (in vitro) | No | Pgp (w/r) OATPs |
| **NNRTI** | | | | | | |
| Efavirenz (EFV) | CYP3A4, CYP2B6 (in vitro) | CYP3A4 | CYP2C9, CYP2C19, CYP3A4 | Unknown | No | BCRP (in vitro), MRP1/2-3 |

Abbreviations: CYP, cytochrome P450; UGT, uridine glucosyl transferase; MRP2, multidrug resistance protein; Pgp, p-glycoprotein; BCRP breast cancer resistance protein; OAT, organic anion transporter; OCT2, organic cation transporter

# Chapter 2: *In Vitro* Model for CNS Pharmacology (4-cell Model)

## 2.1 Introduction and Background

This chapter will discuss a developed 4-cell *in vitro* model where cells relevant to the BBB were grown and co-cultured together to allow for drug penetration studies to be performed. Briefly, astrocytes, pericytes, human brain microvascular endothelial cells (hBMECs), and neurons were grown and transepithelial electrical resistance (TEER) measurements were taken to confirm BBB integrity. After, drug was given to the apical side to assess how much gets through to the basal side of the plates. These studies provide a tool for assessing potential drug penetration through cells relevant to the BBB.

Briefly, the BBB constitutes a crucial protective anatomical layer with a microenvironment that tightly controls material transit. To replicate in vivo features, constructing an *in vitro* BBB model requires the sequential layering of constituent cell types. The crucial aspect of maintaining heightened integrity in the observed tight junctions during both the establishment and post-experiment phases is essential for the success of these models. As such, Chapter 2 discusses comprehensive procedures and steps aimed at enhancing the integration of the *in vitro* model. Our BBB model includes all four major different primary cell types, which are structural parts of the human BBB. This 4-cell-based BBB model can emerge as a promising experimental platform for drug screening processes.

## 2.2 A Novel 4-cell In-vitro Blood-Brain Barrier Model and its Characterization by Confocal Microscopy and TEER Measurement

*#Corresponding Author*

Adapted from[104, 105]:

Malik J, Dyavar RS, Fletcher CV, Podany AT, Dyavar RS, Scarsi KK, Paid GM, Scheetz MH, **Avedissian SN[#]**. *A novel four-cell in-vitro blood-brain barrier model and its characterization by confocal microscopy and TEER measurement.* Journal of Neuroscience Methods. April 26 2023. PMID: 37116621

Malik J, Modebelu UO, Fletcher CV, Podany AT, Scarsi KK, Byrareddy SN, Anand R, Buch S, Brown A, Le J, Bradley J, **Avedissian SN[#].** *Establishment of a four-cell in vitro blood-brain barrier model with human primary brain cells*. Current Protocols. June 10 2024. PMID: 38857108

### 2.2.1 Abstract

The BBB is a protective cellular anatomical layer with a dynamic micro-environment, tightly regulating the transport of materials across it. To achieve in-vivo characteristics, an in-vitro BBB model requires the constituent cell types to be layered in an appropriate order. A cost-effective in-vitro BBB model is desired to facilitate central nervous system CNS drug penetration studies. Enhanced integrity of tight junctions observed during the in-vitro BBB establishment and post-experiment is essential in these models. We successfully developed an in-vitro BBB model mimicking the in-vivo cell composition and a distinct order of seeding primary human brain cells. Unlike other in-vitro BBB models, our work avoids the need for pre-coated plates for cell adhesion and provides better cell visualization during the procedure. We found that using bovine collagen-I coating, followed by bovine fibronectin coating and poly-L-lysine coating, yields better adhesion and layering of cells on the transwell membrane compared to earlier reported use of collagen and poly-L-lysine only. Our results indicated better cell visibility and imaging with the polyester transwell membrane as well as point to a higher and more stable Trans Endothelial

Electrical Resistance values in this plate. In addition, we found that the addition of zinc induced higher claudin 5 expressions in neuronal cells. Dolutegravir, a drug used in the treatment of HIV, is known to appear in moderate concentrations in the CNS. Thus, dolutegravir was used to assess the functionality of the final model and cells. Using primary cells and an in-house coating strategy substantially reduces costs and provides superior imaging of cells and their tight junction protein expression. Our 4-cell-based BBB model is a suitable experimental model for the drug screening process.

## 2.2.2 Introduction

The BBB represents a dynamic microenvironment where the transport of molecules into and out of the brain is tightly regulated[106]. The unique structure of the BBB is maintained primarily by brain microvascular endothelial cells (hBMECs), astrocytes, pericytes, and neuronal projections. Cell-to-cell contact and communication among hBMECs, astrocytes, pericytes, and neuronal cells are critical for the integrity and effective functioning of the BBB. The BBB is important as it regulates paracellular exchange, cytoplasmic intake, and exocytosis of essential molecules[106, 107]. Claudins, occludins, and junctional adhesion molecules (JAMs) form tight junctions between cells in the BBB. Cytoplasmic zonula occludens protein 1 and 2 (ZO-1, ZO-2) play vital roles in linking the transmembrane proteins to actin filaments of the cytoskeleton[11]. Together, the tight junction complexes and participating proteins ensure the regulated transport of molecules across the BBB[108]. During a homeostatic condition, only small molecules (molecular mass <400-500 Da) can cross the BBB without needing any modulation of the barrier[109]. Most drugs used to treat disorders of the CNS need specific properties to cross the BBB. However, a study that looked at over 7000 drugs found that less than 5% of the screened

drugs were able to effectively cross BBB, showcasing the significance of this potential obstacle in the brain tissue penetrating drug development process[110].

It is essential to understand the structural and functional aspects of the BBB for the success of CNS drug delivery. It has been debated that relying on the rodent BBB models does not provide critical answers on the human BBB as there are significant differences between species based on transporter expression, the complexity of tight junctions, and drug receptors[111-115]. Species-dependent variations in BBB function has been reported in a positron emission tomography (PET) study on brain pharmacokinetics of a Pgp substrate[116]. Thus, in-vitro humanized BBB models are crucial experiments and methodologies to understand drug transport across the human BBB. Furthermore, there is a distinct movement towards animal reduction in pre-clinical testing[117]. The 117th U.S. Congress approved the non-requirement of animal testing for procuring a license. Accordingly, FDA no longer has to require animal testing for toxicology data and encourages readily available in-vitro based experiments[118, 119].

In-vitro BBB models are based on the transwell apparatus, which closely mimics in-vivo barrier properties[120, 121]. This method is also cost-effective for screening a large number of drug candidates. Since the incorporation of endothelial cells on a transparent collagen filter, transwell technology has advanced significantly to make it more suitable for BBB studies[122, 123]. Initially, experiments using immortalized brain endothelial cells were performed to understand the complexity and functionality of the human BBB[124, 125]. Despite the successful monolayer BBB model on the transwell membrane, cross-talk between different cell types was not possible given the simplicity of the model[126]. Although easily accessible and highly reproducible, the immortalized cells demonstrate poor BBB properties and lose important in-vivo BBB functions[127, 128]. To mimic the BBB more accurately[129], an in-vitro system with primary human brain cells was developed by Stone et al.[130]. Our model was based on this initial methodology and other previous models[130-

[132]. Further, because of supply issues and manufacture discontinuations, adjustments were needed to the previous methodology. Utilizing primary human cells is necessary as non-human primary cells are not representative of their human counterpart and exhibit substantial differences in tight junction protein properties[133, 134]. To completely recapitulate the BBB microenvironment with the associated paracellular stimuli, in-vivo constituent cells of BBB were used as primary cells in an in-vitro model employing a transwell membrane system for contact-based co-culture including neurons in non-contact (at the bottom of the well on cover slip)[135, 136]. In earlier works, various combinations of cell types, plate selection, transparency, and porosity of transwell membranes have been tested in the development of in-vitro models[121, 122, 137, 138]. Despite its static model drawback, the transwell insert-based human BBB model remains the most affordable and direct way to replicate conditions representing the BBB[139].

In this study, the 4-cell in-vitro BBB model was modified and optimized from earlier work performed by Stone et al.[130]. Because the specific pre-coated collagen plates utilized in Stone et al.[130] have been discontinued (Collagen coated 12 well, 3µm and 12mm inserts, Corning COSTAR, UK), we alleviated the need for these particular plates with our modified methodology. In the present work, we developed a collagen coating strategy for 12 well plates with dimensions of 12mm and 3µm pore size of the transwell membrane. In this process, polyester plates (Corning COSTAR #3462) were used to visualize cells during various stages of BBB development. The role of zinc (Zn) and serum starvation of cells have been shown to enhance the TEER value, but to our knowledge, these conditions have not been tested in a 4-cell BBB model using primary human brain cells[140,141]. Visualization of cells and tight junction proteins after BBB formation has always been challenging to capture with in-vitro models. In an in-vitro BBB model, the expression of tight junction proteins on the non-contact cultured neurons is unknown, though these proteins have been identified in non-BBB-associated neuronal cells. A previous study by

Miyamoto et al. utilized knock-out mice showed the presence of tight junction protein in the myelinated axon of peripheral neuron cells[142]. Other studies have also reported the presence of claudin 5, claudin 1, and ZO-1 in ipsilateral sciatic nerve samples from legs[143, 144]. Focused investigation on the neuronal tight junction proteins would also help in understanding the BBB layer and developing cures for neuronal diseases. Researchers have also used non-human species for in-vitro BBB model development, however, given the specific complexities of the BBB, it is essential to validate the results from various species-based BBB models with a human in-vitro BBB model if these models are going to be extrapolated for clinical applications[145].

### 2.2.3 Material and Methods

### 2.2.4 Cell and Culture System

Human brain primary astrocytes (#1800), pericytes (#1200), and human brain microvascular endothelial cells (hBMECs # 1000) were purchased from ScienCell Research Laboratories (SCRL), USA. Required media and growth supplements for the respective cells were also obtained from SCRL. Astrocytes were cultured in astrocyte media (AM) (Catalogue # 1801) and astrocyte growth supplement (AGS) (Catalogue # 1852); Pericytes were cultured in Pericyte media (PM) (Catalogue # 1201), Pericyte growth supplement (PGS) (Catalogue # 1252); hBMECs were cultured in Endothelial cell medium (ECM) (Catalogue # 1001), endothelial growth supplement (ECGS) (Catalogue # 1052), all procured from SCRL. Supplements including FBS (Catalogue # 0010), and penicillin/streptomycin solution (P/S) (Catalogue # 0503) were also purchased from SCRL. Frozen cells were revived and cultured according to the manufacturer's instructions. Cells were grown in either $25cm^2$, $75cm^2$, or $150cm^2$ culture flask (TPP # 90076) in accordance

with experimental requirements. For human brain cells, culturing flasks and plates were pre-coated with bovine fibronectin at 2µg/ml (SCRL, # 8248). Approximately 90% of cells in a confluent flask were harvested by trypsinization (0.25 % trypsin, Lonza # CC-5012) and washed in DPBS (Dulbecco's # 1960454). Cells were prepared for counting by mixing 10 µl of cell suspension with 10 µl of trypan blue. 10 µl of the mixture was read in a cell counter (Invitrogen Countess). Cells from passage number 5-8 were used as needed for experimental procedures. Human neuronal cells were also purchased from SCRL (catalogue# 1520), thawed and used on the day of experiment without prior culturing.

## 2.2.5 Model Optimization

Our model was based on the initial methodology established by Stone et al and previous models by Hind et al, and Allen et al[130-132]. However, we modified the model given the current availability of necessary supplies, specifically collagen coated inserts of 3.0 µm and 12 mm (no longer available). Further, we performed numerous preliminary experiments, including the stepwise addition of each cell type to confirm cell organization (data not shown).

## 2.2.6 Transwell Plates and Coating

Twelve-well polycarbonate and polystyrene transwell insert plates (12mm, 3 µm pore) were purchased from Corning (Corning COSTAR, #3402 and 3462). In consecutive treatments, the transwell membrane was coated with bovine collagen I (Gibco, #A10644-01), fibronectin, and poly-L-Lysine. Briefly, the membrane was initially treated with bovine collagen I (50µg/ml, Gibico, #A10644-01) in PBS overnight at $4^0$C. Next, fibronectin (ScienCell, #8248) 3µg/ml in PBS was added to the transwell membrane and incubated

at $37^0$C for 3hrs. The membrane was left to air dry between treatments. Finally, Poly-L-Lysine (Sigma, #P4707-50ML) was added to the membrane and incubated for 10 minutes at RT.

## 2.2.7 Cell Seeding on Transwell Membrane

The experimental timeline and stepwise schematic is described in **Figure 7**. All steps were carried out in a biosafety cabinet under aseptic conditions.

Astrocytes (1st cell)-Astrocytes with a cell count of $6x10^5$/150µl, $3x10^5$/150µl, and $1.5x10^5$/150µl were seeded on the basolateral side of the flipped transwell insert membranes and incubated in $37^0$C cell culture for 3 hrs. After the incubation, excess media was removed, flipped to the original position, and media was added to the wells covering the apical compartment. Astrocytes were grown for 48 hrs.

Pericytes (2nd cell)-After 48 hrs of incubation with astrocytes, the transwell was flipped again, and excess media was removed from the top of the monolayer. Keeping the ratio 1:5 for astrocyte: pericytes, $1.2x10^5$/150µl, $0.6x10^5$/150µl, and $0.12x10^5$/150µl of pericytes were seeded on the growing astrocytes monolayer on the basolateral side of the transwell insert membrane. These pericyte-seeded transwells were incubated for 3 hrs in the cell incubator. After the incubation period, the inserts were flipped to normal position, and excess media was removed from the membrane. A 1:1 proportion mixture of astrocyte/pericyte media was filled into the transwell and incubated for five additional days to allow the formation of a confluent monolayer of astrocytes and pericytes. The media was changed every 48 hrs.

hBMECs (3rd cell) and Neuron (4th cell) Seeding-Seven days after the initial seeding with astrocytes, the apical layer media was removed, and $7.51x10^4$/200µl hBMECs in endothelial media were seeded on the transwell membrane containing

astrocytes and pericytes ($6x10^5$/150µl and $1.2x10^5$/150µl), in the basolateral part. Plates with seeded cells were incubated for 6 hours, and then 400µl of endothelial media was added to the apical region of the transwell membrane. In parallel, 200µl of $2.5x10^4$ human neurons were seeded on a collagen-coated coverslip in a separate 12-well plate and incubated for 2 hours. The media was changed every 48 hours.

Combining all Four Cells- On the 11th day from initiation of the experiment, the transwell inserts with apical hBMECs, and basolateral astrocyte and pericytes were carefully transferred to the 12-well plate containing neurons on the coverslip at the bottom of the well. The apical side of the transwell was topped with fresh endothelial media, while the basolateral part was filled with a 1:1:2 ratio of astrocyte, pericyte, and neuronal media.

## 2.2.8 Trans Epithelial Electrical Resistances Measurements

Before changing the media on Day 3 of 4-cell growth, the first TEER value was measured using an Epithelial volt-ohm meter ($EVOM^2$). $EVOM^2$ has been specifically designed to measure the electrical resistance in tissue culture (https://www.wpiinc.com/company/our-history/). The instrument precisely measures the electrical resistance between the different layers of cells. The measured electrical resistance between tissue layers is usually known as TEER. The resistance measuring probe was washed in 70% ethanol and dried before equilibrating in endothelial media for 15 minutes. After equilibration, the probe was carefully placed into the insert with the shorter arm just above the hBMECs (apical) layer and the long arm just above the neurons on the coverslip at the bottom of the well. TEER value was checked every day until the completion of the experiment. A schematic of TEER measuring of all 4 cells can be found in **Figure 8.**

## 2.2.9 Processing Transwell Membrane

Upon completion of the experiment, wells with the membrane inserts were washed twice with PBS, and the cells were fixed with paraformaldehyde (Thermo Scientific, #J19943-K2) for 10 minutes. Fixed membranes with cells were washed with PBS, and the membrane-containing cells were carefully cut into four pieces for further staining.

## 2.2.10 Staining Cells on the Membranes for Imaging

A piece of the membrane containing cells on both sides was incubated in a blocking buffer comprising 5% goat serum (Abcam, #ab7481), 0.1% TritonX 100 (Sigma, # 9036-19-5), and 1% BSA (MP, #180561) for 2 hours. Cells were washed in PBS with 0.1% Tween-20 (Sigma, #P2287-100ML). Conjugated antibodies for claudin 5 (Invitrogen, #362588) at 1:200 and ZO-1 (Invitrogen, #MA3-39100-A647) at 1:100 dilution in PBS with 0.1% Tween-20 were added to the samples and incubated overnight at $4^0$C. A separate piece of the same membrane was used for cell identification by staining it with cell marker conjugated-antibodies, anti-S1OO beta for astrocytes (Abcam, #ab196175), anti-CD146 (Abcam, #ab196448) for pericytes and hBMECs, and anti-NeuN antibody (Abcam, ab190565) for neurons, with all Abs at 1:200 dilution. The following day, samples were washed twice with PBS and 0.1% Tween-20. After washing, samples were fixed with 4% paraformaldehyde for 10 minutes in the dark. The fixed samples were washed with PBS and air-dried on a glass cover slip. Samples were analyzed for expression of tight junction proteins using a laser scanning microscope (Zeiss LSM800). Of note, no quantification of fluorescence intensities for proteins was performed and comparison of fluorescence was assessed visually.

## 2.2.11 Apical and Basolateral Visualization of Cells on the Same Membrane

For optimal visualization of cells on both sides of the membrane, one drop of nucleus staining DAPI (4',6-diamidino-2-phenylindole) mounting dye (Invitrogen-ProLongTMDiamond Antifade Mountant with DAPI, #P3692) was added on a glass coverslip. A quarter piece of the air-dried membrane was placed on the DAPI drop, and a drop of DAPI mounting dye was added on top of the membrane. Finally, another glass coverslip was carefully placed. under nitrogen and reconstituted in 0.3 mL of mobile phase. The plate was sealed and placed into an auto-sampler at 15°C to await LC-MS/MS analysis.

## 2.2.12 Quantification of Fluorescence Intensity

The confocal images were analyzed for their respective fluorescence pixel intensity by importing the images into Fiji ImageJ software for image analysis[146, 147]. We selected the visually brightest cell in each sample as a representative of the triplicates of each BBB type. The image analysis program calculated the whole cell surface area for mean fluorescence intensity (MFI). Black background or no cell region MFI was also obtained using the same selected cell area and was subtracted from the cell MFI for the final MFI. The software delivers the mean intensity for the entire area selected.

## 2.2.13 Functional Evaluation of the 4-cell Model with Drug Penetration Analysis

DTG is an integrase strand transfer inhibitor commonly used in ART to treat HIV. Here, DTG was utilized as a control to show the functionality of the model. We mixed the corresponding media mentioned above with 4000ng/ml of DTG dissolved in vehicle [Dimethyl sulfoxide (DMSO)/Polyethene glycol-400 (PEG400)/Propylene glycol (PG)/ethanol/kolliphor/1× PBS (8/25/15/10/7/35% v/v)]. The drug-containing media was then added to the apical layer of the transwell membrane. A total of 2000 ng DTG in 0.5ml media was added to the apical layer of BBB. After 48 hours of drug treatment, 0.5ml of media from the apical and basal layer was collected and preserved at $-70^0$ for further analysis. The concentration of DTG in the collected media was analyzed using validated LC-MS/MS methodology previously described[58, 85, 148].

## 2.2.14 Results

## 2.2.15 TEER Measurements

Optimization of Collagen, Poly L-Lysine, and Fibronectin Coating in a Polycarbonate Transwell Membrane Containing hBMECs and Neurons. Following hBMECs and neuron cells grown in a polycarbonate transwell membrane plate, the highest TEER value of 145 ohm/cm$^2$ was observed when the wells were coated with collagen, poly L-Lysine and fibronectin as compared with collagen and poly L-Lysine or collagen and fibronectin as presented in **Figure 9**. The TEER value reduced to approximately 30 ohm/cm$^2$ on day eight post-seeding of cells (all coating combinations).

Despite the TEER drop, these results indicate that coating with bovine collagen I, fibronectin, and Poly-L-Lysine could be a viable strategy.

Optimization of Astrocyte and Pericyte Cell Numbers in a Co-culture in Polyester Insert Membrane Improves TEER. In the polycarbonate plate, we could not observe a stable $TEER_{max,}$ which could be due to different plates and the in-house coating combinations. To achieve the desired stability in $TEER_{max}$, a polyester transwell plate was used to establish the BBB model. A steady-state reading of 100 ohm/cm$^2$ TEER was reached and was continued for four consecutive days after reaching $TEER_{max}$. Seeding density of astrocytes and pericytes influenced the TEER value, and 0.6:0.12 million astrocytes:pericytes showed the highest TEER compared to 0.3:0.06 and 0.15:0.03 million astrocytes: pericytes (**Figure 10**). These results indicate that astrocytes and pericytes at the appropriate cell seeding population are essential to forming a layer with higher integrity and maximum TEER potential. Thus, further experiments were performed with 0.6:0.12 million astrocytes: pericytes.

4-Cell Model and Effect of Zn and Serum Deprivation on BBB Integrity. A steady-state TEER value in the polyester plate still showed lower values compared to previous models, indicating the need for further optimization. Various conditions, including the addition of Zn or serum to media, were used to improve TEER values. The effect of Zn supplementation, added as $ZnSO_4$, on barrier proteins expression and TEER value was measured. As depicted in **Figure 11**, Zn moderately increased the TEER to a maximum of 230 ohm/cm$^2$ (day 10) compared to untreated controls (155 ohm/cm$^2$) and serum-deprived conditions (≤80 ohm/cm$^2$). Neurons combined with hBMECs, astrocytes, and pericytes significantly enhanced TEER demonstrating the higher integrity of the 4-cell model vs. the 3-cell BBB model (**Figures 11, 12**).

## 2.2.16 Imaging

Expression of Tight Junction Proteins in Astrocytes, Pericytes, and hBMECs**.** Expression of claudin 5 and ZO-1 proteins on the co-cultured astrocytes and pericytes at the basolateral part of the polyester transwell membrane was determined with immunostaining and analyzed with laser scanning microscopy (**Figure 12a**). The membrane was then probed for expression of claudin 5 and ZO-1 in the contact-cultured hBMECs in the same transwell membrane sample (**Figure 13c**). Both astrocytes:pericyte **(Figure 12a**) and hBMECs (**Figure 12c**) expressed claudin 5 and ZO-1 tight junctions, and their expression was increased with the addition of Zn to the medium of astrocyte: pericyte (**Figure 12b**) and hBMECs (**Figure12c**).

Validation of Cell Types**-** Cellular markers for astrocytes (S100B), pericytes, and hBMECs (CD146) expressed on the cell surface were visualized with specific antibodies. In **Figure 13a**, astrocyte s100b are shown in red color detected with the Alexa-647 conjugated antibody, and pericytes are illuminated in green by an Alexa-488 anti-CD146 antibody. The opposite side of the same membrane was also probed for hBMECs with the Alexa-488 anti-CD146 antibody and showed CD146 expression on hBMECs (**Figure 13b**).

Expression of Tight Junction Proteins on hBMECs, Astrocytes, and Pericytes during Serum Deprivation and Influence of Zn Sulfate Treatment. Astrocytes: pericytes and hBMECs during serum-deprived conditions or with the addition of Zn were stained for claudin 5 and ZO-1 expression. They were not affected on ZO-1 with Zn treatment in both astrocytes: pericytes (**Figure 14a** vs. 1**4b**, Column 1 and 4) and in hBMECs (**Figure 14c** vs. 15d, Column 1 and 4). However, Zn increased the expression of claudin 5 on astrocyte: pericyte co-cultures (**Figure 14a** vs. **14b**, Columns 2 and 4), whereas no significant difference for claudin 5 was observed in hBMECs (**Figure 14c** vs. **14d**, Column 2). These results indicate that astrocytes:pericytes, and hBMECs express ZO-1 and claudin 5 even

during serum deprivation, and claudin 5 expression is inducible and is increased in astrocytes:pericytes during Zn sulfate treatment.

3-Cells: Astrocytes, Pericytes, hBMEC, without neurons and Poor Expression of Barrier Proteins. The sample with astrocytes and pericytes at the basolateral layer and hBMECs in the apical layer of the membrane (no neurons added) had similar ZO-1 expression as the 4-cell model but had a poor presentation of claudin 5 (**Figure 15a** and **15c**) compared to the 4-cell model (**Figure 12**). Surprisingly, adding Zn did not improve claudin 5 expression when there were no neurons (**Figures 15b** and **15d**). Cells were analyzed for their phenotype based on specific marker expressions (see published supplemental material)[104].

hBMECs Monolayer with Claudin 5 and ZO-1 Expression. The hBMEC monolayer present on the transwell membrane was probed with anti-ZO-1 and anti-claudin 5 antibodies to determine expression on cells. hBMECs expressed ZO-1 and claudin 5 tight junction proteins (**Figure 16a**). The image analysis shows that hBMECs alone can produce tight junction proteins; their expression is not optimal in these conditions.

Neuronal Cell with Claudin 5 Expression. In the presence or absence of neuronal cells, there was a difference in the expression of claudin 5 (**Figures 12 and 15**). Thus we analyzed neurons for claudin 5 expression on the neuron cell surface. We found a basal level of claudin 5 expression on neurons, and the supplementation of Zn to the medium showed a visible increase in expression (**Figure 16b** vs. **16c** and column 4).

Fluorescence intensity measurement. We quantified the MFI of the claudin 5 protein in each represented cell from the various combinations of BBB representation. As can be seen in Figure 18a, in the presence of Zn in the media, the claudin 5 MFI of astrocyte:pericytes increased by 33%, and 43% in hBMECs. Similarly, the analysis revealed more than a 50% increase of claudin 5 MFI in astrocyte:pericyte from the 4-cell model in the absence of serum. Other BBB representations did not show any substantial

difference in MFI. Neuronal cells from the 4-cell model yielded an MFI of 10, but the addition of Zn in the media increased the MFI to 19.

Functionality Testing: DTG penetration. DTG is known to cross the BBB[149]. As shown in **Figure 17b**, there is a difference of approximately 33% DTG distribution across the transwell membrane of the 4-cell model. We also found approximately 17% inhibition in drug penetration when the transwell membrane had only hBMECs monolayer without astrocyte:pericyte and without the involvement of neurons. The data also supports the idea of Zn addition to the 4-cell model for enhancing tight junction formation as the penetration of DTG.

## 2.2.17 Discussion

This study demonstrated a novel, reproducible, in-vitro BBB model using four primary human brain cells, illustrating a more comprehensive image analysis compared to existing BBB models. The transwell plates used by earlier groups are specific and expensive[129, 130, 150, 151]. Further, some methodology is no longer reproducible due to manufacturers' discontinuation of required supplies. Given the importance of drug permeability studies, less expensive, flexible, and reproducible transwell plate methodologies are desired. Consequently, we developed methods that utilize readily available uncoated transwell plates and standardized a strategy for developing a functional BBB in-vitro model. Although we have used the specific pore size and dimensions for the transwell membrane as discussed by Stone et al., we established ways of improving and mitigating dependence on particular aspects of their BBB model.[130] The initial visualization issue for co-cultured cells on the membrane raises uncertainty of cell attachment and growth because of poor visibility of cells when they are growing on the transwell membrane[152]. We found that polyester membranes with the same pore size of 3μm are better than polycarbonate for visual confirmation of cell adherence and growth

under a microscope (**Figure 10a and b**). Because we used uncoated transwell membrane plates, different coating strategies were performed, and our data revealed that 50µg/ml of bovine collagen I followed by 3µg/ml of bovine fibronectin and Poly-L-Lysine yielded the most optimal TEER values (**Figure 10c**). We observed $TEER_{max}$ on day six, which agreed with an earlier in-vitro primary human brain cell BBB model report[138]. However, the TEER was not static, and there was a sharp decline in TEER value after reaching $TEER_{max}$ after day six (**Figure 10c**)[130]. Because of unsatisfactory results from the translucent polycarbonate transwell plates, we decided to use polyester transwell plates, and its semi-transparency was better for visualization. The best coating combination of collagen, followed by fibronectin and finally poy-L-lysine, observed with the polycarbonate membrane, was carried forward with the polyester membrane. As a standardization procedure, initially, we used only astrocyte and pericyte co-cultured with different cell seeding densities in the basolateral part of the transwell membrane. As indicated in **Figure 11**, the seeding density of $6x10^5$ astrocyte and $1.2x10^5$ pericyte in 150 µl exhibited TEER values nearly 2-fold greater than half of these cell densities, which is in agreement with results of earlier work[153]. Notably, the $TEER_{max}$ was established on day 6, and there was a steady state in TEER value for four consecutive days, with a drop in TEER observed on day 10 (**Figure 11**). A $TEER_{max}$ of ~100 ohm/cm$^2$ has been reported in previous studies with co-cultures of two different cell types[154, 155]. Following our standardization results and evaluation of different conditions, we developed a 4-cell in-vitro BBB model that included human primary hBMECs, astrocytes, pericytes, and neuronal cells. According to previous reports, adding Zn and starving cells of serum media has been shown to improve TEER values in the in-vitro BBB model[140,141]. Thus, as depicted in **Figure12**, we included these conditions by adding 100 µM $ZnSO_4$ in the culture media and using media without serum. As presented in **Figure 12**, out of several different combinations, adding Zn increased TEER values[140]. However, we did not find enhancement of TEER in the

absence of serum (i.e., starving condition); instead, we found a decrease in TEER compared to normal media. This can be explained by the need for donor-specific serum requirement for human neuronal cells[130, 156] and the use of primary cells. Our data emphasized the necessity of neurons for optimal BBB formation regardless of the presence or absence of Zn supplementation in media. Our approach is also supported by visualizing tight junction proteins via laser scanning microscopy. Cells were visualized, and the expression pattern of tight junction proteins at both sides of the membrane (apical and basolateral sides) was analyzed without the dependence on Z-stacking, an advancement over existing in-vitro primary brain cells BBB models. It is important to note that on day 11, membranes with cells were fixed for microscopy, and by that time, there was already a decrease in TEER measurement (**Figure 12**). Typically, it is challenging to visualize tight junction proteins when three human primary brain cells are present on the insert membrane. Previous studies have shown tight junction protein images for a monolayer of single cell type using immortalized cells[141] or an endothelial monolayer on cellulose acetate scaffold[157]. In this study, we successfully studied the tight junction proteins ZO-1 (Zona occludens) and claudin 5 together with the identification of 4-cell types present. Confocal images of tight junction proteins ZO-1 and claudin 5 were better detected in astrocytes and pericytes when the BBB was developed in normal media with and without Zn (**Figure 13a and 13b**). Additionally, there was an apparent difference in claudin 5 expression on hBMECs in the presence and absence of Zn (**Figure 13c and 13d**). Thus, the confocal study results supported the recorded TEER values, even though samples were preserved for microscopy on day 11 when the TEER value was in decline (**Figure 12**). Regarding tight junction microscopy, the previous study by Miranda-Azpiazu et al. imaged tight junction proteins in the multicellular BBB model, but only endothelial cells were stained for ZO-1[158]. Our present study also showed the expression of specific surface proteins using protein-specific antibodies. The individual cell type from the

basolateral astrocyte:pericyte co-culture and apical hBMECs were identified with astrocyte-specific anti-S100B antibody (red), and the co-cultured pericyte along with hBMECs in the contact culture was recognized by anti-CD146 (green) antibody (**Figure 14a and 14b**). Initially, in the absence of serum, there was poor detection of claudin 5 on astrocytes and pericytes, as documented in **Figure 15a**, but the expression of claudin 5 increased in the presence of Zn (**Figure 15b**). No visible difference was noted for ZO-1, and similar fluorescence visibilities for claudin 5 were detected in hBMECs regardless of the presence of Zn (Figure 10a). This could be due to the potential saturation of ZO-1 or samples collected during the decline in TEER measurement (i.e., day 11). Similar to **Figure 14**, individual cells on both sides of the transwell membrane were confirmed (Figure S1). A study by Antje et al. presented confocal images for tight junction protein ZO-1 but not claudin 5, and the experiment was performed with human induced pluripotent stem cells (hiPSCs). In contrast, we carried out our experiment with primary cells[151]. Importantly, we investigated the role of neuronal cells in the expression of tight junction proteins with confocal microscopy. Again, no significant difference was observed for ZO-1. However, there was some improvement of claudin 5 expression in the presence of Zn (**Figure 16a, 16b** column 4), but the improved claudin 5 expression is better visualized for hBMECs (**Figure 16c, 16d** column 4). Regardless of tight junction protein expression, cells were seen intact and were successfully classified by their respective markers (see published supplemental material). As expected, a monolayer of hBMECs on the transwell membrane manifested tight junction proteins (**Figure 17a**, columns 1, 2, and 4), but the visible expression level was lower than the 4-cell model (Figure 5). Furthermore, neurons at the bottom of the wells for BBB development were also recorded for neuronal marker and claudin 5 (**Figure 17b and 9c**, columns 2 and 4). From the analyzed images, the basal level of claudin 5 on neuronal cells could be debatable; nevertheless, we observed a better claudin 5 distribution on the neuronal cells in the presence of supplementary Zn.

Here for the first time, we are showing the confocal image of non-contact neurons from the 4-cell model exhibiting claudin 5 on its surface. There is not enough research on barrier proteins in neuronal cells. An early report by De Lorenzo et al. found a detectable level of claudin 5 in neurons by immunohistochemistry analysis, and the same study also suggested a better expression level of claudin 5 in astrocytes[159]. Previously mRNA analysis indicated the existence of tight junction proteins in synapses of chick ciliary ganglion[159, 160]. Though the immunohistochemistry analysis revealed a low claudin 5 in neurons[159], the studies did not perform confocal microscopy. Here, our study provides visual evidence of claudin 5 on neuronal cells from the BBB model, which can be modulated in the presence of Zn. Since all the component cells from different BBB setups exhibited similar expressions of ZO-1, we only analyzed the fluorescence intensity for the visually evident claudin 5 to confirm the level of difference. The fluorescence intensity analysis also agrees with the visually predictable difference of intensity in the presence or absence of Zn. Also, it supports the notion that neuronal cells express claudin 5 when they are in contact with astrocytes and pericytes. (**Figure 18a**). Regarding specific applicability of drug penetration, we present DTG data to show functionality of the 4-cell model in regulating drug penetration into the CNS (calculation for DTG penetration estimation: 4000ng/mL given, end of 48 hrs, 750ng/mL found on the apical side, ~450 ng/mL found on the basal side, some drug lost to experimental conditions and or adherence to wells). This new model will allow more drugs to be studied in the future.

This study presents a simplified and effective methodology for multi-cell in-vitro BBB model development and TEER characterization completed with a comprehensive confocal microscopy confirmation. For a better understanding of the time course for the steps of model development, a flow chart has been included for the strategic time points (**Figure 8**). Critically, we are also showing the neuronal cells in the BBB model expressing claudin 5, which could be inducible by adding Zn micronutrient in the media. This valuable

information needs further research work and validation. Going forward, our neuronal cell data from the 4-cell model can be helpful in future research work of various fields of neuroscience. The present study is part of a larger goal to analyze antimicrobial drug penetration through the BBB. Given the recent statement from the FDA to minimize in vivo animal work, this methodology will be a helpful tool for both toxicology and drug screening studies to assess penetration of various xenobiotics into the CNS. Further, incorporation of tight junction protein expression in neuronal cells of BBB model makes this work more translational (bench to bedside). We anticipate this model will better our understanding of CNS pharmacology with the ultimate goal of better patient care and clinical outcomes.

**A).**

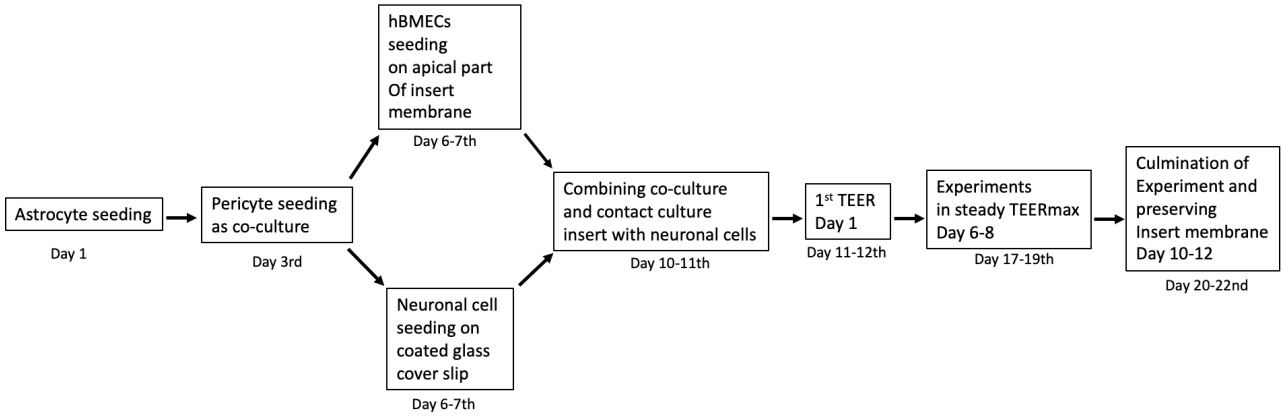


**B).**

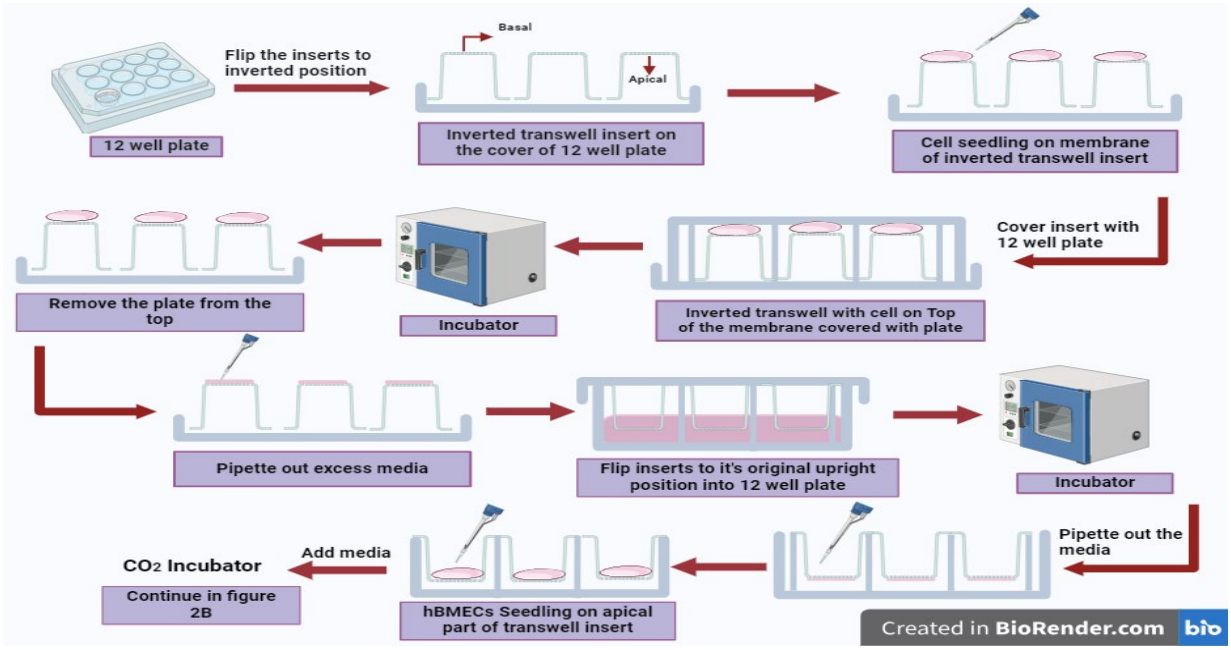


**Figure 7.** Model development flow chart outlining steps and time points (a) and schematic representation of all critical time points and steps in the in-vitro BBB model development (b). Days represent the total days starting from astrocyte seeding until the completion of the experiment.

Abbreviations: hBMEC, Human brain microvascular endothelial cells TEER, Trans Epithelial Electrical Resistances

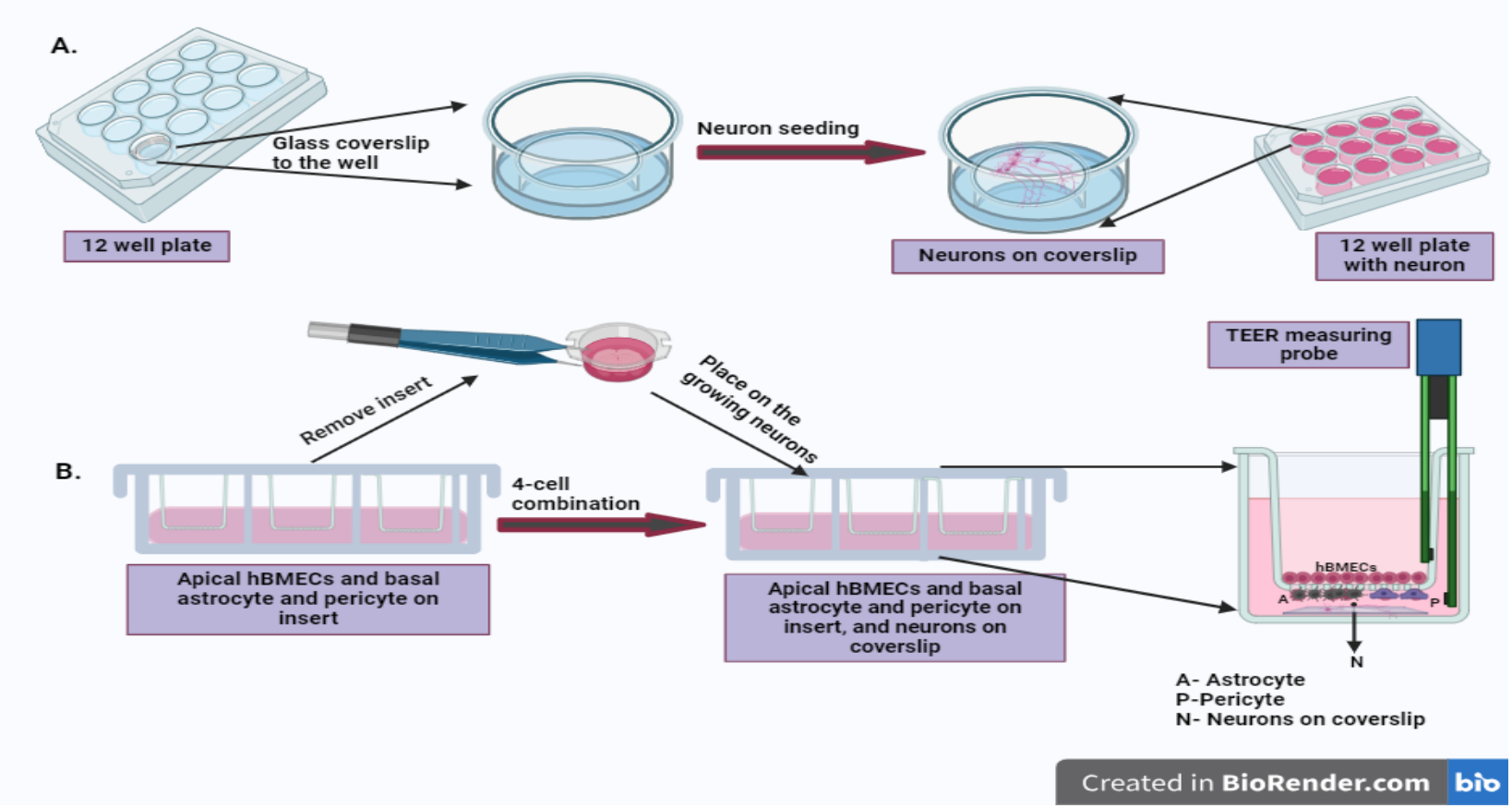


**Figure 8.** Diagrammatic presentation of glass coverslip handling for neuron seeding (a) and combining all four cells for BBB model and TEER measuring (b)

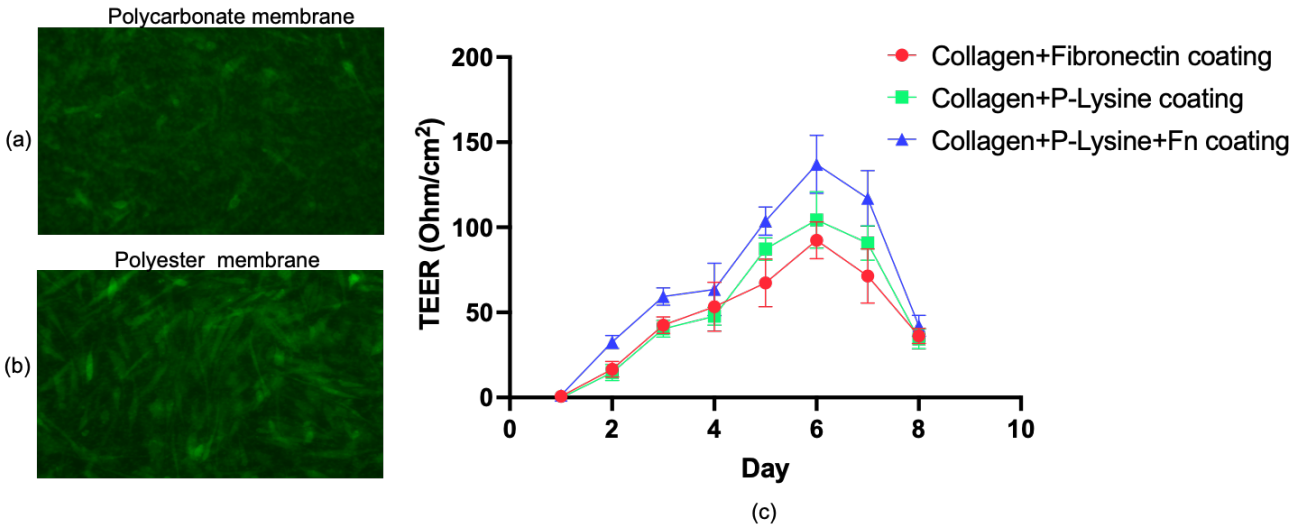


**Figure 9.** Comparative cell visualization and 4-cell model on polycarbonate membrane. Visualization of unstained cells growing on a polycarbonate (a) and a polyester (b) transwell membrane. The TEER in polycarbonate Transwell inserts was measured with an EVOM2 meter for eight days (c). Measurement was carried out three times daily, and the average is shown. Data represent values for samples in triplicates.

Abbreviations: Fn, Fibronectin; Collagen, bovine Collagen I, and P-Lysine, Poly-L-Lysine; TEER, Trans Epithelial Electrical Resistances

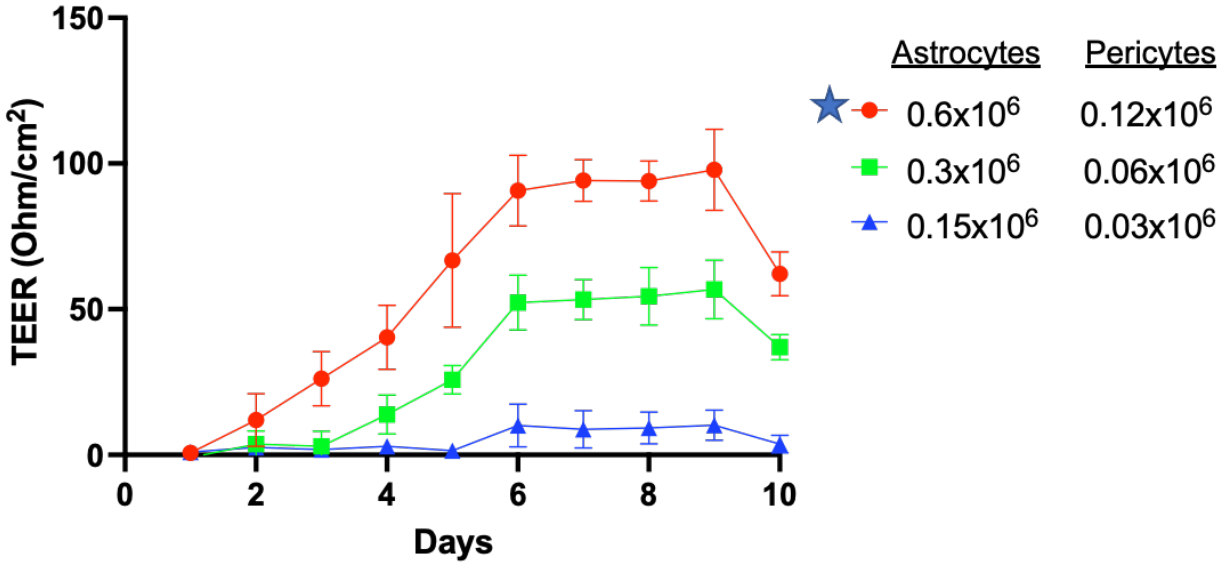


**Figure 10**. TEER value of 4-cell BBB model with various modulations. Standardization of cell density for better TEER**.** TEER in astrocyte and pericyte co-cultures seeded in polyester Transwell insert. Data represent values from triplicate wells on each day for six days post-seeding. Star-marked cell density was carried forward for further experiments.

Abbreviations: TEER, Trans Epithelial Electrical Resistances

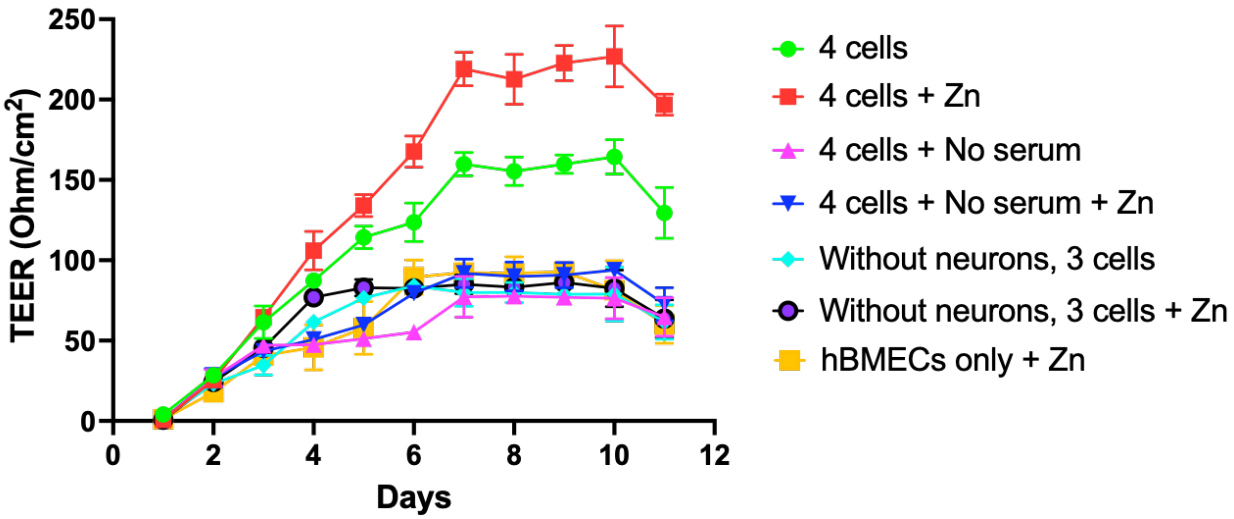


**Figure 11.** TEER in 4-cell model containing hBMCEs, astrocytes, pericytes, and neurons in a polyester Transwell insert or with changing various conditions, ± Zn; ± Serum; ± neurons or only hBMECs. At each point, triplicates are used for rigor and TEER measured three times. On day 11 post-cell seeding, cells on the transwell insert membrane were fixed and preserved for confocal microscopy study.

Abbreviations: TEER, Trans Epithelial Electrical Resistances; Zn, zinc; hBMEC, Human brain microvascular endothelial cells.

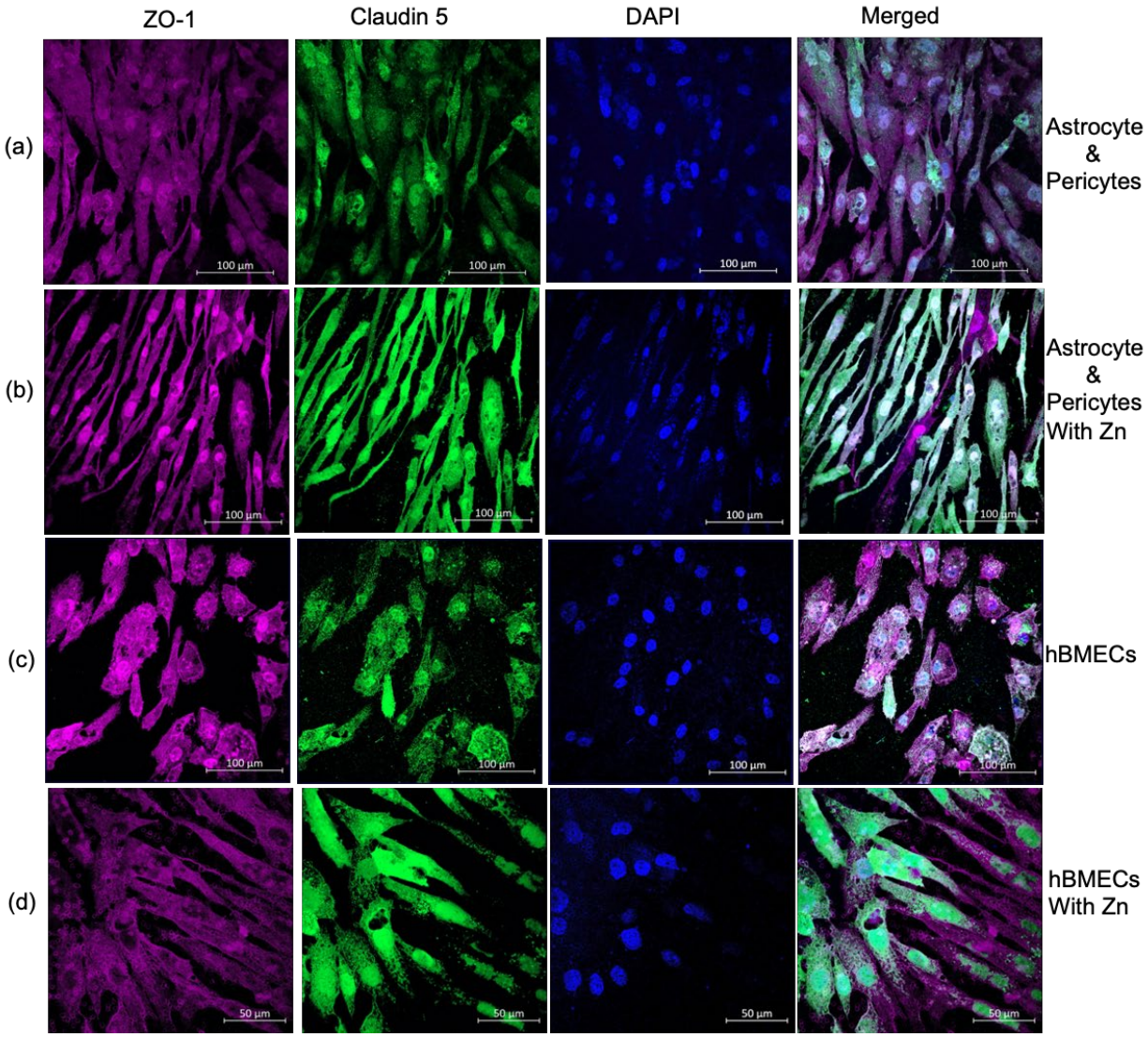


**Figure 12**. Imaging cells form a 4-cell model for tight junction proteins detection. Expression of TJs, ZO-1, and claudin 5 on human brain cells, layered on polyester transwell insert membrane. ZO-1 (Red) and claudin 5 (Green), and the nucleus (blue) were stained with DAPI (4,6-diamidino-2-phenylindole). TJs were observed on- astrocytes and pericytes in medium alone (a), with the addition of Zn sulfate (b), and hBMECs in medium alone (c) with Zn sulfate (d).

Abbreviations: Zn, zinc; TJ, tight junctions; Z0-1, Zona occludens; hBMCE, Human brain microvascular endothelial cells; DAPI, 4',6-diamidino-2-phenylindole.

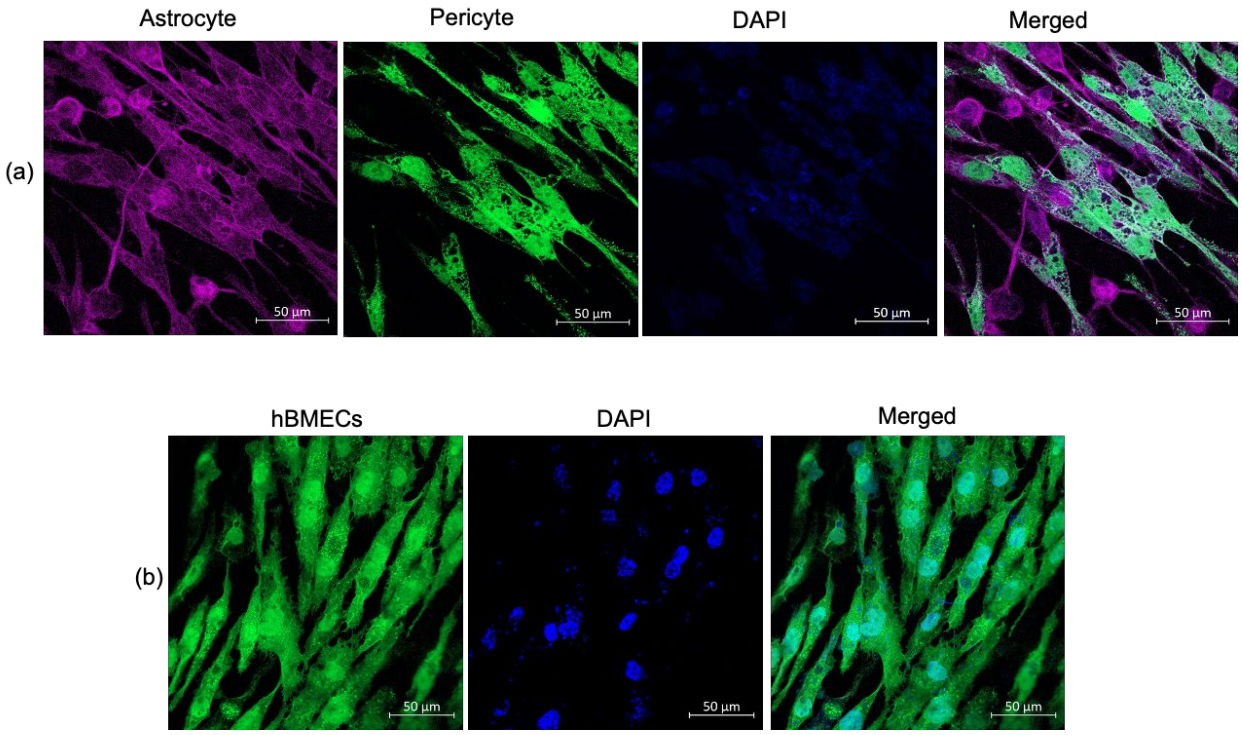


**Figure 13**. Imaging cells form a 4-cell model for cell type identification. Cell identification by detecting s100 beta on astrocytes and CD146 on pericytes and hBMECs as respective cell markers. Astrocytes, pericytes, and hBMEc on a transwell membrane, immunostained with a cocktail of s100beta antibody (red), an antibody against CD146 (green), and the nucleus was stained with DAPI (blue). The basolateral surface of the transwell membrane shows astrocyte and pericyte (a), and the apical part of the same transwell membrane shows hBMECs only (b).

Abbreviations: hBMEC, Human brain microvascular endothelial cells; DAPI, 4',6-diamidino-2-phenylindole.

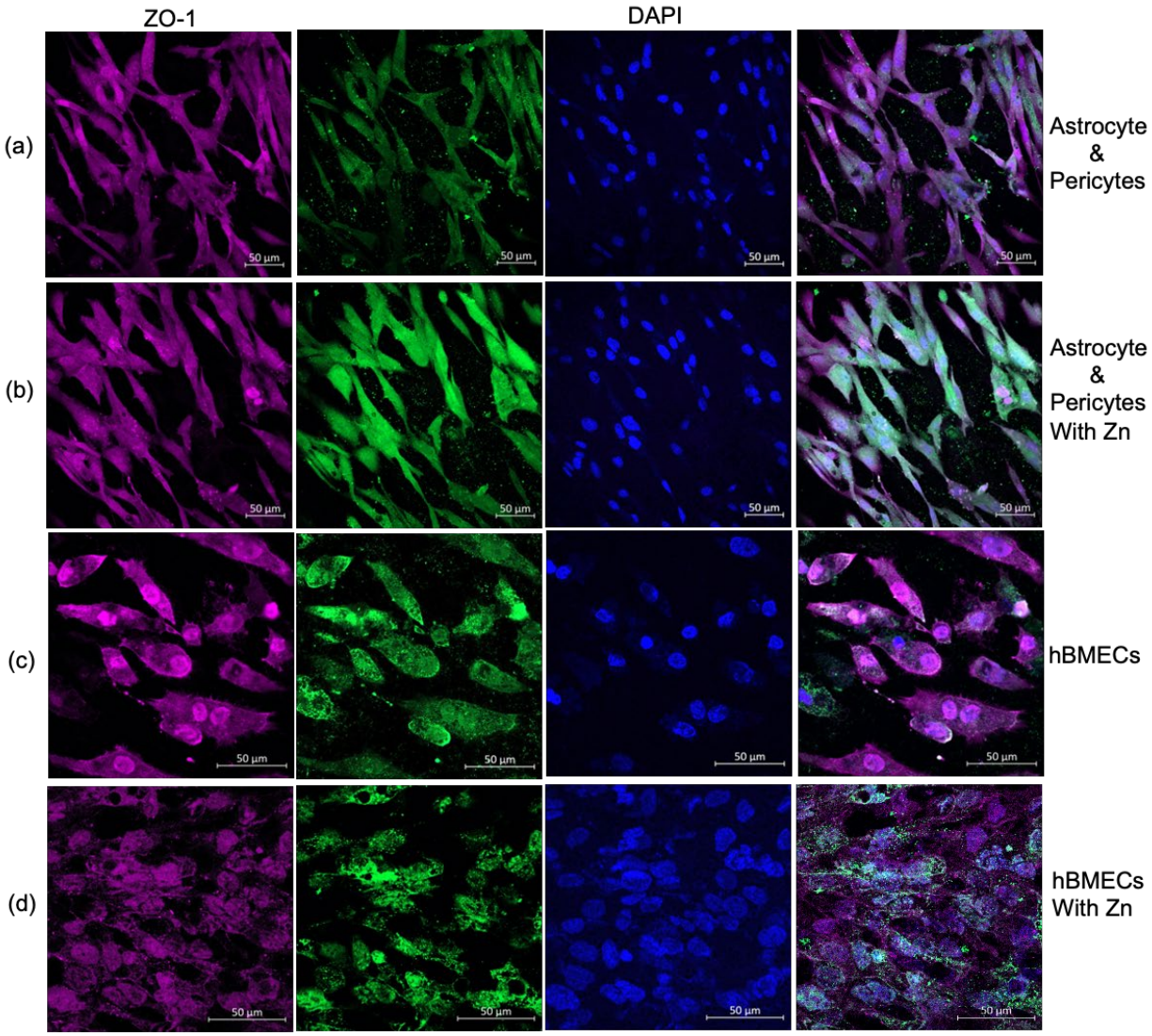


**Figure 14**. Detection of tight junction proteins on cells from a 4-cell model in no serum media. Serum-free medium, confocal images of TJ protein ZO-1 (red), Claudin 5 (green) expression on astrocytes and pericytes (a) or following treatment with Zn sulfate (b) and for hBMECs (c) following treatment with Zn (d) localized to transwell insert membrane in BBB model. The nucleus was stained with DAPI.

Abbreviations: Zn, zinc; TJ, tight junctions; Z0-1, Zona occludens; hBMEC, Human brain microvascular endothelial cells; DAPI, 4',6-diamidino-2-phenylindole; BBB, blood brain barrier.

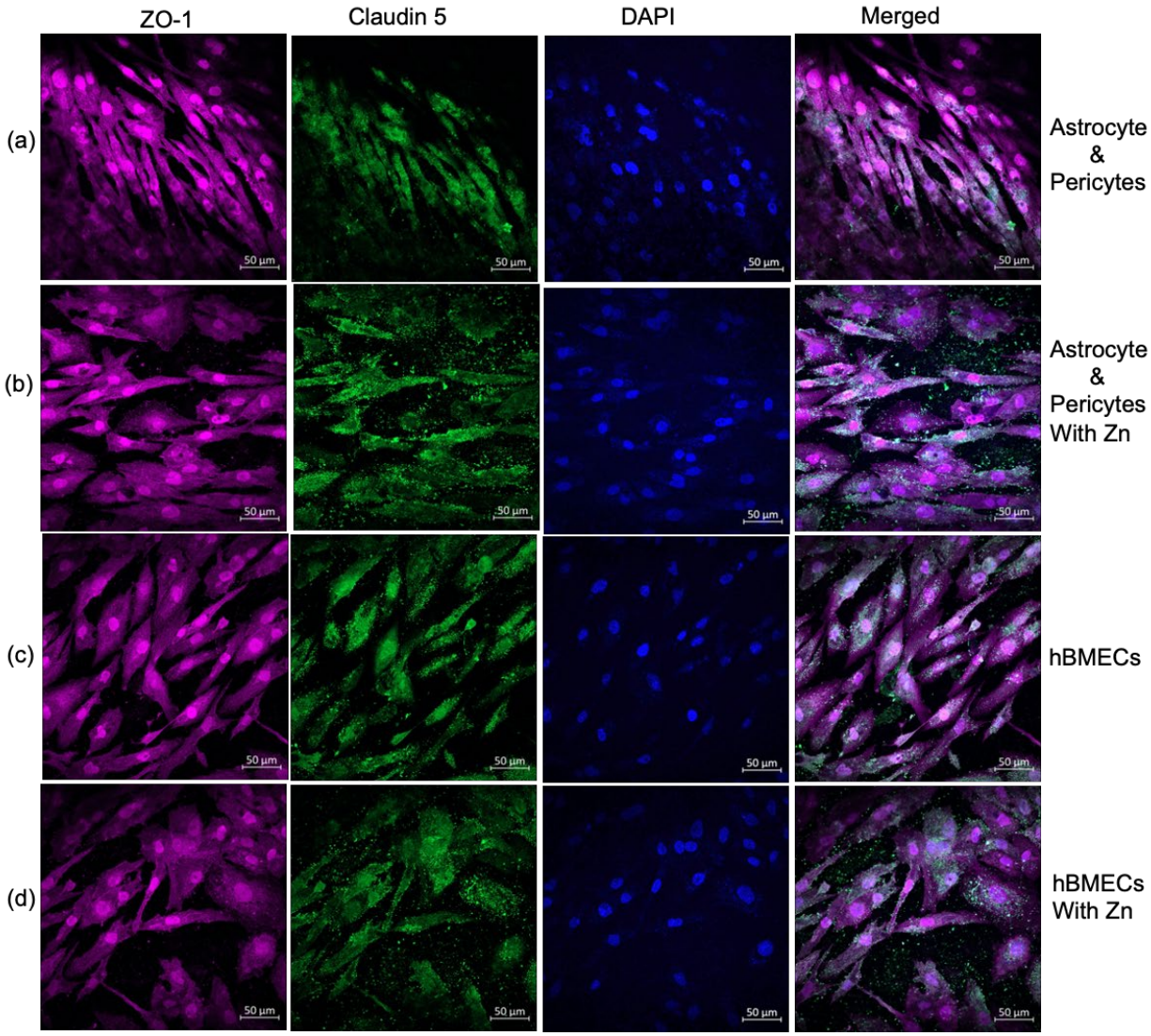


**Figure 15.** Imaging cells form a 3-cell model for tight junction proteins detection, no neurons. In the absence of neuronal cells, expression of ZO-1 (red) and claudin 5 (green) in astrocytes and pericytes (a) and when supplemented with Zn in the medium (b) and the corresponding contact cultured hBMECs (c) supplemented with Zn (d). DAPI was used for nucleus staining.

Abbreviations: Zn, zinc; Z0-1, Zona occludens; hBMEC, Human brain microvascular endothelial cells; DAPI, 4',6-diamidino-2-phenylindole.

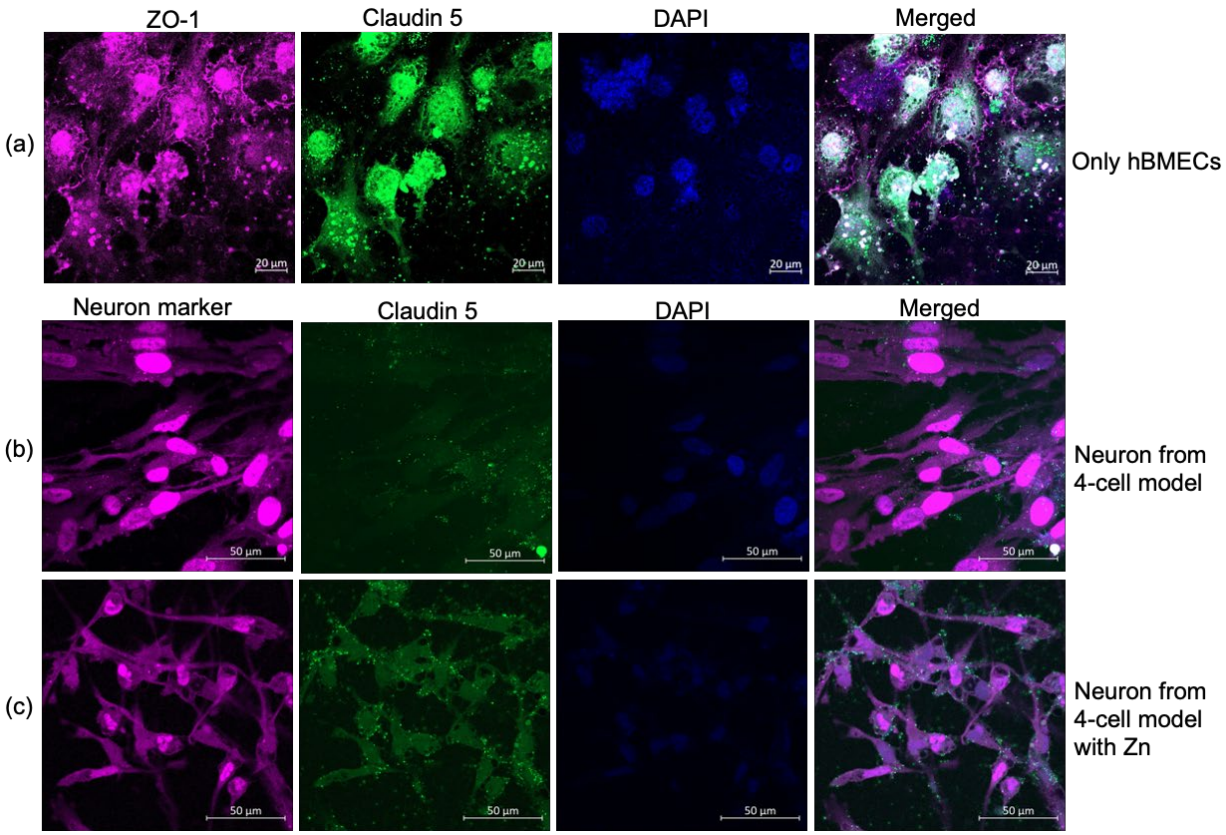


**Figure 16.** Image evaluation for tight junction proteins on monolayered hBMECs, claudin 5 on neurons. Expression of ZO-1 (red), claudin 5 (green) in mono-culture of hBMECs on a transwell membrane (a) and determination of claudin 5 on neuron cell from the non-contact 4-cell model with neuronal cell marker in red (b) and when the medium for the BBB model was supplemented with Zn (c).

Abbreviations: Zn, zinc; Z0-1, Zona occludens; hBMEC, Human brain microvascular endothelial cells; DAPI, 4',6-diamidino-2-phenylindole.

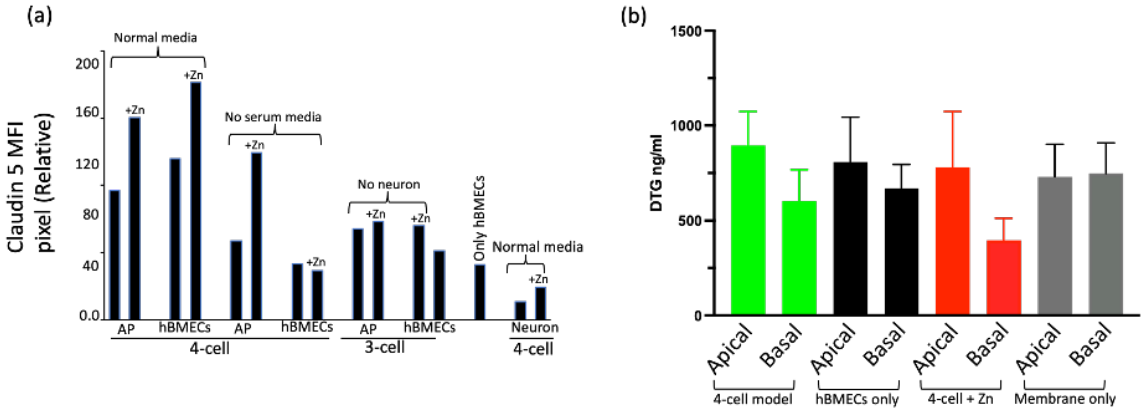


**Figure 17.** Fluorescence intensity and functional analysis of tight junction formation in 4-cell model. Average fluorescence intensity analysis of claudin 5 for one representative corresponding to the image shown from the triplicate of BBB model types and drug penetration for different sets of BBB representation. (a) Cell surface pixel intensity for claudin 5 measured using FIJI ImageJ-win64 software and (b) evaluation of tight junction integrity and the penetration of HIV-ART drug *DTG in the 4-cell model. The color-coded bar pairs show drug distribution in the apical and bottom layers of the indicated in-vitro models and control (membrane only) from a transwell membrane plate. Media from the apical and basal layer of the transwell membrane was collected after 48 hours of drug treatment. Data represent the mean concentrations from 3 replicates.

*Calculation for DTG penetration estimation: 4000ng/mL given, end of 48 hrs, 750ng/mL found on the apical side, ~450 ng/mL found on the basal side, some drug lost to experimental conditions and or adherence to wells

Abbreviations: MFI, mean fluorescence intensity; AP, astrocytes and pericytes; DTG, dolutegravir; hBMEC, Human brain microvascular endothelial cells; Zn, zinc

# Chapter 3: In Vivo Models to Assess CNS Penetration

## 3.1 Introduction

Chapter 3 details an *in vivo* (major) and some *in vitro* (minor) investigations in rats and human CNS cells that was used to assess CNS penetration of NMR/r. As Chapter 1 discussed various different therapeutic agents available for treatment of COVID-19 based on severity and patient setting, this Chapter will focus primarily on NMR/r as it is listed as one of the preferred agents for outpatient treatment and can be taken orally which is more convenience for patients. Ten male Sprague-Dawley rats were purchased from Charles River that came with intracisternal catheters and double jugular catheters. This allowed for extensive sampling of CSF and blood after dosing with NMR/r. At the completion of experiments, tissues and peripheral blood mononuclear cells (PBMCS) were also collected and processed/counted for NMR quantification. The NMR/r dose given to the animals was an oral humanized equivalent based on principles of allometry. The current FDA approved dose of NMR/r for patients with normal renal function is 300 mg NMR + 100 mg RTV given orally twice daily for 5 days. The humanized equivalent of NMR/r based on this fixed dosing for rats would be approximately: 60 kg patient [human], 300 mg NMR + 100 mg RTV twice daily, = 10 mg/kg NMR + 3.33 mg/kg RTV daily x scaling factor of 6.2 = ~60 mg/kg NMR + ~20 mg/kg RTV daily[161]. Thus, the rats were administered an oral dose of NMR/r at 20mg/kg/60mg/kg divided into a twice daily dose x 5 days via oral gavage. We chose the oral route because we wanted to replicate human relevance as much as possible.

After completion and quantification of all NMR in all matrices, formal PK/PD analysis was conducted to assess CSF penetration as a ratio of plasma:CSF levels. This

was done by comparing different plasma and CSF exposure metrics to each other at the same time point (i.e., maximum concentration [$C_{max}$], area under the curve [AUC]). This provided an estimate of how well NMR was getting into the CSF from the blood (i.e., central compartment to the CSF compartment). Further, the PK modeling allowed full NMR prediction profiles for both plasma and CSF to be estimated which allowed us to compare these to known PD endpoints for SARS-CoV-2.

Tissue, CNS cell, and PBMC level of NMR displayed interesting results. NMR was not found in therapeutic concentrations in brain tissue. Full details for these methods and findings are described below.

## 3.2 In-vitro and In-vivo Assessment of Nirmatrelvir Penetration Into CSF, Central Nervous System Cells, Tissues, and Peripheral Blood Mononuclear Cells

*#Corresponding Author & First Author*

Reproduced with permission from Springer Nature*:* **Avedissian SN#**, Malik J, Podany AT, Neely M, Rhodes NJ, Scarsi KK, Duryee M, Modebelu UO, Mykris TM, Winchester LC, Byrareddy SN, Fletcher CV#. *Assessing the penetration of nirmatrelvir into cerebrospinal fluid, central nervous system cells and tissues, peripheral blood mononuclear cells, and its implications for SARS-CoV-2 clearance.* Scientific Reports. May 10 2024. (PMCID: PMC11087525

### 3.2.1 Abstract

Three years after SARS-CoV-2 emerged as a global infectious threat, the virus has become endemic. The neurological complications such as depression, anxiety, and other CNS complications after COVID-19 disease are increasing. The brain, and CSF have been shown as viral reservoirs for SARS-CoV-2, yielding a potential hypothesis for CNS effects. Thus, we investigated the CNS pharmacology of orally dosed nirmatrelvir/ritonavir (NMR/r). Using both an *in vitro* and an *in vivo* rodent model, we investigated CNS penetration and potential pharmacodynamic activity of NMR. Through pharmacokinetic modeling, we estimated the median CSF penetration of NMR to be low at 18.11% of plasma with very low accumulation in rodent brain tissue. Based on the multiples of the 90% maximal effective concentration ($EC_{90}$) for SARS-CoV-2, NMR concentrations in the CSF and brain do not achieve an exposure level similar to that of plasma. A median of only 16% of all the predicted CSF concentrations in rats were >3x$EC_{90}$ (unadjusted for protein binding). This may have implications for viral persistence and neurologic post-acute sequelae of COVID-19 if increased NMR penetration in the CNS leads to decreased CNS viral loads and decreased CNS inflammation.

## 3.2.2 Introduction

Global cases of COVID-19 continue to rise daily[162, 163]. Although SARS-CoV-2 is often referred to as a respiratory virus, in addition to the lung it has been found in tissues including the brain, liver, intestine, feces, heart, and kidneys of individuals with COVID-19[31]. Moreover, COVID-19 has been demonstrated to infect mononuclear cells. In postmortem lung T-cells, the presence of COVID-19 antigen was observed, with CD4 positive T-cells indicating SARs-CoV-2 infection, and there have been reports of antibody-mediated infection in monocytes and macrophages as well[164-166].The impact of COVID-19 on human health has led to significant investment in new strategies including the development of new therapeutic agents to reduce the risk of infection, disease, and negative outcomes.

One available oral antiviral treatment for COVID-19 is ritonavir boosted NMR (NMR/r; PAXLOVID™)[66]. This drug is a combination of a SARS-CoV-2 MSP5 PI NMR, and r/ weak-PI used in a low-dose as a pharmacokinetic PK enhancer to increase the concentrations of NMR in the blood via inhibition of hepatic oxidative metabolism[167]. NMR is a peptidomimetic inhibitor of the SARS-CoV-2 main protease (Mpro), also referred to as 3C-like protease (3CLpro) or nonstructural protein 5 (nsp5) protease. Inhibition of SARS-CoV-2 Mpro renders the virus incapable of processing the polyproteins pp1a and pp1ab, preventing replication[168]. NMR/r received FDA approval on May 25$^{th}$ 2023, as the first oral antiviral treatment for mild to moderate COVID-19 in adults who are at high risk for severe COVID-19[169]. Currently this combination's only utility is against SARs-CoV-2 infection.

Neurological complications associated with SARS-CoV-2 infection are not well understood. PASC, also known as Long COVID, is a chronic syndrome that affects some individuals who have recovered from acute COVID-19 illness[32]. Based on available

literature, the related incidence, risk factors, possible pathophysiology, and proposed management of neurological manifestations has been summarized by Moghimi et al.[35]. While the majority of SARs-CoV-2 infected persons no longer show symptoms after recovering from infection, some experience persistent neuroPASC symptoms (e.g., depression, anxiety, difficulty concentrating, central nervous system [CNS] disturbances)[36] lasting months or even years after the infection[34, 37]. Interestingly, fatigue has been observed as one of the most common symptoms associated with Long COVID[38, 39]. The etiology of neuroPASC is unclear, and the exact mechanisms of SARS-CoV-2 entry into the CNS are uncertain. Some theories for entry include infection of the endothelium, access through the blood-brain barrier (BBB), and through nervous tissue conduits that bypass the BBB. Given that cells in the CNS can be infected with SARS-CoV2[40], it is plausible that CNS infections lead to the neurological complications described by neuroPASC[41-43]. Mechanisms for SARS-CoV-2 associated neurological complications are still currently being explored[170]. Another theory is that neuroPASC is due to prolonged inflammation present in the CNS post-infection. This theory is supported by both clinical and animal data in persistent SARs-CoV-2 infection[44, 45]. Clinical data from autopsy sampling performed on the CNS of patients who died from COVID-19 found viral RNA, with patients having detectable CNS virus from 4-230 days after infection[46]. A study by Beckman et al. showed that COVID neuroinvasion (non-human primate model) was more significant and widespread throughout the olfactory cortex in older animals than younger ones. They also found axonal spread of the virus from the nasal olfactory epithelium. In the older monkeys, there was an increase in viral load, more pronounced cellular alterations, and neuroinflammation[47]. Given data to support viral entry into the CNS[48], and the known neurological issues associated with neuroPASC, early and effective antiviral treatment of acute COVID-19 may offer hope in preventing or reducing neuroPASC occurrence and severity[49, 50].

Currently, there are no published data on NMR concentrations in the CNS when given orally. It is unknown if NMR can cross the BBB and achieve therapeutic concentrations necessary to treat SARS-CoV-2 infection in the CNS. Given the limited treatment options available for COVID, it is essential to evaluate whether current treatment can be maximized to ensure viral eradication. Treatment and prevention of neuroPASC caused by virus in the CNS would require therapeutic CNS NMR concentrations, which are a function of effective concentration goals ($EC_{50-90}$), brain penetration and dose. Suboptimal drug concentrations in the CNS during acute treatment may unintentionally contribute to neuroPASC. A general principle for treatment of infectious diseases is the need for adequate drug concentration at site of infection[171]. CNS penetration is dependent on many factors that control the ability and amount of a drug that can cross the BBB (e.g., lipophilicity, molecular weight, molecular charge, etc.). Thus, to reach effective drug concentrations in the CNS, strategies to raise the systemic drug levels by increasing dose, frequency or duration, or changing formulation or route of administration, may be necessary[172]. However, increasing the drug dose may significantly increase the risk of systemic toxicity. Preclinical studies investigating penetration into reservoirs are necessary to determine if therapeutic concentrations are clinically achievable. Several clinical trials are currently ongoing looking at using NMR/r as a treatment strategy for patients that are highly symptomatic with Long COVID. One ongoing trial is using NMR/r for 15-days at the current dose to see if this treatment will provide relief in those suffering with Long COVID (NCT05576662; NCT0559369; NCT05668091). These efforts support the need to assess CNS penetration of NMR/r. In this premise, the critical and initial step is to understand NMR/r penetration utilizing pre-clinical models. Accordingly, the objective of this study was to use *in vitro* and *in vivo* preclinical models to determine NMR penetration into the CNS. Astrocytes and pericytes are integral to BBB structure controlling the drug penetration across BBB and uptake of the chemotherapeutic

agents for CNS entry. Animal models provide a way to probe questions that require invasive sampling clinically. Our approach was to use an *in vitro* system consisting of cells of the BBB to explore the ability of NMR/r to enter these cells, and *in vivo* measurements of NMR/r in CSF and other anatomical sites utilizing a rat model.

## 3.2.3 Methods

## 3.2.4 Study

This study was conducted at the University of Nebraska Medical Center in Omaha, NE. All study methods were approved by the Institutional Animal Care and Use Committee (IACUC; Protocol #2006507) and conducted in an AAALAC-accredited animal facility. This study was reported in accordance with ARRIVE guidelines.

## 3.2.5 Chemicals and Reagents

Animals were administered NMR/RTV (NMR: Medkoo Biosciences, Catalog#555985 Lot#: C22R06B23, Morrisville, NC, USA. RTV: Medkoo Biosciences, Catalog#318671, Lot#: A22M08B04) for oral dosing. Artificial CSF (TOCRIS Biotechne, #3525) and normal saline (B/BRAUN, Lot#: R5200-01) were used as described in sampling methods below. LC-MS/MS standard curves were generated using commercially obtained NMR (Cayman Chemical, Lot#:0635075, Ann Arbor, MI, USA) with a purity of >98%. Nirmatrelvir-2H9 (2H9-PF-07321332, Lot#: NA-ALS-22-044-P3, Alsachim, Illkirch, France) was used as an internal standard for the NMR quantification. Formic acid, methanol and acetonitrile were obtained from Fischer Scientific (Waltham, MA, USA). Ultra-pure water was obtained from UNMC via a Barnstead GenPure xCAD Plus water

purification system (Thermo-Fisher, Waltham, MA, USA). Frozen, non-medicated, non-immunized, pooled Sprague-Dawley rat plasma and pooled human CSF (BioIVT, Westbury, NY, USA) were used for calibration of standard curves. For oral dosing, NMR and RTV were mixed into a premade vehicle formulation similar to previous methods[173-175].

## 3.2.6 Cells and Culture System

Human brain primary astrocytes (#1800), pericytes (#1200), and human neurons (#1520) were purchased from ScienCell Research Laboratories (SCRL), USA. Required media and growth supplements for the respective cells were also obtained from SCRL. Astrocytes were cultured in astrocyte media (AM) (Catalog#1801) and astrocyte growth supplement (AGS) (Catalog#1852); pericytes were cultured in pericyte media (PM) (Catalogue#1201), pericyte growth supplement (PGS) (Catalog#1252) and human neurons were seeded in neuronal media (NM) (Catalog#1521) with neuronal growth supplement (NSG) (Catalog#1562). Supplements, including FBS (Catalog#0010), and penicillin/streptomycin solution (P/S) (Catalog#0503) were also purchased from ScienCell. Frozen cells were revived and cultured according to the manufacturer's instructions. Astrocytes and pericyte cells were grown in either a 25 $cm^2$, 75 $cm^2$, or 150 $cm^2$ culture flask (TPP#90076) in accordance with experimental requirements. Culturing flasks were pre-coated for human brain cells with bovine fibronectin at 2 µg/mL (ScienCell#8248). The 6-well plates (TPP#92006) were coated with Poly-L-Lysine (Sigma#RNBL4935) for 10 minutes at room temperature for human neuron cells, washed with PBS, and air dried. Astrocytes and pericytes were harvested by trypsinization (0.25% trypsin, Lonza#CC-5012) from the flasks having close to 90% confluency of growing cells and washed in DPBS (Dulbecco's#1960454). Cells were prepared for counting by mixing 10µl of cell

suspension with 10µl of trypan blue. 10µl of the mixture was read in a cell counter (Invitrogen Countess). Neuron cells were directly seeded on the pre-coated 6-well plates after thawing the frozen vials.

### 3.2.7 Procedures

All steps were carried out in a biosafety cabinet under aseptic conditions, similar to methods previously described[104]. Astrocytes with a cell count of $0.5x10^6$/well were seeded into 6-well plates containing 2 mL of astrocyte media in each well. Seeding was performed in triplicate for each drug or drug combination and incubated in $37^0$C cell culture incubator, as described in our previous work. Pericytes with a cell count of $0.5x10^6$/well were seeded into 6-well plates containing 2 mL of pericyte media in each well. Cell seeding was performed in triplicate for each drug or drug combination and incubated in $37^0$C cell culture incubator. Neurons with a cell count of $0.3x10^6$/well were seeded into 6-well plates containing 2 mL of neuronal media in each well. Seeding was performed in triplicates for each drug or drug combination and incubated in $37^0$C cell culture incubator.

### 3.2.8 Drug Formulation for *In Vitro* Work

Powdered NMR (Medkoo Biosciences, Catalog#555985, Lot#: C22R06B23) was dissolved in 1 mL of 100% DMSO to make a stock concentration of 4.4 mg/mL. Powdered RTV (Medkoo Biosciences, Catalog#318671, Lot#: A22M08B04) was dissolved in 1 mL of 100% DMSO to achieve the stock concentration of 2 mg/mL. NMR and RTV were weighed and dissolved in 1mL of 100% DMSO to achieve 4.4 and 2 mg/mL stock concentration for NMR and r/, respectively.

### 3.2.9 Drug Addition to Cells and Sample Preparation

NMR and RTV, individually or in combination, were added to the cultured cells at 2200 ng/mL and 1000 ng/mL final concentration, respectively. The *in vitro* doses of NMR and RTV were selected based on previous studies[176, 177]. After 24-hour incubation with drugs, astrocytes, pericytes, and neuron cells were washed once with PBS and harvested using a cell scraper (Corning #3010) in 500 µl of 70% methanol. Samples were kept at -$20^0$ C prior to drug quantification.

### 3.2.10 Experimental Design and Animals

Male Sprague-Dawley rats (n=10, mean weight=306 g, age=~65-70 days) were obtained from Charles River (Raleigh, NC 27610). All catheters (cisternal and vein cannulation) for the animals were surgically implanted [178, 179] at Charles River prior to shipping. On arrival to the housing facility, animals were acclimated for 72 hrs prior to starting study protocol. Catheter management was performed daily to ensure viable sampling. Animals were administered 30 mg/kg NMR + 10 mg/kg RTV twice a day (60 mg/kg NMR and 20 mg/kg RTV total daily dose) daily for five days (as described below). All NMR/r doses were administered orally via gavage. The dose chosen for this study allometrically scaled to a humanized equivalent of NMR/r based on fixed dosing (i.e., 60 kg patient, 300 mg NMR + 100 mg RTV twice daily, = 10 mg/kg NMR + 3.33 mg/kg RTV daily x scaling factor of 6.2 = ~60 mg/kg NMR + ~20 mg/kg RTV daily). The five day duration of the study also aligns with the current FDA recommendation for treatment of COVID-19 with NMR/r in patients[169]. Rats were housed in a light and temperature-controlled room for the duration of the study and allowed free access to water and food, except during sampling. Data were analyzed for all animals that entered the protocol.

When animals contributed incomplete data (i.e., early protocol termination), all available samples were analyzed for PK. Concentrations below the lower limit of quantification were inputted as 0[180].

### 3.2.11 Blood, CSF, PBMC, and Tissue Sampling and Determination of NMR Concentrations

Blood samples were drawn from a single right-sided internal jugular vein catheter in a sedation-free manner when possible. Blood catheter lines were flushed with normal saline after each blood draw to prevent blood contamination. CSF was collected via an intracisternal catheter. Isoflurane gas was used for temporary sedation when needed (5% initially, followed by 1-3% maintenance). Within each 24 hrs, planned sample collection was eight blood and two CSF samples per animal. An approximation of the full sampling strategy over the five day study can be found in supplemental material in publication[181]. Each sample obtained (0.25 mL blood and 0.05-0.1 mL CSF aliquots) was replaced with either an equivalent volume of normal saline or artificial CSF (as appropriate) to maintain euvolemia. Blood and CSF samples from NMR-treated animals were processed similar to our previous reports[85, 89, 182, 183].

Upon completion of the protocol, rats were euthanized, and tissues (lungs, heart, kidney, brain, liver) were harvested. The tissues were perfused, rinsed with cold saline solution, blotted with paper towel, and snap-frozen. Rat tissues (lungs, heart, kidney, brain, liver) were analyzed for NMR content by preparing tissue homogenate samples. PBMC sampling was conducted on each rat prior to termination using mononuclear cell preparation tubes per manufacture protocol (BD Biosciences, Franklin Lakes, NJ).

Plasma, CSF, tissue, and PBMC concentrations of NMR were quantified with LC-MS/MS using individual standard curves for each matrix (ranges: CSF, 1 to 250 ng/mL; plasma, 20 to 10,0000 ng/mL; PBMC, 0.01 to 5 ng/mL). Standard calibrators, quality controls, and samples were prepared in microcentrifuge tubes. Internal standard was added to track the analyte of interest through the extraction and instrumentation processes. NMR was extracted from 20 µL of rat plasma, PBMCs or CSF with a stable labeled IS [2H9]-PF-07321332 by a protein precipitation using 50:50 ACN:MeOH to provide a protein free extract. CSF samples were treated with ammoniated methanol prior to extraction to ensure no analyte adsorbs to the tube wall as previously described[89]. Supernatant was removed and diluted with mobile phase in a 96-well plate prior to injection. HPLC was used to separate the analytes from potential interferences on a C18 100 x 3.00mm column (MAC MOD, Chadds Ford, PA, USA) for stationary phase, using 60% acetonitrile, 0.1% formic acid in water as an isocratic mobile phase. Detection of NMR and the IS in plasma and CSF was done with an ABSciex 5500 Q-trap mass spectrometer (ABSciex, Framingham, MA, USA) in positive ion mode. PBMC levels were converted to µM concentrations based on the single cell volume for PMBCs[184]. The assays were linear between plasma concentrations of 20 and 10000 ng/mL, CSF concentrations of 1 and 250 ng/mL, and PBMC concentrations of 0.01 and 5 ng/mL. The plasma component underwent a complete validation and had a precision of <4.73 for all measurements, including intra- and inter-assay measurements. Briefly, all bioanalyses are within the pre-determined acceptance criteria of +/- 15% for each level (+/- 20% for LLOQ)[185].

Tissues were homogenized using a Precellys Evolution Cryolys homogenizer (Bertin Technologies, Montigny-le-Bretonneux, France). Each tissue was homogenized with 0.5 mL of 70:30 methanol: 25 mM phosphate buffer. Calibration curves for the tissue homogenates were prepared as described above in the section on estimation of NMR in

plasma. Tissues were quantified by weight (mg of drug/g of tissues), reported as mg/g, and converted to mg/mL as previously described[85, 186]. Calibration curves for the tissue homogenates were prepared as described above. All units were reported in ng.

PBMC cellular and tissue AR were calculated as observed NMR PBMC and tissue concentrations to NMR plasma concentrations at the same time of collection[187, 188].

## 3.2.12 NMR PK and Drug Exposure

The simplest base PK model considered was a 3-compartment model with an oral compartment (first order absorption), plasma compartment, and a CSF compartment. Three and four-compartment models with/without a lag constant were similarly fit using the nonparametric adaptive grid (NPAG) algorithm within the Pmetrics package version 1.5.0 (Los Angeles, CA) for R version 3.2.1 (R Foundation for Statistical Computing, Vienna, Austria)[189, 190]. Multiple different CSF models were considered where CSF intercompartmental clearance (CL)/transfer and CSF CL were added and omitted based on investigator judgement, and other PK CSF studies[191-194]. A model comparison table can be found in Supplemental material (PREPRINT). The initial estimate of parameter weighting was accomplished using the inverse of the assay variance. Model performance was quantitatively described using observed vs. predicted concentrations to calculate bias, imprecision, and coefficients of determination[195]. The final model was selected based on regression of observed vs. predicted concentrations, prediction bias, visual plots of parameter estimates, lowest -2LL/Akaike information criterion and rule of parsimony. We modeled the relative bioavailability (F) for each dose in a given rat to account for inter-occasion variability in concentrations among doses, by taking the maximum post-dose peak concentration observed for that rat over all doses and calculating F for each dose as the peak after that dose divided by the maximum peak. The

dose which was followed by the maximum peak then had F=1, and all other doses were F≤1.

To compare NMR concentrations in animals to a putative PD endpoint, the concentration needed for three times the 90% maximal effective concentration ($3xEC_{90}$) for the SARS-CoV-2 was utilized[196]. The FDA integrated review from the clinical studies (EPIC-HR) showed 95% of participants had NMR trough concentrations ≥$3xEC_{90}$[197]. Therefore, the goal for the CSF was set to achieve the same exposure conditions as for plasma. The plasma $EC_{90Adjusted}$ concentration for plasma is 292 ng/mL (585 nM), and the $EC_{90Un\_adjusted}$ for CSF is 90.5 ng/mL. Therefore, the $3xEC_{90}$ PD values would be 876 ng/mL for plasma and tissue, and 271.5 ng/mL for CSF. This $EC_{90}$ value is based on the study on bronchial epithelial cells infected with USA_WAI/2020 isolate[174].

### 3.2.13 Estimation of PK Exposure and Percent (%) CSF Penetration

The best-fit model was used to calculate median maximum a posteriori probability Bayesian NMR plasma and CSF concentration estimates at 12-minute intervals over the 5-day study period using each animal's measured NMR concentrations, exact dose, and dosing schedule. From these concentrations we calculated the $AUC\_{0\text{-}5days}$ over the entire experiment using "makeAUC" function within Pmetrics[189, 198]. $C_{max\_0\text{-}5days}$ from the 12-minute interval Bayesian estimates was determined to be each animal's $C_{max\_0\text{-}5days}$.

Ratios of the estimated $AUC_{csf}$ /$AUC_{plasma}$ and $C_{max\_csf}$ /$C_{max\_plasma}$ were used to determine percent CSF penetration[191, 199-202]. AUC was standardized to $AUC_{0\text{-}24hrs}$ by dividing $AUC\_{0\text{-}5days}$ by 5 (i.e., 5-days protocol) to provide an estimated $AUC_{0\text{-}24hrs}$ value. For $C_{max\_0\text{-}5days,}$ the highest predicted CSF concentration and corresponding plasma concentration were used calculate precent penetration. Only animals with CSF concentrations sampled were used for estimation of CSF penetration.

### 3.2.14 Statistics

Summary statistics were calculated using GraphPad Prism V7.02 (GraphPad Software Inc., La Jolla, CA). Nonparametric summary statistics were reported given the small sample size and distribution of data.

### 3.2.15 Results

### 3.2.16 *In Vitro* Drug Uptake

The mean ± SD uptake of NMR alone compared with in the presence of RTV by neurons was 34.7 ng/mL ± 0.88 and 122.8 ± 7.8 ng/mL, respectively ($P<0.0001$). The mean ± SD of RTV uptake in astrocytes and pericytes in the presence or absence of NMR was 419.7 ng/mL ± 12.8 ng/mL vs 665.2 ng/mL ± 28.3 ng/mL for astrocytes ($P<0.0002$) and 202.6 ng/mL ± 11.5 ng/mL vs 321.9 ng/mL ± 72.6 ng/mL vs. for pericytes ($P<0.05$), respectively. Overall, the maximum NMR uptake was low (5.5%; i.e., 2200 ng/mL administered vs. 122.8 ng/mL uptake: 122.8/2200=5.5%; **Figure 18a**: neurons), as seen with neurons in the presence of RTV. The uptake for NMR increased >3.6-fold in neurons in the presence of RTV (34.7 ng/mL to 122.8 ng/mL). We observed low (<2%) uptake of NMR by astrocytes or pericytes (**Figure 18a**: astrocytes, pericytes) in the presence or absence of RTV. Further, we observed moderate (42%) uptake of RTV in astrocytes (**Figure 18b**: astrocytes, 1000 ng/mL administered vs. 419.7 ng/mL uptake), and in the presence of NMR, RTV uptake significantly increased to 66.5% (1000 ng/mL administered vs. 665.2 ng/mL uptake).

## 3.2.17 Characteristics of Animal Cohort

A total of 10 rats received NMR/r orally by gavage and had plasma and CSF concentrations obtained throughout dosing and tissue samples collected at completion. Each day, rats had an average of 6.5 plasma concentrations and 1.8 CSF concentrations sampled over the 5-day protocol (Total: 327 plasma, 83 CSF concentrations). One animal had intracisternal catheter failure before the collection of any CSF samples.

## 3.2.18 NMR PK Model and Parameter Estimates

The final PK model was a three-compartment first-order oral absorption model with a bioavailability (F) covariate (published supplemental material[181]), AIC=771.4 (published supplemental material[181]). The final model's median PK parameter values are given in **Table 8**. The PK model was fit-for-purpose with low bias in both plasma and CSF (-0.0778 mg/L and -0.0263 mg/L). Bayesian predictions from the final model explained the variation in the observed individual animal concentrations well ($r^2$=0.76 and 0.51 for plasma and CSF, respectively [supplemental material PREPRINT]).

## 3.2.19 NMR PK Exposures and Percent (%) CSF Penetration

The overall PK exposures for all rats are summarized in **Table 9**. The median (IQR) NMR penetration into the CSF was low at 18.1% (7.65-30.59) (calculated from highest predicted concentration [$C_{max}$]) and 15.2% (7.55-29.92) (calculated from area under the concentration-time curve [AUC]). The complete list of NMR penetration into CSF for each animal can be found in **Table 9**. Further, Bayesian observed versus predicted concentration time profiles for plasma and CSF vs. 90% maximal effective concentration

[$EC_{90}$] and 3x$EC_{90}$ values can be found in **Figure 19**. The CSF Bayesian prediction concentration time profiles for all animals showed the median (IQR) percent of time CSF concentrations were ≥ 3x$EC_{90}$ unadjusted for plasma protein binding ($EC_{90Un\_adjusted,}$ note: adjusted = $EC_{90Adjusted}$) was 16% (0-20.5) **(Figure 19b).**

## 3.2.20 Tissue and Peripheral Blood Mononuclear Cells (PBMC) NMR Concentrations

The overall tissue accumulation ratio (AR [desirable AR: >1]) and tissue concentrations for NMR can be found in **Figure 20** and in published supplemental material available online[181]**.** The highest median (IQR) NMR tissue ARs were observed in the liver (2.71 [1.14-9.55]), and kidney (1.71 [0.82-11.09]) while the lowest median NMR tissue AR was observed in brain tissue at 0.15 (0.03-1.12). Compared to all the tissues, the brain had the lowest median (23.83 ng/g, IQR: 10.94-46.85) NMR concentrations, which were all <3x$EC_{90}$ regardless of adjustment for protein binding. For PBMCs, the median (IQR) value for the cellular AR for NMR was 0.998 (0.48-27.05).

## 3.2.21 Discussion

We found that NMR CSF concentrations in rats given oral NMR/r twice daily for five days were 15-18% of those in plasma, whether determined as a ratio of $C_{max}$ or AUC (**Table 9**). Further, we found that tissue penetration of NMR in brain of the rats was low, which was consistent with the NMR cell uptake in our *in vitro* model. Saleh et al. used physiologically based pharmacokinetic (PBPK) modelling to predict whether NMR, remdesivir, and molnupiravir achieve effective concentrations against SARS-CoV-2 in

human brain cells[203]. Their model predicted NMR concentrations exceeded the $EC_{90}$ values in brain extracellular fluid concentrations, which is similar to what we found in rat CSF. However, they did not evaluate $3xEC_{90}$, or other multiplicative factors of the $EC_{90}$ values, reflecting levels of plasma exposure observed clinically. Exposure-response relationships for SARS-CoV-2 viral loads relative to $EC_{90}$ factors have not been evaluated in the CNS or other potential viral reservoirs. We utilized the concentration needed for $3xEC_{90}$ for SARS-CoV-2 as our PD target for the CSF, based on the FDA review from EPIC-HR showing 95% of participants had NMR trough concentrations $\geq 3xEC_{90}$[196, 197]. If the two $EC_{90}$ values utilized in the PBPK simulation study by Saleh et al. for the Delta variant are multiplied by a factor of 3 (0.149 μM:~100 ng/mL x 3 = 300 ng/mL), the majority of time is spent below this PD goal. In our study, we found that CSF concentrations of NMR aren't maintained above the $3xEC_{90Un\_adjusted}$ for SARS-CoV-2 (**Figure 19b,** median overall CSF Concentrations $\geq 3xEC_{90}$: 16%) for the entire dosing interval. As an exercise, we conducted Monte Carlo simulations (N = 1000, assuming 300 g rat, fraction unbound = 1) from the final rat population PK model to assess what doses (30-90 mg/kg) of NMR would be required to achieve the probability of target attainment of 50-100% time above different $EC_{90}$ multiples (e.g., $0.5\text{-}3xEC_{90}$) in the CSF. Based on the simulations, doses of >90 mg/kg BID (published supplemental material[181]) in rats would be necessary to ensure all concentrations are $>3xEC_{90Un\_adjusted}$ (i.e., 271.5 ng/mL). Humanizing this dose based on allometric scaling would result in clinical doses of 900 mg of NMR BID (three times the current FDA approved dose) or potentially more frequent dosing of 300 mg every 4 hrs. The simulations did not account for varying the doses of r/ (which increase NMR concentrations) given the toxicity and drug-drug interactions of RTV that make it clinically difficult to justify pushing its dose higher[204]. Our study is unique as we also looked at homogenized liver, brain, lung, kidney, and heart tissues, and PBMC concentrations of NMR in rats. As shown in **Figure 21** and in the published

supplemental material[181], brain tissues had the lowest concentrations and AR compared with other tissues. Only rat 7, who died within 4 hrs after the 2nd dose, had NMR concentrations >$EC_{90Un\_adjusted}$ , but no rat had NMR concentrations >3x$EC_{90}$ regardless if comparing to adjusted or unadjusted for protein binding. For PBMCs, we found that intracellular NMR concentrations from PBMCs were detectable, and some rats had NMR PBMC concentrations above 3x$EC_{90Adjusted\ and\ Un_adjusted}$. When compared to other PIs used in the treatment of HIV, the desirable human PBMC cellular AR is >1[187, 188]. Our PBMC median (IQR) cellular AR for NMR was 0.998 (0.48-27.05) but the value demonstrated high variability among rats. Overall, it appears that NMR, in the presence of RTV, shows similar intracellular uptake to other PIs. This finding is important as previous studies have shown that SARs-CoV-2 can infect monocytes and T-lymphocytes[165, 205].

To evaluate specific drug uptake by relevant cells of the CNS rather than only CSF, we investigated the uptake of NMR and r/ in astrocytes, pericytes and neurons individually **(Figure 19).** We found that the uptake of NMR and or r/ in the presence of the other drug differed significantly in neurons, astrocytes and pericytes. For neurons, the presence of r/ increased the uptake of NMR significantly. This increased uptake effect on NMR is likely a result of efflux transporter inhibition (i.e., Pgp) via RTV[206]. A study by Eng et al. looked at efflux transporter inhibition effects on NMR using Caco-2 cell monolayers[173]. They showed that inhibition of BCRP and MDR1 enhanced the apparent permeability of NMR from 0.80 ± 0.15 to 4.05 ± 0.26 cm/s in Caco-2 cell monolayers[173]. Specific to CNS, a study by Ghosh et al. looked at cellular localization and functional significance of CPY3A4 and MDRI in the CNS and found coexpression by BBB endothelial cells and neurons showing potential implications on drug metabolism and cytoprotective mechanisms[207]. As RTV is a substrate to many of the efflux transporters (relevant to the BBB), we predict similar effects of RTV on NMR permeability through the BBB[208]. The expression of Pgp in human brain capillary endothelial cells is well documented[209]. However, its expression in

astrocyte, pericytes, and neurons is still under investigation[210-213]. No significant differences were noted in astrocytes and pericytes when NMR was administered alone or with RTV (**Figure 18a**). More investigation is needed to further substantiate our hypothesis of the RTV-Pgp-NMR transporter interaction. Further studies by our group will evaluate NMR/r penetration utilizing a more novel 4-cell *in vitro* model, with transporter expression[104]. When comparing NMR to other PIs used to treat HIV, as a class, they achieve poor CSF exposure[214]. However, when co-administered with RTV (or other boosters), CSF penetration has been shown to increase[71, 72]. For example, increased CSF concentrations of ATV were found when administered with RTV (7.9 to 10.3 ng/mL)[73]. When looking at RTV in our *in vitro* model, uptake by astrocytes was high at 41.97% and moderate by pericytes at 20.2%. In the presence of NMR, RTV uptake increased to 66.65% in astrocytes and 32.19% in pericytes. RTV CSF distribution is low[215-217]. To our knowledge, there are no prior studies for human neuronal uptake of RTV, and our results indicated moderate neuronal entry of RTV in the presence or absence of NMR **(Figure 18b)**. Nevertheless, a CNS drug delivery experiment for RTV in a mouse model showed moderate penetration of RTV in brain parenchyma tissue[218]. Additional characterization of RTV uptake for human neuronal tissue is desired. A study by Anthonypillai et al. in guinea pigs found that CSF levels of RTV were low, but RTV levels in the choroid plexus and brain were higher[215]. They hypothesized this was due to RTV regulation in the CSF and choroid plexus by efflux transporters that may limit drug accumulation in the CSF. In our study, we found that RTV uptake in astrocytes and pericytes was affected by NMR **(Figure 18b).** Thus, we believe this is likely due to NMR's effect on associated transporters. Transporter inhibition studies are warranted to provide insight on the mechanisms behind the differences seen between cell lines.

We developed a 3-compartment PK model to predict individual animal concentration-time profiles for plasma and CSF, as shown in **Figure 19.** This allowed us

to accurately predict CSF and plasma exposures, which were used to calculate CSF penetration **(Table 9).** This also allowed us to make comparisons of our PK estimates with clinical and animal data. For example, the median half-life for NMR in the presence of RTV for the rats was 2.4x faster than what is seen in humans (2.55 hrs vs. 6.05 hrs)[168]. This is expected as smaller animals clear most drugs faster given the principles of allometry [161, 173]. When comparing our NMR half-life to other animal models for NMR, we found that our half-life estimation was within the range of other oral rat PK studies (10 mg/kg: 4 hrs [range:2.9-5.1], 10 mg/kg: 2.8 hrs ± 1.4 hrs)[173, 174]. Our estimation for time at which $C_{max}$ is first observed ($T_{max}$), was similar to other rodent models (mean:1.84 hrs vs. mean:1.5 hrs)[173, 174]. The median relative F value of 54.5% in our study was also consistent with other literature values estimated in rats for NMR (34%-50%)[173]. We note our animals were not restricted of food or water, and this is likely why we saw variability in F between and within animals (**Table 10b**: range: 32%-62%). For NMR Ka, our model estimate of 0.51 $h^{-1}$ was also in agreement with finding reported by others (0.55 $h^{-1}$)[197]. We compared our values for $C_{max}$ and AUC with clinical data from healthy volunteers. Rat geometric mean plasma values for $C_{max}$ (2.48 µg/mL or 2480 ng/mL) and $AUC_{daily\ average}$ (20.25 µg*hr/mL) compared well with healthy human geometric mean values of $C_{max}$ (2.21 µg/mL) and $AUC_{0\text{-}12hrs}$ (23.01 µg*hr/mL) supporting our allometric dose scaling strategies[197]. Our AUC estimation was a daily average given the difficulty of standardizing twice-daily dosing in animals and the healthy volunteer data was based on an AUC of 0-12 hrs. When comparing our rat CSF concentrations to the PBPK modeling performed by Saleh et al., our CSF $C_{max}$ (median 0.41 mg/L or 410 ng/mL) is in agreement with what was projected in human brain extracellular fluid (~0.3-0.44 mg/L, points extrapolated using graphgrabber 2.02)[203, 219]. This shows the potential clinical application of our rat model as we were able to humanize $C_{max}$ exposure in both plasma and CSF. Last, it is important to also mention NMR's lipophilicity in relation to BBB penetration. A drug metabolism study on NMR

disposition indicated that it is moderately lipophilic with a LogP of 1.68, showing low passive apparent permeability ($P_{app}$) of $1.76 \times 10^{-6}$ cm/s[173]. Utilizing different cell lines (i.e., Caco-2 cell monolayers), NMR exhibited similar trends of low permeability across the monolayer barrier[173]. Our findings of low penetration of NMR through the BBB are also in agreement with Lipinski's rule of five that postulates a lipophilicity range of 2.0 to 3.5 is a fundamental predictor for BBB penetration via passive diffusion[86]. Other PIs exhibit a range of lipophilicity from 1.0-5.69 depending on specific physiochemical properties[220, 221].

Our study has limitations. First, we did not design this study for animals infected with SARS-CoV-2 and thus could not assess viral loads in the CSF vs. CSF concentrations of NMR. Because our findings indicate that CNS levels of NMR may not be adequate to achieve therapeutic concentrations, plans for utilizing an infection model with the golden Syrian hamster model are ongoing. Second, our tissue concentrations represent total drug concentrations based on homogenized tissues. Understanding the dynamic relationship of unbound tissue concentrations vs. time or site-specific tissue concentrations would require microdialysis or other techniques. Further, it is unknown if CSF catheter placement could have influenced CSF penetration or if concentration-mediated changes to CSF transit occur. Future work to address concentration- mediated penetration utilizing a 4-cell *in vitro* model is planned[104]. In addition, it is unclear how our animal model compares to active infection where inflammation could increase drug penetration through the BBB in active SARs-CoV-2 infection. In this context, a recent review on BBB integrity alteration by SARs-CoV-2 pointed to the increased expression of matrix metalloproteinase-9 (MMP9) in COVID-19 infection. The increased MMP9 activates RhoA (Ras homolog family member A), causing more degradation of type IV collagen of the BBB basement membrane and altering the barrier's integrity[222]. Moreover, in our *in vitro* experiment for cellular uptake of NMR/r by human brain cells, we did not include hBMECs because our earlier finding suggested no infection of hBMECs by SARs-CoV-2,

while we observed high infection in human astrocytes and pericytes[40]. This was consistent with the lack of ACE-2 receptor expression in hBMECs, when compared to astrocytes and astrocytes. Additionally, the cells were not available at the time of these experiments. Differences in the expression of BBB transporters (i.e., Pgp) among species exist, and variations could result in differences in clinical extrapolation. A study by Morris et al. showed cross species expression of BBB transporters and that rats and humans have many of the same transporters present[22]. However, describing species differences in transporter expression is a difficult task given all the potential transporters involved with NMR and RTV and was beyond the scope of this study. A mechanistic study by Verscheijden et al. used PBPK modelling and calculated plasma concentration-corrected brain concentrations (Kp) values for humans and rodents specific only for Pgp correction for various medications[223]. We acknowledge the complexity of the BBB transporter expression between species. However, regardless of transporter differences, our dosing achieved humanized exposures in plasma and CSF. Further studies specific to transporter expression are warranted and planned. Also, we quantified total NMR concentrations and did not quantify free drug (NMR is 69% protein bound)[168]. CSF penetration via plasma to CSF estimation should also consider free drug in the plasma as drug found in the CSF is unbound to proteins, and future studies might quantify free NMR concentrations to capture this consideration more accurately. It is important to note that the protein content in CSF is 50-100 times lower than plasma (typical plasma protein concentrations: 60-70 mg/mL, normal CSF protein concentrations: 0.2-0.7 mg/mL)[224]. The PD endpoints we utilized for CSF, plasma, tissues, and PBMC were adjusted and unadjusted for plasma protein-binding, depending on the matrix. Last, our final model estimation of $K_{30}$ denotes overall elimination of NMR from the CSF, including uptake by various types of cells in the CNS. This may be an oversimplification and a more mechanistic description should be evaluated utilizing an advanced quantitative systems pharmacology approach.

In this study, we determined NMR CSF and CNS penetration utilizing *in vitro* and *in vivo* models and quantitatively described the transit of NMR from plasma to the CSF. In addition to NMR, molnupiravir and remdesivir are two other antiviral agents for the treatment of SARS-CoV-2. Similarly, CNS penetration data for them are lacking. The data from our *in vivo* rat model demonstrates that NMR penetration into CSF and CNS tissues may be inadequate. Our *in vitro* model data shows minimal NMR uptake into cells relevant to the CNS. Collectively, these findings may have implications for viral persistence in these compartments and neurologic post-acute sequelae of COVID-19. These data motivate future investigations utilizing an infection model to understand the pharmacodynamic effects of NMR drug concentrations in the CNS on viral loads in the CNS. If longer treatment or higher doses correspond to increased NMR penetration in the CNS, decreased viral loads, and decreased CNS inflammation, they provide a basis to investigate alternative dosing strategies. This information would be fundamental for optimizing treatment of Long COVID-19.

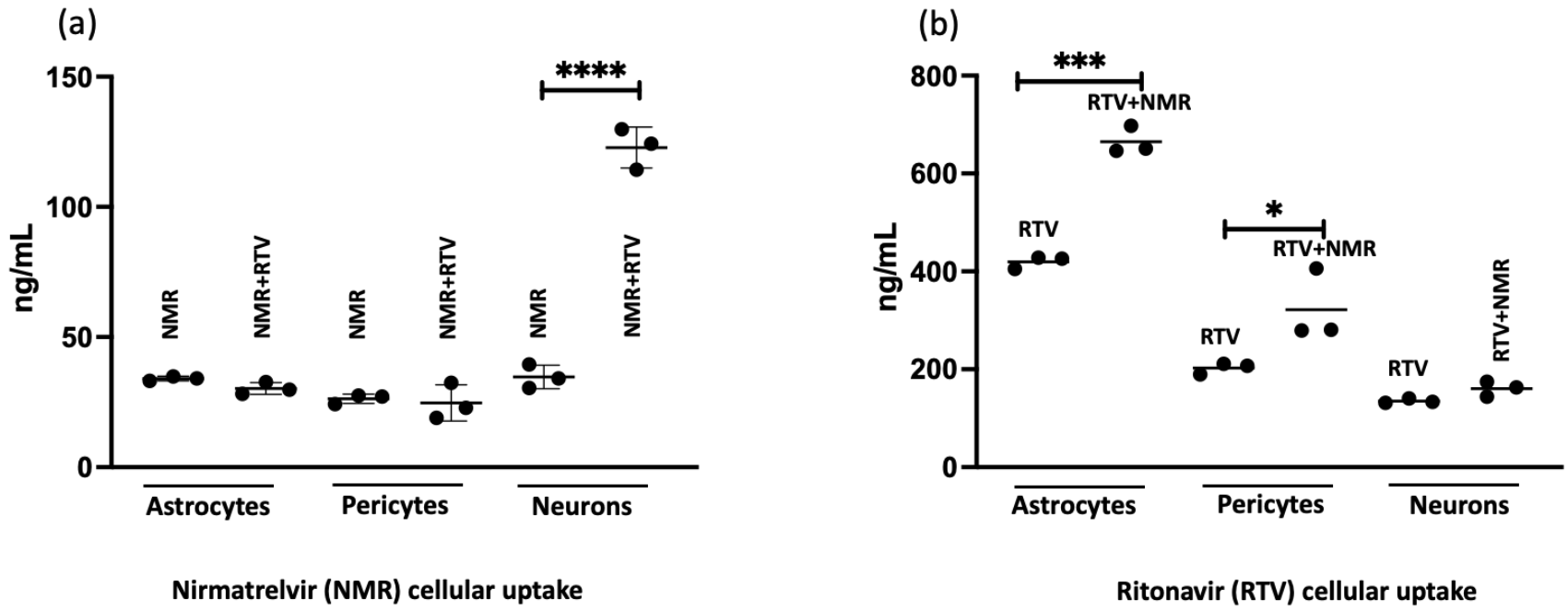


**Figure 18.** In-vitro analysis of NMR and RTV penetration into three different human brain cells. (a) Evaluation of NMR uptake by cells in the absence or presence of RTV and (b) intracellular RTV uptake in the absence or presence of NMR. The p-values (*) indicate, *=<0.05, ***=<0.0002 and ****=<0.0001.

Abbreviations: NMR=nirmatrelvir, RTV=ritonavir

(a)

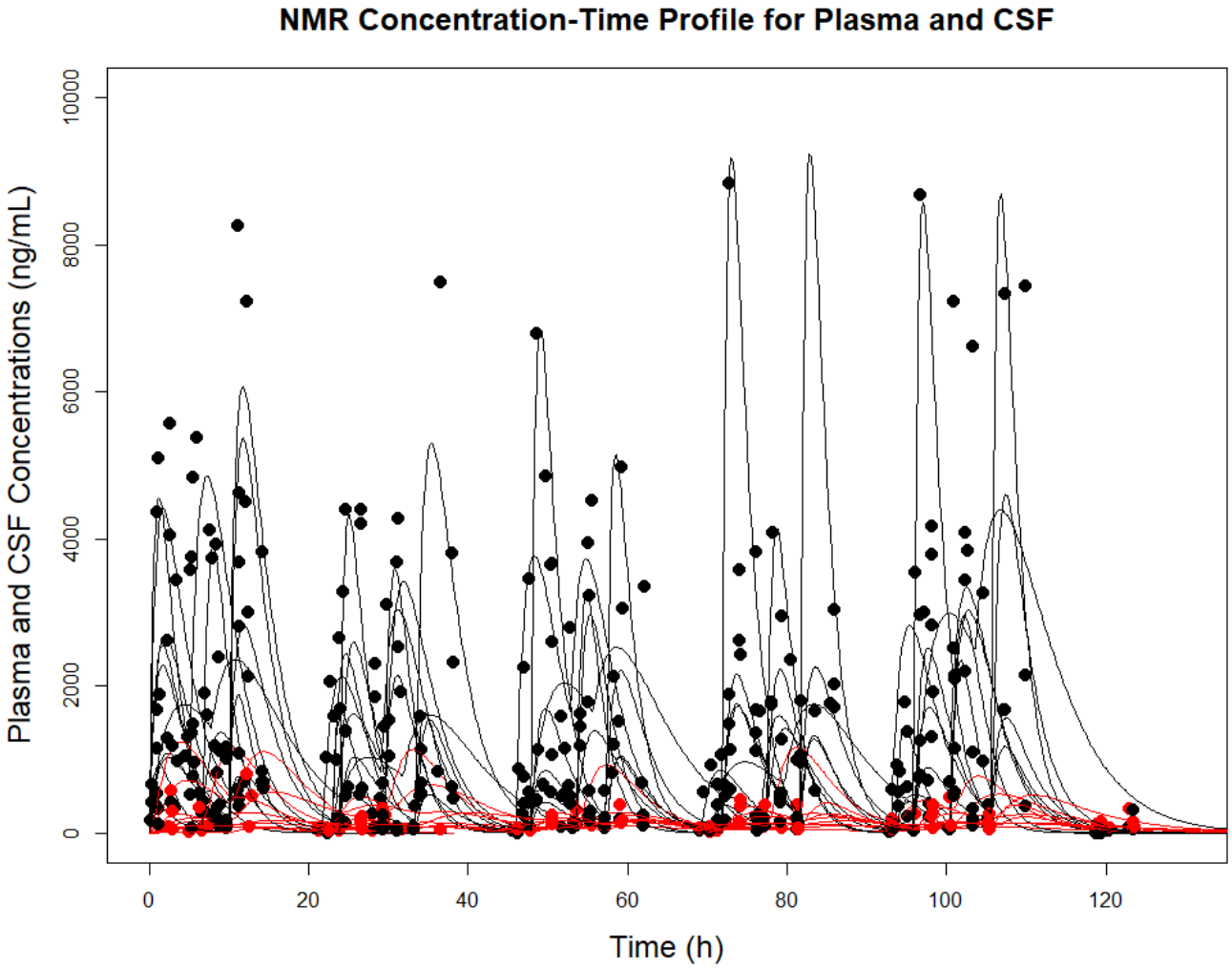


**Figure 19.** Plasma ([a] black) and CSF ([b] red) Bayesian observed versus predicted plots for all animals compared to $EC_{90Un\_adjusted}$ values (dotted black line). The black and red lines represent the predictions where the filled circles represent the observed collected concentrations. A median of 16% of all the predicted CSF concentrations in rats were >3x$EC_{90Un_adjusted}$.

(b)

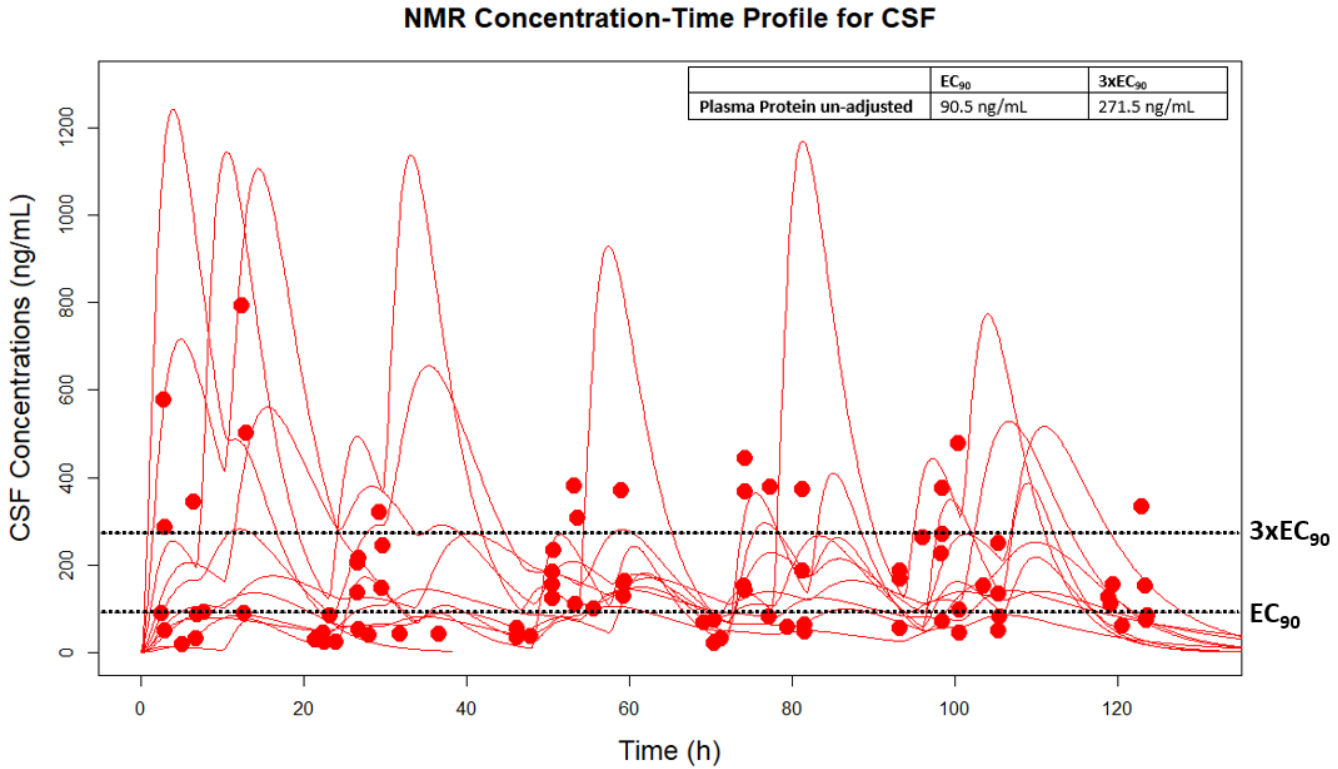


| Rat | 1 | 2 | 3 | 4 | 5 | 6 | 7 | 8 | 9 | 10 | Median (IQR) |
|---|---|---|---|---|---|---|---|---|---|---|---|
| %CSF Concentrations ≥ 3xEC$_{90Un_adjusted}$ | 0 | 0 | 28 | 0 | 55 | 31 | NA | 21 | 16 | 0.3 | 16 (0 -20.5) |

*Units on plot converted to ng/mL for consistency

Abbreviation: NMR=nirmatrelvir, CSF=cerebrospinal fluid, $EC_{90}$= 90% maximal effective concentration (unadjusted for protein binding given CSF, 90.5 ng/mL, and 271.5 ng/mL)

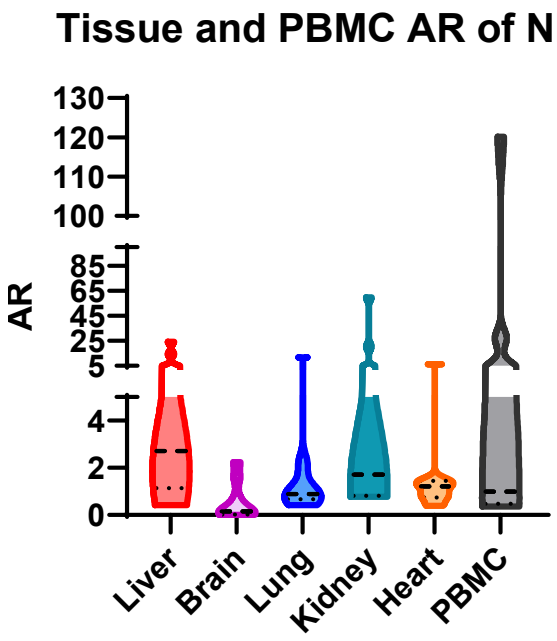


| Rat | AR# Liver | AR# Brain | AR# Lung | AR# Kidney | AR# Heart | AR# PBMC |
|---|---|---|---|---|---|---|
| 1 | 0.418^ | 0 | * | 1.744 | * | 0.543 |
| 2 | 4.722 | 2.248 | * | 20.411 | * | 29.511 |
| 3 | 2.850^ | 0.112^ | 2.169 | 0.775 | 1.450 | 0.859 |
| 4 | 24.412^ | 0 | 11.845 | 59.809 | 6.375 | 120.169 |
| 5 | 1.322 | 1.573 | 0.666 | 0.829 | 0.738 | 24.595 |
| 6 | 1.470 | 0.148 | 0.744 | 1.708 | 1.207 | 0.426 |
| 7* | - | - | - | - | - | - |
| 8 | 2.706 | 0.673 | 0.888 | 1.044 | 1.406 | 1.243 |
| 9 | 0.950 | 0.052 | 0.416 | 0.801 | 0.396 | 0.367 |
| 10 | 14.373 | 0.191 | 1.218 | 1.773 | 0.924 | 0.998 |
| Median (IQR) | 2.71 (1.14-9.55) | 0.15 (0.03-1.12) | 0.89 (0.67-2.17) | 1.71 (0.82-11.09) | 1.21 (0.74-1.45) | 0.998 (0.48-27.05) |

**Figure 20.** Violin plots of tissue and PBMC AR for NMR. The highest median NMR tissue AR was observed in the liver and kidney, while the lowest median NMR tissue AR was observed in brain tissue.

*Rat 7 only completed 1 day of treatment, no PMBC levels available. Rats 1 and 2 do not have lung or heart NMR concentrations due to tissue processing complications.

#Calculated as a ratio of observed plasma NMR levels vs. tissue/PBMC levels at equivalent time of sampling

^Calculated using plasma level predictions vs. observed concentrations due to plasma NMR levels being BLOQ

Abbreviations: AR=accumulation ratio, BLOQ=below level of quantification, IQR=interquartile range

**Table 8.** Median parameter values from final model (a) and individual animal NMR half-life and average bioavailability (b)

(a)

| PK parameter | Median | CV% | Variance | Shrink%^ |
|---|---|---|---|---|
| **Ka (hr-1)** | 0.51 | 47.17 | 0.1 | 2.37 |
| **CL (L/hr)** | 0.23 | 49.98 | 0.02 | 0.58 |
| **$K_{23}$ (hr-1)** | 0.05 | 105.93 | 0.05 | 1.13 |
| **$\$K_{30}$ (hr-1)** | 0.24 | 43.73 | 0.01 | 11.96 |
| **Vc (L)** | 1.05 | 41.12 | 0.15 | 0.78 |
| **Vcsf (L)** | 3.46 | 63.98 | 6.49 | 5.56 |

(b)

| Rat | Half-Life (hrs) | Average Relative Bioavailability (F)* | Average $T_{max}$ (hrs) |
|---|---|---|---|
| 1 | 1.87 | 0.58 | 2.17 |
| 2 | 3.86 | 0.58 | 3.63 |
| 3 | 2.46 | 0.46 | 2.25 |
| 4 | 1.32 | 0.55 | 1.56 |
| 5 | 3.23 | 0.54 | 1.22 |
| 6 | 1.46 | 0.48 | 1.65 |
| 7** | 3.23 | 0.58 | 1.19 |
| 8 | 2.80 | 0.32 | 1.7 |
| 9 | 0.98 | 0.62 | 1.15 |
| 10. | 2.65 | 0.41 | 1.9 |
| **Median (IQR)** | 2.55 (1.43-3.23) | 0.545(0.45-0.58) | 1.675 (1.21-2.19) |
| **Mean (SD)[#]** | | | 1.84 (0.73) |

*Bioavailability was estimated after each dose given the variability of oral absorption, as described in Methods.
**Rat 7 only completed 1 day of treatment.

#Calculated to compare to literature values

^Estimation to assess if the data are insufficient to precisely estimate the individual parameters.

$Estimation denotes overall elimination of NMR from the CSF, including uptake by various types of cells in the CNS.

Abbreviations: PK=pharmacokinetic, CV%=coefficient of variation percent, CL==NMR clearance, $V_c$=volume central compartment, $V_{csf}$=volume cerebrospinal fluid compartment, $K_{23}$=rate constant to cerebrospinal fluid from central compartment, $K_{30}$= elimination rate constant from CSF compartment, IQR= interquartile range, $T_{max}$=time at which $C_{max}$ was first observed.

**Table 9**. NMR plasma and CSF PK exposures estimated using Bayesian posteriors for $AUC_{0\text{-endoftreatment}}$ and $C_{max\_0\text{-}5days}$ and percent penetration of NMR into the CSF compared to blood

| Animal | $C_{max\_0\text{-}5days}$ (ng/mL) Plasma | $AUC_{0\text{-}endoftreatment}$ (µg*hr/mL) Plasma | $AUC_{daily\_average}$ (µg*hr/mL) Plasma | $C_{max\_0\text{-}5days}$ (ng/mL) CSF | $AUC_{0\text{-}endoftreatment}$ (µg*hr/mL) CSF | $AUC_{daily\_average}$ (µg*hr/mL) CSF | % Penetration by $C_{max}$ CSF/Plasma | % Penetration by AUC CSF/Plasma |
|---|---|---|---|---|---|---|---|---|
| **1** | 2270 | 160 | 32 | 105.81 | 7.11 | 1.42 | 4.66 | 4.44 |
| **2** | 3660 | 189 | 37.8 | 252 | 12.5 | 2.5 | 6.89 | 6.61 |
| **3** | 2020 | 92.7 | 18.54 | 655.8 | 28.9 | 5.78 | 32.47 | 31.175 |
| **4** | 796 | 76.3 | 15.26 | 144 | 11.6 | 2.32 | 18.10 | 15.20 |
| **5** | 1860 | 80.7 | 16.14 | 1169.9 | 52.21 | 10.44 | 62.84 | 64.7 |
| **6** | 2218 | 128 | 25.6 | 560 | 30.2 | 6.04 | 25.27 | 23.59 |
| **7#** | 4550 | 19.55 | 3.91 | NA | NA | NA | NA | NA |
| **8** | 3857.9 | 99.8 | 19.96 | 1107 | 28.6 | 5.72 | 28.70 | 28.66 |
| **9** | 4879.3 | 205 | 41 | 410 | 17.4 | 3.48 | 8.41 | 8.49 |
| **10** | 1862.7 | 128 | 25.6 | 271.6 | 17.6 | 3.52 | 14.58 | 13.75 |
| **Median (IQR)** | 2240 (1860-4030) | 113.9 (79.6-167.3) | 22.78 (15.92-33.45) | 410 (200-880) | 17.6 (12.05-29.55) | 3.52 (2.41-5.91) | 18.1 (7.65-30.59) | 15.2 (7.55-29.92) |
| **Median (IQR)*** | 2220 (1860-3760) | 128 (86.7-174.5) | 25.6 (17.34-34.9) | - | - | - | - | - |
| **Geometric mean*# (Geometric SD factor)** | 2480 (1730) | - | 20.25 (1.956) | - | - | - | - | - |

*Excluding rat 7 as no CSF was obtained from this animal, #Calculated to compare to clinical data

Units for $C_{max}$ converted to ng/mL for consistency. AUC kept in µg*hr/mL.

Abbreviations: $C_{max}$= maximum concentration, AUC= area under the curve, CSF= cerebral spinal fluid, T ½= half=life, IQR=interquartile range, SD=standard deviatio

# Chapter 4: CNS Penetration of Nine ARVs in PLWH and Outcomes

## 4.1 Introduction and Background

Chapter 4 details results from a prospective study of HIV reservoirs among PLWH long-term virologically-suppressed on ART (AIDS Clinical Trials Group [ACTG] 5321 Cohort). More details specific to A5321 protocol have been previously published[225-227]. As mentioned in earlier chapters, HIV has been shown to persist in CNS in persons on ART. Consequently, CNS persistence may be linked to inadequate ART exposure. When assessing CNS drug levels in participants on ART, it is difficult to estimate drug exposure given sparse sampling and to standardize exposure given different sampling times among participants. In this chapter, we describe PK methods to estimate CNS exposure ($C_{max}$], AUC, and $C_{Trough}$) among individuals from ACTG 5321 that allows a standardized evaluation of relative CNS drug exposure.

Briefly, population PK modeling was performed for nine ARVs. The PK model was used to obtain predicted plasma and CSF estimates at 12-minute intervals from each participant's measured ARV plasma and CSF concentrations. Noncompartmental analysis was used to calculate AUC. Relative CNS penetration for each ARV was estimated by comparing CSF $C_{max}$ and AUC to plasma $C_{max}$ and AUC (i.e., relative CNS penetration= $C_{max\_CSF}$/ $C_{max\_Plasma}$ and $AUC_{CSF}/AUC_{plasma}$ The CSF $C_{Trough}$ for each ARV was compared to *in vitro* literature values of HIV $IC_{50or90}$ for each ARV. CSF IQs were calculated for each ARV in a regimen as ratio of predicted CSF trough to literature values for *in vitro* HIV $IC_{50or90}$. These values were used for comparison of different PD endpoints in this cohort of patients. More specific details can be found in the following sections.

## 4.2. A New Measure of ART Activity in CSF and Association with Persistence and Cognitive Function

*Adapted from:*
. **Avedissian SN**, McCarthy C, Bosch RJ, Mu Y, Spudich S, Rubin LH, Winchester L, Mykris T, Weinhold JA, Cyktor JC, Eron JJ, Mellors JW, Gandhi R, McMahon DK, Fletcher CV. A New Measure of ART Activity in CSF and Association with Persistence and Cognitive Function. CROI 2024 Abstract#1416, Denver, CO. 2024 Poster#558

Population Pharmacokinetic Approaches to Standardize Antiviral Exposure in the Cerebrospinal Fluid. **Avedissian SN**, Mu Y, McCarthy C, Bosch RJ, Spudich S, Gandhi R, McMahon DK, Eron JJ, Mellors JW, Fletcher CV. Population Pharmacokinetic Approaches to Standardize Antiviral Exposure in the Cerebrospinal Fluid. CROI 2024 Abstract#1301, Denver, CO. 2024 Poster #607

**Avedissian SN#**, Mu Y, McCarthy C, Bosch, RJ, Spudich S, Gandhi R, McMahon DK, Eron JJ, Mellors JW, Liu J, Fletcher CV. *Pharmacokinetic approaches to standardize antiviral exposure in cerebrospinal fluid.* IJAA (Planned Submission)

### 4.2.1 Abstract

Background: HIV has been shown to persist in the CNS in persons on ART, which may be linked with inadequate ART exposure in the CSF, and potentially contributing to HAND. The assessment of CSF drug concentrations is challenging because of sparse sampling and different sampling times among participants. Our objective was to use PK methods to estimate CSF exposure obtained from individuals on various ART regimens to obtain standardized CSF metrics ($C_{max}$, AUC, and $C_{Trough}$). Further, we sought to compare calculated IQ ratios of the whole ART regimen to different patient outcomes (i.e., HIV DNA/RNA, inflammatory biomarkers, global deficit score [GDS]).

Methods: A5321 is a prospective study of HIV reservoirs among persons with HIV on long-term virologically-suppressive ART. Plasma and CSF concentrations, obtained 1 to 23 hrs post ART dose from 74 participants, were measured. PK modeling was performed for FTC, 3TC, TFV, EFV, ATV/r, DRV/r, DTG, EVG and RAL. The final PK model was used to obtain predicted plasma and CSF concentrations at 12-minute intervals from each

participant's measured plasma and CSF concentrations. Relative CSF penetration for each ARV was estimated by comparing CSF $C_{max}$ and AUC to plasma $C_{MAX}$ and AUC (i.e., relative CSF penetration= $C_{max\_CSF}$/ $C_{MAX\_Plasma}$ and $AUC_{CSF}/AUC_{Plasma}$ ). The CSF $C_{Trough}$ for each ARV was compared with *in vitro* literature values of HIV inhibitory concentration values ($IC_{50\ or\ 90}$). For comparison of patient outcomes, only 44 patients of the 74 were evaluated given patients needed to be on similar base regimens (FTC/TDF) and restricted to Group 1 (chronic-treated participants) per ACTG protocol. For simplicity, 74 patients will be referred to as PK Cohort and the 44 as PK/PD Cohort. CSF IQs were calculated for each ARV in a regimen as ratio of predicted CSF $C_{Trough}$ to literature values for *in vitro* HIV $IC_{50or90}$. The geometric mean (GeoM) of CSF IQs of all drugs in each participant's ARV regimen was also calculated (ART-$IQ_{-GeoM}$). Statistical analyses evaluated associations among the ART-$IQ_{-GeoM}$ and CSF HIV DNA, biomarkers and GDS.

Results: FTC exhibited the highest median CSF penetration ($C_{max}$, 46.3%; AUC, 72%). The lowest median penetration was observed for DRV (DRV $C_{max}$, 0.95%; AUC, 1%) and DTG ($C_{max}$, 0.57%; AUC, 0.57%). All drugs had median CSF $C_{Trough}$ concentrations > $IC_{50\ or\ 90}$ except tenofovir ($C_{Trough,}$ 1.6 ng/mL < $IC_{50}$ of 143.7 ng/mL). The median (Q1, Q3) ART-$IQ_{-GeoM}$ was higher in those with undetectable vs detectable CSF HIV DNA 0.9 (0.5, 1.6) vs 0.5 (0.3, 0.9), p=0.027. A rank-based analysis gave similar findings. Higher ART-$IQ_{-GeoM}$ was associated with lower GDS (i.e., better global cognitive function, Spearman: -0.30, p=0.05). There was no association between CSF inflammatory biomarkers and ART-$IQ_{-GeoM}$.

Conclusion: These methods demonstrate an approach of utilizing PK modeling to standardize ARV concentrations to a given time point (i.e., $C_{max}$ or $C_{Trough}$) and assess if desired therapeutic drug goals are obtainable in the CSF. The ART IQ metric is a new approach to assess ART regimen activity. Higher ART-$IQ_{-GeoM}$ was associated with a lack of detection of CSF HIV DNA and better global cognitive function. These findings suggest

ART regimen activity affects HIV persistence in CSF. This tool provides a basis for further investigations of relationships between regimen activity and biomarkers of HIV persistence in the CSF and other viral reservoirs.

### 4.2.2 Introduction

Soon after HIV infection, the virus disseminates throughout the body and establishes multiple reservoir sites, including the central nervous system CNS, adipose tissue, male and female reproductive tracts, the secondary LN, and gut-associated lymphoid tissue (GALT)[228, 229]. The persistence of HIV in cells of these reservoirs is a major obstacle to virus eradication. These same anatomical sites also may be pharmacologic sanctuaries, as evidenced by concentrations of ARVs that are lower than those in peripheral blood; in some cases, these low ARV concentrations have been associated with evidence for low-level ongoing virus replication[57, 58]. Neurological complications associated with HIV infection are well recognized and are a continuing problem as the population ages.

The term HAND is used to describe neurocognitive dysfunction associated with HIV and represents a spectrum of cognitive impairment. Despite the success of combination ART in achieving potent, long-term HIV suppression, HAND remains common in PLWH and increases the risk of morbidity and mortality. A recent review looking at HAND diagnosis, treatment and potential mental health implications evaluated literature looking at different aspects of this multifaceted disease[230]. Their review of the literature found that treatment of HAND encompasses a multidisciplinary approach, and that ART remains the most important aspect of treatment, with the goal of reducing viral load and preventing neurocognitive decline. They also found that patients with HAND are at higher risk of developing other neurological issues (i.e., psychological distress,

depression, anxiety, reduced social functioning). The review concludes by highlighting the need for ongoing research to better understand the mechanisms of HAND and develop targeted interventions.

With the growing concern for HAND, data from ARV concentrations and PK analysis in CSF have resulted in the development of a CNS penetration effectiveness (CPE) rankings[231]. CPE rankings have been used to classify ARV penetration into the CSF. The CPE was created in 2008 as a proposed method of estimating CNS penetration of ARVs[231, 232]. Each drug is given a rank ranging from 1 to 4 based on PK/PD data, drug characteristics, results of clinical studies, and effectiveness in reducing CSF viral load or improving cognition. A rank of 4 represents the best penetration or effectiveness. The CPE score for a given ART regimen is calculated by summing the ranks of each drug in the regimen. The total score for a regimen is then classified as low (<8), medium (8–9), or high (>9)[231, 232]. This means that every person receiving the same regimen gets the same CPE score. An implicit assumption of the CPE is all persons taking the same ARV have the same CSF concentrations of that ARV. This method, as widely accepted, does not incorporate individual-level exposure metrics (i.e., exposure). As such, the goal of ARV therapy for PLWH with HAND has been ensuring adequate ARV exposure with guideline recommend ART and maintaining viral suppression. Numerous studies have looked at effects of higher CPE score ARV based therapy for treatment and/or development of HAND in PLWH and found conflicting or inconclusive results[233-241]. Studies have also looked at intensifying treatment in PLWH with neurocognitive impairment mainly with the addition of MVC to ART and found conflicting results[242-245]. Two of the smaller single center trials of MVC intensification found evidence of potential improvement in neurocognitive impairment in PLWH[244, 245]. A smaller study by Force et al. also found that in 31 PLWH with confirmed HAND, significant cognitive improvement was observed after ARV intensification (not specific to MVC) with higher CPE ranked ARVs[243]. The largest

intensification study, a study by Letendre et al. conducted a 96-week randomized controlled trial of ART intensification in 191 enrolled PLWH on suppressive ART comparing addition of DTG + MVC (n=61), DTG + placebo (n=67), and dual placebo groups (n=63). The study found that there was no difference in neurocognitive impairment between groups and concluded that ART intensification is not recommended as a treatment for neurocognitive impairment in PWLH on suppressive ART. However, the authors provided potential reasons for their negative findings (i.e., specific drugs chosen for the trial, insufficient power).

Controlling CSF HIV-RNA levels are important as it has been shown to correlate with cognitive improvements in PLWH[81]. The CNS is considered both an HIV reservoir and pharmacologic sanctuary. Ensuring that ARVs can cross the BBB and maintain adequate exposure to inhibit viral replication in the CNS is a therapeutic challenge. Strategies to maximize these efforts include optimizing the selection of an ART regimen based off known CSF penetrating potential. The inhibitory concentration is commonly the level at which 50%, 90%, or 95% ($IC_{50\text{-}95}$) of *in-vitro* viral replication is inhibited utilizing wild-type viruses. PK/PD endpoints are further complicated as no clear exposure thresholds (i.e., how much is enough) have been identified in the CSF or CNS. The lack of such information leaves gaps in our understanding of the relative efficacy of various ART regimens in the CSF/CNS. Fundamental to an understanding of relative CSF efficacy of ART regimens is knowledge of the common PK metrics for CSF exposure: $C_{max}$, AUC, and $C_{Trough}$.

In this paper, we aim to characterize the disposition and mass transit of various ART components in plasma and CSF in PLWH. Using Bayesian estimates, we seek to standardize CSF exposures and quantify the relationship between exposure and viral PD endpoints. Further, we will use these estimates to calculate total regimen IQ ratios and

compare them to patient specific outcomes to evaluate if any relationships between regimen and outcomes can be identified.

### 4.2.3 Methods

### 4.2.4 Participants

*Study participants and clinical procedures:* AIDS Clinical Trials Group study A5321 is a longitudinal prospective cohort study of changes in HIV reservoirs. Eligible PLWH had started combination ART as a participant of an ACTG treatment-naïve trial and were on ART for ≥2 years with well-documented sustained plasma viral suppression. Seventy-four participants were included for the PK cohort and only 44 qualified to be evaluated for viral outcomes (PKPD Cohort). PKPD Cohort were restricted to GROUP 1 (chronic-treated) participants not on RPV or NVP (since those drug levels were unavailable) The full details of A5321 have been previously published[63, 225-227]. Participants in A5321 provided informed consent for a single cross-sectional lumbar puncture, a concurrent blood sample, and neuropsychological assessment. Lumbar punctures were performed using 22-gauge pencil-point needles in most cases to withdraw 22 to 25 mL of CSF. CSF samples were promptly centrifuged, and supernatants and cell pellets stored at –80°C according to established ACTG CSF processing protocols. CSF and blood samples were drawn from each participant at various time points post dose. All participants from this cohort have received TFV (majority TDF, few TAF) and FTC or ABC and 3TC, in addition to anchor ARVs, EFV, DTG, EVG/c, RAL (twice daily), ATV/r, or DRV/r: (daily). All participants that were on FTC based regimens received TDF except for three that received TAF. TAF levels were not included for PK modeling. Each participant included in analysis contributed at least one plasma or one CSF sample. For TDF (n=33), FTC (n=44), and DTG (n=12),

participants from previous protocols (ClinicalTrials.gov [NCT02049307], ACTG: 5372) that had rich plasma PK sampling (>5 samples per subject) were included in the final dataset to improve the precision of PK parameter estimates[246]. No specific demographics were recorded for these patients as they were only used for model development

*Virologic and immunologic methods:* HIV persistence was measured as cell-assocaited HIV (CA-HIV) DNA and RNA and cell-free HIV RNA. CA-HIV DNA and RNA were measured by qPCR assays in PBMCs and CSF cell pellets derived from approximately 13 mL CSF and normalized by amplifiable CCR5 cell equivalents[63].Cell-free HIV RNA was quantified by integrase single copy assay in CSF supernatant (3–5 mL) and blood plasma (5 mL). Six inflammatory biomarkers were measured in cell-free CSF by ELISA (IL-6, IP-10, MCP-1 sCD14, sCD163, and neopterin [GenWay Biotech]).

*Neurocognitive outcomes*: Methods were adapted from previous A5321 neurocognitive analysis[63]. Briefly neuropsychological assessment consisted of 15 individual tests administered prior to or on the same day as the lumbar puncture. Z-scores were calculated by standardizing each raw test score by age, sex, race, and years of education. Global Deficit Scores (GDS), a measure of neurological impairment, were calculated for each individual test based on the z-score. If the z-score was missing, then the GDS was also missing. GDS range from 0 – 5, with higher scores indicating more severe impairment. GDS were assigned for each of the 15 individual tests using the following conversion: z-score > -1.0 corresponds to a GDS of 0 (Normal), -1.5 ≤ z-score ≤ -1.0 corresponds to a GDS of 1 (Mild), -2.0 ≤ z-score < -1.5 corresponds to a GDS of 2 (Mild to Moderate), -2.5 ≤ z-score < -2.0 corresponds to a GDS of 3 (Moderate), -3.0 ≤ z-score < -2.5 corresponds to a GDS of 4 (Moderate to Severe), z-score < -3.0 corresponds to a GDS of 5 (Severe). In some cases, raw scores were unavailable. Reasons included the test not being administered, the test omitted in error, or the participant exceeded the allotted time for the test. In such cases, the corresponding z-score and GDS were set to

missing. The mean z-score and mean GDS, as well as the corresponding domain-specific scores, were calculated by averaging all non-missing scores.

### 4.2.5 Determination of ARV Concentrations in Plasma and CSF

Plasma and CSF concentrations of each ARV (total drug) were quantified using LC-MS/MS using individual standard curves for each matrix as previously described[58,89]. ARV concentrations reported to be below LLOQ were imputed to one-half of the LLOQ[180]. Briefly for CSF, samples of CSF were taken via lumbar puncture and stored in polypropylene for analysis. CSF storage tubes were treated with 1% ammonia in MeOH 1:1 (v:v) to recover non-polar analyte binding to the tubes. Aliquots of 0.10 mL were taken, and analytes were extracted via protein precipitation after the addition of internal standards. Extracted samples were analyzed via LC/MS/MS. LC conditions were isocratic and reversed phase separation chromatography. MS detection was performed on an ABSciex 5500 triple quadrupole mass spectrometer. Briefly, for plasma, whole blood was collected, centrifuged, the plasma component removed, and stored in polypropylene tubes for analysis. Plasma aliquots were taken for the different ARV assays and extracted via protein precipitation after the addition of internal standards. LC conditions were isocratic reversed-phase chromatography. MS detection was performed on an ABSciex 5500 triple quadrupole mass spectrometer. More details for plasma methodology can be found in our previous work[58, 148]. ABC, RTV, COBI, TAF, BIC, ZDV, concentrations were not quantified given priority to drugs of interest, some only use for boosting effects, and small number of sample considerations. For all nine ARVs, total drug was quantified. As it is known that that most of these ARVs are highly protein bound in plasma (**Table 12**), the focus of this study was for CSF penetration, and protein content in CSF is much lower than plasma

(50-100 times lower)[247]. While typical plasma protein concentrations range between 60 and 70 mg/mL, normal CSF protein concentrations are 0.2–0.7 mg/mL[247].

### 4.2.6 ART PK Analysis

Available PK data were examined for LLOQ and for outliers. Base models were developed for each ARV (n=9) using a 3-compartment model, including a CSF compartment, with oral absorption and linear elimination from the central compartment. PK modeling was conducted with the nonparametric adaptive grid (NPAG) algorithm within the Pmetrics package version 2.1.0 (Los Angeles, CA) for R version 4.3.1 (R Foundation for Statistical Computing, Vienna, Austria)[189, 190]. Four- and five-compartment models were also explored. For the base PK model development, the absorption rate constant (Ka) was held constant throughout based on literature values (**Table 12**)[248-256]. Multiple model structures were also considered for describing mass transit of drug concentrations in the CSF (model comparison not shown given number of drugs) based on investigator judgement, and other PK CSF studies[191-194]. The observation variance was proportional with a multiplicative (gamma) model (error = SD x gamma) where SD = $C_0$ + $C_1$Y (with inputs for plasma and CSF specific for each ARV). Model performance was quantitatively described using observed vs. predicted concentrations to calculate bias, imprecision, and coefficients of determination[257]. The final PK model was selected according to the lowest Akaike information criterion (AIC) score, goodness-of-fit plots, prediction bias, parameter precision, successful convergence, and rule of parsimony. Notably, the objective of the PK analysis was to develop an explanatory model that describes the PK of ART and to standardize CSF exposure timing for each patient based on the posterior predictions. As such, no formal covariate analysis was performed. Further, patient specific covariate information was unavailable for the subset of data

included for FTC, TDF and DTG modeling. A summary of all available concentrations for each ARV that was used in each ARV's model build can be found in **Figure 21.**

## 4.2.7 Estimation of PK Exposure and Percent (%) CSF Penetration

The final model was utilized to obtain the median maximum *a posteriori* probability (MAP) Bayesian plasma and CSF concentrations at 12-minute intervals over a 24hr study period using each participant's measured ARV plasma and CSF concentrations, exact dose, and self-reported dosing schedule. Steady-state conditions were assumed for all participants with the appropriate dosing interval (daily vs. twice daily). Bayesian posterior predictions for each participant on each ARV were used to determine plasma and CSF exposures over a 24hr period (i.e., $AUC_{0\text{-}24h}$) using Phoenix® WinNonlin® Version 8.3 (Certara USA, Inc., Princeton, NJ)[189, 198]. Noncompartmental analysis (NCA) was used to estimate CL/F and steady-state V/F based on Bayesian posterior predictions from the final PK model for comparison to other literature PK estimate values for each ARV. The highest predicted concentration [$C_{max\_0\text{-}24h}$] from the 12-minute interval Bayesian estimates was taken to be each participant's $C_{max\_0\text{-}24h}$. The lowest concentration within the dosing interval (i.e., 24-hours for once daily, 12-hours for twice daily) was determined to be the $C_{Trough}$. The estimated PK exposures ($AUC_{0\text{-}24h}$, $C_{MAX\_0\text{-}24h,}$ $C_{Trough}$) for plasma and CSF were used to calculate the percent penetration into the CSF for each ARV and participant (i.e., CSF penetration = $C_{max\_CSF}/C_{MAX\_Plasma}$ and $AUC_{CSF}/AUC_{Plasma}$). The protein free $IC_{50or90}$ for each ARV was used to assess CSF exposure based on literature values[214]. Summary statistics were calculated using GraphPad Prism version 10.00 (GraphPad Software Inc., La Jolla, CA).

### 4.2.8 Calculation of IQ Ratio for ART Regimen

CSF IQs were calculated for each ARV in a regimen as ratio of predicted CSF trough to literature values for *in vitro* HIV inhibitory concentration (i.e., $IC_{50}$, $IC_{90}$ [references for ICs used for each ARV can be found on **Table 10**). Briefly, the protein free $IC_{50or90}$ values used were: $FTC_{IC50}$ = 1.7 ng/mL, $TDF_{IC50}$ = 143.7 ng/mL, $3TC_{IC90}$ = 21 ng/mL, $EFV_{IC90}$ = 1.3 ng/mL, $DTG_{IC90}$ = 0.2 ng/mL, $RAL_{IC90}$ = 3.2 ng/mL, $EVG_{IC90}$ = 0.072 ng/mL, $ATV_{IC90}$ = 1.7 ng/mL, and $DRV_{IC90}$ = 0.67 ng/mL. The CSF ART-$IQ_{-GeoM}$ of all drugs in each participant's ARV regimen was calculated. Statistical analyses were conducted to evaluate potential associations among the ART-$IQ_{-GeoM}$ and CSF HIV DNA, biomarkers and GDS.

### 4.2.9 Statistical Considerations

An average IQ for the entire ARV regimen was derived for each participant by taking the geometric mean of the IQs of the individual agents, i.e., of the TFV $IQ_{50}$, the FTC $IQ_{50}$, and the third drug $IQ_{90}$ (referred to as the geometric mean IQ), to be used in subsequent analyses (note average IQs are unavailable for n=8 participants taking RPV or NVP since CSF concentrations for these drugs were unavailable at the time of analysis). As a supplemental approach to measuring ARV regimen activity, an arithmetic mean IQ for the regimen was also calculated and evaluated for relationships. The arithmetic and geometric mean IQs correlate reasonably well. As a supporting analysis rank-based analyses were used to evaluate associations between ARV concentrations/drugs in CSF and detection of HIV in CSF (median, Q1, Q3, min, max; Wilcoxon tests comparing HIV detected vs. TND groups). Because all in the PK/PD analysis population were on TDF + FTC, but differed with respect to the 3rd drug, a ranking approach based on CPE scores

was used to incorporate information on the 3rd drug. For TFV and FTC concentrations in CSF, differing time since last dose was incorporated and addressed by using PK model predictions to obtain, for each participant, a model-predicted 24hr post-dose concentration. Groups were compared using the exact Wilcoxon rank-sum test for continuous variables and the Fisher's exact test for categorical variables. Regression analyses were used to assess whether associations were influenced by potential confounders. All p-values and confidence intervals presented are unadjusted for multiple comparisons performed.

### 4.2.10 Results

### 4.2.11 Characteristics of Participants and ARVs

Complete demographics for these participants stratified by regimen and anchor can be found in **Table 11a and b**. A total of 9 different ARVs were included in this analysis. Fifty-nine patients were on an FTC based regimen. Fifteen patients were on non-FTC based regimens. Of the total 74 PK Cohort patients, only 44 qualified to be evaluated for viral outcomes (PKPD Cohort).

### 4.2.12 ARV PK Model Predictions

All available CSF and plasma levels were utilized in the PK modeling. For the 9 ARVs, models converged for a 3-compartment oral absorption model. A schematic of the final structural model utilized for all 9 of the ARVs can be found in **Figure 22.** Of note, for EVG, only CSF levels were available for PK analysis. Goodness-of-fit plots for each ARV

in plasma and CSF (mcg/mL) are shown in **Figure 23**. The estimated PK parameters (CL/F, V/F) from both the final PK model and NCA for each ARVs can be found in supplemental material provided in the **Table 12.**

### 4.2.13 ARV Exposures and Percent (%) CSF Penetration

The overall PK exposures with observed concentrations and predicted exposures for all participants are summarized in **Table 13.** An example of the full posterior observed vs. predicted concentration-time profile plot for each participant on each ARV can be found in **Figure 24.** Out of all the ARVs, FTC exhibited the highest median percent CSF penetration at 46-72% (including both $C_{max}$ and AUC based CSF penetration). The lowest median percent penetration was observed for EFV ($C_{max}$, 0.9%; AUC, 0.92%), DRV ($C_{max}$, 0.95%; AUC, 1%), and DTG ($C_{max}$, 0.57%; AUC, 0.57%). When comparing median $C_{Trough}$ to the $IC_{50\ or\ 90}$ for each respective ARV, all ARVs had median CSF $C_{Trough}$ concentrations > $IC_{50\ or\ 90}$ except TFV (median $C_{Trough}$, 1.6 ng/mL; *in vitro* $IC_{50}$, 143.7 ng/mL).

### 4.2.14 IQ Ratio ART Regimen

A summary of IQ scores for the PKPD Cohort can be found in **Figure 25**. The geometric mean IQ was higher in participants with undetectable CSF HIV DNA versus those with detectable CSF HIV DNA (median [Q1, Q3]: 0.9 [0.5, 1.6] for not detected vs. 0.5 [0.3, 0.9] for detected; p=0.027 [**Figure 26**]). A rank-based analysis gave similar findings. This corresponds to undetected CSF HIV DNA being associated with higher predicted ARV trough levels/activity in CSF. Conversely, the geometric mean IQ was numerically lower in participants with undetectable cell-associated HIV RNA (CA-RNA) versus those with detectable CA-RNA (median [Q1, Q3]: 0.7 [0.4, 1.1] for TND vs. 1.3

[0.5, 1.7] for detected), though not statistically significantly different (data not shown: p= 0.37). However, only 4 participants had detectable HIV RNA in the CSF providing poor power to investigate this relationship.

### 4.2.15 Inflammatory Biomarkers in the CSF

There was no association found between CSF inflammatory biomarkers and ART-IQ$_{\text{-GeoM}}$. The complete analysis can be found on **Table 14**.

### 4.2.16 ART IQ and GDS

Overall, components of GDS were evaluated for correlation with ART activity in the CSF. Higher ART-IQ$_{\text{-GeoM}}$ was associated with lower GDS (i.e., better global cognitive function, Spearman: -0.30, p=0.05). The full analysis can be found on **Table 15.**

### 4.2.17 Discussion

Evidence suggests increasing the CSF activity of ART may be associated with improved CSF viral suppression and lower prevalence of CSF escape[258]. As such, it is important to explore CSF exposures standardized to time of currently available ART regimens via pharmacometric approaches to ensure a comparable understanding of CSF exposure in PLWH. Using our pharmacometric methodology, we have demonstrated how Bayesian estimates from the PK model can be used to standardize CSF exposure timing of ARV between individuals to assess if adequate exposures are maintained above the

$IC_{50\ or\ 90}$ for each ARV. In our analysis, we found that FTC exhibited the highest median CSF penetration (46.3% based on $C_{MAX}$; 72% based on AUC). The lowest CSF penetration was observed for DRV/r (0.95% based on $C_{MAX}$; 1% based on AUC) and DTG (0.57% based on both $C_{MAX}$ and on AUC) (Table 3). For FTC, this finding is consistent with its high CPE score of 3[231]. A study by Lahiri et al looked at CSF concentrations of TDF and FTC in protease inhibitor-based regimens and found the median FTC CSF:plasma ratio to be 0.7 (IQR: 0.4-0.9) in the presence of atazanavir and 0.6 (IQR: 0.5-07) in the presence of DRV[259]. Similar to our findings, they found median $C_{Trough}$ to be 33.4 ng/mL (IQR:28.6-47.5) in the presence of atazanavir and 50.0 ng/mL (IQR: 39.9-109.9) in the presence of DRV. For DTG, our CSF penetration was low (0.57%) and consistent with previous work by Letendre et al. and Gele et al. that showed median CSF-plasma ratios of 0.516% (range: 0.115-0.658% [week 2])[149], 0.412 (range: 0.299-2.04% [week 16])[149], and 0.65% (range: 0.19-5.11%)[260]; and median levels of 18.2 ng/mL (range: 4.0-23.2 ng/mL [week 2])[149], 13.2 ng/mL (range: 3.7-18.3 [week 16])[149], and 9.6 ng/mL (3.6-22.8 ng/mL)[260]. However, even with low concentrations in the CSF, our median $C_{Trough}$ DTG predictions were above the $IC_{90}$ (10.4>0.2 ng/mL). Our estimated CSF penetration and DRV/r $C_{Trough}$ predictions was in agreement with other data that found DRV/r had a median plasma-CSF ratio of (0.007 [IQR: 0.006-0.012])[72] and 0.5% (IQR: 0.3-0.9)[258], with median CSF levels of 16.4 ng/mL(with RTV, IQR: 8.6–20.3)[72], 15.9 ng/mL (/c, IQR: 6.7–31.6)[72], and 15.7 ng/mL (IQR: 8.5-30.9)[258]. Our median $C_{Trough}$ CSF concentrations for DRV/r was above the $IC_{90}$ (15 ng/mL > 0.67 ng/mL), which is consistent with having a high CPE score of 3.

For EFV, our estimated %CSF penetration was low (~0.9%) but still adequate compared to the $IC_{90}$ value (median $C_{Trough}$: 12ng/mL > $IC_{90}$: 1.3ng/mL). This is consistent with its associated CPE score of 3 which showcases another example of an ARV that has low penetration but still achieves adequate concentrations based on PD goals. Specific to EFV, it is important to discuss its potential association with neurotoxicity. EFV's

metabolites (8-OH and 7-OH) have been shown to induce direct neuronal toxicity and death in an in-vitro model[261]. A study by Tovar-y-Romo et al. found that 7-OH and 8-OH each induced neuronal damage in a dose-dependent manner but that 8-OH was more toxic than both EFV and 7-OH. 8-OH was found to cause damage to dendritic spines at 10 nM concentration. This study also provided a hypothesis for the mechanism of EFV neurotoxicity, which was attributed to 8-OH perturbation of calcium homeostasis. In the clinical setting, studies have shown conflicting results regarding EFV levels and neurocognitive performance in PLWH[262-264]. Marzolini et al. showed that high plasma levels of EFC (>4000 µg/L) resulted in three times more frequent CNS toxicity (CNS adverse effects, 9% vs. 24%, p=0.093) compared to those with lower plasma levels (1000-4000 µg/L) of EFV[264]. However, another study by Nwogu et al. found that higher EFV concentrations were associated with better neurocognitive performance (r=0.23, p=0.043) via neuropsychological examination[263]. Similarly, our group has shown that better neurocognitive function was associated with higher 8-OH levels but lower EFV plasma concentrations, potentially due to higher patient plasma clearance of EFV[265]. Most recently, a study by Ranzani et al looked at EFV and 8-OH plasma levels in comparison to cognitive impairment in 104 PLWH[266]. Notably, they did not look at CSF levels of drug. The study found that neither level was linked to cognitive impairment; there was a trend towards higher EFV levels in those with impaired executive function (p=0.055) and language performances (p=0.021). Further, elevated 8-OH levels were associated with more CNS side effects (222 vs. 151 ng/mL, p=0.078). The authors concluded that higher plasma levels of the 8-OH metabolite were associated with CNS side effects and EFV levels were only marginally associated with cognitive impairment, suggesting differences in how EFV and its metabolite act in the CNS. As clinical studies looking directly at EFV metabolites and CNS toxicity are lacking, more studies are warranted.

Conceptually, the CPE is an attractive tool. Methodologically, each drug is given a rank from 1 to 4 based on PK/PD data, drug characteristics, clinical studies, and effectiveness in reducing CSF viral load or improving cognition. However, limitations exist[81]. Studies have shown a higher CPE score results in lower CSF HIV-RNA and a correlation between CPE score and CSF escape; however, these associations have not been uniformly observed[81]. Further, the CPE score does not take into consideration the patient-specific exposure and interpatient variability. As CPE scores are calculated with preexisting values attributed to each ARV, there is no guarantee that the patient will maintain exposure above the $IC_{50\ or\ 90}$ prior to the next dose being administered. Furthermore, newer ART regimens include medications not yet assigned CPE scores (i.e., DTG, BIC, doravirine), displaying the need for an update to the CPE metric to include newer agents/regimens[267].

One main objective of this study was to utilize Bayesian estimates from PK analysis to obtain standardized measures of CSF exposure among individuals taking the same ARVs. Such standardized measures (e.g., $C_{max}$, AUC, $C_{Trough}$) would allow comparisons of exposure across individuals that we believe would be more informative than a single CSF concentration obtained at different times post dose. We found that all ARVs from all participants had a summarized median CSF $C_{Trough}$ concentration > $IC_{50\ or\ 90}$ except TFV: $C_{Trough}$: 1.6 ng/mL < $IC_{50}$: 143.7 ng/mL. This finding for TFV is consistent with its low CPE score of 1 whereas the other ARVs have assigned CPE scores ≥2. As PK modeling was performed, the final parameter estimates from the PK model and NCA derived PK parameters (i.e., steady state parameters) from the posterior predictions are summarized in **Table 14.** When compared to other PK studies, our estimates were reasonably within range of what other studies have found for each ARV [248-250, 252-254, 268-277] (PK comparison not shown given the number of drugs and studies, references for comparisons can be found on table). Notably, some of the anchor drugs on the regimen

included in our study had limited sample size (<10) and very low concentrations which accounts for high variability and potential bias/imprecision given small numeric values. For TDF, FTC, and DTG, we pooled data from other studies (outside of the A5321 cohort) to allow for robust estimation of primary PK parameters and parameter shrinkage. As our study looked at CSF concentrations of ARVs in participants, penetration into other parts of the CNS does not always agree with CSF penetration. It is a common misconception that drug distribution into the CSF is an indicator of BBB transport[278, 279]. The Blood CSF barrier (BCB) is considered "leakier" compared to the BBB and transport across is inversely related to molecular weight of compound. This is due to the BCSFB being comprised of ependymal cells of the choroid plexus. This results in looser tight junctions compared to the ones found in the BBB. As such, drug penetration into the CSF is not an index of BBB transport, but rather a measure of transport across the choroid plexus at the BCSFB. Specific to ARVs, animal models have also shown that ARV CSF penetration does not always correlate with brain tissue penetration[79]. Discrepancies have been attributed to ARV affinity for drug uptake and efflux at the BBB and BCSFB[280]. Protein-binding also plays a major role in this as active transport of ARVs across the BBB and blood-CSF barrier disturbs the equilibrium of passive unbound drug movement (the "free drug hypothesis"), which may result in differences in ARV concentrations in plasma, CSF, and brain tissues[79]. The CSF has low binding protein concentrations compared with plasma, and studies of ARVs in the CSF have found the drug present is mostly unbound[247]. Further, a methodological challenge for ARV quantitation in CSF was described by our group, that showed non-polar ARVs can adsorb to polypropylene collection tubes[89, 183]. This suggests some re-examination of former studies of ARV concentrations in CSF in PLWH who are/are not virologically suppressed may be warranted to account for this adsorption. In this study, CSF ARV quantification was conducted with methods previously described[89].

In our study, we found that a higher regimen-based ART-IQ-$_{GeoM}$ was associated with more participants that had non-detectable HIV DNA in the CSF and better GDS scores. This observation warrants further investigation as it provides some evidence to support that CSF viral outcomes may be linked to overall ART regimen rather than individual ARVs. This work builds upon previous studies that have specifically looked at individual ART IQ as a measure of CSF activity[258]. Further, the study of persistent HIV in the CNS is the topic of much debate as studies have shown varying results of ART for treating NeuroHIV. It is important to mention that we chose to use GeoM summaries for IQ because of the differences in IC values among different ARVs. This allows for a better comparison and control of extremes since all ICs contribute to the IQ for each ARV which then contributes to the overall IQ for the regimen.

We found that ART-IQ-$_{GeoM}$ was not associated with differences in inflammation in the CSF. However, it is important to note that these participants were on ART and virally suppressed for >8 years and thus, this finding is expected. Future work should evaluate other CSF inflammatory biomarkers that may be more consistent with long-term ongoing inflammation.

Several limitations in our study exist. Firstly, this study protocol only obtained one sample for plasma and CSF per participant on each respective ARV. As such, an effort was maintained to not over-parameterize the population PK model build (i.e., the simplest and most explanatory model for describing drug disposition). The limited PK samples contributed per participant may also potentially affect the predicted concentrations in each matrix. However, the individual predictions are largely in agreement with the observed data based on goodness-of-fit plots as demonstrated by the coefficient of determination values. The bias and imprecision were likely a result of the low concentrations included in the PK analysis. Secondly, steady-state concentrations were assumed for all participants. Because adherence was self-reported, missed doses may have resulted in low plasma

and CSF concentrations, and this could not be accounted for during PK analysis. Further, the intended purpose of the PK modeling was to characterize the available, limited PK data to derive individual exposures rather than to develop a population model for other purposes. No plasma samples were collected from individuals receiving EVG/c. Therefore, it was not possible to estimate the CSF penetration for that ARV. Our model estimations of CSF mass transit denotes an overall process occurring at the level of the CSF, including uptake by various types of cells in the CNS. This may be an oversimplification and a more mechanistic description should be evaluated utilizing an advanced quantitative systems pharmacology approach. Lastly, the role of BBB transporters on drug penetration is outside the scope of this study. Further investigations may be needed to characterize the impact of BBB transporters and drug concentrations in the CSF.

In summary, these data demonstrate the ability to use patient specific drug level data, and PK modeling to obtain standardized PK measures of CSF exposure to a given time point (i.e., $C_{MAX}$ or $C_{Trough}$), and to use those measures to assess if putative PD endpoints are maintained. These results provide a PK/PD framework to explore individual ARV CSF exposures and virologic outcomes and provide a quantitative understanding of the ART regimen activity. The ART IQ metric is a new approach to assess ART regimen activity. We found that ART-$IQ_{-GeoM}$ was associated with a lack of detection of CSF HIV DNA and better GDS. These findings suggest ART regimen activity affects HIV persistence in CSF. This tool provides a basis for further investigations of relationships between regimen activity and biomarkers of HIV persistence in the CSF and other viral reservoirs.

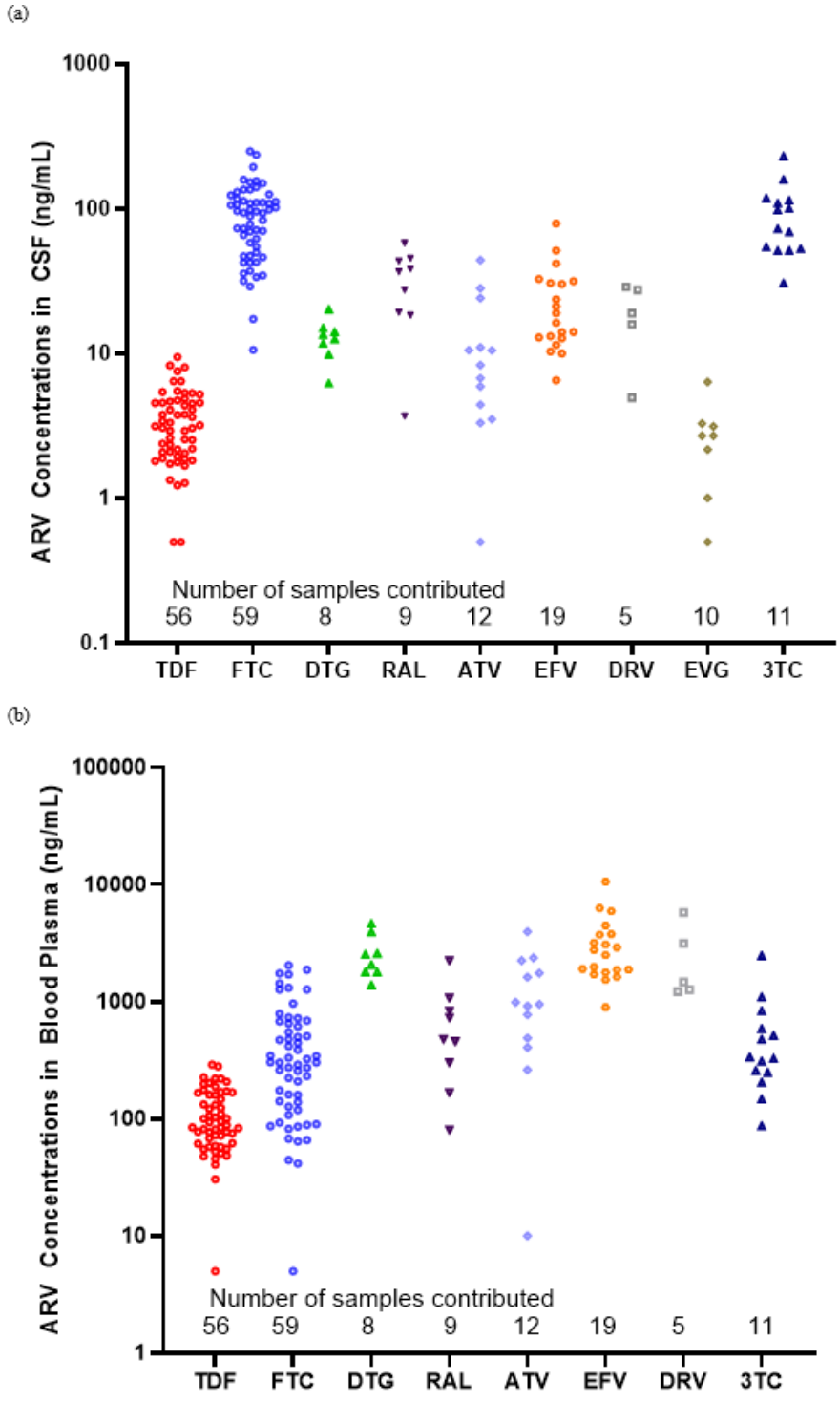


**Figure 21**. ARV concentrations (ng/mL) in CSF (a) and plasma (b) for the various ARVs used in the PK modeling.

Abbreviations: ARV, antiretroviral; CSF, cerebrospinal fluid; TDF, tenofovir disoproxil; FTC, emtricitabine; EFV, efavirenz; DTG, dolutegravir; RAL, raltegravir; EVG, elvitegravir; ATV, atazanavir; DRV, darunavir/r; PK, pharmacokinetic

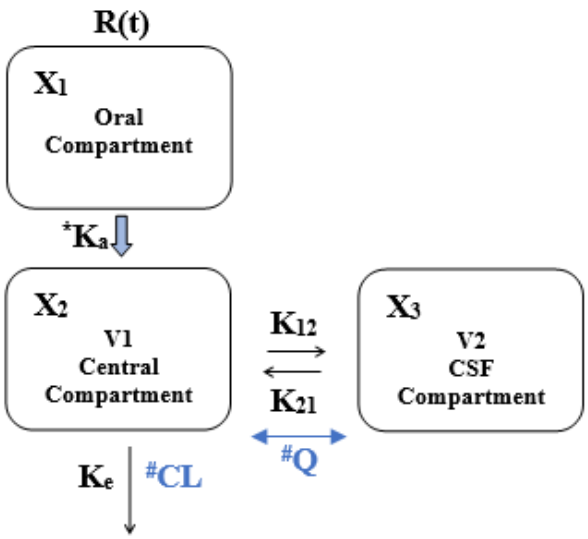


Differential Equations

$dx_1(t)/dt = -Ka^* X_1$

$dx_2(t)/dt = Ka^*X_1 + R(t) - (Ke+K_{12})^*X_2 + K_{21}^*X_3$

$dx_3(t)/dt = K_{12}^* X_2 - K_{21}^*X_3$

*Ka: the absorption rate constant was held constant based on literature values.

#A CL model was used for TDF whereas a Ke model was used for all other antivirals.

**Figure 22**. Schematic and differential equations of base three-compartmental PK model

Abbreviations: PK=pharmacokinetic, Ke=elimination rate constant, $V_1$=volume central compartment, $V_2$=volume cerebral spinal fluid compartment, $K_{12}$=rate constant to cerebral spinal fluid compartment, $K_{21}$=rate constant to central from the cerebral spinal fluid compartment, CSF=cerebral spinal fluid, $X_1$=amount in the oral compartment, $X_2$= amount in the central compartment, $X_3$= amount in the CSF compartment, Q=flow, CL=Clearance, TDF= tenofovir disoproxil fumarate

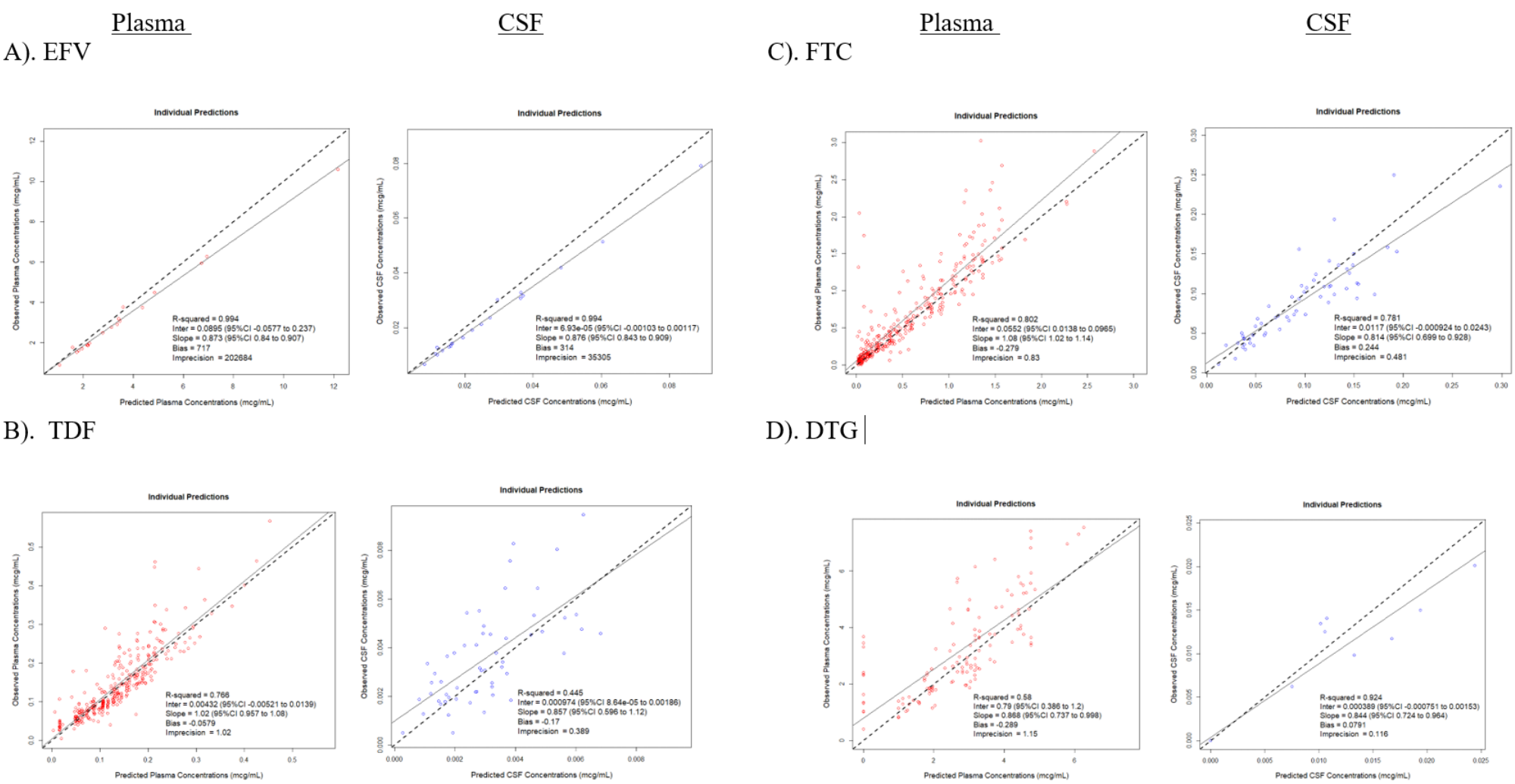


**Figure 23**. Observed versus predicted concentration (mcg/mL) plots for each CSF and Plasma for 9 ARV

Plasma CSF

E). RAL

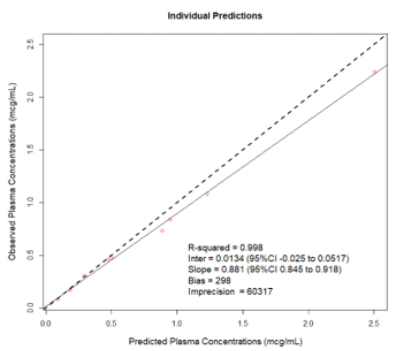


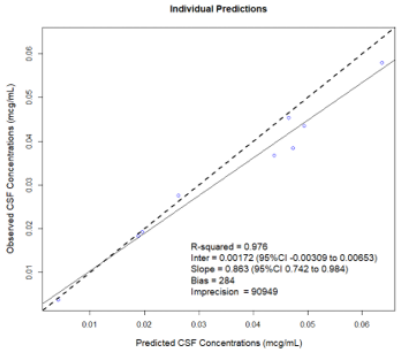


F). ATV

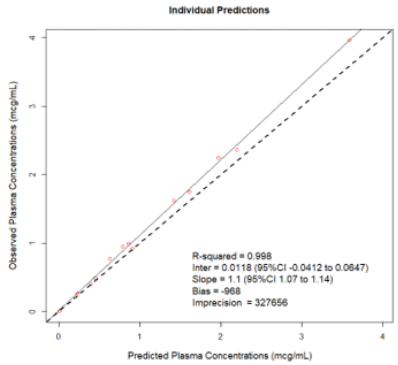


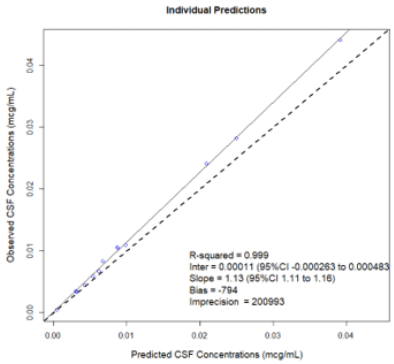


G) 3TC

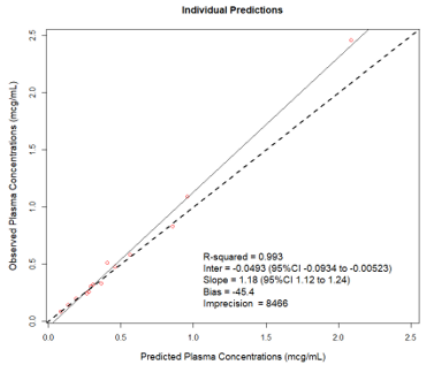


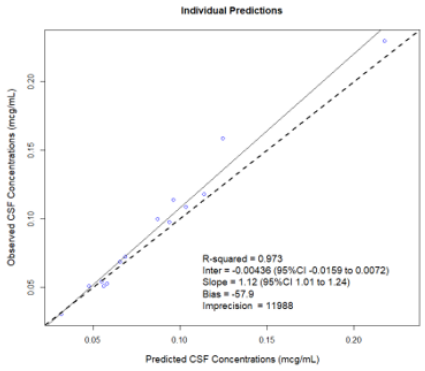


Plasma CSF

H). DRV

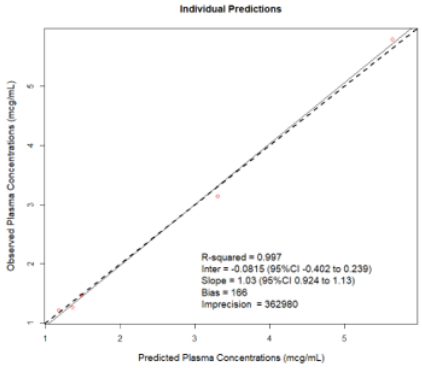


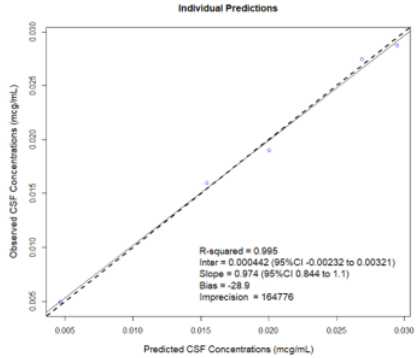


I). EVG

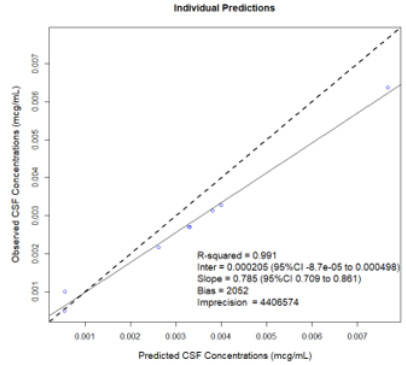

Abbreviations: TFV, tenofovir; FTC, emtricitabine; EFV, efavirenz; DTG, dolutegravir; RAL, raltegravir; EVG, elvitegravir; ATV, atazanavir; DRV, darunavir/r

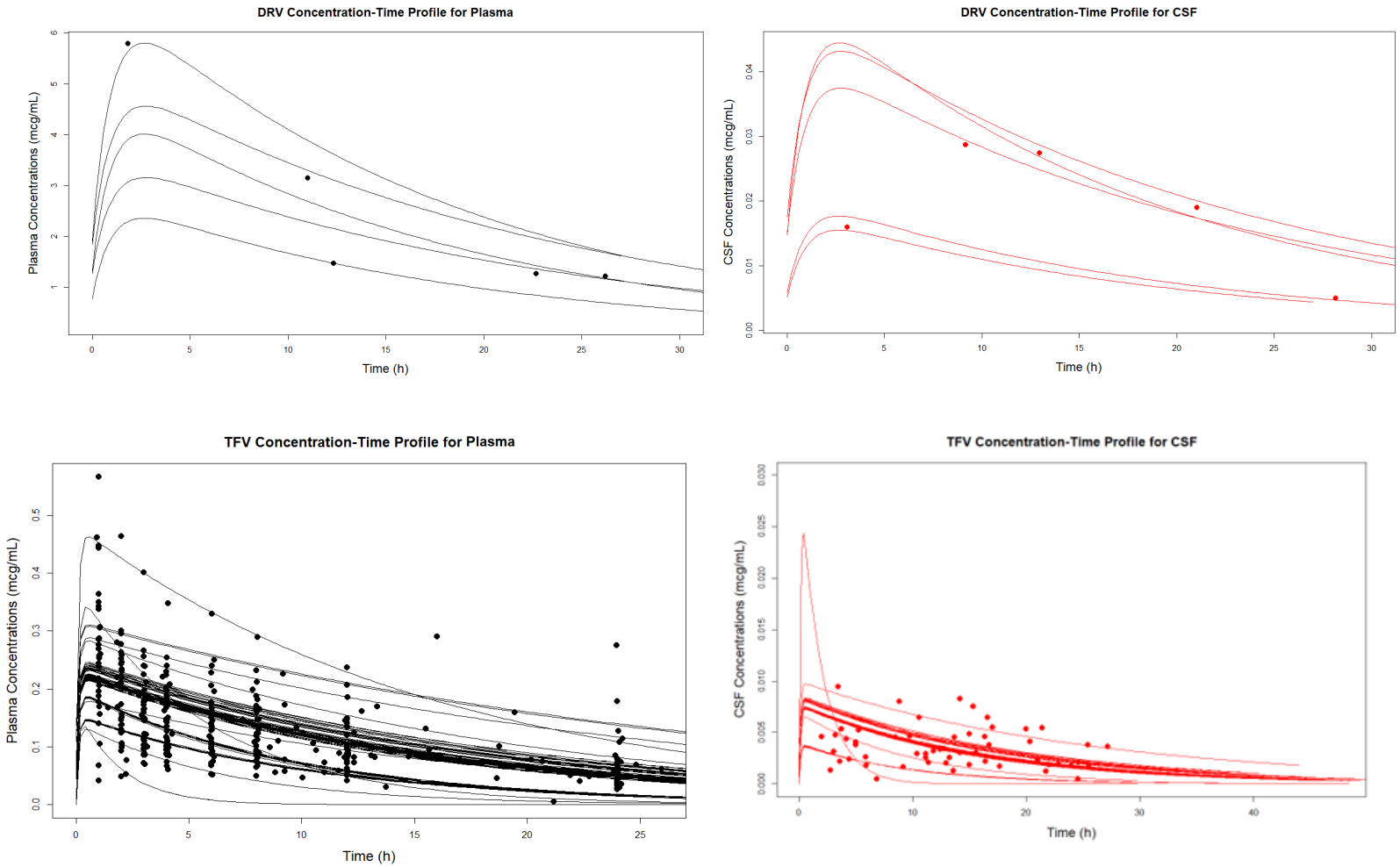


**Figure 24**: Plotted posterior concentration (y axis: mcg/mL) vs. time plots for each drug and for all participants.

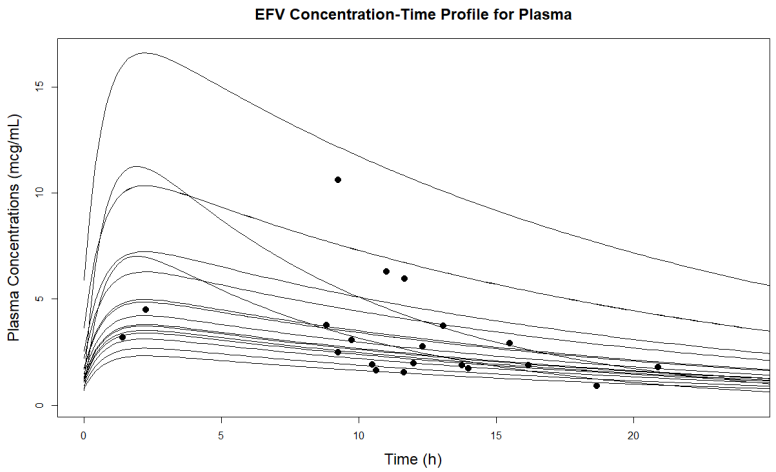
EFV Concentration-Time Profile for Plasma
Plasma Concentrations (mcg/mL)
Time (h)

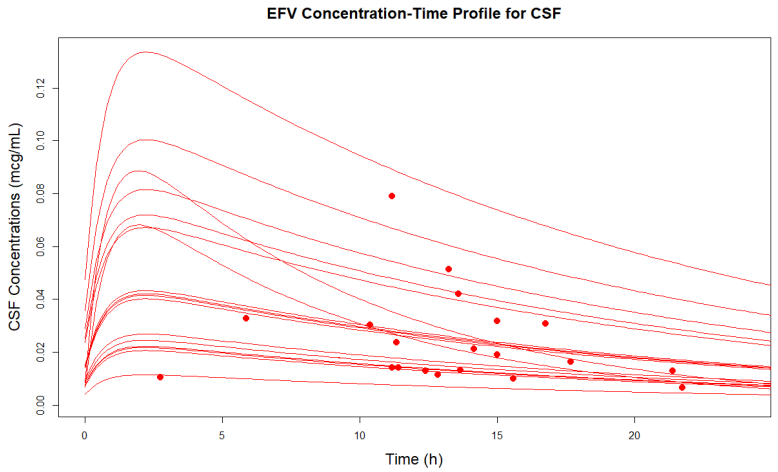
EFV Concentration-Time Profile for CSF
CSF Concentrations (mcg/mL)
Time (h)

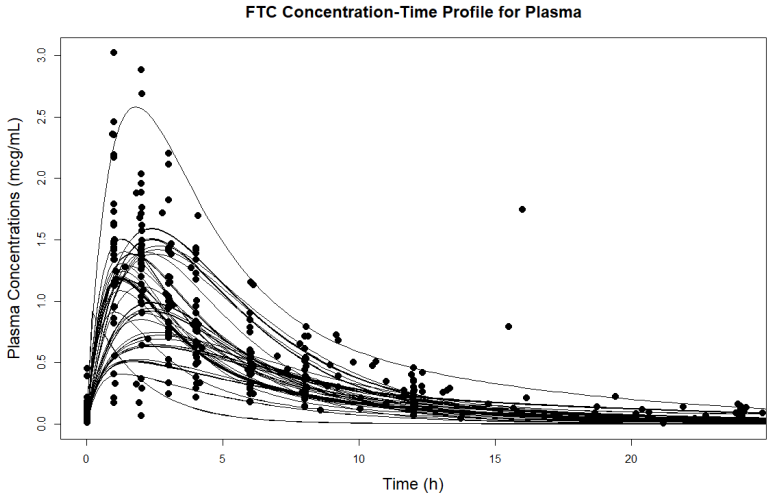
FTC Concentration-Time Profile for Plasma
Plasma Concentrations (mcg/mL)
Time (h)

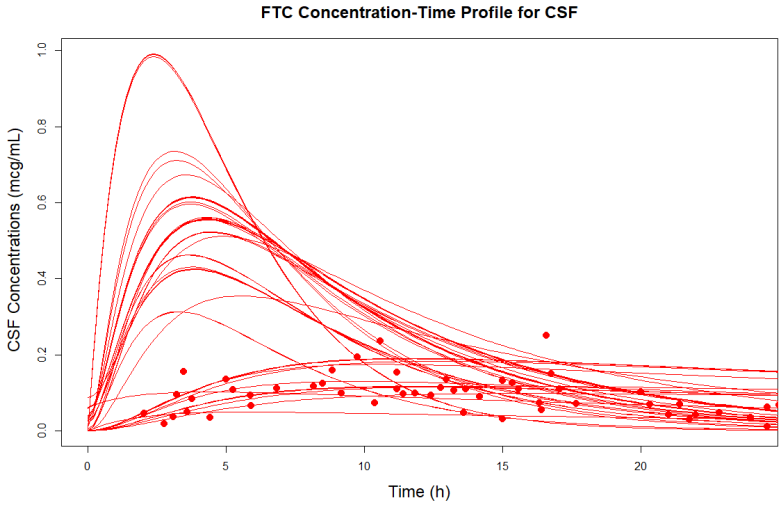
FTC Concentration-Time Profile for CSF
CSF Concentrations (mcg/mL)
Time (h)

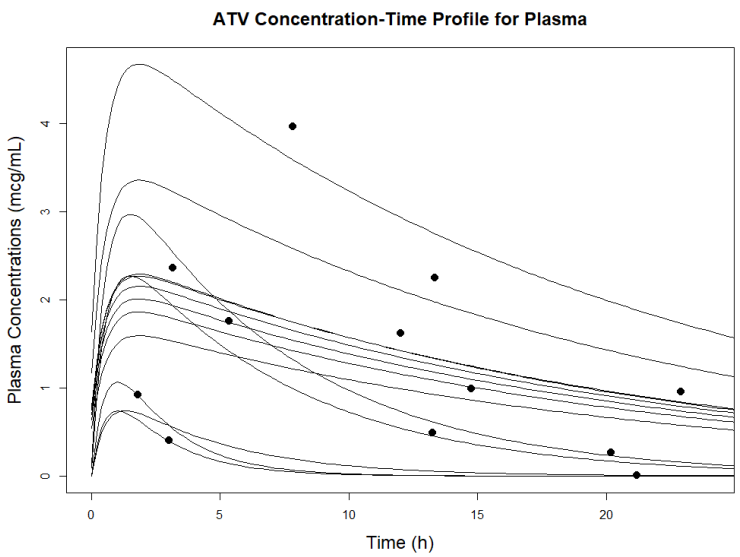
ATV Concentration-Time Profile for Plasma
Plasma Concentrations (mcg/mL)
Time (h)

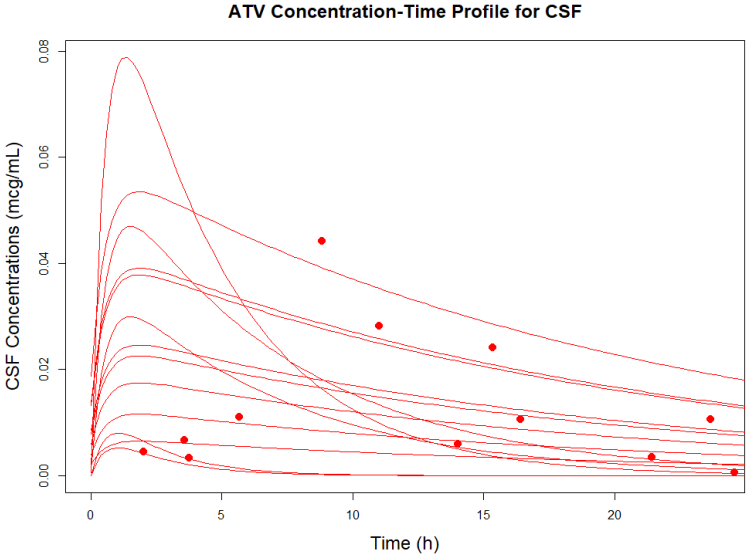
ATV Concentration-Time Profile for CSF
CSF Concentrations (mcg/mL)
Time (h)

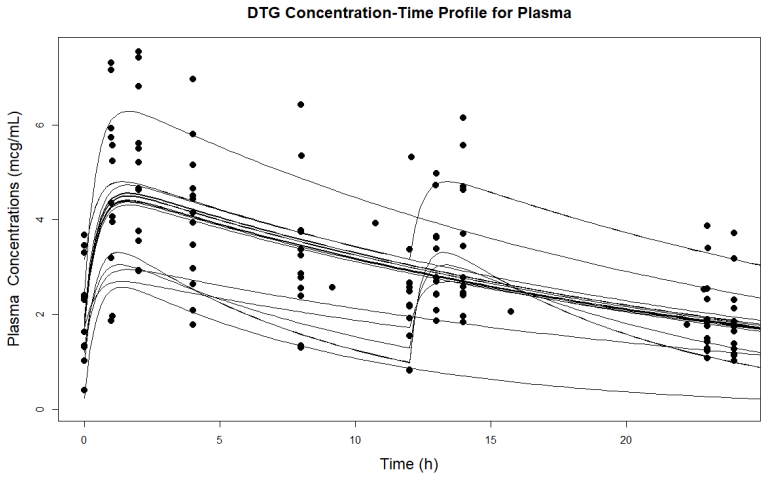
DTG Concentration-Time Profile for Plasma
Plasma Concentrations (mcg/mL)
Time (h)

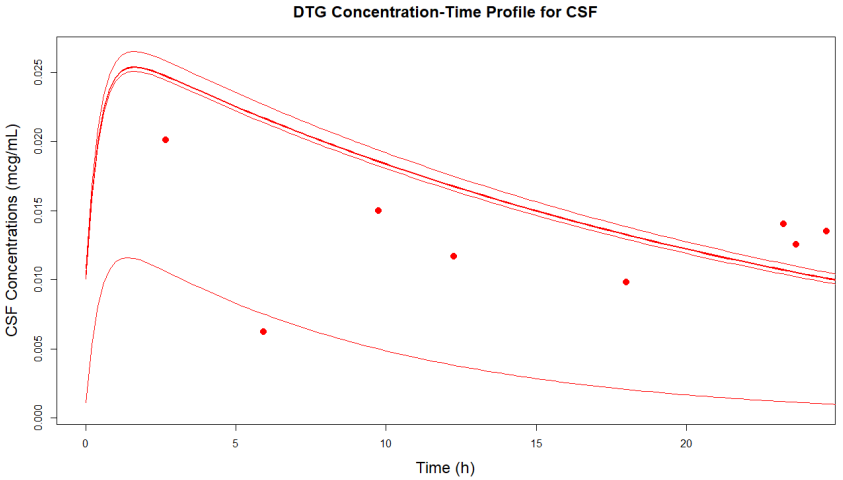
DTG Concentration-Time Profile for CSF
CSF Concentrations (mcg/mL)
Time (h)

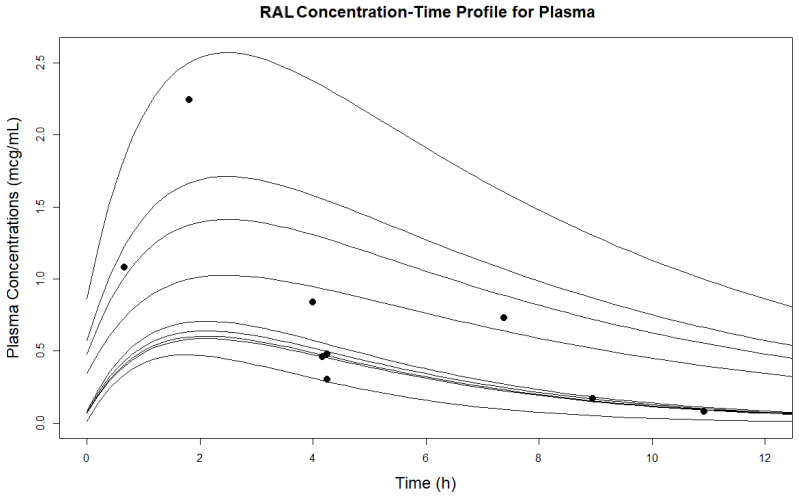
RAL Concentration-Time Profile for Plasma
Plasma Concentrations (mcg/mL)
Time (h)

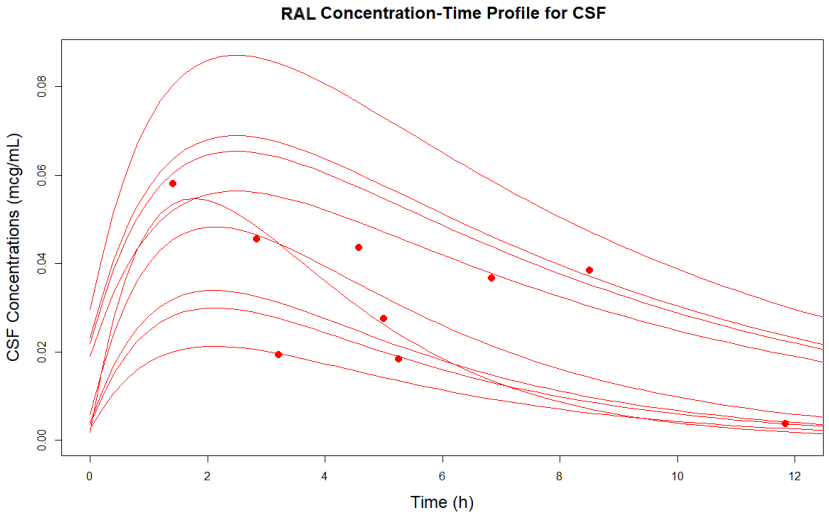
RAL Concentration-Time Profile for CSF
CSF Concentrations (mcg/mL)
Time (h)

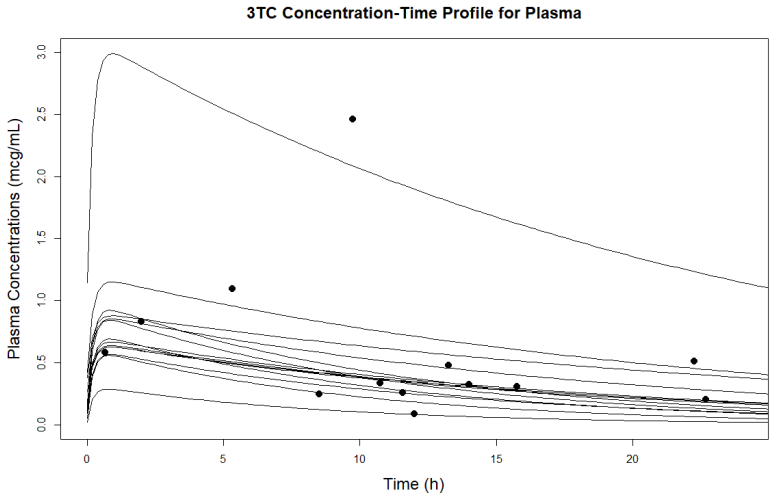
3TC Concentration-Time Profile for Plasma
Plasma Concentrations (mcg/mL)
Time (h)

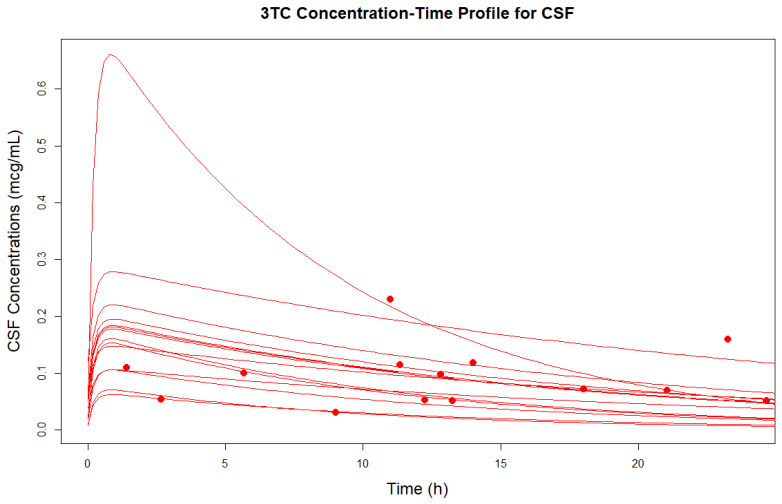
3TC Concentration-Time Profile for CSF
CSF Concentrations (mcg/mL)
Time (h)

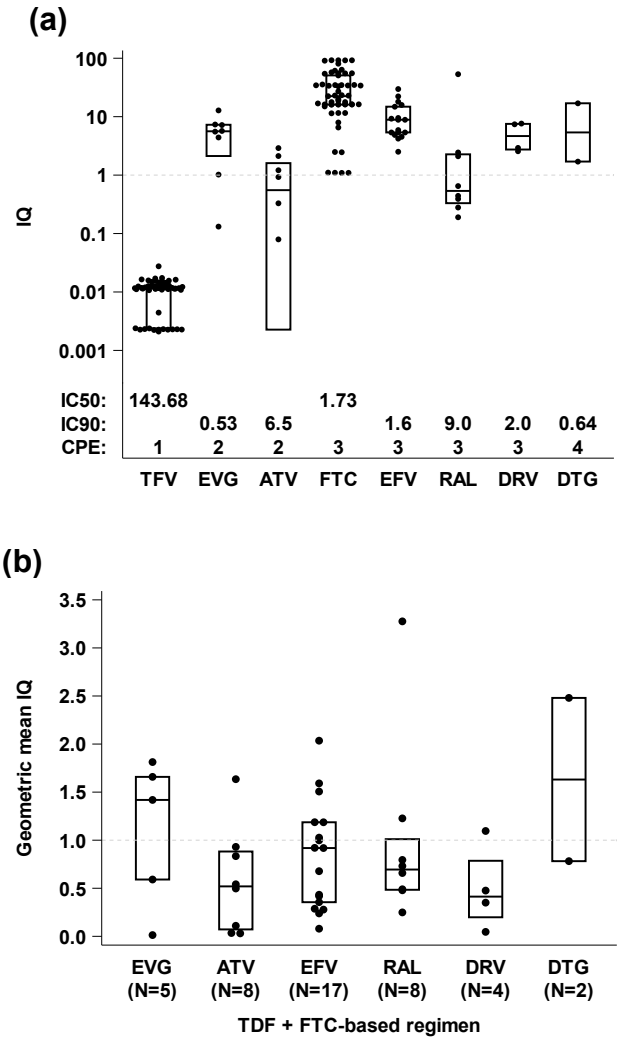


**Figure 25.** CSF IQ scores of each ARV (a) and ART-IQ GeoM CSF IQ (b). Inhibitory quotients were calculated as the ratio of the PK model-based trough concentrations to the literature-defined inhibitory concentrations shown in (a) (50% inhibitory concentrations were used to calculate the $IQ_{50}$ where 90% inhibitory concentrations were unavailable). IQs are plotted by the CPE score for their respective ARVs. Sensitivity analyses examined alternative approaches to combining information about the CNS penetration of the component ARVs for deriving a measure of the activity of the entire regimen.

Abbreviations: TFV, tenofovir disoproxil fumarate; FTC, emtricitabine; EFV, efavirenz; DTG, dolutegravir; RAL, raltegravir; EVG, elvitegravir; ATV, atazanavir; DRV, darunavir/ritonavir; IQ, inhibitory quotients; CSF, cerebrospinal fluid; CNS, central nervous system; IC, inhibitory concentration; CPE, CNS penetration effectiveness score; ARV, antiviral agent

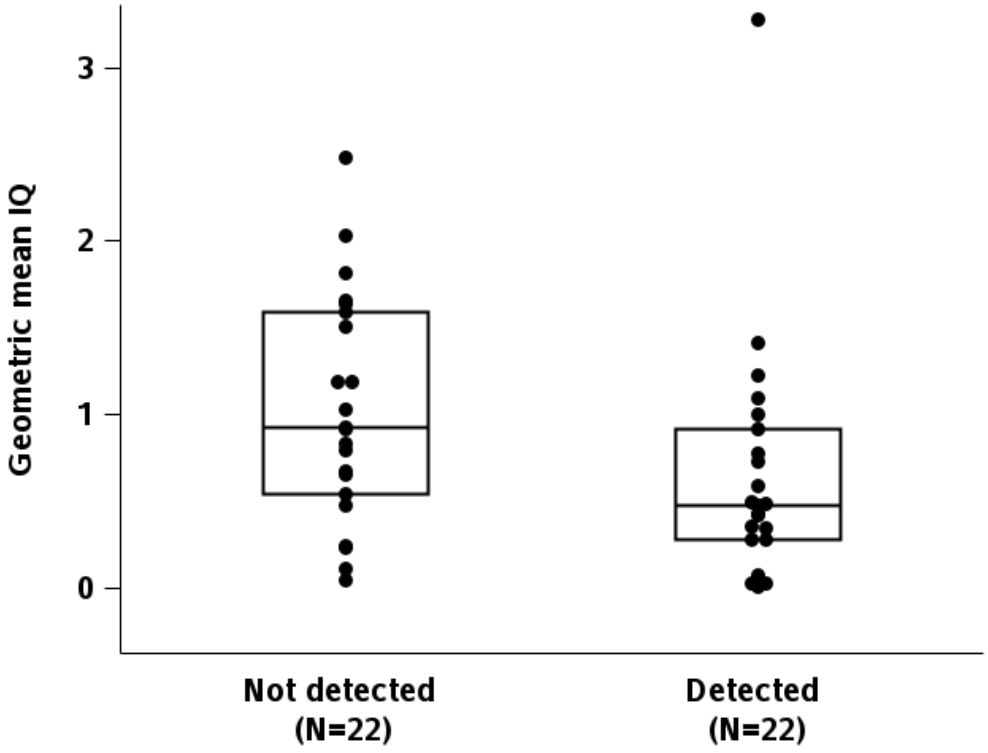


| | | CSF HIV DNA | | | |
|---|---|---|---|---|---|
| | | Total (N=44) | TND (N=22) | Detected (N=22) | P-Value* |
| $IQ_{50}$ for TFV $C_{trough}$ | Median | 0.01 | 0.01 | 0.01 | 0.17 |
| | Q1, Q3 | 0.00, 0.01 | 0.00, 0.01 | 0.00, 0.01 | |
| | Min, Max | 0.00, 0.02 | 0.00, 0.02 | 0.00, 0.02 | |
| $IQ_{50}$ for FTC $C_{trough}$ | Median | 21.1 | 28.0 | 17.0 | 0.20 |
| | Q1, Q3 | 15.5, 54.7 | 16.2, 54.3 | 6.5, 55.0 | |
| | Min, Max | 1.1, 92.2 | 1.1, 92.2 | 1.1, 80.5 | |
| $IQ_{90}$ for 3rd drug $C_{trough}$ | Median | 4.4 | 3.7 | 4.8 | 0.87 |
| | Q1, Q3 | 1.0, 8.8 | 1.2, 9.5 | 0.9, 7.6 | |
| | Min, Max | 0.0, 53.3 | 0.1, 22.2 | 0.0, 53.3 | |
| Arithmetic mean IQ | Median | 10.8 | 11.5 | 7.5 | 0.16 |
| | Q1, Q3 | 6.2, 18.6 | 8.2, 18.9 | 5.7, 18.4 | |
| | Min, Max | 2.2, 36.2 | 2.2, 32.5 | 2.2, 36.2 | |
| Geometric mean IQ | Median | 0.7 | 0.9 | 0.5 | 0.027 |
| | Q1, Q3 | 0.4, 1.2 | 0.5, 1.6 | 0.3, 0.9 | |
| | Min, Max | 0.0, 3.3 | 0.0, 2.5 | 0.0, 3.3 | |

*Exact Wilcoxon Test

**Figure 26.** IQ-GeoM and CSF HIV DNA detection. ART-IQ-GeoM was higher in those with undetectable vs detectable CSF HIV DNA (0.9 [0.5, 1.6] vs 0.5 [0.3, 0.9], p=0.027

**Table 10**. ARV pharmacologic characteristics and CSF exposure

| Drug Class | Plasma Protein Binding (%) | Protein Free $IC_{50or90}$ (ng/mL) | CSF Concentration (ng/mL) Median values | CSF IQ | CPE[231, 232] | Ka^ |
|---|---|---|---|---|---|---|
| **NRTIs** | | | | | | |
| **Emtricitabine** [97, 248] | <4 | 1.7 | 68 | 0.97 | 3 | 0.53 |
| **Tenofovir Disoproxil Fumarate*** [97, 249] | <7 | 143.7 | 6 | 0.52 | 1 | 9 |
| **Lamivudine** [214, 250] | 16-36 | 21 | 95 | 4.5 | 2 | 4.6 |
| **NNRTIs** | | | | | | |
| **Efavirenz** [81, 98, 251] | 99.78 | 1.3 | 18.8 | 14.5 | 3 | 1.39 |
| **INSTIs** | | | | | | |
| **Dolutegravir** [81, 252] | >98.9 | 0.2 | 18.2 | 91 | 4[149, 281] | 2.24 |
| **Raltegravir** [81, 101, 253] | 83 | 3.2 | 31 | 9.7 | 3[281] | 0.723 |
| **Elvitegravir** [254] | >98 | 0.072 | 4.3 | 59.7 | 2 | 0.134 |
| **PIs** | | | | | | |
| **Atazanavir** [102, 255] | 86 | 1.7 | 7.9 | 4.65 | 2 | 1.81 |
| **Darunavir** [102, 256] | 95 | 0.67 | 30 | 75 | 3 | 1.04 |

*Based on active moiety of TFV, #extrapolated from raltegravir CPE score, ^fixed based off literature accepted values which can be found Drug Class column references. Tenofovir disoproxil fumarate and emtricitabine used $IC_{50}$ values, $IC_{90}$ was used for all other ARVs.

Abbreviations: NRTIs, Nucleoside reverse transcriptase inhibitors; NNRTIs, Non-nucleoside reverse transcriptase inhibitors; INSTIs, Integrase Strand Transfer Inhibitor; PIs, protease inhibitors; $IC_{50or90}$, inhibitory concentration at which 50% or 90% of in-vitro viral replication is inhibited; CSF, cerebrospinal fluid; IQ, inhibitory quotient; CPE, CNS penetration effectiveness score; NA, not available.

**Table 11.** Participant demographic variables for PK analysis (a) and viral PKPD Cohort outcome analysis (b)

(a)

| Demographic | Variable Name | Total |
|---|---|---|
| **Sex** | | **(N=74)** |
| **TDF/FTC groups:** | Male, number of patients (%) | 56 (95%) **n=59** |
| | Female | 3 (5%) |
| **Other groups^** | | 15 (100%) **n=15** |
| | | 0 (0%) |
| **Race/ethnicity** | White, number of patients (%) | 43 (73%) |
| | Black | 10 (17%) |
| | Hispanic | 4 (7%) |
| | American Indian/Alaskan Native | 2 (3%) |
| **Other groups^** | | 9 (60%) |
| | | 2 (13%) |
| | | 3 (20%) |
| | | 1 (7%) |
| **Age (years) at LP** | Median | 48 |
| | (IQR) | (40-55) |
| | [Min, Max] | [26, 72] |
| **Other groups^** | | 54 |
| | | (47-64) |
| | | [37-68] |
| **Years on ART at LP** | Median | 8.1 |
| | (IQR) | (6.2-9.3) |
| | [Min, Max | [2.3, 16.4] |
| **Other groups^** | | |
| **A5321: main ARVs in regimen modeled** | TDF, number of patients | 56# (n=59) |
| | FTC | 59 |
| | ABC/3TC | 11 (n=15) |
| | 3TC/ZDV | 2 |
| | 3TC only (w/DTG) | 1 |
| | ATV only (w/DTG) | 1 |
| **A5321: other ARVs in regimen (anchor) modeled** | EFV, number of patients | 19 **(N=74)** |
| | EVG (/c) | 10 |
| | DTG | 8 |
| | 3TC | 11 |
| | RAL | 9 |
| | ATV (/r) | 12 |
| | DRV (/r) | 5 |

(b)

| | | Total (N=44) |
|---|---|---|
| Sex | Male | 43 (98%) |
| | Female | 1 (2%) |
| Gender | N | 37 |
| | Male | 36 (97%) |
| | Female | 1 (3%) |
| Race/ethnicity | White Non-Hispanic | 33 (75%) |
| | Black Non-Hispanic | 6 (14%) |
| | Hispanic (Regardless of Race) | 4 (9%) |
| | American Indian, Alaskan Native | 1 (2%) |
| Age (years) at LP | N | 44 |
| | Median | 49 |
| | Q1, Q3 | 42, 57 |
| | Min, Max | 26, 72 |
| Years on ART at LP | N | 44 |
| | Median | 8.1 |
| | Q1, Q3 | 6.3, 9.4 |
| | Min, Max | 5.4, 16.4 |
| Other ARVs in regimen | EFV | 17 (39%) |
| | RAL | 8 (18%) |
| | RTV ATV | 8 (18%) |
| | EVG COBI | 5 (11%) |
| | RTV DRV | 4 (9%) |
| | DTG | 2 (5%) |
| Pre-ART CD4+ T-cell count (cells/mm$^3$) | N | 44 |
| | Median | 267 |
| | Q1, Q3 | 139, 316 |
| | Min, Max | 17, 533 |
| CD4+ T-cell count (cells/mm$^3$) most recent prior to LP | N | 44 |
| | Median | 642 |
| | Q1, Q3 | 498, 822 |
| | Min, Max | 240, 1,099 |
| Pre-ART CD4:CD8 ratio | N | 44 |
| | Median | 0.2 |
| | Q1, Q3 | 0.1, 0.4 |
| | Min, Max | 0.0, 1.3 |
| CD4:CD8 ratio most recent prior to LP | N | 44 |
| | Median | 1.0 |
| | Q1, Q3 | 0.7, 1.3 |
| | Min, Max | 0.4, 2.0 |
| Pre-ART plasma HIV-1 RNA ($log_{10}$cps/mL) | N | 44 |
| | Median | 4.7 |
| | Q1, Q3 | 4.5, 5.0 |
| | Min, Max | 3.7, 6.1 |
| Plasma HIV-1 RNA (cps/mL) most recent prior to LP | <40 | 43 (98%) |
| | ≥40 | 1 (2%) |

Abbreviations: EFV, efavirenz; DTG, dolutegravir; RAL, raltegravir; EVG, elvitegravir; ATV, atazanavir; DRV, darunavir/ritonavir; LP, lumbar puncture; ART, antiviral therapy

**Table 12.** Population PK parameter and NCA PK Parameter estimations

| ARV* | Estimated Population PK Parameters | | | | NCA PK Parameters for Plasma | |
|---|---|---|---|---|---|---|
| | Median (CV%) | | | | Median (IQR) | |
| Drugs/CLass | Vd/F (L) | Vcsf /F (L) | $Ke_{plasma}$ ($hr^{-1}$) | $CL_{plasma}$/F (L/hr) | Vd/F (L) | $CL_{plasma}$/F (L/hr) |
| **NRTIs** | | | | | | |
| **Emtricitabine**[248, 268] | 60.58 (50.78) | 122.32 (41.46) | - | 30.05 (59.79) | 264.4 (225.8-342.7) | 29.68 (26.67-42.86) |
| **Tenofovir (given as TDF)**[249, 269, 270] | 749.93 (11.70) | 499.96 (3.59) | 0.07 (96.1) | - | 598.3 (576.6-694.5) | 38.39 (34.82-71.89) |
| **Lamivudine**[250] | 437.398 (26.32) | 428.223 (16.58) | 0.067 (52.94) | | 414.2 (322.3-463.7) | 24.97 (15.91-35.48) |
| **NNRTIs** | | | | | | |
| **Efavirenz**[271, 272] | 170.742 (47.99) | 114.603 (36.53) | 0.056 (24.44) | - | 118.2 (70.41-155.6) | 6.61 (4.31-7.72) |
| **INSTIs** | | | | | | |
| **Dolutegravir**[252, 282] | 14.67 (40.53) | 288.09 (26.733) | 0.05 (51.07) | - | 10.28 (7.78-10.64) | 0.43 (0.41-0.62) |
| **Raltegravir**[253, 274, 275] | 329.785 (30.52) | 364.964 (35.44) | 0.282 (32.23) | - | 326.8 (179.6-388.6) | 82.94 (23.89-98.84) |
| **Elvitegravir/c***[254, 273] | 17.71 (63.11) | 310.665 (25.52) | 0.017 (187.83) | - | - | - |
| **PIs** | | | | | | |
| **Atazanavir/r**[276] | 176.012 (35.239) | 295.475 (19.429) | 0.045 (105.267) | - | 126.5 (94.18-175.9) | 7.203 (5.837-41.83) |
| **Darunavir/r**[277] | 235.239 (30.902) | 261.266 (25.63) | 0.054 (6.75) | | 170.5 (135.8-256.3) | 9.224 (6.59-12.73) |

Note: Summaries include all patients included in the models (PK Cohort). *Only CSF levels available

Abbreviations: NRTIs, Nucleoside reverse transcriptase inhibitors; NNRTIs, Non-nucleoside reverse transcriptase inhibitors; INSTIs, Integrase Strand Transfer Inhibitor; PIs, protease inhibitors; /r, ritonavir; c/, cobicistat

**Table 13.** ARV Exposure Summaries for all Participants

| ARV | Measured Concentration Median (IQR) | | Predicted Plasma Exposures Median (IQR) | | | Predicted CSF Exposures Median (IQR) | | | Median CSF Penetration based off exposures | CPE[231, 232] | $C_{Trough}$ / $I_{50 \text{ or } 90}$ (based off median values, ng/mL) |
|---|---|---|---|---|---|---|---|---|---|---|---|
| | Plasma (ng/mL) | CSF (ng/mL) | AUC (mg*h/L) | Cmax (ng/mL) | $C_{Trough}$ (ng/mL) | AUC (mg*h/L) | Cmax (ng/mL) | $C_{Trough}$ (ng/mL) | | | |
| **Emtricitabine[259] N=59** | 270 (120-560) | 90 (50-120) | 6.29 (4.521-6.563) | 920 (530-1180) | 22 (13-27) | 4.527 (3.37-6.46) | 426 (190-560) | 40 (28-95) | $C_{MAX}$:46.3% AUC:72% | 3 | Y 40 > 1.7 |
| **Tenofovir (TDF)[259, 283] N=56** | 90 (60-160) | 3 (2-5) | 2.8 (1.75-2.96) | 220 (156-230) | 50 (17.1-55) | 0.093 (0.056-0.098) | 7.3 (6.7-8) | 1.6 (0.3-1.8) | $C_{MAX}$: 3.33% AUC: 3.33% | 1 | N 1.6 < 143.7 |
| **Lamivudine[81] N=14** | 330 (250-570) | 85 (50-112) | 9.02 (7.31-12.88) | 680 (620-890) | 173 (99-290) | 2.39 (1.54-2.85) | 170 (110-200) | 49 (20-56) | $C_{MAX}$: 25% AUC: 26.53% | 2 | Y 49 > 21 |
| **Efavirenz[258] N=20** | 2500 (1820-3500) | 1.9 (1.3-30) | 69.79 (53.57-109.5) | 4540 (3430-7180) | 1320 (1100-2100) | 0.64 (0.38-1.02) | 41 (24-71) | 12 (8-22) | $C_{MAX}$: 0.90% AUC: 0.92% | 3 | Y 12 > 1.3 |
| **Dolutegravir[149] N=8** | 2290 (1790-2910) | 13 (10-14) | 71.76 (70.67-73.16) | 4400 (4330-4480) | 1790 (1763-1830) | 0.42 (0.41-0.42) | 25.4 (25.2-25.4) | 10.4 (10.18-10.8) | $C_{MAX}$:0.57% AUC: 0.57% | NA | Y 10.4 > 0.2 |
| **Raltegravir[284] N=9** | 480 (300-840) | 40 (20-40) | 4.49 (4.49-12.93) | 710 (600-1560) | 83.5 (70-530) | 0.31 (0.20-0.55) | 55 (32-67) | 5.8 (3-23) | $C_{MAX}$: 7.75% AUC: 6.90% | 3 | Y 5.8 > 3.2 |
| **Elvitegravir[285] N=8** | N/A | 2.7 (2-3) | N/A | N/A | N/A | 0.078 (0.026-0.010) | 3.4 (1.1-4.4) | 3 (0.95-3.9) | N/A | 3 | Y 3 > 0.072 |
| **Atazanavir[102] N=13** | 950 (490-1750) | 8 (4-10) | 28.64 (11.65-35.19) | 2150 (1330-2630) | 640 (51-790) | 0.349 (0.139-0.53) | 25 (10-43) | 4 (0.9-11) | $C_{MAX}$: 1.16% AUC: 1.22% | 2 | Y 04 > 1.7 |
| **Darunavir[72] N=5** | 1470 (1270-3140) | 20 (15-30) | 62.18 (44.59-82.91) | 4020 (2760-5180) | 1330 (1033-1880) | 0.62 (0.27-0.69) | 38 (18-43) | 15 (5.8-15) | $C_{MAX}$: 0.95% AUC: 1.00% | 3 | Y 15 > 0.67 |

*References for literature IC values listed next to drug name, ^TDF and FTC utilized $IC_{50}$ values, $IC_{90}$ was used for all other ARVs.

Abbreviations: CSF, cerebrospinal fluid; IQR, interquartile range (25%-75%); PL, plasma; AUC, area under the curve; $C_{MAX}$, maximum concentration predicted; $C_{Trough}$, minimum concentration predicted (based on interval); TDF, tenofovir disoproxil fumarate formulation; NA, not available; Y, yes; N, No

**Table 14.** Spearman rank-based correlations between CSF inflammatory biomarkers and ARV drug activity in the CSF

| | Arithmetic mean IQ | | | | Geometric mean IQ | | | |
|---|---|---|---|---|---|---|---|---|
| | Spearman | P-value | Partial Spearman | P-value | Spearman | P-value | Partial Spearman | P-value |
| CSF IL-6 (pg/mL) | 0.16 | 0.31 | 0.10 | 0.54 | 0.10 | 0.50 | 0.13 | 0.41 |
| CSF IP-10 (pg/mL) | 0.11 | 0.46 | 0.10 | 0.53 | -0.19 | 0.23 | -0.20 | 0.20 |
| CSF MCP-1 (pg/mL) | -0.02 | 0.87 | -0.23 | 0.14 | -0.26 | 0.08 | -0.27 | 0.08 |
| CSF neopterin (nMol/L) | 0.08 | 0.59 | 0.15 | 0.35 | 0.04 | 0.82 | 0.01 | 0.95 |
| CSF sCD14 (ng/mL) | 0.13 | 0.39 | 0.06 | 0.70 | 0.13 | 0.41 | 0.13 | 0.40 |
| CSF sCD163 (ng/mL) | 0.22 | 0.15 | 0.15 | 0.35 | -0.01 | 0.94 | -0.02 | 0.90 |

Abbreviations: IQ, inhibitory quotients; CSF, cerebrospinal fluid; IL, interleukin; IP, interferon gamma-induced protein; MCP, monocyte chemotactic protein; CD, cluster of differentiation

**Table 15.** Spearman rank-based correlation between GDS and measures of ARV drug activity in the CSF

| | IQ50 for TFV | | | IQ50 for FTC | | | IQ90 for 3rd drug | | | Arithmetic mean IQ | | | Geometric mean IQ | | |
|---|---|---|---|---|---|---|---|---|---|---|---|---|---|---|---|
| | N | Spearman | P-value | N | Spearman | P-value | N | Spearman | P-value | N | Spearman | P-value | N | Spearman | P-value |
| Mean GDS | 41 | -0.41 | 0.007 | 41 | -0.10 | 0.55 | 41 | -0.09 | 0.56 | 41 | -0.10 | 0.52 | 41 | **-0.30** | **0.05** |
| Fine motor GDS | 41 | -0.10 | 0.54 | 41 | 0.09 | 0.57 | 41 | -0.08 | 0.60 | 41 | 0.06 | 0.72 | 41 | -0.14 | 0.38 |
| Verbal learning GDS | 41 | -0.22 | 0.16 | 41 | -0.11 | 0.49 | 41 | 0.12 | 0.46 | 41 | -0.10 | 0.52 | 41 | -0.02 | 0.90 |
| Verbal memory GDS | 41 | -0.24 | 0.12 | 41 | -0.33 | 0.037 | 41 | 0.26 | 0.09 | 41 | -0.26 | 0.11 | 41 | -0.07 | 0.68 |
| Executive functioning GDS | 41 | -0.24 | 0.13 | 41 | -0.05 | 0.76 | 41 | -0.07 | 0.68 | 41 | -0.04 | 0.80 | 41 | -0.19 | 0.24 |
| Speed of processing GDS | 41 | -0.43 | 0.005 | 41 | -0.06 | 0.73 | 41 | -0.20 | 0.21 | 41 | -0.15 | 0.35 | 41 | -0.44 | 0.004 |
| Attention GDS | 41 | -0.22 | 0.16 | 41 | -0.08 | 0.60 | 41 | -0.01 | 0.97 | 41 | -0.02 | 0.92 | 41 | -0.17 | 0.28 |
| Language GDS | 39 | -0.10 | 0.53 | 39 | 0.27 | 0.09 | 39 | -0.33 | 0.041 | 39 | 0.22 | 0.17 | 39 | -0.24 | 0.15 |

Abbreviations: GDS, global deficit scores; IQ, inhibitory quotients

# Chapter 5: Summary, Conclusion and Future Directions

## 5.1 Summary of Overall Findings

Within the scope of this dissertation, new pharmacological insights into the PKPD of AVs to treat COVID-19 and HIV have been uncovered, aiming to elucidate the relationship between AV activity and penetration into the CNS. Chapter 2 introduces a novel 4-cell *in vitro* model developed to assess AV penetration, bypassing the need for invasive in vivo experiments or clinical sampling.

Chapter 3 delves into in vivo rodent experiments, demonstrating that NMR/r may not achieve adequate concentrations within the CNS to combat SARS-CoV-2 in the brain or CSF, a novel experimental finding recently published in Scientific Reports[181].

Chapter 4, drawing from the groundwork laid in ACTG 5321, shows how PK modeling can be a valuable tool for estimating CSF exposure based on non-standardized collection times, enabling the estimation of CSF penetration and the calculation of a regimen IQ for assessing virological endpoints or outcomes.

Cumulatively, these investigations have advanced methods and our understanding of antiviral PKPD in the CNS and provide the imperative for further research into viral reservoirs within the CNS, potentially reshaping the treatment landscape for CNS viral infections.

Detailed findings specific to the objectives and projects discussed in this dissertation will be discussed below.

The **first objective** was to develop a reliable *in vitro* cell model to estimate drug penetration into the BBB. Also in Chapter 2, methodology showing the successful development of a CNS 4-cell BBB model was described with confirmation of BBB integrity via TEER measurements and imaging to confirm TJ formation in the co-cultured cells. We found that addition of Zn increased the stability of the cell model and established TEER values at higher ranges compared to other conditions tested and controls. Further, for proof of concept, the ARV DTG was administered to the apical side of the 4-cell model at a concentration of 4000 ng/mL. After 48hrs media at the basal side was collected and quantified to estimate the concentration of DTG that passed through the cells. We found that ~11% of DTG was found on the basal side. As Zn increased the integrity and TEER values of our model, this was also confirmed by a decrease in 38% of DTG passing through the cells compared to experiments without Zn. As a DTG estimation of 11% may look inconsistent from clinical data (~1%), it is important to note that CSF levels of DTG and BBB penetration are not the same. Drugs collected from the CSF pass through BCB which is made of different cells and formed of TJ that have lower TEER values than BBB TJ. Further, our model utilized media that only contained 5% albumin which would affect the amount of drug that could pass through each barrier. DTG is highly protein bound and only free drug would be able to cross the BBB and BCB. Future work includes testing conditions that resemble similar protein conditions to human blood to compare and contrast differences seen in penetration of AVs.

The **second objective** was to determine if NMR can penetrate the CNS at adequate concentrations to treat SARS-CoV-2. Chapter 3 shows data from our animal work where we dosed 10 rats with an allometrically scaled dose of NMR/r to determine if

it can be detected in CSF, BBB cells, and brain tissue. Secondarily, we also looked at other tissues, PBMCs, and blood to compare to available literature and probe questions about NMR's ability to concentrate in different parts of the body. Our results showed that based on PD protein adjusted and unadjusted EC values for SARS-CoV-2 (based on the EPIC-HR FDA document)[197], NMR concentrations are not optimal to treat CNS viral infection. This was further showcased by undetectable brain tissue concentrations of NMR in the 10 rats. This brings to question whether NMR treatment can be optimized to ensure adequate concentrations are maintained to effectively treat virus potentially found in the brain. This also could explain why patients that are treated with NMR/r still develop neuroPASC ("Long COVID").

The **third objective**, which was broken up into 2 parts, was to (A) Utilize PK modeling to standardize ART exposure to allow for more accurate calculation of an IQ ratio and CSF penetration, and (B) Develop a regimen IQ for ART and correlate it with viral PD outcomes (i.e., viral DNA, inflammation, GSD score) in patients. As described in Chapter 4, population PK modeling allowed for standardization of ARV levels to allow for accurate CSF penetration estimation. This was confirmed by the agreement of our ARV CSF penetration with other studies and CPE score. Further, our regimen calculated $IQ_{geoM}$ showed that higher regimen $IQ_{geoM}$ ratios resulted in a higher number of patients that had undetectable CSF viral DNA. We found that biomarkers of inflammation were not associated with the regimen $IQ_{geoM}$. We think this is likely due to the specific inflammatory biomarkers evaluated and the fact that these participants were virally suppressed for many years on ART. Last, we found that higher $IQ_{geoM}$ was associated with better GSD scores. We are excited to further evaluate these findings in multiple manuscripts.

## 5.2 Limitations

There are limitations from the data derived from the studies described in this dissertation. First, drug penetration into the CNS is highly regulated by transporters found on cells of the BBB and BCB. Unfortunately, this was something we were not able to account for or control for (all studies discussed in this dissertation). However, work and experiments are ongoing to capture transporter expressions (especially efflux transporters) in the 4-cell model. Further, there are plans to incorporate PBPK modeling so that a more quantitative systems pharmacology approach can be applied which can account for transporter effects. Also, the 4-cell model represents a static model where the drug is administered at a $C_{max}$ equivalent concentration. Unfortunately, this fails to capture drug elimination and the dynamic flow of drug from the blood to the CNS. As such, plans to develop a 4-cell microfluidic CNS model are in progress. This will allow us to probe the same questions of drug penetration in more physiologically relevant conditions. Next, our in vivo work for NMR penetration utilized uninfected rats with implanted CSF catheters. As they were uninfected, it is difficult to know the effects of virus on the BBB and BCB integrity. Studies have shown that inflammation can cause barriers to become leaky. Rats are resilient to SARS-CoV-2 given they do not express ACE-2 receptors in abundance. Plans to repeat the same experiment discussed in Chapter 3 with the GSH model are ongoing. On the topic of transporters, it is known that different species of animal express different transporters at different sites. While rats and humans do express similar efflux transporters at the level of the CNS, some subtle differences do exist. Regardless of these differences, our allometric scaling showed similar exposure profiles to humans (as discussed in greater detail in Chapter 3) which provides evidence to support our dosing strategy in the animals. Last, Chapter 4 showcased methodology to estimate CSF exposure in participants from A5321 who had sparse sampling from the CSF. This is

common clinically given the invasiveness of CSF sample collection. Nonetheless, our PK modeling allowed us to standardize exposure profiles for all participants so that more direct comparisons could be made.

## 5.3 Future Directions

There is an ongoing need for CNS penetration studies to be conducted evaluating the potential to treat CNS related infections. This need is not specific for infectious diseases and is important for many other areas of pharmacology (i.e., oncology, stroke, epilepsy). The NIH has made it a priority to evaluate these questions with special RFAs for both COVID-19 and NeuroHIV. The US Department of Health and Human Services recently announced the formation of the Office of Long COVID Research and Practice and the launch of Long COVID clinical trials through the RECOVR initiative. Several clinical trials are currently ongoing looking at using NMR/r/r as a treatment strategy for persons highly symptomatic with Long COVID. In one of these ongoing trials, they are using NMR/r for 15-days at the current dose to see if this treatment will provide relief in those suffering with Long COVID. To date, the NMR data generated within this dissertation remains the only CSF PK data available. As the field of neuropharmacology moves toward newer treatments and better strategies, more therapies will need rapid and rigorous evaluation for their ability to penetrate the CNS and treat CNS related infections. This dissertation describes tools and approaches that will be useful in meeting these needs.

**References**


1. Anatomy, Central Nervous System. StatPearls. 2024.
2. Viscusi ER, Viscusi AR. Blood-brain barrier: mechanisms governing permeability and interaction with peripherally acting μ-opioid receptor antagonists. Reg Anesth Pain Med. 2020;45(9):688-95. Epub 20200728. doi: 10.1136/rapm-2020-101403. PubMed PMID: 32723840; PMCID: PMC7476292.
3. Daneman R, Prat A. The blood-brain barrier. Cold Spring Harb Perspect Biol. 2015;7(1):a020412. Epub 20150105. doi: 10.1101/cshperspect.a020412. PubMed PMID: 25561720; PMCID: PMC4292164.
4. Obermeier B, Daneman R, Ransohoff RM. Development, maintenance and disruption of the blood-brain barrier. Nat Med. 2013;19(12):1584-96. Epub 20131205. doi: 10.1038/nm.3407. PubMed PMID: 24309662; PMCID: PMC4080800.
5. Johansen A, Hansen HD, Svarer C, Lehel S, Leth-Petersen S, Kristensen JL, Gillings N, Knudsen GM. The importance of small polar radiometabolites in molecular neuroimaging: A PET study with [(11)C]Cimbi-36 labeled in two positions. J Cereb Blood Flow Metab. 2018;38(4):659-68. doi: 10.1177/0271678X17746179. PubMed PMID: 29215308; PMCID: PMC5888860.
6. Alahmari A. Blood-Brain Barrier Overview: Structural and Functional Correlation. Neural Plast. 2021;2021:6564585. Epub 20211206. doi: 10.1155/2021/6564585. PubMed PMID: 34912450; PMCID: PMC8668349.
7. Abbott NJ. Dynamics of CNS barriers: evolution, differentiation, and modulation. Cell Mol Neurobiol. 2005;25(1):5-23. doi: 10.1007/s10571-004-1374-y. PubMed PMID: 15962506.
8. Armulik A, Genové G, Betsholtz C. Pericytes: developmental, physiological, and pathological perspectives, problems, and promises. Dev Cell. 2011;21(2):193-215. doi: 10.1016/j.devcel.2011.07.001. PubMed PMID: 21839917.
9. Wolburg H, Noell S, Wolburg-Buchholz K, Mack A, Fallier-Becker P. Agrin, aquaporin-4, and astrocyte polarity as an important feature of the blood-brain barrier. Neuroscientist. 2009;15(2):180-93. doi: 10.1177/1073858408329509. PubMed PMID: 19307424.
10. Sofroniew MV, Vinters HV. Astrocytes: biology and pathology. Acta Neuropathol. 2010;119(1):7-35. Epub 20091210. doi: 10.1007/s00401-009-0619-8. PubMed PMID: 20012068; PMCID: PMC2799634.
11. Stamatovic SM, Johnson AM, Keep RF, Andjelkovic AV. Junctional proteins of the blood-brain barrier: New insights into function and dysfunction. Tissue Barriers. 2016;4(1):e1154641. Epub 20160226. doi: 10.1080/21688370.2016.1154641. PubMed PMID: 27141427; PMCID: PMC4836471.
12. Berndt P, Winkler L, Cording J, Breitkreuz-Korff O, Rex A, Dithmer S, Rausch V, Blasig R, Richter M, Sporbert A, Wolburg H, Blasig IE, Haseloff RF. Tight junction proteins at the blood-brain barrier: far more than claudin-5. Cell Mol Life Sci. 2019;76(10):1987-2002. Epub 20190207. doi: 10.1007/s00018-019-03030-7. PubMed PMID: 30734065.
13. Sasson E, Anzi S, Bell B, Yakovian O, Zorsky M, Deutsch U, Engelhardt B, Sherman E, Vatine G, Dzikowski R, Ben-Zvi A. Nano-scale architecture of blood-brain barrier tight-junctions. Elife. 2021;10. Epub 20211224. doi: 10.7554/eLife.63253. PubMed PMID: 34951586; PMCID: PMC8747500.
14. Furtado D, Björnmalm M, Ayton S, Bush AI, Kempe K, Caruso F. Overcoming the Blood-Brain Barrier: The Role of Nanomaterials in Treating Neurological Diseases. Adv Mater. 2018;30(46):e1801362. Epub 20180731. doi: 10.1002/adma.201801362. PubMed PMID: 30066406.

15. Bernacki J, Dobrowolska A, Nierwińska K, Małecki A. Physiology and pharmacological role of the blood-brain barrier. Pharmacol Rep. 2008;60(5):600-22. PubMed PMID: 19066407.
16. Srinivasan B, Kolli AR, Esch MB, Abaci HE, Shuler ML, Hickman JJ. TEER measurement techniques for in vitro barrier model systems. J Lab Autom. 2015;20(2):107-26. Epub 20150113. doi: 10.1177/2211068214561025. PubMed PMID: 25586998; PMCID: PMC4652793.
17. Engelhardt B, Sorokin L. The blood-brain and the blood-cerebrospinal fluid barriers: function and dysfunction. Semin Immunopathol. 2009;31(4):497-511. Epub 20090925. doi: 10.1007/s00281-009-0177-0. PubMed PMID: 19779720.
18. Nakagawa S, Deli MA, Kawaguchi H, Shimizudani T, Shimono T, Kittel A, Tanaka K, Niwa M. A new blood-brain barrier model using primary rat brain endothelial cells, pericytes and astrocytes. Neurochem Int. 2009;54(3-4):253-63. Epub 20081207. doi: 10.1016/j.neuint.2008.12.002. PubMed PMID: 19111869.
19. Kadry H, Noorani B, Cucullo L. A blood-brain barrier overview on structure, function, impairment, and biomarkers of integrity. Fluids Barriers CNS. 2020;17(1):69. Epub 20201118. doi: 10.1186/s12987-020-00230-3. PubMed PMID: 33208141; PMCID: PMC7672931.
20. Abbott NJ, Rönnbäck L, Hansson E. Astrocyte-endothelial interactions at the blood-brain barrier. Nat Rev Neurosci. 2006;7(1):41-53. doi: 10.1038/nrn1824. PubMed PMID: 16371949.
21. Wolburg H, Wolburg-Buchholz K, Fallier-Becker P, Noell S, Mack AF. Structure and functions of aquaporin-4-based orthogonal arrays of particles. Int Rev Cell Mol Biol. 2011;287:1-41. doi: 10.1016/B978-0-12-386043-9.00001-3. PubMed PMID: 21414585.
22. Morris ME, Rodriguez-Cruz V, Felmlee MA. SLC and ABC Transporters: Expression, Localization, and Species Differences at the Blood-Brain and the Blood-Cerebrospinal Fluid Barriers. Aaps J. 2017;19(5):1317-31. Epub 20170629. doi: 10.1208/s12248-017-0110-8. PubMed PMID: 28664465; PMCID: PMC6467070.
23. Löscher W, Potschka H. Blood-brain barrier active efflux transporters: ATP-binding cassette gene family. NeuroRx. 2005;2(1):86-98. doi: 10.1602/neurorx.2.1.86. PubMed PMID: 15717060; PMCID: PMC539326.
24. Sun H, Dai H, Shaik N, Elmquist WF. Drug efflux transporters in the CNS. Adv Drug Deliv Rev. 2003;55(1):83-105. doi: 10.1016/s0169-409x(02)00172-2. PubMed PMID: 12535575.
25. Demeule M, Régina A, Jodoin J, Laplante A, Dagenais C, Berthelet F, Moghrabi A, Béliveau R. Drug transport to the brain: key roles for the efflux pump P-glycoprotein in the blood-brain barrier. Vascul Pharmacol. 2002;38(6):339-48. doi: 10.1016/s1537-1891(02)00201-x. PubMed PMID: 12529928.
26. Cisternino S, Mercier C, Bourasset F, Roux F, Scherrmann JM. Expression, up-regulation, and transport activity of the multidrug-resistance protein Abcg2 at the mouse blood-brain barrier. Cancer Res. 2004;64(9):3296-301. doi: 10.1158/0008-5472.can-03-2033. PubMed PMID: 15126373.
27. Agarwal S, Hartz AM, Elmquist WF, Bauer B. Breast cancer resistance protein and P-glycoprotein in brain cancer: two gatekeepers team up. Curr Pharm Des. 2011;17(26):2793-802. doi: 10.2174/138161211797440186. PubMed PMID: 21827403; PMCID: PMC3269897.
28. Power EA, Rechberger JS, Gupta S, Schwartz JD, Daniels DJ, Khatua S. Drug delivery across the blood-brain barrier for the treatment of pediatric brain tumors - An update. Adv Drug Deliv Rev. 2022;185:114303. Epub 20220421. doi: 10.1016/j.addr.2022.114303. PubMed PMID: 35460714.

29. Neumaier F, Zlatopolskiy BD, Neumaier B. Drug Penetration into the Central Nervous System: Pharmacokinetic Concepts and In Vitro Model Systems. Pharmaceutics. 2021;13(10). Epub 20210923. doi: 10.3390/pharmaceutics13101542. PubMed PMID: 34683835; PMCID: PMC8538549.
30. Holshue ML, DeBolt C, Lindquist S, Lofy KH, Wiesman J, Bruce H, Spitters C, Ericson K, Wilkerson S, Tural A, Diaz G, Cohn A, Fox L, Patel A, Gerber SI, Kim L, Tong S, Lu X, Lindstrom S, Pallansch MA, Weldon WC, Biggs HM, Uyeki TM, Pillai SK, Team WS-nCI. First Case of 2019 Novel Coronavirus in the United States. N Engl J Med. 2020;382(10):929-36. Epub 20200131. doi: 10.1056/NEJMoa2001191. PubMed PMID: 32004427; PMCID: PMC7092802.
31. Yao XH, Li TY, He ZC, Ping YF, Liu HW, Yu SC, Mou HM, Wang LH, Zhang HR, Fu WJ, Luo T, Liu F, Chen C, Xiao HL, Guo HT, Lin S, Xiang DF, Shi Y, Li QR, Huang X, Cui Y, Li XZ, Tang W, Pan PF, Huang XQ, Ding YQ, Bian XW. [A pathological report of three COVID-19 cases by minimally invasive autopsies]. Zhonghua Bing Li Xue Za Zhi. 2020;49(0):E009. doi: 10.3760/cma.j.cn112151-20200312-00193. PubMed PMID: 32172546.
32. Callard F, Perego E. How and why patients made Long Covid. Soc Sci Med. 2021;268:113426. Epub 20201007. doi: 10.1016/j.socscimed.2020.113426. PubMed PMID: 33199035; PMCID: PMC7539940.
33. Long COVID or Post-COVID Conditions. Symptoms. Available at: https://www.cdc.gov/coronavirus/2019-ncov/long-term-effects/index.html.
34. Soriano JB, Murthy S, Marshall JC, Relan P, Diaz JV, Condition WCCDWGoP-C-. A clinical case definition of post-COVID-19 condition by a Delphi consensus. Lancet Infect Dis. 2022;22(4):e102-e7. Epub 20211221. doi: 10.1016/S1473-3099(21)00703-9. PubMed PMID: 34951953; PMCID: PMC8691845.
35. Moghimi N, Di Napoli M, Biller J, Siegler JE, Shekhar R, McCullough LD, Harkins MS, Hong E, Alaouieh DA, Mansueto G, Divani AA. The Neurological Manifestations of Post-Acute Sequelae of SARS-CoV-2 infection. Curr Neurol Neurosci Rep. 2021;21(9):44. Epub 20210628. doi: 10.1007/s11910-021-01130-1. PubMed PMID: 34181102; PMCID: PMC8237541.
36. Long COVID or Post-COVID Conditions. Symptoms. https://www.cdc.gov/coronavirus/2019-ncov/long-term-effects/index.html. Updated July 20, 2023. Accessed August 4, 2023.
37. Pandey K, Thurman M, Johnson SD, Acharya A, Johnston M, Klug EA, Olwenyi OA, Rajaiah R, Byrareddy SN. Mental Health Issues During and After COVID-19 Vaccine Era. Brain Res Bull. 2021;176:161-73. Epub 20210903. doi: 10.1016/j.brainresbull.2021.08.012. PubMed PMID: 34487856; PMCID: PMC8414813.
38. Shanley JE, Valenciano AF, Timmons G, Miner AE, Kakarla V, Rempe T, Yang JH, Gooding A, Norman MA, Banks SJ, Ritter ML, Ellis RJ, Horton L, Graves JS. Longitudinal evaluation of neurologic-post acute sequelae SARS-CoV-2 infection symptoms. Ann Clin Transl Neurol. 2022;9(7):995-1010. Epub 20220615. doi: 10.1002/acn3.51578. PubMed PMID: 35702954; PMCID: PMC9268882.
39. Goërtz YMJ, Van Herck M, Delbressine JM, Vaes AW, Meys R, Machado FVC, Houben-Wilke S, Burtin C, Posthuma R, Franssen FME, van Loon N, Hajian B, Spies Y, Vijlbrief H, van 't Hul AJ, Janssen DJA, Spruit MA. Persistent symptoms 3 months after a SARS-CoV-2 infection: the post-COVID-19 syndrome? ERJ Open Res. 2020;6(4). Epub 20201026. doi: 10.1183/23120541.00542-2020. PubMed PMID: 33257910; PMCID: PMC7491255.
40. Malik JR, Acharya A, Avedissian SN, Byrareddy SN, Fletcher CV, Podany AT, Dyavar SR. ACE-2, TMPRSS2, and Neuropilin-1 Receptor Expression on Human Brain

Astrocytes and Pericytes and SARS-CoV-2 Infection Kinetics. International Journal of Molecular Sciences. 2023;24(10):8622. PubMed PMID: doi:10.3390/ijms24108622.
41. Desforges M, Le Coupanec A, Dubeau P, Bourgouin A, Lajoie L, Dube M, Talbot PJ. Human Coronaviruses and Other Respiratory Viruses: Underestimated Opportunistic Pathogens of the Central Nervous System? Viruses. 2019;12(1). doi: 10.3390/v12010014. PubMed PMID: 31861926; PMCID: PMC7020001.
42. Gholami M, Safari S, Ulloa L, Motaghinejad M. Neuropathies and neurological dysfunction induced by coronaviruses. J Neurovirol. 2021;27(3):380-96. Epub 20210513. doi: 10.1007/s13365-021-00977-x. PubMed PMID: 33983506; PMCID: PMC8117458.
43. Acharya A, Kevadiya BD, Gendelman HE, Byrareddy SN. SARS-CoV-2 Infection Leads to Neurological Dysfunction. J Neuroimmune Pharmacol. 2020;15(2):167-73. Epub 20200523. doi: 10.1007/s11481-020-09924-9. PubMed PMID: 32447746; PMCID: PMC7244399.
44. Nuzzo D, Cambula G, Bacile I, Rizzo M, Galia M, Mangiapane P, Picone P, Giacomazza D, Scalisi L. Long-Term Brain Disorders in Post Covid-19 Neurological Syndrome (PCNS) Patient. Brain Sci. 2021;11(4). Epub 20210402. doi: 10.3390/brainsci11040454. PubMed PMID: 33918426; PMCID: PMC8066611.
45. Pandey K, Rajaiah RR, Kumar KM, Ambikan AA, Guda RS, Cohen SC, Neogi UN, Byrareddy SNB. The 27th Scientific Conference of the Society on NeuroImmune Pharmacology: New Delhi, India, March 15–18, 2023. Differential Immunopathogenesis of Delta and Omicron Variants of SARS-CoV-2 in Golden Syrian Hamsters. Abstract #22. NeuroImmune Pharmacology and Therapeutics. 2023. doi: doi:10.1515/nipt-2023-0006.
46. Stein SR, Ramelli SC, Grazioli A, Chung JY, Singh M, Yinda CK, Winkler CW, Sun J, Dickey JM, Ylaya K, Ko SH, Platt AP, Burbelo PD, Quezado M, Pittaluga S, Purcell M, Munster VJ, Belinky F, Ramos-Benitez MJ, Boritz EA, Lach IA, Herr DL, Rabin J, Saharia KK, Madathil RJ, Tabatabai A, Soherwardi S, McCurdy MT, Peterson KE, Cohen JI, de Wit E, Vannella KM, Hewitt SM, Kleiner DE, Chertow DS, Consortium NC-A. SARS-CoV-2 infection and persistence in the human body and brain at autopsy. Nature. 2022;612(7941):758-63. Epub 20221214. doi: 10.1038/s41586-022-05542-y. PubMed PMID: 36517603; PMCID: PMC9749650.
47. Beckman D, Bonillas A, Diniz GB, Ott S, Roh JW, Elizaldi SR, Schmidt BA, Sammak RL, Van Rompay KKA, Iyer SS, Morrison JH. SARS-CoV-2 infects neurons and induces neuroinflammation in a non-human primate model of COVID-19. Cell Rep. 2022;41(5):111573. Epub 20221012. doi: 10.1016/j.celrep.2022.111573. PubMed PMID: 36288725; PMCID: PMC9554328.
48. de Melo GD, Perraud V, Alvarez F, Vieites-Prado A, Kim S, Kergoat L, Coleon A, Trüeb BS, Tichit M, Piazza A, Thierry A, Hardy D, Wolff N, Munier S, Koszul R, Simon-Lorière E, Thiel V, Lecuit M, Lledo PM, Renier N, Larrous F, Bourhy H. Neuroinvasion and anosmia are independent phenomena upon infection with SARS-CoV-2 and its variants. Nat Commun. 2023;14(1):4485. Epub 20230726. doi: 10.1038/s41467-023-40228-7. PubMed PMID: 37495586; PMCID: PMC10372078.
49. HHS opens new office to study long COVID response, NIH begins clinical trials. https://www.msn.com/en-us/health/medical/hhs-opens-new-office-to-study-long-covid-response-nih-begins-clinical-trials/ar-AA1eBBzW. Updated July 31, 2023. Accessed September 20, 2023.
50. NIH RECORD: Long Covid Clinical Trials Launch, Enrollment Opens. https://nihrecord.nih.gov/2023/08/18/long-covid-clinical-trials-launch-enrollment-opens. Updated August 18, 2023. Accessed September 1, 2023.
51. Fauci AS. HIV and AIDS: 20 years of science. Nat Med. 2003;9(7):839-43. doi: 10.1038/nm0703-839. PubMed PMID: 12835701.

52. Vynnycky E, Fine PE. The natural history of tuberculosis: the implications of age-dependent risks of disease and the role of reinfection. Epidemiol Infect. 1997;119(2):183-201. doi: 10.1017/s0950268897007917. PubMed PMID: 9363017; PMCID: PMC2808840.
53. Heaton RK, Clifford DB, Franklin DR, Jr., Woods SP, Ake C, Vaida F, Ellis RJ, Letendre SL, Marcotte TD, Atkinson JH, Rivera-Mindt M, Vigil OR, Taylor MJ, Collier AC, Marra CM, Gelman BB, McArthur JC, Morgello S, Simpson DM, McCutchan JA, Abramson I, Gamst A, Fennema-Notestine C, Jernigan TL, Wong J, Grant I, Group C. HIV-associated neurocognitive disorders persist in the era of potent antiretroviral therapy: CHARTER Study. Neurology. 2010;75(23):2087-96. doi: 10.1212/WNL.0b013e318200d727. PubMed PMID: 21135382; PMCID: PMC2995535.
54. Heaton RK, Velin RA, McCutchan JA, Gulevich SJ, Atkinson JH, Wallace MR, Godfrey HP, Kirson DA, Grant I. Neuropsychological impairment in human immunodeficiency virus-infection: implications for employment. HNRC Group. HIV Neurobehavioral Research Center. Psychosom Med. 1994;56(1):8-17. doi: 10.1097/00006842-199401000-00001. PubMed PMID: 8197319.
55. Saylor D, Dickens AM, Sacktor N, Haughey N, Slusher B, Pletnikov M, Mankowski JL, Brown A, Volsky DJ, McArthur JC. HIV-associated neurocognitive disorder - pathogenesis and prospects for treatment. Nat Rev Neurol. 2016;12(5):309. Epub 20160415. doi: 10.1038/nrneurol.2016.53. PubMed PMID: 27080521; PMCID: PMC5842923.
56. Gott C, Gates T, Dermody N, Brew BJ, Cysique LA. Cognitive change trajectories in virally suppressed HIV-infected individuals indicate high prevalence of disease activity. PLoS One. 2017;12(3):e0171887. doi: 10.1371/journal.pone.0171887. PubMed PMID: 28264037; PMCID: PMC5338778.
57. Estes JD, Kityo C, Ssali F, Swainson L, Makamdop KN, Del Prete GQ, Deeks SG, Luciw PA, Chipman JG, Beilman GJ, Hoskuldsson T, Khoruts A, Anderson J, Deleage C, Jasurda J, Schmidt TE, Hafertepe M, Callisto SP, Pearson H, Reimann T, Schuster J, Schoephoerster J, Southern P, Perkey K, Shang L, Wietgrefe SW, Fletcher CV, Lifson JD, Douek DC, McCune JM, Haase AT, Schacker TW. Defining total-body AIDS-virus burden with implications for curative strategies. Nat Med. 2017;23(11):1271-6. doi: 10.1038/nm.4411. PubMed PMID: 28967921; PMCID: PMC5831193.
58. Fletcher CV, Staskus K, Wietgrefe SW, Rothenberger M, Reilly C, Chipman JG, Beilman GJ, Khoruts A, Thorkelson A, Schmidt TE, Anderson J, Perkey K, Stevenson M, Perelson AS, Douek DC, Haase AT, Schacker TW. Persistent HIV-1 replication is associated with lower antiretroviral drug concentrations in lymphatic tissues. Proc Natl Acad Sci U S A. 2014;111(6):2307-12. Epub 2014/01/29. doi: 10.1073/pnas.1318249111. PubMed PMID: 24469825; PMCID: PMC3926074.
59. Balcom EF, Roda WC, Cohen EA, Li MY, Power C. HIV-1 persistence in the central nervous system: viral and host determinants during antiretroviral therapy. Curr Opin Virol. 2019;38:54-62. doi: 10.1016/j.coviro.2019.06.004. PubMed PMID: 31390580.
60. Winston A, Antinori A, Cinque P, Fox HS, Gisslen M, Henrich TJ, Letendre S, Persaud D, Price RW, Spudich S. Defining cerebrospinal fluid HIV RNA escape: editorial review AIDS. AIDS. 2019;33 Suppl 2:S107-S11. doi: 10.1097/QAD.0000000000002252. PubMed PMID: 31790376.
61. Perez-Valero I, Ellis R, Heaton R, Deutsch R, Franklin D, Clifford DB, Collier A, Gelman B, Marra C, McCutchan JA, Navis A, Sacktor N, Simpson D, Grant I, Letendre S. Cerebrospinal fluid viral escape in aviremic HIV-infected patients receiving antiretroviral therapy: prevalence, risk factors and neurocognitive effects. AIDS. 2019;33(3):475-81. doi: 10.1097/QAD.0000000000002074. PubMed PMID: 30702516; PMCID: PMC6361539.

62. Mastrangelo A, Turrini F, de Zan V, Caccia R, Gerevini S, Cinque P. Symptomatic cerebrospinal fluid escape. AIDS. 2019;33 Suppl 2:S159-S69. doi: 10.1097/QAD.0000000000002266. PubMed PMID: 31789816.
63. Spudich S, Robertson KR, Bosch RJ, Gandhi RT, Cyktor JC, Mar H, Macatangay BJ, Lalama CM, Rinaldo C, Collier AC, Godfrey C, Eron JJ, McMahon D, Jacobs JL, Koontz D, Hogg E, Vecchio A, Mellors JW. Persistent HIV-infected cells in cerebrospinal fluid are associated with poorer neurocognitive performance. J Clin Invest. 2019;129(8):3339-46. Epub 20190715. doi: 10.1172/JCI127413. PubMed PMID: 31305262; PMCID: PMC6668666.
64. Mangus LM, Beck SE, Queen SE, Brill SA, Shirk EN, Metcalf Pate KA, Muth DC, Adams RJ, Gama L, Clements JE, Mankowski JL. Lymphocyte-Dominant Encephalitis and Meningitis in Simian Immunodeficiency Virus-Infected Macaques Receiving Antiretroviral Therapy. Am J Pathol. 2018;188(1):125-34. doi: 10.1016/j.ajpath.2017.08.035. PubMed PMID: 29229308; PMCID: PMC5745520.
65. Avalos CR, Abreu CM, Queen SE, Li M, Price S, Shirk EN, Engle EL, Forsyth E, Bullock BT, Mac Gabhann F, Wietgrefe SW, Haase AT, Zink MC, Mankowski JL, Clements JE, Gama L. Brain Macrophages in Simian Immunodeficiency Virus-Infected, Antiretroviral-Suppressed Macaques: a Functional Latent Reservoir. mBio. 2017;8(4). doi: 10.1128/mBio.01186-17. PubMed PMID: 28811349; PMCID: PMC5559639.
66. COVID-19 Treatment Guidelines Panel. Coronavirus Disease 2019 (COVID-19) Treatment Guidelines. National Institutes of Health. https://www.covid19treatmentguidelines.nih.gov/. Updated October 10, 2023. Accessed October 1, 2023.
67. Department of Health and Human Services. Guidelines for the Use of Antiretroviral Agents in Adults and Adolescents with HIV Developed by the DHHS Panel on Antiretroviral Guidelines for Adults and Adolescents-A Working Group of the Office of AIDS Research Advisory Council (OARAC) How to Cite the Adult and Adolescent Guidelines: Panel on Antiretroviral Guidelines for Adults and Adolescents. Guidelines for the Use of Antiretroviral Agents in Adults and. Available at: http://hivinfo.nih.gov. Accessed 8 April 2024.
68. Ene L, Duiculescu D, Ruta SM. How much do antiretroviral drugs penetrate into the central nervous system? J Med Life. 2011;4(4):432-9. PubMed PMID: 22514580; PMCID: PMC3227164.
69. Ocque AJ, Hagler CE, Morse GD, Letendre SL, Ma Q. Development and validation of an LC-MS/MS assay for tenofovir and tenofovir alafenamide in human plasma and cerebrospinal fluid. J Pharm Biomed Anal. 2018;156:163-9. doi: 10.1016/j.jpba.2018.04.035. PubMed PMID: 29709783; PMCID: PMC5984727.
70. Takasawa K, Terasaki T, Suzuki H, Ooie T, Sugiyama Y. Distributed model analysis of 3'-azido-3'-deoxythymidine and 2',3'-dideoxyinosine distribution in brain tissue and cerebrospinal fluid. J Pharmacol Exp Ther. 1997;282(3):1509-17. PubMed PMID: 9316866.
71. Letendre S, Marquie-Beck J, Capparelli E, Best B, Clifford D, Collier AC, Gelman BB, McArthur JC, McCutchan JA, Morgello S, Simpson D, Grant I, Ellis RJ, Group C. Validation of the CNS Penetration-Effectiveness rank for quantifying antiretroviral penetration into the central nervous system. Arch Neurol. 2008;65(1):65-70. doi: 10.1001/archneurol.2007.31. PubMed PMID: 18195140; PMCID: PMC2763187.
72. Bartels H, Decosterd L, Battegay M, Marzolini C. Darunavir concentrations in CSF of HIV-infected individuals when boosted with cobicistat versus ritonavir. J Antimicrob Chemother. 2017;72(9):2574-7. doi: 10.1093/jac/dkx165. PubMed PMID: 28575323.
73. Best BM, Letendre SL, Brigid E, Clifford DB, Collier AC, Gelman BB, McArthur JC, McCutchan JA, Simpson DM, Ellis R, Capparelli EV, Grant I, Group C. Low atazanavir

concentrations in cerebrospinal fluid. AIDS. 2009;23(1):83-7. doi: 10.1097/QAD.0b013e328317a702. PubMed PMID: 19050389; PMCID: PMC2642983.
74. Capparelli EV, Holland D, Okamoto C, Gragg B, Durelle J, Marquie-Beck J, van den Brande G, Ellis R, Letendre S, Group H. Lopinavir concentrations in cerebrospinal fluid exceed the 50% inhibitory concentration for HIV. AIDS. 2005;19(9):949-52. doi: 10.1097/01.aids.0000171409.38490.48. PubMed PMID: 15905676.
75. DiCenzo R, DiFrancesco R, Cruttenden K, Donnelly J, Schifitto G. Lopinavir cerebrospinal fluid steady-state trough concentrations in HIV-infected adults. Ann Pharmacother. 2009;43(12):1972-7. doi: 10.1345/aph.1M399. PubMed PMID: 19934383.
76. Letendre S, Best B, Rossi S, Way L, Grant I, Ellis R, al. E. Therapeutic amprenavir and abacavir concentrations in CSF from the same individuals [abstract P_18], in 10th International Workshop on Clinical Pharmacology of HIV Therapy; 2009; Amsterdam, the Netherlands.
77. letendre S, FitzSimons C, Ellis R, Clifford D, Collier AC, Gelman B, McArthur J, Vaida F, Heaton RK. Grant I, and the CHARTER Group, Correlates of CSF Viral Loads in 1221 Volunteers of the CHARTER Cohort, in 17th Conference on Retroviruses and Opportunistic infections; 2010: San Francisco.
78. Tashima KT, Caliendo AM, Ahmad M, Gormley JM, Fiske WD, Brennan JM, Flanigan TP. Cerebrospinal fluid human immunodeficiency virus type 1 (HIV-1) suppression and efavirenz drug concentrations in HIV-1-infected patients receiving combination therapy. J Infect Dis. 1999;180(3):862-4. doi: 10.1086/314945. PubMed PMID: 10438381.
79. Srinivas N, Rosen EP, Gilliland WM, Jr., Kovarova M, Remling-Mulder L, De La Cruz G, White N, Adamson L, Schauer AP, Sykes C, Luciw P, Garcia JV, Akkina R, Kashuba ADM. Antiretroviral concentrations and surrogate measures of efficacy in the brain tissue and CSF of preclinical species. Xenobiotica. 2019;49(10):1192-201. doi: 10.1080/00498254.2018.1539278. PubMed PMID: 30346892; PMCID: PMC6579712.
80. Letendre SL, Mills A, Hagins D, Swindells S, Felizarta F, Devente J, Bettacchi C, Lou Y, Ford S, Sutton K, Shaik JS, Crauwels H, D'Amico R, Patel P. Pharmacokinetics and antiviral activity of cabotegravir and rilpivirine in cerebrospinal fluid following long-acting injectable administration in HIV-infected adults. J Antimicrob Chemother. 2020;75(3):648-55. doi: 10.1093/jac/dkz504. PubMed PMID: 31873746; PMCID: PMC7021098.
81. Calcagno A, Di Perri G, Bonora S. Pharmacokinetics and pharmacodynamics of antiretrovirals in the central nervous system. Clin Pharmacokinet. 2014;53(10):891-906. doi: 10.1007/s40262-014-0171-0. PubMed PMID: 25200312.
82. Tiraboschi J, Imaz A, Khoo S, Niubo J, Prieto P, Saumoy M, Penchala SD, Garcia B, Padilla C, Videla S, Podzamczer D. Total and Unbound Bictegravir Concentrations and Viral Suppression in Cerebrospinal Fluid of Human Immunodeficiency Virus-Infected Patients (Spanish HIV/AIDS Research Network, PreEC/RIS 56). J Infect Dis. 2020;221(9):1425-8. doi: 10.1093/infdis/jiz624. PubMed PMID: 31784745.
83. World Health Organization. Consolidated guidelines on HIV prevention, testing, treatment, service delivery and monitoring: recommendations for a public health approach. July 2021. Accessed May 29, 2024.
84. Nau R, Sorgel F, Eiffert H. Penetration of drugs through the blood-cerebrospinal fluid/blood-brain barrier for treatment of central nervous system infections. Clin Microbiol Rev. 2010;23(4):858-83. doi: 10.1128/CMR.00007-10. PubMed PMID: 20930076; PMCID: 2952976.
85. Dyavar SR, Gautam N, Podany AT, Winchester LC, Weinhold JA, Mykris TM, Campbell KM, Alnouti Y, Fletcher CV. Assessing the lymphoid tissue bioavailability of antiretrovirals in human primary lymphoid endothelial cells and in mice. J Antimicrob

Chemother. 2019;74(10):2974-8. doi: 10.1093/jac/dkz273. PubMed PMID: 31335938; PMCID: PMC6753470.
86. Lipinski CA. Lead- and drug-like compounds: the rule-of-five revolution. Drug Discov Today Technol. 2004;1(4):337-41. doi: 10.1016/j.ddtec.2004.11.007. PubMed PMID: 24981612.
87. Stepien KM, Tomaszewski M, Tomaszewska J, Czuczwar SJ. The multidrug transporter P-glycoprotein in pharmacoresistance to antiepileptic drugs. Pharmacol Rep. 2012;64(5):1011-9. doi: 10.1016/s1734-1140(12)70900-3. PubMed PMID: 23238460.
88. Nguyen A, Rossi S, Croteau D, Best BM, Clifford D, Collier AC, Gelman B, Marra C, McArthur J, McCutchan JA, Morgello S, Simpson D, Ellis RJ, Grant I, Capparelli E, Letendre S, Group C. Etravirine in CSF is highly protein bound. J Antimicrob Chemother. 2013;68(5):1161-8. doi: 10.1093/jac/dks517. PubMed PMID: 23335197; PMCID: PMC3625433.
89. Mykris TM, Weinhold J, Winchester LC, Scarsi KK, Fletcher CV, Podany AT, Avedissian SN. Quantification of nine antiretroviral drugs in cerebrospinal fluid: An approach to overcome sample collection tube adsorption. J Chromatogr B Analyt Technol Biomed Life Sci. 2023;1227:123810. Epub 20230630. doi: 10.1016/j.jchromb.2023.123810. PubMed PMID: 37429153.
90. Giacomini KM, Huang SM, Tweedie DJ, Benet LZ, Brouwer KL, Chu X, Dahlin A, Evers R, Fischer V, Hillgren KM, Hoffmaster KA, Ishikawa T, Keppler D, Kim RB, Lee CA, Niemi M, Polli JW, Sugiyama Y, Swaan PW, Ware JA, Wright SH, Yee SW, Zamek-Gliszczynski MJ, Zhang L, Consortium IT. Membrane transporters in drug development. Nat Rev Drug Discov. 2010;9(3):215-36. doi: 10.1038/nrd3028. PubMed PMID: 20190787; PMCID: PMC3326076.
91. Cattaneo D, Minisci D, Cozzi V, Riva A, Meraviglia P, Clementi E, Galli M, Gervasoni C. Dolutegravir plasma concentrations according to companion antiretroviral drug: unwanted drug interaction or desirable boosting effect? Antivir Ther. 2017;22(4):353-6. Epub 20161223. doi: 10.3851/IMP3119. PubMed PMID: 28008867.
92. Taneva E, Crooker K, Park SH, Su JT, Ott A, Cheshenko N, Szleifer I, Kiser PF, Frank B, Mesquita PM, Herold BC. Differential Mechanisms of Tenofovir and Tenofovir Disoproxil Fumarate Cellular Transport and Implications for Topical Preexposure Prophylaxis. Antimicrob Agents Chemother. 2015;60(3):1667-75. Epub 20151228. doi: 10.1128/AAC.02793-15. PubMed PMID: 26711762; PMCID: PMC4775922.
93. Kearney BP, Flaherty JF, Shah J. Tenofovir disoproxil fumarate: clinical pharmacology and pharmacokinetics. Clin Pharmacokinet. 2004;43(9):595-612. doi: 10.2165/00003088-200443090-00003. PubMed PMID: 15217303.
94. Roberts AG. The Structure and Mechanism of Drug Transporters. Methods Mol Biol. 2021;2342:193-234. doi: 10.1007/978-1-0716-1554-6_8. PubMed PMID: 34272696; PMCID: PMC8542452.
95. Rotondo JC, Martini F, Maritati M, Mazziotta C, Di Mauro G, Lanzillotti C, Barp N, Gallerani A, Tognon M, Contini C. SARS-CoV-2 Infection: New Molecular, Phylogenetic, and Pathogenetic Insights. Efficacy of Current Vaccines and the Potential Risk of Variants. Viruses. 2021;13(9). Epub 20210825. doi: 10.3390/v13091687. PubMed PMID: 34578269; PMCID: PMC8473168.
96. Capparelli EV, Letendre SL, Ellis RJ, Patel P, Holland D, McCutchan JA. Population pharmacokinetics of abacavir in plasma and cerebrospinal fluid. Antimicrob Agents Chemother. 2005;49(6):2504-6. doi: 10.1128/AAC.49.6.2504-2506.2005. PubMed PMID: 15917556; PMCID: PMC1140502.
97. Calcagno A, Bonora S, Simiele M, Rostagno R, Tettoni MC, Bonasso M, Romito A, Imperiale D, D'Avolio A, Di Perri G. Tenofovir and emtricitabine cerebrospinal fluid-to-

plasma ratios correlate to the extent of blood-brainbarrier damage. AIDS. 2011;25(11):1437-9. doi: 10.1097/QAD.0b013e3283489cb1. PubMed PMID: 21712657.
98. Avery LB, Sacktor N, McArthur JC, Hendrix CW. Protein-free efavirenz concentrations in cerebrospinal fluid and blood plasma are equivalent: applying the law of mass action to predict protein-free drug concentration. Antimicrob Agents Chemother. 2013;57(3):1409-14. doi: 10.1128/AAC.02329-12. PubMed PMID: 23295919; PMCID: PMC3591913.
99. Mora-Peris B, Watson V, Vera JH, Weston R, Waldman AD, Kaye S, Khoo S, Mackie NE, Back D, Winston A. Rilpivirine exposure in plasma and sanctuary site compartments after switching from nevirapine-containing combined antiretroviral therapy. J Antimicrob Chemother. 2014;69(6):1642-7. doi: 10.1093/jac/dku018. PubMed PMID: 24521854.
100. Biktarvy® [package insert]. Foster City, CA. Gilead Sciences, Inc. February 2018.
101. Calcagno A, Cusato J, Simiele M, Motta I, Audagnotto S, Bracchi M, D'Avolio A, Di Perri G, Bonora S. High interpatient variability of raltegravir CSF concentrations in HIV-positive patients: a pharmacogenetic analysis. J Antimicrob Chemother. 2014;69(1):241-5. doi: 10.1093/jac/dkt339. PubMed PMID: 23975735.
102. Delille CA, Pruett ST, Marconi VC, Lennox JL, Armstrong WS, Arrendale RF, Sheth AN, Easley KA, Acosta EP, Vunnava A, Ofotokun I. Effect of protein binding on unbound atazanavir and darunavir cerebrospinal fluid concentrations. J Clin Pharmacol. 2014;54(9):1063-71. doi: 10.1002/jcph.298. PubMed PMID: 24691856; PMCID: PMC4396178.
103. Croteau D, Best BM, Letendre S, Rossi SS, Ellis RJ, Clifford DB, Collier AC, Gelman BB, McArthur JC, McCutchan JA, Morgello S, Grant I, Group C. Lower than expected maraviroc concentrations in cerebrospinal fluid exceed the wild-type CC chemokine receptor 5-tropic HIV-1 50% inhibitory concentration. AIDS. 2012;26(7):890-3. doi: 10.1097/QAD.0b013e328351f627. PubMed PMID: 22313954; PMCID: PMC3454507.
104. Malik JR, Fletcher CV, Podany AT, Dyavar SR, Scarsi KK, Pais GM, Scheetz MH, Avedissian SN. A novel 4-cell in-vitro blood-brain barrier model and its characterization by confocal microscopy and TEER measurement. J Neurosci Methods. 2023;392:109867. Epub 20230426. doi: 10.1016/j.jneumeth.2023.109867. PubMed PMID: 37116621; PMCID: PMC10275325.
105. Malik JR, Modebelu UO, Fletcher CV, Podany AT, Scarsi KK, Byrareddy SN, Anand RK, Buch S, Sil S, Le J, Bradley JS, Brown AN, Sutar D, Avedissian SN. Establishment of a Four-Cell In Vitro Blood-Brain Barrier Model With Human Primary Brain Cells. Curr Protoc. 2024;4(6):e1067. doi: 10.1002/cpz1.1067. PubMed PMID: 38857108.
106. Cecchelli R, Berezowski V, Lundquist S, Culot M, Renftel M, Dehouck MP, Fenart L. Modelling of the blood-brain barrier in drug discovery and development. Nat Rev Drug Discov. 2007;6(8):650-61. doi: 10.1038/nrd2368. PubMed PMID: 17667956.
107. Liu WY, Wang ZB, Zhang LC, Wei X, Li L. Tight junction in blood-brain barrier: an overview of structure, regulation, and regulator substances. CNS Neurosci Ther. 2012;18(8):609-15. Epub 20120612. doi: 10.1111/j.1755-5949.2012.00340.x. PubMed PMID: 22686334; PMCID: PMC6493516.
108. Dörfel MJ, Huber O. Modulation of tight junction structure and function by kinases and phosphatases targeting occludin. J Biomed Biotechnol. 2012;2012:807356. Epub 20120123. doi: 10.1155/2012/807356. PubMed PMID: 22315516; PMCID: PMC3270569.
109. Aday S, Cecchelli R, Hallier-Vanuxeem D, Dehouck MP, Ferreira L. Stem Cell-Based Human Blood-Brain Barrier Models for Drug Discovery and Delivery. Trends Biotechnol. 2016;34(5):382-93. Epub 20160203. doi: 10.1016/j.tibtech.2016.01.001. PubMed PMID: 26838094.

110. Ghose AK, Viswanadhan VN, Wendoloski JJ. A knowledge-based approach in designing combinatorial or medicinal chemistry libraries for drug discovery. 1. A qualitative and quantitative characterization of known drug databases. J Comb Chem. 1999;1(1):55-68. doi: 10.1021/cc9800071. PubMed PMID: 10746014.
111. Hoshi Y, Uchida Y, Tachikawa M, Inoue T, Ohtsuki S, Terasaki T. Quantitative atlas of blood-brain barrier transporters, receptors, and tight junction proteins in rats and common marmoset. J Pharm Sci. 2013;102(9):3343-55. Epub 20130506. doi: 10.1002/jps.23575. PubMed PMID: 23650139.
112. Ito K, Uchida Y, Ohtsuki S, Aizawa S, Kawakami H, Katsukura Y, Kamiie J, Terasaki T. Quantitative membrane protein expression at the blood-brain barrier of adult and younger cynomolgus monkeys. J Pharm Sci. 2011;100(9):3939-50. Epub 20110119. doi: 10.1002/jps.22487. PubMed PMID: 21254069.
113. Nakagomi O, Uesugi S. [Molecular diagnosis and characterization of rotaviruses]. Rinsho Byori. 1990;Suppl 85:136-48. PubMed PMID: 2170707.
114. Uchida Y, Ohtsuki S, Katsukura Y, Ikeda C, Suzuki T, Kamiie J, Terasaki T. Quantitative targeted absolute proteomics of human blood-brain barrier transporters and receptors. J Neurochem. 2011;117(2):333-45. Epub 20110225. doi: 10.1111/j.1471-4159.2011.07208.x. PubMed PMID: 21291474.
115. Uchida Y, Tachikawa M, Obuchi W, Hoshi Y, Tomioka Y, Ohtsuki S, Terasaki T. A study protocol for quantitative targeted absolute proteomics (QTAP) by LC-MS/MS: application for inter-strain differences in protein expression levels of transporters, receptors, claudin-5, and marker proteins at the blood-brain barrier in ddY, FVB, and C57BL/6J mice. Fluids Barriers CNS. 2013;10(1):21. Epub 20130608. doi: 10.1186/2045-8118-10-21. PubMed PMID: 23758935; PMCID: PMC3691662.
116. Syvänen S, Lindhe O, Palner M, Kornum BR, Rahman O, Långström B, Knudsen GM, Hammarlund-Udenaes M. Species differences in blood-brain barrier transport of three positron emission tomography radioligands with emphasis on P-glycoprotein transport. Drug Metab Dispos. 2009;37(3):635-43. Epub 20081201. doi: 10.1124/dmd.108.024745. PubMed PMID: 19047468.
117. USDA National Agricultural Library. Animal Use Alternatives. available at: https://www.nal.usda.gov/animal-health-and-welfare/animal-use-alternatives.
118. FDA Modernization Act 2.0. 117th Congress. Accessed 1/31/2023. https://www.congress.gov/bill/117th-congress/senate-bill/5002.
119. Wadman M. FDA no longer has to require animal testing for new drugs. Science. 2023;379(6628):127-8. Epub 20230112. doi: 10.1126/science.adg6276. PubMed PMID: 36634170.
120. Ghaffarian R, Muro S. Models and methods to evaluate transport of drug delivery systems across cellular barriers. J Vis Exp. 2013(80):e50638. Epub 20131017. doi: 10.3791/50638. PubMed PMID: 24192611; PMCID: PMC3947959.
121. Santaguida S, Janigro D, Hossain M, Oby E, Rapp E, Cucullo L. Side by side comparison between dynamic versus static models of blood-brain barrier in vitro: a permeability study. Brain research. 2006;1109(1):1-13. Epub 20060720. doi: 10.1016/j.brainres.2006.06.027. PubMed PMID: 16857178.
122. Abbott NJ, Hughes CC, Revest PA, Greenwood J. Development and characterisation of a rat brain capillary endothelial culture: towards an in vitro blood-brain barrier. J Cell Sci. 1992;103 ( Pt 1):23-37. doi: 10.1242/jcs.103.1.23. PubMed PMID: 1429907.
123. Pardridge WM, Triguero D, Yang J, Cancilla PA. Comparison of in vitro and in vivo models of drug transcytosis through the blood-brain barrier. J Pharmacol Exp Ther. 1990;253(2):884-91. PubMed PMID: 2338660.

124. Weksler BB, Subileau EA, Perrière N, Charneau P, Holloway K, Leveque M, Tricoire-Leignel H, Nicotra A, Bourdoulous S, Turowski P, Male DK, Roux F, Greenwood J, Romero IA, Couraud PO. Blood-brain barrier-specific properties of a human adult brain endothelial cell line. FASEB journal : official publication of the Federation of American Societies for Experimental Biology. 2005;19(13):1872-4. Epub 20050901. doi: 10.1096/fj.04-3458fje. PubMed PMID: 16141364.
125. Sano Y, Shimizu F, Abe M, Maeda T, Kashiwamura Y, Ohtsuki S, Terasaki T, Obinata M, Kajiwara K, Fujii M, Suzuki M, Kanda T. Establishment of a new conditionally immortalized human brain microvascular endothelial cell line retaining an in vivo blood-brain barrier function. J Cell Physiol. 2010;225(2):519-28. doi: 10.1002/jcp.22232. PubMed PMID: 20458752.
126. Banks WA, Kovac A, Morofuji Y. Neurovascular unit crosstalk: Pericytes and astrocytes modify cytokine secretion patterns of brain endothelial cells. J Cereb Blood Flow Metab. 2018;38(6):1104-18. Epub 20171106. doi: 10.1177/0271678X17740793. PubMed PMID: 29106322; PMCID: PMC5998993.
127. Watanabe T, Dohgu S, Takata F, Nishioku T, Nakashima A, Futagami K, Yamauchi A, Kataoka Y. Paracellular barrier and tight junction protein expression in the immortalized brain endothelial cell lines bEND.3, bEND.5 and mouse brain endothelial cell 4. Biol Pharm Bull. 2013;36(3):492-5. doi: 10.1248/bpb.b12-00915. PubMed PMID: 23449334.
128. Rist RJ, Romero IA, Chan MW, Couraud PO, Roux F, Abbott NJ. F-actin cytoskeleton and sucrose permeability of immortalised rat brain microvascular endothelial cell monolayers: effects of cyclic AMP and astrocytic factors. Brain research. 1997;768(1-2):10-8. doi: 10.1016/s0006-8993(97)00586-6. PubMed PMID: 9369295.
129. Bagchi S, Chhibber T, Lahooti B, Verma A, Borse V, Jayant RD. In-vitro blood-brain barrier models for drug screening and permeation studies: an overview. Drug Des Devel Ther. 2019;13:3591-605. Epub 20191018. doi: 10.2147/DDDT.S218708. PubMed PMID: 31695329; PMCID: PMC6805046.
130. Stone NL, England TJ, O'Sullivan SE. A Novel Transwell Blood Brain Barrier Model Using Primary Human Cells. Front Cell Neurosci. 2019;13:230. Epub 2019/06/06. doi: 10.3389/fncel.2019.00230. PubMed PMID: 31244605; PMCID: PMC6563620.
131. Hind WH, Tufarelli C, Neophytou M, Anderson SI, England TJ, O'Sullivan SE. Endocannabinoids modulate human blood-brain barrier permeability in vitro. Br J Pharmacol. 2015;172(12):3015-27. Epub 20150410. doi: 10.1111/bph.13106. PubMed PMID: 25651941; PMCID: PMC4459020.
132. Allen CL, Bayraktutan U. Antioxidants attenuate hyperglycaemia-mediated brain endothelial cell dysfunction and blood-brain barrier hyperpermeability. Diabetes Obes Metab. 2009;11(5):480-90. Epub 20080218. doi: 10.1111/j.1463-1326.2008.00987.x. PubMed PMID: 19236439.
133. Thomsen MS, Humle N, Hede E, Moos T, Burkhart A, Thomsen LB. The blood-brain barrier studied in vitro across species. PLoS One. 2021;16(3):e0236770. Epub 20210312. doi: 10.1371/journal.pone.0236770. PubMed PMID: 33711041; PMCID: PMC7954348.
134. O'Brown NM, Pfau SJ, Gu C. Bridging barriers: a comparative look at the blood-brain barrier across organisms. Genes Dev. 2018;32(7-8):466-78. doi: 10.1101/gad.309823.117. PubMed PMID: 29692355; PMCID: PMC5959231.
135. Rauh J, Meyer J, Beuckmann C, Galla HJ. Development of an in vitro cell culture system to mimic the blood-brain barrier. Prog Brain Res. 1992;91:117-21. doi: 10.1016/s0079-6123(08)62325-0. PubMed PMID: 1357719.

136. Gumbleton M, Audus KL. Progress and limitations in the use of in vitro cell cultures to serve as a permeability screen for the blood-brain barrier. J Pharm Sci. 2001;90(11):1681-98. doi: 10.1002/jps.1119. PubMed PMID: 11745727.
137. Booth R, Kim H. Characterization of a microfluidic in vitro model of the blood-brain barrier (μBBB). Lab Chip. 2012;12(10):1784-92. Epub 20120315. doi: 10.1039/c2lc40094d. PubMed PMID: 22422217.
138. Linz G, Djeljadini S, Steinbeck L, Köse G, Kiessling F, Wessling M. Cell barrier characterization in transwell inserts by electrical impedance spectroscopy. Biosens Bioelectron. 2020;165:112345. Epub 20200602. doi: 10.1016/j.bios.2020.112345. PubMed PMID: 32513645.
139. Williams-Medina A, Deblock M, Janigro D. Models of the Blood-Brain Barrier: Tools in Translational Medicine. Front Med Technol. 2020;2:623950. Epub 20210215. doi: 10.3389/fmedt.2020.623950. PubMed PMID: 35047899; PMCID: PMC8757867.
140. Shao Y, Wolf PG, Guo S, Guo Y, Gaskins HR, Zhang B. Zinc enhances intestinal epithelial barrier function through the PI3K/AKT/mTOR signaling pathway in Caco-2 cells. J Nutr Biochem. 2017;43:18-26. Epub 20170131. doi: 10.1016/j.jnutbio.2017.01.013. PubMed PMID: 28193579.
141. Brown RC, Morris AP, O'Neil RG. Tight junction protein expression and barrier properties of immortalized mouse brain microvessel endothelial cells. Brain research. 2007;1130(1):17-30. Epub 20061212. doi: 10.1016/j.brainres.2006.10.083. PubMed PMID: 17169347; PMCID: PMC1995120.
142. Miyamoto T, Morita K, Takemoto D, Takeuchi K, Kitano Y, Miyakawa T, Nakayama K, Okamura Y, Sasaki H, Miyachi Y, Furuse M, Tsukita S. Tight junctions in Schwann cells of peripheral myelinated axons: a lesson from claudin-19-deficient mice. J Cell Biol. 2005;169(3):527-38. doi: 10.1083/jcb.200501154. PubMed PMID: 15883201; PMCID: PMC2171943.
143. Moreau N, Mauborgne A, Bourgoin S, Couraud PO, Romero IA, Weksler BB, Villanueva L, Pohl M, Boucher Y. Early alterations of Hedgehog signaling pathway in vascular endothelial cells after peripheral nerve injury elicit blood-nerve barrier disruption, nerve inflammation, and neuropathic pain development. Pain. 2016;157(4):827-39. doi: 10.1097/j.pain.0000000000000444. PubMed PMID: 26655733.
144. Reinhold AK, Schwabe J, Lux TJ, Salvador E, Rittner HL. Quantitative and Microstructural Changes of the Blood-Nerve Barrier in Peripheral Neuropathy. Front Neurosci. 2018;12:936. Epub 20181218. doi: 10.3389/fnins.2018.00936. PubMed PMID: 30618565; PMCID: PMC6305433.
145. Lippmann ES, Azarin SM, Kay JE, Nessler RA, Wilson HK, Al-Ahmad A, Palecek SP, Shusta EV. Derivation of blood-brain barrier endothelial cells from human pluripotent stem cells. Nat Biotechnol. 2012;30(8):783-91. doi: 10.1038/nbt.2247. PubMed PMID: 22729031; PMCID: PMC3467331.
146. Schindelin J, Arganda-Carreras I, Frise E, Kaynig V, Longair M, Pietzsch T, Preibisch S, Rueden C, Saalfeld S, Schmid B, Tinevez JY, White DJ, Hartenstein V, Eliceiri K, Tomancak P, Cardona A. Fiji: an open-source platform for biological-image analysis. Nat Methods. 2012;9(7):676-82. Epub 20120628. doi: 10.1038/nmeth.2019. PubMed PMID: 22743772; PMCID: PMC3855844.
147. Rueden CT, Schindelin J, Hiner MC, DeZonia BE, Walter AE, Arena ET, Eliceiri KW. ImageJ2: ImageJ for the next generation of scientific image data. BMC Bioinformatics. 2017;18(1):529. Epub 20171129. doi: 10.1186/s12859-017-1934-z. PubMed PMID: 29187165; PMCID: PMC5708080.
148. Podany AT, Winchester LC, Robbins BL, Fletcher CV. Quantification of cell-associated atazanavir, darunavir, lopinavir, ritonavir, and efavirenz concentrations in

human mononuclear cell extracts. Antimicrob Agents Chemother. 2014;58(5):2866-70. doi: 10.1128/AAC.02551-13. PubMed PMID: 24614370; PMCID: PMC3993270.
149. Letendre SL, Mills AM, Tashima KT, Thomas DA, Min SS, Chen S, Song IH, Piscitelli SC, team eIs. ING116070: a study of the pharmacokinetics and antiviral activity of dolutegravir in cerebrospinal fluid in HIV-1-infected, antiretroviral therapy-naive subjects. Clin Infect Dis. 2014;59(7):1032-7. Epub 20140618. doi: 10.1093/cid/ciu477. PubMed PMID: 24944232; PMCID: PMC4166983.
150. Wang Y, Wang N, Cai B, Wang GY, Li J, Piao XX. In vitro model of the blood-brain barrier established by co-culture of primary cerebral microvascular endothelial and astrocyte cells. Neural Regen Res. 2015;10(12):2011-7. doi: 10.4103/1673-5374.172320. PubMed PMID: 26889191; PMCID: PMC4730827.
151. Appelt-Menzel A, Cubukova A, Günther K, Edenhofer F, Piontek J, Krause G, Stüber T, Walles H, Neuhaus W, Metzger M. Establishment of a Human Blood-Brain Barrier Co-culture Model Mimicking the Neurovascular Unit Using Induced Pluri- and Multipotent Stem Cells. Stem Cell Reports. 2017;8(4):894-906. Epub 20170323. doi: 10.1016/j.stemcr.2017.02.021. PubMed PMID: 28344002; PMCID: PMC5390136.
152. Kim MY, Li DJ, Pham LK, Wong BG, Hui EE. Microfabrication of High-Resolution Porous Membranes for Cell Culture. J Memb Sci. 2014;452:460-9. doi: 10.1016/j.memsci.2013.11.034. PubMed PMID: 24567663; PMCID: PMC3931465.
153. Paradis A, Leblanc D, Dumais N. Optimization of an in vitro human blood-brain barrier model: Application to blood monocyte transmigration assays. MethodsX. 2016;3:25-34. Epub 20151211. doi: 10.1016/j.mex.2015.11.009. PubMed PMID: 26865992; PMCID: PMC4710797.
154. Daneman R, Zhou L, Kebede AA, Barres BA. Pericytes are required for blood-brain barrier integrity during embryogenesis. Nature. 2010;468(7323):562-6. Epub 20101013. doi: 10.1038/nature09513. PubMed PMID: 20944625; PMCID: PMC3241506.
155. Hayashi K, Nakao S, Nakaoke R, Nakagawa S, Kitagawa N, Niwa M. Effects of hypoxia on endothelial/pericytic co-culture model of the blood-brain barrier. Regul Pept. 2004;123(1-3):77-83. doi: 10.1016/j.regpep.2004.05.023. PubMed PMID: 15518896.
156. Cestelli A, Catania C, D'Agostino S, Di Liegro I, Licata L, Schiera G, Pitarresi GL, Savettieri G, De Caro V, Giandalia G, Giannola LI. Functional feature of a novel model of blood brain barrier: studies on permeation of test compounds. J Control Release. 2001;76(1-2):139-47. doi: 10.1016/s0168-3659(01)00431-x. PubMed PMID: 11532320.
157. Marino A, Baronio M, Buratti U, Mele E, Ciofani G. Porous Optically Transparent Cellulose Acetate Scaffolds for Biomimetic Blood-Brain Barrier. Front Bioeng Biotechnol. 2021;9:630063. Epub 20210210. doi: 10.3389/fbioe.2021.630063. PubMed PMID: 33681166; PMCID: PMC7928328.
158. Miranda-Azpiazu P, Panagiotou S, Jose G, Saha S. A novel dynamic multicellular co-culture system for studying individual blood-brain barrier cell types in brain diseases and cytotoxicity testing. Sci Rep. 2018;8(1):8784. Epub 20180608. doi: 10.1038/s41598-018-26480-8. PubMed PMID: 29884831; PMCID: PMC5993789.
159. De Lorenzo AJ. Electron microscopy: tight junctions in synapses of the chick ciliary ganglion. Science. 1966;152(3718):76-8. doi: 10.1126/science.152.3718.76. PubMed PMID: 5910012.
160. Tikiyani V, Babu K. Claudins in the brain: Unconventional functions in neurons. Traffic. 2019;20(11):807-14. doi: 10.1111/tra.12685. PubMed PMID: 31418988.
161. Food and Drug Administration C. Guidance for Industry: Estimating the Maximum Safe Starting Dose in Initial Clinical Trials for Therapeutics in Adult Healthy Volunteers. 2005.

162. Center for Disease Control and Prevention: Coronavirus Disease 2019 (COVID-19). Cases in the U.S. https://www.cdc.gov/coronavirus/2019-ncov/cases-updates/index.html. Updated May 11, 2023. Accessed June 3, 2023.
163. Johns Hopkins Coronavirus Resource Center. Last Updated (5/18/2022). Covid-10 Dashboard by the Center for Systems Science and Engineering (CSSE) at Johns Hopkins University. https://coronavirus.jhu.edu/map.html. Updated May 18, 2022. Accessed September 7, 2023.
164. Brewer RC, Robinson WH, Lanz TV. SARS-CoV-2 infection of monocytes: balancing acts of antibodies and inflammasomes. Signal Transduct Target Ther. 2022;7(1):250. Epub 20220723. doi: 10.1038/s41392-022-01112-w. PubMed PMID: 35871170; PMCID: PMC9308028.
165. Shen XR, Geng R, Li Q, Chen Y, Li SF, Wang Q, Min J, Yang Y, Li B, Jiang RD, Wang X, Zheng XS, Zhu Y, Jia JK, Yang XL, Liu MQ, Gong QC, Zhang YL, Guan ZQ, Li HL, Zheng ZH, Shi ZL, Zhang HL, Peng K, Zhou P. ACE2-independent infection of T lymphocytes by SARS-CoV-2. Signal Transduct Target Ther. 2022;7(1):83. Epub 20220311. doi: 10.1038/s41392-022-00919-x. PubMed PMID: 35277473; PMCID: PMC8914143.
166. Chaple AR, Vispute MM, Mahajan S, Mushtaq S, Muthuchelvan D, Ramakrishnan MA, Sharma GK. Relational interaction between T-lymphocytes and SARS-CoV-2: A review. Acta Virol. 2021;65(2):107-14. doi: 10.4149/av_2021_202. PubMed PMID: 34130462.
167. Hashemian SMR, Sheida A, Taghizadieh M, Memar MY, Hamblin MR, Bannazadeh Baghi H, Sadri Nahand J, Asemi Z, Mirzaei H. Paxlovid (Nirmatrelvir/Ritonavir): A new approach to Covid-19 therapy? Biomed Pharmacother. 2023;162:114367. Epub 20230206. doi: 10.1016/j.biopha.2023.114367. PubMed PMID: 37018987; PMCID: PMC9899776.
168. PAXLOVID™ [package insert]. New York, NY. Pfizer Labs, Inc. May 2023. https://www.accessdata.fda.gov/drugsatfda_docs/label/2023/217188s000lbl.pdf. Updated May 25, 2023. Accessed May 25, 2023.
169. FDA News Release: FDA Approves First Oral Antiviral for Treatment of COVID-19 in Adults. https://www.fda.gov/news-events/press-announcements/fda-approves-first-oral-antiviral-treatment-covid-19-adults. Updated May 25, 2023. Accessed May 26, 2023.
170. Wan D, Du T, Hong W, Chen L, Que H, Lu S, Peng X. Neurological complications and infection mechanism of SARS-COV-2. Signal Transduct Target Ther. 2021;6(1):406. Epub 20211123. doi: 10.1038/s41392-021-00818-7. PubMed PMID: 34815399; PMCID: PMC8609271.
171. White CN, Rolston KV. Osteomyelitis: drug bioavailability and bone penetration are key. JAAPA. 2012;25(7):21, 7. doi: 10.1097/01720610-201207000-00005. PubMed PMID: 22894029.
172. Lu CT, Zhao YZ, Wong HL, Cai J, Peng L, Tian XQ. Current approaches to enhance CNS delivery of drugs across the brain barriers. Int J Nanomedicine. 2014;9:2241-57. Epub 20140510. doi: 10.2147/IJN.S61288. PubMed PMID: 24872687; PMCID: PMC4026551.
173. Eng H, Dantonio AL, Kadar EP, Obach RS, Di L, Lin J, Patel NC, Boras B, Walker GS, Novak JJ, Kimoto E, Singh RSP, Kalgutkar AS. Disposition of Nirmatrelvir, an Orally Bioavailable Inhibitor of SARS-CoV-2 3C-Like Protease, across Animals and Humans. Drug Metab Dispos. 2022;50(5):576-90. Epub 20220213. doi: 10.1124/dmd.121.000801. PubMed PMID: 35153195.
174. Owen DR, Allerton CMN, Anderson AS, Aschenbrenner L, Avery M, Berritt S, Boras B, Cardin RD, Carlo A, Coffman KJ, Dantonio A, Di L, Eng H, Ferre R, Gajiwala KS, Gibson SA, Greasley SE, Hurst BL, Kadar EP, Kalgutkar AS, Lee JC, Lee J, Liu W, Mason

SW, Noell S, Novak JJ, Obach RS, Ogilvie K, Patel NC, Pettersson M, Rai DK, Reese MR, Sammons MF, Sathish JG, Singh RSP, Steppan CM, Stewart AE, Tuttle JB, Updyke L, Verhoest PR, Wei L, Yang Q, Zhu Y. An oral SARS-CoV-2 M. Science. 2021;374(6575):1586-93. Epub 20211102. doi: 10.1126/science.abl4784. PubMed PMID: 34726479.
175. Abdelnabi R, Foo CS, Jochmans D, Vangeel L, De Jonghe S, Augustijns P, Mols R, Weynand B, Wattanakul T, Hoglund RM, Tarning J, Mowbray CE, Sjö P, Escudié F, Scandale I, Chatelain E, Neyts J. The oral protease inhibitor (PF-07321332) protects Syrian hamsters against infection with SARS-CoV-2 variants of concern. Nat Commun. 2022;13(1):719. Epub 20220215. doi: 10.1038/s41467-022-28354-0. PubMed PMID: 35169114; PMCID: PMC8847371.
176. Toussi SS, Neutel JM, Navarro J, Preston RA, Shi H, Kavetska O, LaBadie RR, Binks M, Chan PLS, Demers N, Corrigan B, Damle B. Pharmacokinetics of Oral Nirmatrelvir/Ritonavir, a Protease Inhibitor for Treatment of COVID-19, in Subjects With Renal Impairment. Clin Pharmacol Ther. 2022;112(4):892-900. Epub 20220705. doi: 10.1002/cpt.2688. PubMed PMID: 35712797; PMCID: PMC9349773.
177. Hsu A, Granneman GR, Witt G, Locke C, Denissen J, Molla A, Valdes J, Smith J, Erdman K, Lyons N, Niu P, Decourt JP, Fourtillan JB, Girault J, Leonard JM. Multiple-dose pharmacokinetics of ritonavir in human immunodeficiency virus-infected subjects. Antimicrob Agents Chemother. 1997;41(5):898-905. doi: 10.1128/AAC.41.5.898. PubMed PMID: 9145841; PMCID: PMC163822.
178. Charles River Laboratories International Inc. Intracisternal Cannulation. 2018. Available at https://www.criver.com/sites/default/files/resource-files/intracisternal-cannulation.pdf.
179. Charles River Laboratories International Inc. Jugular Vein Catheter Surgery Code: JUGVEIN. https://www.criver.com/sites/default/files/resource-files/jugular-vein-catheter.pdf. Updated January 1, 2022. Accessed February 4, 2022.
180. Beal SL. Ways to fit a PK model with some data below the quantification limit. J Pharmacokinet Pharmacodyn. 2001;28(5):481-504. Epub 2002/01/05. PubMed PMID: 11768292.
181. Avedissian SN, Malik JR, Podany AT, Neely M, Rhodes NJ, Scarsi KK, Scheetz MH, Duryee MJ, Modebelu UO, Mykris TM, Winchester LC, Byrareddy SN, Fletcher CV. In-vitro and in-vivo assessment of nirmatrelvir penetration into CSF, central nervous system cells, tissues, and peripheral blood mononuclear cells. Sci Rep. 2024;14(1):10709. Epub 20240510. doi: 10.1038/s41598-024-60935-5. PubMed PMID: 38729980; PMCID: PMC11087525.
182. Fletcher CV, Podany AT, Thorkelson A, Winchester LC, Mykris T, Anderson J, Jorstad S, Baker JV, Schacker TW. The Lymphoid Tissue Pharmacokinetics of Tenofovir Disoproxil Fumarate and Tenofovir Alafenamide in HIV-Infected Persons. Clin Pharmacol Ther. 2020;108(5):971-5. Epub 20200611. doi: 10.1002/cpt.1883. PubMed PMID: 32385902; PMCID: PMC7935460.
183. Winchester LC, Mykris TM, Weinhold JA, Fletcher CV, podany AT. Quantification of Antiretroviral Drugs in Human Cerebrospinal Fluid. Presented at ASMS 2019, Atlanta, GA.
184. Simiele M, D'Avolio A, Baietto L, Siccardi M, Sciandra M, Agati S, Cusato J, Bonora S, Di Perri G. Evaluation of the mean corpuscular volume of peripheral blood mononuclear cells of HIV patients by a coulter counter to determine intracellular drug concentrations. Antimicrob Agents Chemother. 2011;55(6):2976-8. Epub 20110314. doi: 10.1128/AAC.01236-10. PubMed PMID: 21402849; PMCID: PMC3101420.
185. for CPQACG, Bioanalytical Chromatographic Method Development V, and, V2.0. A. Clinical Pharmacology Quality Assurance 2019.

186. Dyavar SR, Kumar S, Gautam N, Podany AT, Winchester LC, Weinhold JA, Mykris TM, Nallasamy P, Alnouti Y, Fletcher CV. Intramuscular and subcutaneous administration of antiretroviral drugs, compared with oral, enhances delivery to lymphoid tissues in BALB/c mice. J Antimicrob Chemother. 2021;76(10):2651-8. doi: 10.1093/jac/dkab228. PubMed PMID: 34312680; PMCID: PMC8446911.
187. D'Avolio A, Simiele M, Calcagno A, Siccardi M, Larovere G, Agati S, Baietto L, Cusato J, Tettoni M, Sciandra M, Trentini L, Di Perri G, Bonora S. Intracellular accumulation of ritonavir combined with different protease inhibitors and correlations between concentrations in plasma and peripheral blood mononuclear cells. J Antimicrob Chemother. 2013;68(4):907-10. Epub 20121205. doi: 10.1093/jac/dks484. PubMed PMID: 23221630.
188. Khoo SH, Hoggard PG, Williams I, Meaden ER, Newton P, Wilkins EG, Smith A, Tjia JF, Lloyd J, Jones K, Beeching N, Carey P, Peters B, Back DJ. Intracellular accumulation of human immunodeficiency virus protease inhibitors. Antimicrob Agents Chemother. 2002;46(10):3228-35. doi: 10.1128/AAC.46.10.3228-3235.2002. PubMed PMID: 12234849; PMCID: PMC128776.
189. Neely MN, van Guilder MG, Yamada WM, Schumitzky A, Jelliffe RW. Accurate detection of outliers and subpopulations with Pmetrics, a nonparametric and parametric pharmacometric modeling and simulation package for R. Ther Drug Monit. 2012;34(4):467-76. doi: 10.1097/FTD.0b013e31825c4ba6. PubMed PMID: 22722776; PMCID: 3394880.
190. Tatarinova T, Neely M, Bartroff J, van Guilder M, Yamada W, Bayard D, Jelliffe R, Leary R, Chubatiuk A, Schumitzky A. Two general methods for population pharmacokinetic modeling: non-parametric adaptive grid and non-parametric Bayesian. J Pharmacokinet Pharmacodyn. 2013;40(2):189-99. doi: 10.1007/s10928-013-9302-8. PubMed PMID: 23404393; PMCID: 3630269.
191. Avedissian SN, Pais G, Joshi MD, Rhodes NJ, Scheetz MH. A Translational Pharmacokinetic Rat Model of Cerebral Spinal Fluid and Plasma Concentrations of Cefepime. mSphere. 2019;4(1). doi: 10.1128/mSphere.00595-18. PubMed PMID: 30700511; PMCID: PMC6354808.
192. Zhou Q, Guo P, Kruh GD, Vicini P, Wang X, Gallo JM. Predicting human tumor drug concentrations from a preclinical pharmacokinetic model of temozolomide brain disposition. Clin Cancer Res. 2007;13(14):4271-9. doi: 10.1158/1078-0432.CCR-07-0658. PubMed PMID: 17634557.
193. Abdelgawad N, Tshavhungwe MP, Rohlwink U, McIlleron H, Abdelwahab MT, Wiesner L, Castel S, Steele C, Enslin JN, Thango NS, Denti P, Figaji A. Population Pharmacokinetic Analysis of Rifampicin in Plasma, Cerebrospinal Fluid, and Brain Extracellular Fluid in South African Children with Tuberculous Meningitis. Antimicrob Agents Chemother. 2023;67(3):e0147422. Epub 20230223. doi: 10.1128/aac.01474-22. PubMed PMID: 36815838; PMCID: PMC10019224.
194. Li S, Wang Y, Dong H, Zhu Y, Cao P, Meng L. Population Pharmacokinetics and Dosing Regimen Optimization of Linezolid in Cerebrospinal Fluid and Plasma of Post-operative Neurosurgical Patients. J Pharm Sci. 2023;112(3):884-92. Epub 20221222. doi: 10.1016/j.xphs.2022.12.016. PubMed PMID: 36566928.
195. Pmetrics User Manual. http://www.lapk.org/software/Pmetrics/PM_User_manual.pdf. Updated July 17, 2015. Accessed August 23, 2023.
196. Rosales R, McGovern BL, Rodriguez LM, Rai DK, Cardin RD, Anderson AS, group Ps, Sordillo EM, van Bakel H, Simon V, Garcia-Sastre A, White KM. Nirmatrelvir, Molnupiravir, and Remdesivir maintain potent in vitro activity against the SARS-CoV-2 Omicron variant. bioRxiv. 2022. doi: https://doi.org/10.1101/2022.01.17.476685.

197. Center for Drug Evaluation and Research. Application Number:217188Orig1s000. Integrated Review. NDA 217188. PAXLOVID (nirmatrelvir and ritonavir). https://www.accessdata.fda.gov/drugsatfda_docs/nda/2023/217188Orig1s000IntegratedR.pdf. Updated May 5, 2022. Accessed September 10, 2023.
198. Rhodes NJ, Prozialeck WC, Lodise TP, Venkatesan N, O'Donnell JN, Pais G, Cluff C, Lamar PC, Neely MN, Gulati A, Scheetz MH. Evaluation of Vancomycin Exposures Associated with Elevations in Novel Urinary Biomarkers of Acute Kidney Injury in Vancomycin-Treated Rats. Antimicrob Agents Chemother. 2016;60(10):5742-51. doi: 10.1128/AAC.00591-16. PubMed PMID: 27431226; PMCID: PMC5038238.
199. Lodise TP, Jr., Rhoney DH, Tam VH, McKinnon PS, Drusano GL. Pharmacodynamic profiling of cefepime in plasma and cerebrospinal fluid of hospitalized patients with external ventriculostomies. Diagn Microbiol Infect Dis. 2006;54(3):223-30. doi: 10.1016/j.diagmicrobio.2005.09.007. PubMed PMID: 16423490.
200. Tauber MG, Hackbarth CJ, Scott KG, Rusnak MG, Sande MA. New cephalosporins cefotaxime, cefpimizole, BMY 28142, and HR 810 in experimental pneumococcal meningitis in rabbits. Antimicrob Agents Chemother. 1985;27(3):340-2. PubMed PMID: 3838872; PMCID: PMC176273.
201. Tsai YH, Bies M, Leitner F, Kessler RE. Therapeutic studies of cefepime (BMY 28142) in murine meningitis and pharmacokinetics in neonatal rats. Antimicrob Agents Chemother. 1990;34(5):733-8. PubMed PMID: 2360814; PMCID: PMC171682.
202. Lutsar I, McCracken GH, Jr., Friedland IR. Antibiotic pharmacodynamics in cerebrospinal fluid. Clin Infect Dis. 1998;27(5):1117-27, quiz 28-9. PubMed PMID: 9827256.
203. Saleh MAA, Hirasawa M, Sun M, Gülave B, Elassaiss-Schaap J, de Lange ECM. The PBPK LeiCNS-PK3.0 framework predicts Nirmatrelvir (but not Remdesivir or Molnupiravir) to achieve effective concentrations against SARS-CoV-2 in human brain cells. Eur J Pharm Sci. 2023;181:106345. Epub 20221130. doi: 10.1016/j.ejps.2022.106345. PubMed PMID: 36462547; PMCID: PMC9710098.
204. Gonzalez-García R, Roma JR, Rodríguez-García M, Arranz N, Ambrosioni J, Bodro M, Castel M, Cofan F, Crespo G, Diekmann F, Farrero M, Forner A, LLigoña A, Marcos M, Moreno A, Ruiz P, Soy D, Brunet M, Miró JM, Tuset M. Drug-drug interactions of ritonavir-boosted SARS-CoV-2 protease inhibitors in solid organ transplant recipients: experience from the initial use of lopinavir-ritonavir. Clin Microbiol Infect. 2023;29(5):655.e1-.e4. Epub 20230111. doi: 10.1016/j.cmi.2023.01.002. PubMed PMID: 36641051; PMCID: PMC9831976.
205. Junqueira C, Crespo Â, Ranjbar S, de Lacerda LB, Lewandrowski M, Ingber J, Parry B, Ravid S, Clark S, Schrimpf MR, Ho F, Beakes C, Margolin J, Russell N, Kays K, Boucau J, Das Adhikari U, Vora SM, Leger V, Gehrke L, Henderson LA, Janssen E, Kwon D, Sander C, Abraham J, Goldberg MB, Wu H, Mehta G, Bell S, Goldfeld AE, Filbin MR, Lieberman J. FcγR-mediated SARS-CoV-2 infection of monocytes activates inflammation. Nature. 2022;606(7914):576-84. Epub 20220406. doi: 10.1038/s41586-022-04702-4. PubMed PMID: 35385861; PMCID: PMC10071495.
206. Mukwaya G, MacGregor T, Hoelscher D, Heming T, Legg D, Kavanaugh K, Johnson P, Sabo JP, McCallister S. Interaction of ritonavir-boosted tipranavir with loperamide does not result in loperamide-associated neurologic side effects in healthy volunteers. Antimicrob Agents Chemother. 2005;49(12):4903-10. doi: 10.1128/AAC.49.12.4903-4910.2005. PubMed PMID: 16304151; PMCID: PMC1315935.
207. Ghosh C, Marchi N, Desai NK, Puvenna V, Hossain M, Gonzalez-Martinez J, Alexopoulos AV, Janigro D. Cellular localization and functional significance of CYP3A4 in the human epileptic brain. Epilepsia. 2011;52(3):562-71. Epub 20110205. doi: 10.1111/j.1528-1167.2010.02956.x. PubMed PMID: 21294720; PMCID: PMC3056924.

208. Montanha MC, Fabrega F, Howarth A, Cottura N, Kinvig H, Bunglawala F, Lloyd A, Denti P, Waitt C, Siccardi M. Predicting Drug-Drug Interactions between Rifampicin and Ritonavir-Boosted Atazanavir Using PBPK Modelling. Clin Pharmacokinet. 2022;61(3):375-86. Epub 20211012. doi: 10.1007/s40262-021-01067-1. PubMed PMID: 34635995; PMCID: PMC9481493.
209. Ahmed Juvale II, Abdul Hamid AA, Abd Halim KB, Che Has AT. P-glycoprotein: new insights into structure, physiological function, regulation and alterations in disease. Heliyon. 2022;8(6):e09777. Epub 20220622. doi: 10.1016/j.heliyon.2022.e09777. PubMed PMID: 35789865; PMCID: PMC9249865.
210. van Vliet EA, Iyer AM, Mesarosova L, Çolakoglu H, Anink JJ, van Tellingen O, Maragakis NJ, Shefner J, Bunt T, Aronica E. Expression and Cellular Distribution of P-Glycoprotein and Breast Cancer Resistance Protein in Amyotrophic Lateral Sclerosis Patients. J Neuropathol Exp Neurol. 2020;79(3):266-76. doi: 10.1093/jnen/nlz142. PubMed PMID: 31999342; PMCID: PMC7036662.
211. Bendayan R, Ronaldson PT, Gingras D, Bendayan M. In situ localization of P-glycoprotein (ABCB1) in human and rat brain. J Histochem Cytochem. 2006;54(10):1159-67. Epub 20060626. doi: 10.1369/jhc.5A6870.2006. PubMed PMID: 16801529; PMCID: PMC3957801.
212. Berezowski V, Landry C, Dehouck MP, Cecchelli R, Fenart L. Contribution of glial cells and pericytes to the mRNA profiles of P-glycoprotein and multidrug resistance-associated proteins in an in vitro model of the blood-brain barrier. Brain research. 2004;1018(1):1-9. doi: 10.1016/j.brainres.2004.05.092. PubMed PMID: 15262198.
213. Golden PL, Pardridge WM. P-Glycoprotein on astrocyte foot processes of unfixed isolated human brain capillaries. Brain research. 1999;819(1-2):143-6. doi: 10.1016/s0006-8993(98)01305-5. PubMed PMID: 10082869.
214. Avedissian SN, Dyavar SR, Fox HS, Fletcher CV. Pharmacologic approaches to HIV-associated neurocognitive disorders. Curr Opin Pharmacol. 2020;54:102-8. Epub 2020/10/10. doi: 10.1016/j.coph.2020.09.003. PubMed PMID: 33049585; PMCID: PMC7770011.
215. Anthonypillai C, Sanderson RN, Gibbs JE, Thomas SA. The distribution of the HIV protease inhibitor, ritonavir, to the brain, cerebrospinal fluid, and choroid plexuses of the guinea pig. J Pharmacol Exp Ther. 2004;308(3):912-20. Epub 20031121. doi: 10.1124/jpet.103.060210. PubMed PMID: 14634041.
216. Haas DW, Johnson B, Nicotera J, Bailey VL, Harris VL, Bowles FB, Raffanti S, Schranz J, Finn TS, Saah AJ, Stone J. Effects of ritonavir on indinavir pharmacokinetics in cerebrospinal fluid and plasma. Antimicrob Agents Chemother. 2003;47(7):2131-7. doi: 10.1128/AAC.47.7.2131-2137.2003. PubMed PMID: 12821458; PMCID: PMC161873.
217. Hsu A, Granneman GR, Bertz RJ. Ritonavir. Clinical pharmacokinetics and interactions with other anti-HIV agents. Clin Pharmacokinet. 1998;35(4):275-91. doi: 10.2165/00003088-199835040-00002. PubMed PMID: 9812178.
218. Rao KS, Reddy MK, Horning JL, Labhasetwar V. TAT-conjugated nanoparticles for the CNS delivery of anti-HIV drugs. Biomaterials. 2008;29(33):4429-38. Epub 20080828. doi: 10.1016/j.biomaterials.2008.08.004. PubMed PMID: 18760470; PMCID: PMC2570783.
219. Quintessa. Graph Grabber V.2.0.2. https://www.quintessa.org/software/downloads-and-demos/graph-grabber-2.0.2. Updated September 22, 2023. Accessed April 23, 2023.
220. Li C, Nair L, Liu T, Li F, Pichardo J, Agrawal S, Chase R, Tong X, Uss AS, Bogen S, Njoroge FG, Morrison RA, Cheng KC. Correlation between PAMPA permeability and cellular activities of hepatitis C virus protease inhibitors. Biochem Pharmacol.

2008;75(5):1186-97. Epub 20071107. doi: 10.1016/j.bcp.2007.10.031. PubMed PMID: 18164692.
221. Leung D, Abbenante G, Fairlie DP. Protease inhibitors: current status and future prospects. J Med Chem. 2000;43(3):305-41. doi: 10.1021/jm990412m. PubMed PMID: 10669559.
222. Hernández-Parra H, Reyes-Hernández OD, Figueroa-González G, González-Del Carmen M, González-Torres M, Peña-Corona SI, Florán B, Cortés H, Leyva-Gómez G. Alteration of the blood-brain barrier by COVID-19 and its implication in the permeation of drugs into the brain. Front Cell Neurosci. 2023;17:1125109. Epub 20230314. doi: 10.3389/fncel.2023.1125109. PubMed PMID: 36998270; PMCID: PMC10043238.
223. Verscheijden LFM, Koenderink JB, de Wildt SN, Russel FGM. Differences in P-glycoprotein activity in human and rodent blood-brain barrier assessed by mechanistic modelling. Arch Toxicol. 2021;95(9):3015-29. Epub 20210715. doi: 10.1007/s00204-021-03115-y. PubMed PMID: 34268580; PMCID: PMC8380243.
224. Yuan X, Desiderio DM. Proteomics analysis of human cerebrospinal fluid. J Chromatogr B Analyt Technol Biomed Life Sci. 2005;815(1-2):179-89. doi: 10.1016/j.jchromb.2004.06.044. PubMed PMID: 15652808.
225. Lian X, Seiger KW, Parsons EM, Gao C, Sun W, Gladkov GT, Roseto IC, Einkauf KB, Osborn MR, Chevalier JM, Jiang C, Blackmer J, Carrington M, Rosenberg ES, Lederman MM, McMahon DK, Bosch RJ, Jacobson JM, Gandhi RT, Peluso MJ, Chun TW, Deeks SG, Yu XG, Lichterfeld M. Progressive transformation of the HIV-1 reservoir cell profile over two decades of antiviral therapy. Cell Host Microbe. 2023;31(1):83-96.e5. Epub 20230102. doi: 10.1016/j.chom.2022.12.002. PubMed PMID: 36596305; PMCID: PMC9839361.
226. Simonetti FR, White JA, Tumiotto C, Ritter KD, Cai M, Gandhi RT, Deeks SG, Howell BJ, Montaner LJ, Blankson JN, Martin A, Laird GM, Siliciano RF, Mellors JW, Siliciano JD. Intact proviral DNA assay analysis of large cohorts of people with HIV provides a benchmark for the frequency and composition of persistent proviral DNA. Proc Natl Acad Sci U S A. 2020;117(31):18692-700. Epub 20200720. doi: 10.1073/pnas.2006816117. PubMed PMID: 32690683; PMCID: PMC7414172.
227. Gandhi RT, Cyktor JC, Bosch RJ, Mar H, Laird GM, Martin A, Collier AC, Riddler SA, Macatangay BJ, Rinaldo CR, Eron JJ, Siliciano JD, McMahon DK, Mellors JW, Team ACTGA. Selective Decay of Intact HIV-1 Proviral DNA on Antiretroviral Therapy. J Infect Dis. 2021;223(2):225-33. doi: 10.1093/infdis/jiaa532. PubMed PMID: 32823274; PMCID: PMC7857155.
228. Fletcher CV, Dyavar SR, Acharya A, Byrareddy SN. The Contributions of Clinical Pharmacology to HIV Cure Research. Clin Pharmacol Ther. 2021. Epub 2021/03/26. doi: 10.1002/cpt.2237. PubMed PMID: 33763860.
229. Whitney JB, Hill AL, Sanisetty S, Penaloza-MacMaster P, Liu J, Shetty M, Parenteau L, Cabral C, Shields J, Blackmore S, Smith JY, Brinkman AL, Peter LE, Mathew SI, Smith KM, Borducchi EN, Rosenbloom DI, Lewis MG, Hattersley J, Li B, Hesselgesser J, Geleziunas R, Robb ML, Kim JH, Michael NL, Barouch DH. Rapid seeding of the viral reservoir prior to SIV viraemia in rhesus monkeys. Nature. 2014;512(7512):74-7. Epub 2014/07/22. doi: 10.1038/nature13594. PubMed PMID: 25042999; PMCID: PMC4126858.
230. Elendu C, Aguocha CM, Okeke CV, Okoro CB, Peterson JC. HIV-related neurocognitive disorders: Diagnosis, Treatment, and Mental Health Implications: A Review. Medicine (Baltimore). 2023;102(43):e35652. doi: 10.1097/MD.0000000000035652. PubMed PMID: 37904369; PMCID: PMC10615506.
231. Letendre S. Central nervous system complications in HIV disease: HIV-associated neurocognitive disorder. Top Antivir Med. 2011;19(4):137-42. Epub 2011/12/14. PubMed PMID: 22156215; PMCID: PMC4666587.

232. Latendre S. Background and rationale of the CPE score. Presented at the 2nd International Workshop on HIV & Aging. Baltimore; 2011.
233. Fabbiani M, Grima P, Milanini B, Mondi A, Baldonero E, Ciccarelli N, Cauda R, Silveri MC, De Luca A, Di Giambenedetto S. Antiretroviral neuropenetration scores better correlate with cognitive performance of HIV-infected patients after accounting for drug susceptibility. Antivir Ther. 2015;20(4):441-7. Epub 20141217. doi: 10.3851/IMP2926. PubMed PMID: 25516553.
234. Ciccarelli N, Fabbiani M, Colafigli M, Trecarichi EM, Silveri MC, Cauda R, Murri R, De Luca A, Di Giambenedetto S. Revised central nervous system neuropenetration-effectiveness score is associated with cognitive disorders in HIV-infected patients with controlled plasma viraemia. Antivir Ther. 2013;18(2):153-60. Epub 20130313. doi: 10.3851/IMP2560. PubMed PMID: 23486721.
235. Casado JL, Marin A, Moreno A, Iglesias V, Perez-Elias MJ, Moreno S, Corral I. Central nervous system antiretroviral penetration and cognitive functioning in largely pretreated HIV-infected patients. J Neurovirol. 2014;20(1):54-61. Epub 20140114. doi: 10.1007/s13365-013-0228-0. PubMed PMID: 24420449.
236. Vassallo M, Durant J, Biscay V, Lebrun-Frenay C, Dunais B, Laffon M, Harvey-Langton A, Cottalorda J, Ticchioni M, Carsenti H, Pradier C, Dellamonica P. Can high central nervous system penetrating antiretroviral regimens protect against the onset of HIV-associated neurocognitive disorders? AIDS. 2014;28(4):493-501. doi: 10.1097/QAD.0000000000000096. PubMed PMID: 24472743.
237. Carvalhal A, Gill MJ, Letendre SL, Rachlis A, Bekele T, Raboud J, Burchell A, Rourke SB, Centre for Brain Health in HA. Central nervous system penetration effectiveness of antiretroviral drugs and neuropsychological impairment in the Ontario HIV Treatment Network Cohort Study. J Neurovirol. 2016;22(3):349-57. Epub 20151116. doi: 10.1007/s13365-015-0404-5. PubMed PMID: 26572786; PMCID: PMC10748733.
238. Smurzynski M, Wu K, Letendre S, Robertson K, Bosch RJ, Clifford DB, Evans S, Collier AC, Taylor M, Ellis R. Effects of central nervous system antiretroviral penetration on cognitive functioning in the ALLRT cohort. AIDS. 2011;25(3):357-65. doi: 10.1097/QAD.0b013e32834171f8. PubMed PMID: 21124201; PMCID: PMC3022370.
239. Ellis RJ, Letendre S, Vaida F, Haubrich R, Heaton RK, Sacktor N, Clifford DB, Best BM, May S, Umlauf A, Cherner M, Sanders C, Ballard C, Simpson DM, Jay C, McCutchan JA. Randomized trial of central nervous system-targeted antiretrovirals for HIV-associated neurocognitive disorder. Clin Infect Dis. 2014;58(7):1015-22. Epub 20131218. doi: 10.1093/cid/cit921. PubMed PMID: 24352352; PMCID: PMC3952601.
240. Kahouadji Y, Dumurgier J, Sellier P, Lapalus P, Delcey V, Bergmann J, Hugon J, Paquet C. Cognitive function after several years of antiretroviral therapy with stable central nervous system penetration score. HIV Med. 2013;14(5):311-5. Epub 20121004. doi: 10.1111/j.1468-1293.2012.01052.x. PubMed PMID: 23035982.
241. Caniglia EC, Cain LE, Justice A, Tate J, Logan R, Sabin C, Winston A, van Sighem A, Miro JM, Podzamczer D, Olson A, Arribas JR, Moreno S, Meyer L, del Romero J, Dabis F, Bucher HC, Wandeler G, Vourli G, Skoutelis A, Lanoy E, Gasnault J, Costagliola D, Hernan MA, Collaboration H-C. Antiretroviral penetration into the CNS and incidence of AIDS-defining neurologic conditions. Neurology. 2014;83(2):134-41. Epub 20140606. doi: 10.1212/WNL.0000000000000564. PubMed PMID: 24907236; PMCID: PMC4117168.
242. Letendre SL, Chen H, McKhann A, Roa J, Vecchio A, Daar ES, Berzins B, Hunt PW, Marra CM, Campbell TB, Coombs RW, Ma Q, Swaminathan S, Macatangay BJC, Morse GD, Miller T, Rusin D, Greninger AL, Ha B, Alston-Smith B, Robertson K, Paul R, Spudich S, Team AS. Antiretroviral Therapy Intensification for Neurocognitive Impairment in Human Immunodeficiency Virus. Clin Infect Dis. 2023;77(6):866-74. doi: 10.1093/cid/ciad265. PubMed PMID: 37183889; PMCID: PMC10506779.

243. Force G, Ghout I, Ropers J, Carcelain G, Marigot-Outtandy D, Hahn V, Darchy N, Defferriere H, Bouaziz-Amar E, Carlier R, Dorgham K, Callebert J, Peytavin G, Delaugerre C, de Truchis P, Neuro+3 Study G. Improvement of HIV-associated neurocognitive disorders after antiretroviral therapy intensification: the Neuro+3 study. J Antimicrob Chemother. 2021;76(3):743-52. doi: 10.1093/jac/dkaa473. PubMed PMID: 33179033.
244. Gates TM, Cysique LA, Siefried KJ, Chaganti J, Moffat KJ, Brew BJ. Maraviroc-intensified combined antiretroviral therapy improves cognition in virally suppressed HIV-associated neurocognitive disorder. AIDS. 2016;30(4):591-600. doi: 10.1097/QAD.0000000000000951. PubMed PMID: 26825032.
245. Ndhlovu LC, Umaki T, Chew GM, Chow DC, Agsalda M, Kallianpur KJ, Paul R, Zhang G, Ho E, Hanks N, Nakamoto B, Shiramizu BT, Shikuma CM. Treatment intensification with maraviroc (CCR5 antagonist) leads to declines in CD16-expressing monocytes in cART-suppressed chronic HIV-infected subjects and is associated with improvements in neurocognitive test performance: implications for HIV-associated neurocognitive disease (HAND). J Neurovirol. 2014;20(6):571-82. Epub 20140917. doi: 10.1007/s13365-014-0279-x. PubMed PMID: 25227930; PMCID: PMC4268390.
246. Baker JV, Wolfson J, Collins G, Morse C, Rhame F, Liappis AP, Rizza S, Temesgen Z, Mystakelis H, Deeks S, Neaton J, Schacker T, Sereti I, Tracy RP. Losartan to reduce inflammation and fibrosis endpoints in HIV disease. AIDS. 2021;35(4):575-83. doi: 10.1097/QAD.0000000000002773. PubMed PMID: 33252490; PMCID: PMC8062089.
247. Jankovska E, Svitek M, Holada K, Petrak J. Affinity depletion versus relative protein enrichment: a side-by-side comparison of two major strategies for increasing human cerebrospinal fluid proteome coverage. Clin Proteomics. 2019;16:9. Epub 20190226. doi: 10.1186/s12014-019-9229-1. PubMed PMID: 30890900; PMCID: PMC6390343.
248. Valade E, Tréluyer JM, Bouazza N, Ghosn J, Foissac F, Benaboud S, Fauchet F, Viard JP, Urien S, Hirt D. Population pharmacokinetics of emtricitabine in HIV-1-infected adult patients. Antimicrob Agents Chemother. 2014;58(4):2256-61. Epub 2014/02/03. doi: 10.1128/AAC.02058-13. PubMed PMID: 24492366; PMCID: PMC4023733.
249. Gagnieu MC, Barkil ME, Livrozet JM, Cotte L, Miailhes P, Boibieux A, Guitton J, Tod M. Population pharmacokinetics of tenofovir in AIDS patients. J Clin Pharmacol. 2008;48(11):1282-8. Epub 2008/09/08. doi: 10.1177/0091270008322908. PubMed PMID: 18779377.
250. Moore KH, Yuen GJ, Hussey EK, Pakes GE, Eron JJ, Bartlett JA. Population pharmacokinetics of lamivudine in adult human immunodeficiency virus-infected patients enrolled in two phase III clinical trials. Antimicrob Agents Chemother. 1999;43(12):3025-9. doi: 10.1128/AAC.43.12.3025. PubMed PMID: 10582904; PMCID: PMC89609.
251. Pfister M, Labbe L, Hammer SM, Mellors J, Bennett KK, Rosenkranz S, Sheiner LB, Adult ACTGS. Population pharmacokinetics and pharmacodynamics of efavirenz, nelfinavir, and indinavir: Adult AIDS Clinical Trial Group Study 398. Antimicrob Agents Chemother. 2003;47(1):130-7. doi: 10.1128/aac.47.1.130-137.2003. PubMed PMID: 12499180; PMCID: PMC148981.
252. Zhang J, Hayes S, Sadler BM, Minto I, Brandt J, Piscitelli S, Min S, Song IH. Population pharmacokinetics of dolutegravir in HIV-infected treatment-naive patients. Br J Clin Pharmacol. 2015;80(3):502-14. Epub 2015/03/31. doi: 10.1111/bcp.12639. PubMed PMID: 25819132; PMCID: PMC4574835.
253. Rizk ML, Du L, Bennetto-Hood C, Wenning L, Teppler H, Homony B, Graham B, Fry C, Nachman S, Wiznia A, Worrell C, Smith B, Acosta EP. Population pharmacokinetic analysis of raltegravir pediatric formulations in HIV-infected children 4 weeks to 18 years

of age. J Clin Pharmacol. 2015;55(7):748-56. Epub 2015/03/11. doi: 10.1002/jcph.493. PubMed PMID: 25753401; PMCID: PMC4572519.
254. Custodio JM, Gordi T, Zhong L, Ling KH, Ramanathan S. Population Pharmacokinetics of Boosted-Elvitegravir in HIV-Infected Patients. J Clin Pharmacol. 2016;56(6):723-32. Epub 2015/12/21. doi: 10.1002/jcph.657. PubMed PMID: 26449283.
255. Schipani A, Dickinson L, Boffito M, Austin R, Owen A, Back D, Khoo S, Davies G. Simultaneous population pharmacokinetic modelling of atazanavir and ritonavir in HIV-infected adults and assessment of different dose reduction strategies. J Acquir Immune Defic Syndr. 2013;62(1):60-6. Epub 2012/09/27. doi: 10.1097/QAI.0b013e3182737231. PubMed PMID: 23011396; PMCID: PMC3594700.
256. Molto J, Xinarianos G, Miranda C, Pushpakom S, Cedeno S, Clotet B, Owen A, Valle M. Simultaneous pharmacogenetics-based population pharmacokinetic analysis of darunavir and ritonavir in HIV-infected patients. Clin Pharmacokinet. 2013;52(7):543-53. Epub 2013/03/16. doi: 10.1007/s40262-013-0057-6. PubMed PMID: 23494984.
257. Allen-Bridson K, Pollock D. Response to "Potential Misclassification of Urinary Tract Related Bacteremia Upon Applying the 2015 Catheter-Associated Urinary Tract Infection Surveillance Definition From the National Healthcare Safety Network". Infect Control Hosp Epidemiol. 2016;37(9):1121. doi: 10.1017/ice.2016.142. PubMed PMID: 27420639.
258. Calcagno A, Simiele M, Alberione MC, Bracchi M, Marinaro L, Ecclesia S, Di Perri G, D'Avolio A, Bonora S. Cerebrospinal fluid inhibitory quotients of antiretroviral drugs in HIV-infected patients are associated with compartmental viral control. Clin Infect Dis. 2015;60(2):311-7. Epub 20141003. doi: 10.1093/cid/ciu773. PubMed PMID: 25281609.
259. Lahiri CD, Reed-Walker K, Sheth AN, Acosta EP, Vunnava A, Ofotokun I. Cerebrospinal fluid concentrations of tenofovir and emtricitabine in the setting of HIV-1 protease inhibitor-based regimens. J Clin Pharmacol. 2016;56(4):492-6. doi: 10.1002/jcph.612. PubMed PMID: 26247878; PMCID: PMC4744587.
260. Gelé T, Furlan V, Taburet AM, Pallier C, Becker PH, Goujard C, Gasnault J, Barrail-Tran A, Chéret A. Dolutegravir Cerebrospinal Fluid Diffusion in HIV-1-Infected Patients with Central Nervous System Impairment. Open Forum Infect Dis. 2019;6(6):ofz174. Epub 20190603. doi: 10.1093/ofid/ofz174. PubMed PMID: 31198814; PMCID: PMC6546201.
261. Tovar-y-Romo LB, Bumpus NN, Pomerantz D, Avery LB, Sacktor N, McArthur JC, Haughey NJ. Dendritic spine injury induced by the 8-hydroxy metabolite of efavirenz. J Pharmacol Exp Ther. 2012;343(3):696-703. Epub 20120913. doi: 10.1124/jpet.112.195701. PubMed PMID: 22984227; PMCID: PMC3500535.
262. Sandkovsky U, Swindells S, Moore R, Acosta EP, Fletcher CV. Acceptable plasma concentrations of raltegravir and etravirine when administered by gastrostomy tube in a patient with advanced multidrug-resistant human immunodeficiency virus infection. Pharmacotherapy. 2012;32(2):142-7. doi: 10.1002/PHAR.1015. PubMed PMID: 22392423; PMCID: PMC3711779.
263. Nwogu JN, Gandhi M, Owen A, Khoo SH, Taiwo B, Olagunju A, Berzins B, Okochi H, Tallerico R, Robertson K, Babalola CP. Associations between efavirenz concentrations, pharmacogenetics and neurocognitive performance in people living with HIV in Nigeria. AIDS. 2021;35(12):1919-27. doi: 10.1097/QAD.0000000000002984. PubMed PMID: 34115651; PMCID: PMC8462442.
264. Marzolini C, Telenti A, Decosterd LA, Greub G, Biollaz J, Buclin T. Efavirenz plasma levels can predict treatment failure and central nervous system side effects in HIV-1-infected patients. AIDS. 2001;15(1):71-5. doi: 10.1097/00002030-200101050-00011. PubMed PMID: 11192870.

265. Sandkovsky U, Podany AT, Fletcher CV, Owen A, Felton-Coleman A, Winchester LC, Robertson K, Swindells S. Impact of efavirenz pharmacokinetics and pharmacogenomics on neuropsychological performance in older HIV-infected patients. J Antimicrob Chemother. 2017;72(1):200-4. Epub 20160921. doi: 10.1093/jac/dkw403. PubMed PMID: 27655857; PMCID: PMC5161051.
266. Ranzani A, Castelli F, Di Biagio A, d'Arminio Monforte A, D'Avolio A, Soria A, Bai F, Foca E, Taramasso L, Calcagno A, Bresciani E, Torsello A, Bonfanti P, Lapadula G. Influence of efavirenz and 8-hydroxy-efavirenz plasma levels on cognition and central nervous system side effects. HIV Med. 2024;25(4):491-7. Epub 20231217. doi: 10.1111/hiv.13600. PubMed PMID: 38104964.
267. Arentoft A, Troxell K, Alvarez K, Aghvinian M, Rivera Mindt M, Cherner M, Van Dyk K, Razani J, Roxas M, Gavilanes M. HIV Antiretroviral Medication Neuropenetrance and Neurocognitive Outcomes in HIV+ Adults: A Review of the Literature Examining the Central Nervous System Penetration Effectiveness Score. Viruses. 2022;14(6). Epub 20220526. doi: 10.3390/v14061151. PubMed PMID: 35746623; PMCID: PMC9227894.
268. Bertrand J, Barrail-Tran A, Fayette L, Savic R, Goujard C, Teicher E, Barau C, Pruvost A, Taburet AM, Mentré F, Verstuyft C. Pharmacokinetic Model of Tenofovir and Emtricitabine and Their Intracellular Metabolites in Patients in the ANRS 134-COPHAR 3 Trial Using Dose Records. Antimicrob Agents Chemother. 2023;67(5):e0233918. Epub 20230426. doi: 10.1128/aac.02339-18. PubMed PMID: 37098914; PMCID: PMC10190280.
269. Lu Y, Goti V, Chaturvedula A, Haberer JE, Fossler MJ, Sale ME, Bangsberg D, Baeten JM, Celum CL, Hendrix CW. Population Pharmacokinetics of Tenofovir in HIV-1-Uninfected Members of Serodiscordant Couples and Effect of Dose Reporting Methods. Antimicrob Agents Chemother. 2016;60(9):5379-86. Epub 2016/06/30. doi: 10.1128/AAC.00559-16. PubMed PMID: 27353269; PMCID: PMC4997873.
270. Kawuma AN, Wasmann RE, Sinxadi P, Sokhela SM, Chandiwana N, Venter WDF, Wiesner L, Maartens G, Denti P. Population pharmacokinetics of tenofovir given as either tenofovir disoproxil fumarate or tenofovir alafenamide in an African population. CPT Pharmacometrics Syst Pharmacol. 2023;12(6):821-30. Epub 20230404. doi: 10.1002/psp4.12955. PubMed PMID: 37013631; PMCID: PMC10272303.
271. Habtewold A, Aklillu E, Makonnen E, Yimer G, Bertilsson L, Burhenne J, Owen JS. Population Pharmacokinetic Model Linking Plasma and Peripheral Blood Mononuclear Cell Concentrations of Efavirenz and Its Metabolite, 8-Hydroxy-Efavirenz, in HIV Patients. Antimicrob Agents Chemother. 2017;61(8). Epub 20170725. doi: 10.1128/AAC.00207-17. PubMed PMID: 28559276; PMCID: PMC5527565.
272. Robarge JD, Metzger IF, Lu J, Thong N, Skaar TC, Desta Z, Bies RR. Population Pharmacokinetic Modeling To Estimate the Contributions of Genetic and Nongenetic Factors to Efavirenz Disposition. Antimicrob Agents Chemother. 2017;61(1). Epub 20161227. doi: 10.1128/AAC.01813-16. PubMed PMID: 27799204; PMCID: PMC5192152.
273. Barceló C, Gaspar F, Aouri M, Panchaud A, Rotger M, Guidi M, Cavassini M, Buclin T, Decosterd LA, Csajka C, Study SHC. Population pharmacokinetic analysis of elvitegravir and cobicistat in HIV-1-infected individuals. J Antimicrob Chemother. 2016;71(7):1933-42. Epub 20160329. doi: 10.1093/jac/dkw050. PubMed PMID: 27029846.
274. Venuto CS, Cramer YS, Rosenkranz SL, Sulkowski M, Wyles DL, Cohen DE, Schmidt J, Alston-Smith BL, Morse GD. Raltegravir pharmacokinetics before and during treatment with ombitasvir, paritaprevir/ritonavir plus dasabuvir in adults with human immunodeficiency virus-1 and hepatitis C virus coinfection: AIDS Clinical Trials Group

sub-study A5334s. Br J Clin Pharmacol. 2020;86(1):132-42. Epub 20191212. doi: 10.1111/bcp.14148. PubMed PMID: 31656054; PMCID: PMC6983509.
275. Wang L, Soon GH, Seng KY, Li J, Lee E, Yong EL, Goh BC, Flexner C, Lee L. Pharmacokinetic modeling of plasma and intracellular concentrations of raltegravir in healthy volunteers. Antimicrob Agents Chemother. 2011;55(9):4090-5. Epub 20110711. doi: 10.1128/AAC.00593-11. PubMed PMID: 21746959; PMCID: PMC3165315.
276. Colombo S, Buclin T, Cavassini M, Décosterd LA, Telenti A, Biollaz J, Csajka C. Population pharmacokinetics of atazanavir in patients with human immunodeficiency virus infection. Antimicrob Agents Chemother. 2006;50(11):3801-8. Epub 20060828. doi: 10.1128/AAC.00098-06. PubMed PMID: 16940065; PMCID: PMC1635184.
277. Cojutti PG, Londero A, Della Siega P, Givone F, Fabris M, Biasizzo J, Tascini C, Pea F. Comparative Population Pharmacokinetics of Darunavir in SARS-CoV-2 Patients vs. HIV Patients: The Role of Interleukin-6. Clin Pharmacokinet. 2020;59(10):1251-60. doi: 10.1007/s40262-020-00933-8. PubMed PMID: 32856282; PMCID: PMC7453069.
278. Pardridge WM. CSF, blood-brain barrier, and brain drug delivery. Expert Opin Drug Deliv. 2016;13(7):963-75. Epub 20160411. doi: 10.1517/17425247.2016.1171315. PubMed PMID: 27020469.
279. Pardridge WM. Drug transport across the blood-brain barrier. J Cereb Blood Flow Metab. 2012;32(11):1959-72. Epub 20120829. doi: 10.1038/jcbfm.2012.126. PubMed PMID: 22929442; PMCID: PMC3494002.
280. Wong AD, Ye M, Levy AF, Rothstein JD, Bergles DE, Searson PC. The blood-brain barrier: an engineering perspective. Front Neuroeng. 2013;6:7. Epub 20130830. doi: 10.3389/fneng.2013.00007. PubMed PMID: 24009582; PMCID: PMC3757302.
281. Santos GMA, Locatelli I, Métral M, Calmy A, Lecompte TD, Nadin I, Hauser C, Cusini A, Hasse B, Kovari H, Tarr P, Stoeckle M, Fux C, Di Benedetto C, Schmid P, Darling KEA, Du Pasquier R, Cavassini M, Group NAitMaACNS. Cross-Sectional and Cumulative Longitudinal Central Nervous System Penetration Effectiveness Scores Are Not Associated With Neurocognitive Impairment in a Well Treated Aging Human Immunodeficiency Virus-Positive Population in Switzerland. Open Forum Infect Dis. 2019;6(7):ofz277. Epub 20190708. doi: 10.1093/ofid/ofz277. PubMed PMID: 31304188; PMCID: PMC6612860.
282. Barcelo C, Aouri M, Courlet P, Guidi M, Braun DL, Günthard HF, Piso RJ, Cavassini M, Buclin T, Decosterd LA, Csajka C, Study SHC. Population pharmacokinetics of dolutegravir: influence of drug-drug interactions in a real-life setting. J Antimicrob Chemother. 2019;74(9):2690-7. doi: 10.1093/jac/dkz217. PubMed PMID: 31119275.
283. VIREAD (tenofovir disoproxil fumarate), and [package insert]. Last revised: October 2001, Gilead Sciences, Inc: Foster City, CA, USA.
284. Croteau D, Letendre S, Best BM, Ellis RJ, Breidinger S, Clifford D, Collier A, Gelman B, Marra C, Mbeo G, McCutchan A, Morgello S, Simpson D, Way L, Vaida F, Ueland S, Capparelli E, Grant I, Group C. Total raltegravir concentrations in cerebrospinal fluid exceed the 50-percent inhibitory concentration for wild-type HIV-1. Antimicrob Agents Chemother. 2010;54(12):5156-60. Epub 20100927. doi: 10.1128/AAC.00507-10. PubMed PMID: 20876368; PMCID: PMC2981289.
285. Calcagno A, Simiele M, Motta I, Mornese Pinna S, Bertucci R, D'Avolio A, Di Perri G, Bonora S. Elvitegravir/Cobicistat/Tenofovir/Emtricitabine Penetration in the Cerebrospinal Fluid of Three HIV-Positive Patients. AIDS Res Hum Retroviruses. 2016;32(5):409-11. doi: 10.1089/aid.2015.0337. PubMed PMID: 26974711.